Coherence Recovery in Random Environments Using the Autoproduct

by

Nicholas J. Joslyn

A dissertation submitted in partial fulfillment
of the requirements for the degree of
Doctor of Philosophy
(Applied Physics)
in the University of Michigan
2023

Doctoral Committee:

Professor David R. Dowling, Chair
Professor Karl Grosh
Professor Robert Krasny
Assistant Professor Bogdan Popa
Assistant Professor Serife Tol

Nicholas J. Joslyn

njoslyn@umich.edu

ORCID iD: 0000-0002-5735-2854

Acknowledgements

First, I would like to thank my advisor, Professor David R. Dowling. Entering graduate school, I was not entirely sure what I wanted to research, and under your mentorship, I have developed analytical, computational, and experimental skills in a fascinating discipline. The level of professionalism, flexibility, and trust you show in your students allowed me to grow as both a scientist and a person. I will miss our weekly hour-long (often 90-minute) meetings. For this and so much more over the past 5 years, thank you.

To the rest of my committee members, Professors Karl Grosh, Robert Krasny, Bogdan Popa, and Serife Tol, thank you for your willingness to serve on my committee and offer feedback on the research. The breadth of intellectual expertise you each provided significantly increased the quality of this thesis.

Several other contributions to this work deserve recognition. I would like to thank Dr. Peter Dahl of the University of Washington for sharing data collected during at-sea experiments, and for the expeditious manner in which he answered all my questions about those datasets. I would also like to thank Dr. Alexander Douglass for collaborating on one chapter of this thesis. Sonia Gutt and Adam Singer assisted with some experimental data collection, without which, one chapter would not have been possible. Also, none of the work would have been possible without the following funding sources: US Department of Defense (National Defense Science and Engineering Graduate fellowship), Office of Naval Research (Award No: N00014-19-1-2459), and the Univ. of Michigan (Applied Physics Program and Rackham Graduate School).

To all the friends I made in Michigan, thank you for making it a fun place to live for five years. Alex W., you're a great weightlifting partner and meeting you & Lou on Central Campus provided some of my favorite memories. Nick L., I won't soon forget hanging out and slinging around the football in the parking lot after work. To members of the Dowling and Ceccio labs, thank you for making the office an enjoyable place to work. Brandon L., Dave G., Allison K., and Jane K., you guys made attending conferences as fun as I could hope. To past members of the lab I didn't overlap with, Brian W., Alex D., and T. J. Flynn, your work was a constant inspiration of what it means to be a good PhD student.

I would also like to thank my two undergraduate advisors, who inspired my interest in research and physics. Professor Heidi Berger, you always approached research with a genuine curiosity, and I try to emulate that myself. Professor David Olsgaard, little did I know how much I would use the Fourier transform when I first learned it in your class.

To sports talk radio and Spotify, I'm not sure if some of the mathematical derivations or experiments would have been completed without you.

Finally, to my family, your endless support is something I cherish. Dad, you've always inspired me to work hard and think critically. Mom, you've taught me balance and perseverance, even during challenging times. The two of you have helped me at every step in my academic journey. Lou, you're the man. From B. City to MI, you have motivated me to strive for big goals and to have fun, all while being an example of exactly that. You are the definition of a role model, and I know you are always there if I need you, technically or personally.

To Sam, meeting you was a greater discovery than any outlined in this document. Your love and support for me is boundless and I cannot thank you enough for all that you do. I'm so excited to see what lies ahead for us (and Winston and Felix) in our journey.

Table of Contents

List of Tables

List of Figures

Abstract

The study of wave propagation is a mature field of research with numerous avenues of theoretical, numerical, and experimental investigation. A prominent application is remote sensing, where recorded acoustic or electromagnetic waves are analyzed to elucidate information about their source or the environment with which they have interacted. The success of remote sensing tasks is often limited by the coherence of the recorded field, and the coherence of the recorded field is generally reduced by random fluctuations in the propagating medium.

In this thesis, the recovery of coherence in wave propagation through random media is studied. Coherence recovery is facilitated by the frequency-difference autoproduct, a quadratic product of complex fields at nearby frequencies, which synthetically estimates field content at the difference frequency of the two constituent fields. By downshifting to sufficiently low difference frequencies, the effects of random media, which typically scale with frequency, are mitigated or entirely removed. Here, the capability of the frequency-difference autoproduct to recover coherence is primarily assessed in underwater acoustic scattering from the sea surface. Theoretical predictions, numerical simulations, and laboratory experiments demonstrate the frequency-difference autoproduct restores coherent reflection even when the constituent scattered fields are nearly completely incoherent. Acoustic measurements collected in the Pacific Ocean and Atlantic Ocean further verify the conclusion. Analytical development of this concept revealed autoproduct-based recovery depends strongly on the autocorrelation function, or power spectrum by Fourier transform, of the randomly rough surface. A simple inversion strategy,

designed to exploit this dependence for the measurements collected at sea, identified minor adjustments to the nominal surface characteristics within experimental uncertainty and in agreement with a previous study of the Pacific Ocean dataset. Comparisons of frequency-difference autoproduct, frequency-sum autoproduct, and genuine acoustic field spatial coherence, determined from ocean recordings, conclude this portion of the thesis. Notably, autoproduct spatial coherence exists outside the recorded signal bandwidth, and the coherence lengths of the autoproducts were generally greater than that of the constituent acoustic field for the bottom-reflected sound analyzed here.

The second objective of the thesis research focuses on extensions to standard autoproduct theory. Higher-order autoproducts are discussed first, and the cubic frequency-difference autoproduct, capable of mimicking frequency content within the recorded signal bandwidth, receives primary consideration. Mathematical analyses of the governing field equations and examination of the cubic frequency-difference autoproduct's properties in simple propagation environments highlights the similarities with the quadratic autoproduct. Serendipitously, noise suppression is inherent in the bandwidth-averaging step of the cubic frequency-difference autoproduct construction. Using acoustic recordings and ambient ocean noise measurements, cubic autoproduct-based direction of arrival estimation is shown to outperform conventional methods in noisy environments. The other extension considered here is the electromagnetic frequency-difference autoproduct. Constructed as an outer product of the electric field vector with itself at nearby frequencies, the dyadic autoproduct quantity is explored theoretically, numerically, and experimentally. The frequency-shifting concept is maintained in electromagnetics, as confirmed by numerical computation of autoproducts generated from scattering of a TM-polarized plane wave by perfectly conducting infinite cylinders. Active target

localization experiments conducted in forested areas on campus demonstrate remote sensing problems associated with array sparsity and random scattering may be mitigated by the electromagnetic frequency-difference autoproduct, as they are for remote sensing with the acoustic frequency-difference autoproduct.

Chapter 1
Introduction

This thesis covers several phenomena in wave propagation and array signal processing. The purpose of this chapter is to review autoproducts, rough surface scattering, and spatial coherence. The reviews of rough surface scattering and spatial coherence are amalgamations of introductory material in Chapters 2 – 4 and 5, respectively, but are detailed here for convenience. Overall thesis objectives and individual chapter contributions are summarized as well.

1.1 Background

To motivate the physical intuition of coherence recovery, the literature concerning the autoproduct is reviewed first, followed by rough surface scattering and spatial coherence, electromagnetic propagation, and remote sensing.

1.1.1 Autoproduct Review

Consider a recorded acoustic signal with a nontrivial bandwidth. Conventional methods typically analyze the signal within this recorded bandwidth. However, recent research has shown that such a bandwidth restriction is not an inherent constraint. In fact, information outside of this bandwidth may be revealed through quadratic products of the recorded field at different frequencies, with and without complex conjugation of the lower frequency field (Dowling, 2018). The frequency-difference autoproduct, formed with complex conjugation of the lower-frequency field, probes field information at the frequency defined by the difference of the two constituent field frequencies. The frequency-sum autoproduct, formed without complex

conjugation of the lower-frequency field, probes field information at the frequency defined by the sum of the two constituent field frequencies. When averaged through the recorded signal bandwidth, with respect to the difference or sum frequency, these mathematical constructs may mimic genuine acoustic fields at the difference and sum frequencies, which lie outside of the recorded field's bandwidth (Lipa et al., 2018; Worthmann and Dowling, 2017).

Mathematically, the autoproducts may be constructed from any recorded field. In the following, $P(\boldsymbol{r}, \omega)$ defines the complex frequency-domain pressure field measured at position $\boldsymbol{r}$ and angular frequency $\omega = 2\pi f$ within the bandwidth of the source spectrum, $S(\omega)$. The frequency difference autoproduct, AP_Δ, and frequency-sum autoproduct, AP_Σ, are defined as

$$AP_\Delta(\boldsymbol{r}, \omega, \Delta\omega) \equiv P(\boldsymbol{r}, \omega_+)P^*(\boldsymbol{r}, \omega_-)\,, \tag{1.1a}$$

$$AP_\Sigma(\boldsymbol{r}, \omega, \Delta\omega) \equiv P(\boldsymbol{r}, \omega_+)P(\boldsymbol{r}, \omega_-)\,, \tag{1.1b}$$

where the asterisk indicates complex conjugation and $\omega_\pm \equiv \omega \pm \Delta\omega/2$ represent a pair of frequencies within the signal bandwidth with difference frequency $\Delta\omega = \omega_+ - \omega_-$ and sum frequency $\Sigma\omega = \omega_+ + \omega_- = 2\omega$. Equations (1.1a) and (1.1b) may be averaged through the recorded field's bandwidth, $\Omega_L \leq \omega \leq \Omega_H$, by

$$\langle AP_\Delta(\boldsymbol{r}, \Delta\omega)\rangle_{BW} = \frac{1}{\Omega_{BW}^\Delta}\int_{\Omega_C-\frac{1}{2}\Omega_{BW}^\Delta}^{\Omega_C+\frac{1}{2}\Omega_{BW}^\Delta} \frac{AP_\Delta(\boldsymbol{r}, \omega, \Delta\omega)}{S(\omega_+)\,S^*(\omega_-)}\,d\omega\,, \tag{1.2a}$$

$$\langle AP_\Sigma(\boldsymbol{r}, \Delta\omega)\rangle_{BW} = \frac{1}{\Omega_{BW}^\Sigma}\int_0^{\Omega_{BW}^\Sigma} \frac{AP_\Sigma(\boldsymbol{r}, \omega, \Delta\omega)}{S(\omega_+)S(\omega_-)}\,d(\Delta\omega)\,. \tag{1.2b}$$

where $\Omega_C = (\Omega_L + \Omega_H)/2$ is the in-band center frequency. The signal bandwidth available to average $AP_{\Delta,q}$ and $AP_{\Sigma,q}$ is given by $\Omega_{BW}^\Delta = \Omega_H - \Omega_L - \Delta\omega$ and $\Omega_{BW}^\Sigma = \min[2\Omega_H - \Sigma\omega, \Sigma\omega - 2\Omega_L]$, respectively. The division in the integrand of Eq. (2) removes dependence on the source spectrum. Hence, the bandwidth-averaged autoproducts, $\langle AP_\Delta(\boldsymbol{r}, \Delta\omega)\rangle_{BW}$ and $\langle AP_\Sigma(\boldsymbol{r}, \Delta\omega)\rangle_{BW}$,

are determined exclusively by the acoustic propagation characteristics of the medium. The bandwidth-averaging in Eq. (1.2) also suppresses quadratic cross terms, which vary with constituent field frequency, in multipath environments, thereby enhancing mimicry of the genuine difference or sum frequency acoustic field (Lipa et al., 2018; Worthmann and Dowling, 2017).

Autoproduct mimicry of a genuine acoustic field in free space is illustrated in Fig. 1.1. The acoustic field in free space is given by,

$$P(\boldsymbol{r}, \omega) = \frac{e^{ikr}}{r}, \tag{1.3}$$

where $k = \omega/c$, $c = 1480$ m/s is the sound speed in water, and r is the distance from the source. Acoustic fields, determined from Eq. (1.3), at 40 kHz, 50 kHz, and 10 kHz are shown in Fig. 1.1(a), Fig. 1.1(b), and Fig. 1.1(c), respectively. The frequency-difference autoproduct at 10 kHz, computed from applying Eq. (1.1a) to the constituent fields in Fig. 1.1(a) and Fig. 1.1(b), is shown in Fig. 1.1(d). All panels show the real component on height and range axes (with respect to the source location) and are normalized to unity maximum amplitude. Additionally, the wavelength is indicated in the bottom right corner of each panel.

The frequency-difference autoproduct exhibits excellent mimicry of the genuine acoustic field at 10 kHz. The minor amplitude discrepancies between the genuine field in Fig. 1.1(c) and the frequency-difference autoproduct in Fig. 1.1(d), evident by the lighter hue of the autoproducts at large ranges, are attributed to the spherical spreading loss of autoproducts as $1/r^2$ rather than $1/r$. Meanwhile, the phase, indicated by the red-to-blue variation, is a perfect match between panels. The frequency-difference autoproduct synthetically estimated 10 kHz acoustic field content from 40 kHz and 50 kHz recorded fields in the same environment, and it is this idea of synthetically shifting the frequency content that motivates much of the autoproduct

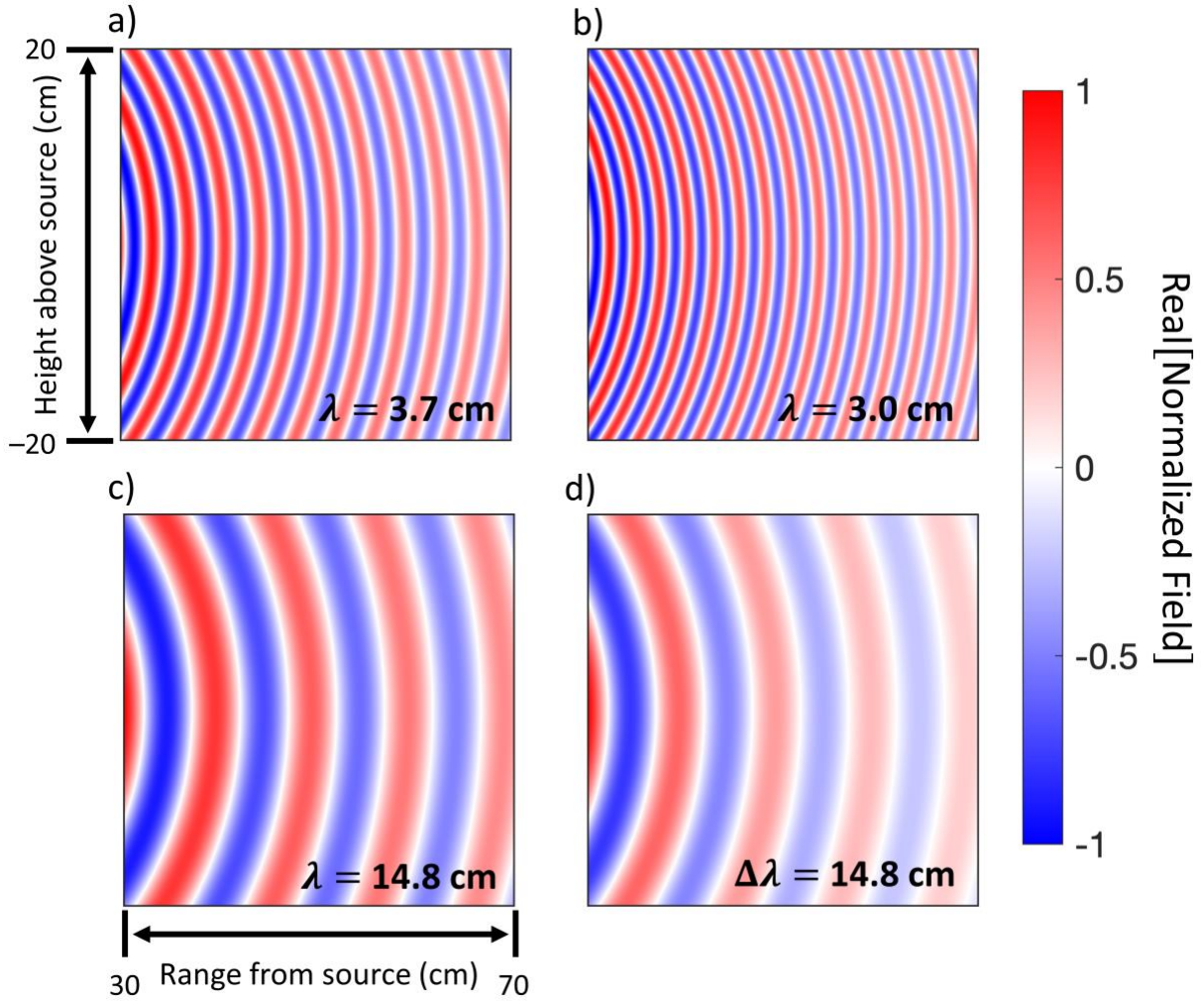

Figure 1.1: Autoproduct mimicry of acoustic fields in free space. The real part of the acoustic field at 40 kHz, 50 kHz, and 10 kHz is shown in (a), (b), and (c), respectively. The real part of the frequency-difference autoproduct at 10 kHz, constructed from panels (a) and (b) using Eq. (1.1a) is shown in (d). The frequency-difference autoproduct, generated entirely from higher frequency fields, provides good mimicry of the phase of the genuine acoustic field at 10 kHz.

work. Frequency-sum autoproducts, investigated much less frequently in this thesis, operate in a similar fashion to manufacture higher frequency content.

Prior work suggests that mimicry of below-band and above-band fields can be exploited for a variety of remote sensing tasks. Beamforming, a well-known array spatial filtering operation used to identify unknown source location or direction (Jensen et al., 2011; Van Veen

and Buckley, 1988), utilizing the frequency-sum autoproduct was successful for mildly inhomogeneous environments (Abadi et al., 2013) and at ultrasound frequencies in cavitation imaging (Abadi et al., 2018). The effectively higher frequency content offered by the frequency-sum autoproduct provided information with finer resolution than traditional methods, but may be hindered more strongly by spatially-separated sources or multipath propagation. Conversely, the frequency-difference autoproduct provides poorer resolution than the source signal but increases robustness (Dowling, 2018). Frequency-difference beamforming has been successfully implemented with broadband sparse-array recordings (Abadi et al., 2012), in laboratory and ocean environments (Douglass et al., 2017), and in the presence of strong, random scattering (Douglass and Dowling, 2019). Matched field processing (Bucker, 1976), another common source localization scheme, has also been explored with the autoproduct. Frequency-difference matched field processing has effectively localized remote sources in the shallow ocean (Worthmann et al., 2015, 2017) and at source-receiver ranges of hundreds of kilometers (Geroski et al., 2023; Geroski and Dowling, 2019, 2021). Extensions to coherent processing (Yuan et al., 2023), compressive sensing (Lee et al., 2023), and adaptive methods (Park et al., 2022; Wang et al., 2022; Xie et al., 2020; Yang et al., 2021) also exist. The larger literature for frequency-difference methods results directly from its improved robustness. Many of the issues hindering array-signal processing algorithms (array sparseness, environmental mismatch, random fluctuations) can be minimized by the low difference frequency field information available from the frequency-difference autoproduct.

The ability proffered by the frequency-difference autoproduct to effectively minimize random fluctuations provides the motivation for much of this thesis. Douglass and Dowling (2019) demonstrate the ability of the frequency-difference autoproduct to reliably provide

beamformed output in an environment with strong, randomly located, spherical scatterers by shifting the signal processing to a lower, below-the-signal-band frequency where the effects of scattering are not as strong. The same principle is utilized in Chapters 2 – 4 for random rough surface scattering. By selecting a sufficiently-low difference frequency, the apparent roughness of a random surface is reduced, and coherent surface reflection may be recovered.

Many of the aforementioned autoproduct studies investigate measured (or simulated) autoproduct cross-spectral density matrices, rather than the autoproduct fields, themselves. Experimental autoproduct pseudofield quantities have been studied in a Lloyd's mirror environment (Lipa et al., 2018; Worthmann and Dowling, 2017) and in a refracting ocean (Geroski et al., 2021). Another thrust of this research, therefore, is to extend the pseudofield analysis to include measurements of autoproducts constructed from constituent fields scattered by a randomly rough surface.

The effect of diffraction on the autoproduct has been studied for shadow zones (Worthmann and Dowling, 2020a) and refracting environments (Worthmann and Dowling, 2020b). Caustics (ray path crossing points due to refraction) significantly hinder autoproduct mimicry of out-of-band fields, but this can be rectified with ad hoc phase corrections (Geroski and Dowling, 2019). Although caustics can be an important ocean acoustic propagation consideration, especially at long ranges, analytically addressing the effects of both a refracting ocean sound speed profile and rough surface scattering is outside of the scope of the thesis.

The autoproduct shares features with other signal processing concepts (Dowling, 2018). The quadratic product of two complex field amplitudes is similar to the spatial coherence function (Dahl, 2004). Additionally, single Fourier transforms of the frequency-difference autoproduct yield the Wigner-Ville transform and the ambiguity function (Cohen, 1989). When

bandwidth-averaged, the frequency-difference autoproduct is a source-spectrum-normalized frequency-domain autocorrelation function. The parametric array (Westervelt, 1963) introduces a frequency shift through a physical nonlinearity in the acoustic propagation, rather than quadratic products of the recorded linear acoustic field. In electromagnetics, Δk radar (Popstefanija et al., 1993; Weissman, 1973) is a two-frequency correlation function that often ignores phase in favor of amplitude. The construction of the frequency-difference autoproduct differs from Δk radar and the electromagnetic frequency correlation function (Sarabandi et al., 1999) in that it does not require an ensemble average nor a normalization.

Although there is no inherent restriction to fluid-borne acoustic waves (Dowling, 2018), the autoproduct has rarely been implemented outside of acoustics. Currently, the only autoproduct studies to not use acoustic fields are seismic wave backprojection of earthquakes (Neo et al., 2022) and preliminary electromagnetic simulations in random media (Geroski, 2021). Chapter 6 and Chapter 7 of this thesis cover extensions to standard autoproduct theory not previously reported in the literature.

1.1.2 Rough Surface Scattering

The scattering of waves from randomly rough surfaces is relevant in both electromagnetics and acoustics. This topic has been studied extensively and review material exists as textbooks (Bass and Fuks, 1979; Beckmann and Spizzichino, 1963; Oglivy, 1991), survey papers (Darmon et al., 2020; Elfouhaily and Guérin, 2004; Fortuin, 1970), and chapters of textbooks (Brekhovskikh and Lysanov, 1991; Medwin and Clay, 1998). Rough surface scattering is particularly pertinent in ocean acoustics, where a randomly rough ocean surface and ocean bottom reflect and scatter sound waves. Here, incoherent scattering of acoustic energy into non-specular directions increases transmission loss and reverberation, both of which reduce the effectiveness of sonar

systems (Urick, 1983). The resulting coherent (specular) surface reflection loss increases with surface roughness (relative to acoustic wavelength) and reduces the effectiveness of acoustic signal processing algorithms and remote sensing tasks.

Acoustic scattering from a rough surface is generally analyzed via one of the following three approaches: perturbation theory (Harper and Labianca, 1975), Kirchhoff approximation (Eckart, 1953), or the small slope approximation (Thorsos and Broschat, 1995). The former two methods may intuitively be considered appropriate for scattering from small and large surface roughness, respectively. These models are generally not in agreement for surfaces with roughness applicable to both (Thorsos and Jackson, 1989). The small slope approximation was developed as a general scattering solution that reduces to perturbation theory and the Kirchhoff approximation in the appropriate limits. An extensive list of applications of all three methods is noted in the recent review paper (Darmon et al., 2020). In the present thesis research, the Kirchhoff approximation was favored over these other scattering formulations due to its validity in the specular direction, validity for large surface roughness, and convenient analytical form.

The utility and limitations of the Kirchhoff (tangent plane) approximation have been studied for decades (Eckart, 1953). In (Meecham, 1956), the Kirchhoff approximation is found to be valid for small slopes and large minimum radius of curvature with respect to the incident wavelength. A quantitative statement of this criterion is derived in (Lynch, 1970). Small grazing angles lead to shadowing and multiple scattering, which can be accounted for [e.g., (Lynch and Wagner, 1970)], but generally limit the applicability of the Kirchhoff approximation. For scattering from a Gaussian roughness spectrum, the ratio of correlation length to incident wavelength is the most important factor governing the Kirchhoff approximation's validity (Thorsos, 1988). The Kirchhoff approximation has also been applied to scattering from a

Pierson-Moskowitz sea surface (Thorsos, 1990), dynamic rough surfaces (Dowling and Jackson, 1993), and sinusoidal surface waves (Richards et al., 2018).

In the Kirchhoff approximation, the mean acoustic field reflected from an ensemble of randomly rough surfaces loses coherence with the incident field as $khcos\theta$ increases (Medwin and Clay, 1998), where k is the incident field wavenumber, h is the root-mean-square roughness height, and θ is the incidence angle. Thus, for fixed rough-surface properties and incidence angle, a reflected field at lower wavenumber should retain more coherence. Hence, a tractable problem is identifying if the frequency-difference autoproduct, a synthetic estimate of field information at a lower frequency, can regain coherence from randomly rough-surface-scattered constituent fields that have lost coherence. Coherence across surface realizations is inherently a single-receiver quantity, but spatial coherence is also an important concern for array signal processing techniques.

1.1.3 Spatial Coherence

As acoustic environments become more variable and complex, the acoustic field's coherence between spatially-separated receivers commonly decreases. Predicting field coherence between two points in space is a difficult task, as it is a function of the locations of the two points, the signal frequency, and the characteristics of the environment between the sound source and the two points. Plus, coherence measurements may be degraded when noise is present. In general, coherence increases with decreasing receiver separation and decreasing frequency, as well as with decreased environmental complexity (Urick, 1983), although coherence in the presence of certain environmental characteristics has been shown to exhibit unintuitive behavior (Heaney, 2011).

Limited coherence length can be problematic for array signal processing in the ocean, especially for towed horizontal arrays or deep ocean vertical arrays, where the array aperture can easily exceed the field's coherence length at the frequencies of interest. Coherence length is directly related to the array gain (Carey, 1998; Carey and Moseley, 1991) and thus has important implications in beamforming (Cox, 1973; Morgan and Smith, 1990) and matched field processing applications (Baggeroer et al., 1993). When an array is nominally shorter than the field's coherence length, all of its elements should contribute positively to the achievable array gain; conversely, adding array elements that extend the array's aperture beyond the coherence length generally does not provide significant improvement and can potentially reduce the performance of array signal processing techniques. In particular, prior work has shown that for shallow water environments, spatial coherence length is a primary factor in predicting performance (Rolt and Abbot, 1997). For a known finite coherence, the theoretical limitations of conventional beamforming methods with a linear array are understood and readily calculated (Cox, 1973; Morgan and Smith, 1990). Coherence length has been studied in a variety of simulation and experimental geometries and scenarios, including with both vertical and horizontal arrays (Wan et al., 2009), in the presence of internal waves (Duda et al., 2012; Finette and Oba, 2003; Lunkov and Petnikov, 2014), with varying channel depth (Carey, 1998), in the presence of multipath propagation (Carey and Moseley, 1991), and at long ranges (Andrew et al., 2005; Gorodetskaya et al., 1999), to understand the influence of various ocean environmental characteristics. The coherence of acoustic waves scattered from the ocean surface (Dahl, 2004, 2010; Dowling and Jackson, 1993) and floor sediment (Berkson, 1980; Brown et al., 2018) has also been investigated.

In spite of the extensive literature, a shared characteristic of all existing work on spatial coherence is the limitation to in-band signal frequencies, a typical constraint of conventional signal processing methods. And, despite the importance of coherence in array signal processing applications, the spatial coherence of autoproducts has yet to be directly examined, outside of initial work in (Douglass, 2019) that developed into Chapter 5 of the current thesis. The autoproducts provide a means for processing signals at frequencies below and above the signal bandwidth; thus, the coherence of the autoproducts relative to that of genuine in-band fields is critical for understanding their performance for various applications. The primary contribution of this component of thesis research, therefore, is to report the horizontal spatial coherence properties of autoproducts computed from ocean measurements and compare them to those of genuine acoustic fields in the same environment.

1.2 Thesis Overview

This thesis contains two major components. The first thesis objective, covered in Chapters 2 – 5, is to thoroughly investigate autoproduct coherence in underwater acoustic random rough surface scattering. Three chapters examine coherent reflection of signals scattered from the ocean surface. A study of the spatial coherence of bottom-reflected sound in the ocean closes the work completed for this objective. The second research objective, covered in Chapters 6 & 7, is to formulate extensions to standard autoproduct theory and investigate their potential utility for robust remote sensing.

Chronological development of this thesis is not mirrored directly in the chapter presentation. The chapter order, outlined below, was favored to provide a logical intellectual development of the coherence work, prior to shifting focus to other autoproduct constructs. Additionally, Chapters 2

– 6 are near reproductions of journal articles or in-preparation manuscripts, and only minor formatting adjustments have been made. Consequently, content overlap between chapters exists, particularly of introductory material, generic figures, and autoproduct equations, but the aim of each section is sufficiently distinct to merit its own chapter. The contributions are summarized below.

Chapter 2 introduces the frequency-difference autoproduct constructed from rough surface scattered acoustic fields. Theoretical, numerical, and laboratory experiments support the premise of coherence recovery possible by the frequency-difference autoproduct. The work has been published in the Journal of the Acoustical Society of America (Joslyn and Dowling, 2022).

Chapter 3 tests the analytic formula derived in Chapter 2. Frequency-difference autoproducts determined from measurements collected at sea of high-frequency acoustic fields scattered by a significantly rough ocean surface match theoretical predictions. This contribution is expected to be submitted to the Journal of the Acoustical Society of America in the coming months.

Chapter 4 expands the theoretical analysis of Chapters 2 & 3 to account for scattering from sea surfaces possessing a non-analytic power spectrum. Theoretical predictions agree well with data collected in the ocean, and an autoproduct-based approach to environmental characterization of surface statistics is presented. This contribution is expected to be submitted to the Journal of the Acoustical Society of America in the coming months.

Chapter 5 presents measurements of spatial coherence and coherence length for the acoustic field, frequency-difference autoproduct, and frequency sum autoproduct from seafloor-reflected sound recorded in the ocean. The work initially began in (Douglass, 2019) and has been published in MDPI Acoustics (Joslyn et al., 2022).

Chapter 6 introduces the concept of higher-order autoproducts. The work primarily focuses on the frequency-difference autoproduct and its serendipitous noise suppression attributes. Successful direction of arrival estimation of noisy ocean recordings underscores the potential of the cubic frequency-difference autoproduct to reduce noise in array signal processing tasks. This contribution is expected to be submitted to the Journal of the Acoustical Society of America in the coming months.

Chapter 7 introduces the electromagnetic frequency-difference autoproduct. Theoretical formulation and numerical modeling precede discussion of the active target localization experiment. Experimental measurements were obtained in collaboration with undergraduate students Sonia Gutt and Adam Singer, and the formative concepts for this contribution were developed in (Geroski, 2021).

Chapter 8 summarizes the seven main conclusions drawn from this thesis and proposes several areas of future research based on the findings presented herein.

Chapter 2

Recovery of Coherent Reflection from Rough-Surface Scattered Acoustic Fields via the Frequency-Difference Autoproduct

The acoustic field reflected from a random rough surface loses coherence with the incident field in the Kirchhoff approximation as $khcos\theta$ increases, where k is the incident field wavenumber, h is the root-mean-square roughness height, and θ is the incidence angle. Thus, for fixed rough-surface properties and incidence angle, a reflected field at lower wavenumber should retain more coherence. Recent results suggest that the frequency-difference autoproduct formed from complex acoustic field amplitudes at two nearby frequencies can recover acoustic information at the difference of those frequencies even when the difference frequency is below the recorded field's bandwidth. Herein analytical, computational, and experimental results are presented for the extent to which the frequency-difference autoproduct recovers coherence from randomly rough-surface-scattered constituent fields that have lost coherence. The analytical results, developed from the Kirchhoff approximation and formal ensemble averaging over randomly rough surfaces with Gaussian height distributions and Gaussian correlation functions, indicate that the coherence of the rough-surface-reflected frequency-difference autoproduct depends on the surface correlation length and $\Delta khcos\theta$, where Δk is the difference of the autoproduct's constituent field wavenumbers. These results compare favorably with Monte-Carlo simulations of rough surface scattering, and with laboratory experiments involving long surface correlation lengths where $1 \leq khcos\theta \leq 3$. The following chapter is a near reproduction of a journal article

(Joslyn and Dowling, 2022). For clarity, formulas and figures repeated elsewhere in this thesis are maintained in this section.

2.1 Introduction

The scattering of waves from randomly rough surfaces is relevant in both electromagnetics and acoustics. This topic has been studied extensively and review material exists as textbooks (Bass and Fuks, 1979; Beckmann and Spizzichino, 1963; Oglivy, 1991), survey papers (Elfouhaily and Guérin, 2004; Fortuin, 1970), and chapters of textbooks (Brekhovskikh and Lysanov, 1991; Medwin and Clay, 1998). Rough surface scattering is particularly pertinent in ocean acoustics, where a randomly rough ocean surface and ocean bottom reflect and scatter sound waves. Here, incoherent scattering of acoustic energy into non-specular directions increases transmission loss and reverberation, both of which reduce the effectiveness of sonar systems (Urick, 1983). The resulting coherent (specular) surface reflection loss increases with surface roughness (relative to acoustic wavelength) and reduces the effectiveness of acoustic signal processing algorithms and remote sensing tasks.

This paper presents theoretical, numerical, and experimental investigations into the recovery of reflected-field coherence that is possible from the frequency-difference autoproduct (Worthmann and Dowling, 2017) when incident acoustic waves, with wavenumber k, are reflected and scattered from a two-dimensional, randomly-rough pressure-release surface (the three-dimensional scattering problem) with root-mean-square (rms) roughness h and correlation length L. The isotropic random rough surfaces considered here are described by Gaussian height distributions and Gaussian correlation functions. The Gaussian correlation function, though limited in applicability to realistic rough surfaces, simplifies theoretical analysis (Thorsos, 1988) and is therefore considered here. The theoretical and simulation results are obtained using the

Kirchhoff approximation (Eckart, 1953; Medwin and Clay, 1998) for point-source-to-receiver geometries that emphasize specular reflection at incidence angle θ measured from the surface normal. The experiments were conducted in a laboratory water tank for $1 \leq kh\cos\theta \leq 3$ under long surface correlation length conditions ($kL \gg 1$). Interestingly, the results from all three approaches agree well and indicate that the coherent reflection coefficient for the frequency-difference autoproduct may be close to one even when the coherent reflection coefficients of its constituent fields are much less than one.

The Kirchhoff approximation is commonly understood to be accurate in the specular direction at large grazing angles. Small grazing angles lead to shadowing and multiple scattering, which can be accounted for [e.g., (Lynch and Wagner, 1970)], but are outside of the scope of this paper. Other prominent scattering methods include perturbation theory (Harper and Labianca, 1975) and the small slope approximation (Thorsos and Broschat, 1995). The Kirchhoff approximation was favored over these other scattering formulations due to its convenient analytical form and its validity for large kh in the specular direction. The utility and limitations of the Kirchhoff (tangent plane) approximation have been studied for decades (Eckart, 1953). In (Meecham, 1956), the Kirchhoff approximation is found to be valid for small slopes and large minimum radius of curvature with respect to the incident wavelength. A quantitative statement of this criterion is derived in (Lynch, 1970). For scattering from a Gaussian roughness spectrum, the ratio of correlation length to incident wavelength is the most important factor governing the Kirchhoff approximation's validity (Thorsos, 1988). The Kirchhoff approximation has also been applied to scattering from a Pierson-Moskowitz sea surface (Thorsos, 1990), dynamic rough surfaces (Dowling and Jackson, 1993), and sinusoidal surface waves (Richards et al., 2018).

A shared focus of these prior studies is consideration of scattering within the acoustic field's bandwidth. However, recent research has shown that such a limitation is not an inherent constraint (Dowling, 2018). The frequency-difference autoproduct, formed from a quadratic product of complex field amplitudes at two different frequencies within the incident field's bandwidth, mimics a genuine field at the (possibly below-band) difference frequency, subject to modified boundary conditions (Lipa et al., 2018; Worthmann and Dowling, 2017).

The frequency-difference autoproduct shares features with other scattered-field constructs. In particular, the derivation provided in Sec. II is similar to the derivations of the rough surface frequency correlation function in (Bozma and Kuc, 1991), (McDaniel, 1992), and (Gulin, 1975). However, different Fresnel approximations and beam functions distinguish the work described here from the former, and different surface correlation functions distinguish the work described here from the latter two. Additionally, the formulation provided here utilizes attributes unique to the frequency-difference autoproduct construction. For additional discussion of the relationship between the autoproduct and other quadratic fields, see (Worthmann and Dowling, 2017) or (Dowling, 2018).

Prior work suggests that the frequency-difference autoproduct can be successfully exploited for beamforming (Abadi et al., 2012; Douglass et al., 2017; Douglass and Dowling, 2019) and source localization (Geroski and Dowling, 2019; Worthmann et al., 2015) when conventional methods fail. In particular, (Douglass and Dowling, 2019) demonstrate the ability of the frequency-difference autoproduct to reliably provide beamformed output in an environment with strong, randomly located, spherical scatterers by shifting the signal processing to a lower, below-the-signal-band frequency where the effects of scattering are not as strong. The

same principle is utilized in this paper. By selecting a sufficiently low difference frequency, the apparent roughness of a random surface is reduced, and coherent reflection may be recovered. The aforementioned autoproduct studies investigate measured (or simulated) autoproduct cross-spectral density matrices, rather than the autoproduct fields, themselves. Autoproduct fields have been studied in a Lloyd's mirror environment (Lipa et al., 2018; Worthmann and Dowling, 2017) and in a refracting ocean (Geroski et al., 2021). This paper extends autoproduct field analysis to include scattering from a randomly rough surface.

The primary purpose of this paper is to report on the recovery of coherent reflection from a randomly rough surface using the frequency-difference autoproduct. A secondary motivation is predicting and measuring the frequency-difference autoproduct fields themselves, in rough-surface scattering environments. To accomplish both aims, analytical results for the frequency-difference autoproduct are developed for diverging spherical waves incident on a randomly rough pressure-release surface with Gaussian height distribution and Gaussian correlation function. The scattering of the constituent acoustic fields in the signal bandwidth is simplified by the Kirchhoff approximation. Numerical evaluations of the Helmholtz-Kirchhoff integral are shown to support the theoretical derivations. Results from an experiment using a laboratory water tank provide verification of the long correlation length limit of the analytical and computational predictions of the frequency-difference autoproduct.

The remainder of this paper is organized as follows. Section 2.2 presents the mathematical background for the frequency-difference autoproduct with rough surface scattering and provides formal results for the ensemble-averaged rough-surface-scattered frequency-difference autoproduct. Section 2.3 describes the simulation environment and shows comparisons of theoretical and numerical results. Section 2.4 describes the experimental setup

and provides comparisons of measured to theoretical results. Section 2.5 provides a summary and three conclusions drawn from this work.

2.2 Theoretical Fields

This section presents the mathematical formulation for the frequency-difference autoproduct and its extension to fields scattered from randomly rough surfaces. The definition of the frequency-difference autoproduct and comparison metrics precede a brief overview of the Helmholtz-Kirchhoff-Fresnel integral formulation. Then, the rough surface frequency-difference autoproduct is derived and discussed.

2.2.1 Frequency-Difference Autoproduct and Comparison Metrics

In the following, $P(\boldsymbol{R_2}, \omega)$ defines the complex frequency-domain surface-reflected pressure field at position $\boldsymbol{R_2}$ and angular frequency ω from an omnidirectional point source at $\boldsymbol{R_1}$ with source spectrum $S(\omega)$. To form the frequency-difference autoproduct, $\widetilde{AP}_\Delta$, two frequencies within the bandwidth of $S(\omega)$ are required:

$$\widetilde{AP}_\Delta(\boldsymbol{R_2}, \omega, \Delta\omega) \equiv P(\boldsymbol{R_2}, \omega_+)P^*(\boldsymbol{R}_2, \omega_-)\,, \tag{2.1}$$

where the asterisk indicates complex conjugation, $\Delta\omega = \omega_+ - \omega_-$ is the (user-selectable) difference frequency, and $\omega_\pm \equiv \omega \pm \Delta\omega/2$ represent a pair of frequencies separated by the desired difference frequency. For a broadcast source with nonzero bandwidth, $\Omega_L \leq \omega \leq \Omega_H$, Eq. (2.1) may be bandwidth-averaged by

$$\langle AP_\Delta(\boldsymbol{R_2}, \Delta\omega)\rangle_{BW} = \frac{1}{\Omega_{BW}^\Delta}\int_{\Omega_C-\frac{1}{2}\Omega_{BW}^\Delta}^{\Omega_C+\frac{1}{2}\Omega_{BW}^\Delta} \frac{\widetilde{AP}_\Delta(\boldsymbol{R_2}, \omega, \Delta\omega)}{S(\omega_+)\,S^*(\omega_-)}\,d\omega\,, \tag{2.2}$$

where $\Omega_{BW}^\Delta = \Omega_H - \Omega_L - \Delta\omega$ is the signal bandwidth available for averaging and $\Omega_C = (\Omega_L + \Omega_H)/2$ is the center frequency of the signal bandwidth. The division in the integrand of

Eq. (2.2) removes dependence on the source spectrum. Hence, the bandwidth-averaged autoproduct, $\langle AP_{\Delta}(\boldsymbol{R_2}, \Delta\omega)\rangle_{BW}$, is determined exclusively by the acoustic propagation characteristics of the medium. The bandwidth-averaging in Eq. (2.2) also suppresses quadratic cross terms, which vary with constituent field frequency, in multipath environments (Lipa et al., 2018; Worthmann and Dowling, 2017). Although it is possible to select $\Delta\omega \geq \Omega_L$ for a sufficiently wideband signal, $\Delta\omega$ will be referred to as a below-band frequency in this paper for simplicity.

To facilitate comparisons between theoretical, simulated, and experimental autoproduct fields, as well as genuine acoustic fields, a normalized complex spatial cross-correlation coefficient is employed as a figure of merit. The definition implemented here matches that used by (Lipa et al., 2018) and (Geroski et al., 2021). For a field, ψ, discretely sampled by K receivers (at locations $\boldsymbol{r_k}$) and a theoretical field, Ψ, the spatial cross-correlation coefficient χ is defined as

$$\chi(\omega) = \frac{\sum_{k=1}^{K} \psi(\boldsymbol{r_k}, \omega)\Psi^*(\boldsymbol{r_k}, \omega)}{[\sum_{k=1}^{K}|\psi(\boldsymbol{r_k}, \omega)|^2]^{1/2}[\sum_{k=1}^{K}|\Psi(\boldsymbol{r_k}, \omega)|^2]^{1/2}} \,. \tag{2.3}$$

This definition leads to a complex number residing within the unit circle on the complex plane and indicates the match of the normalized magnitude and phase of ψ and Ψ. Similar to other complex correlations [for instance spatial coherence, see(Dahl, 2004)], values of $|\chi|$ near 0 indicate a poor match between fields while values of $|\chi|$ near 1 indicate very similar fields. Additionally, a nonzero phase of χ represents a consistent phase difference between ψ and Ψ. When non-normalized magnitudes are of interest, the root-mean-square-error (RMSE) is determined from:

$$\mathrm{RMSE}(\omega) = \sqrt{\frac{1}{K}\sum_{k=1}^{K}|\psi(\boldsymbol{r_k}, \omega) - \Psi(\boldsymbol{r_k}, \omega)|^2} \,. \tag{2.4}$$

To quantitatively compare reflected-field coherence between autoproducts and genuine acoustic fields, the coherent reflection coefficient $\mathcal{R}_{coh}$ [see e.g.,(Medwin and Clay, 1998)] was predicted, computed, and measured. The definition of $\mathcal{R}_{coh}$ is given by

$$\mathcal{R}_{coh} = \frac{\langle \psi_{rough} \rangle}{\psi_{flat}}, \tag{2.5}$$

where $\langle\ \rangle$ indicates an ensemble average over surface realizations, ψ is either an acoustic field or the frequency-difference autoproduct, and the subscripts *rough* and *flat* denote rough-surface-scattered and flat-surface-reflected fields, respectively. Values of $|\mathcal{R}_{coh}|$ near 0 indicate a lack of coherence across surface realizations while values of $|\mathcal{R}_{coh}|$ near 1 indicate significant coherence across surface realizations. The phase of $\mathcal{R}_{coh}$ represents phase shifts that occur during reflection from a rough interface, but do not affect overall coherence.

2.2.2 Helmholtz-Kirchhoff-Fresnel Integral

To construct the rough-surface frequency-difference autoproduct, an accurate scattered pressure field is necessary. For the analytical results, the Helmholtz-Kirchhoff-Fresnel (HKF) integral is utilized to determine this scattered field. A terse overview of the HKF integral derivation found in (Medwin and Clay, 1998) is provided to introduce the equations necessary for the frequency-difference autoproduct and to highlight important features for the numerical simulations described in Sec. III.

The rough surface scattering environment is shown in Fig. 2.1. The randomly rough interface $z = \zeta(x, y)$ divides two homogeneous media, and the mean level of $\zeta(x, y)$ ($z = 0$) defines the x-y plane. The plane of incidence, with source-receiver axis aligned with *x*, defines the x-z plane and the angle of incidence is θ. The origin of the Cartesian coordinate system is at the specular point for flat-surface reflection between the omnidirectional source at $\boldsymbol{R_1}$ and the

receiver at $\boldsymbol{R_2}$. In all analyses, the direct path spherical wave response at the receiver is set aside to focus on the surface-scattered field.

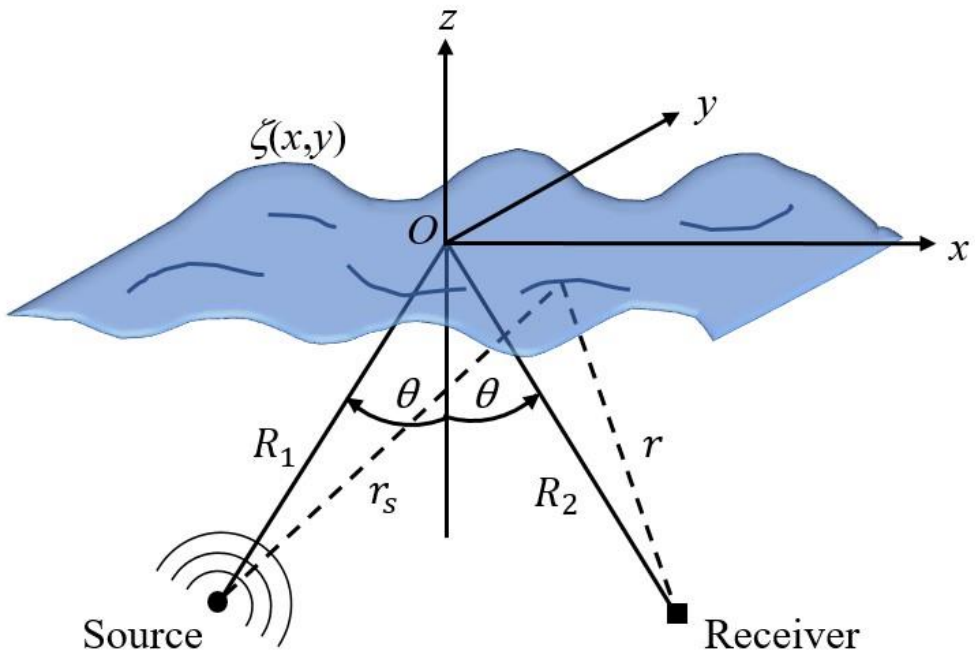

Figure 2.1: Scattering geometry and variables. The Cartesian coordinate system is centered on the specular point for flat-surface reflection between source and receiver, and the mean level of the rough surface determines the $z = 0$ plane. The source is located at $\boldsymbol{R_1}$ and the receiver at $\boldsymbol{R_2}$.

The integral solution for the scattered field at the receiver in a medium with constant sound speed *c* is given by the Helmholtz-Kirchhoff integral [e.g., (Medwin and Clay, 1998)],

$$P(\boldsymbol{R_2}, \omega) = \frac{1}{4\pi}\int_S \left[P\frac{\partial}{\partial n}\left(\frac{e^{ikr}}{r}\right) - \frac{e^{ikr}}{r}\frac{\partial P}{\partial n}\right] dS, \tag{2.6}$$

where S is the two-dimensional rough surface described by $z = \zeta(x, y)$, n is the surface normal into the half-space that contains the source, and r is the distance from a surface point to the receiver. To evaluate the integrand, the Kirchhoff approximation modifies the boundary conditions on the surface:

$$P = \Gamma P_{inc}, \tag{2.7a}$$

$$\frac{\partial P}{\partial n} = -\Gamma \frac{\partial P_{inc}}{\partial \mathrm{n}}, \tag{2.7b}$$

for incident wave, P_{inc}, and reflection coefficient Γ. Equations (2.7a) and (2.7b) are exact for reflection from a flat surface. The validity of this approximation therefore depends on the local radius of curvature (Lynch, 1970; Meecham, 1956) but is generally accurate near the specular direction (Thorsos, 1988, 1990).

The incident wave P_{inc} is radiation from an omnidirectional point source with source strength $S(\omega)$:

$$P_{inc}(\omega) = S(\omega)\frac{e^{ikr_s}}{r_s}, \tag{2.8}$$

where r_s is the distance from the source to a point on the surface. Substitution of Eqs. (2.7) and (2.8) into Eq. (2.6) and assumption of a constant reflection coefficient yields

$$P(\boldsymbol{R_2}, \omega) = \frac{S(\omega)\Gamma}{4\pi}\int_S \frac{\partial}{\partial n}\left(\frac{e^{ik(r+r_s)}}{r r_s}\right) dS. \tag{2.9}$$

Equation (2.9) is the Helmholtz-Kirchhoff integral with the Kirchhoff approximation, and it can be numerically evaluated (see Chapter 2.3). Further analytical manipulation requires expansion of the geometrical terms as well as evaluation of the normal derivative. An overview of this algebraic effort can be found in (Medwin and Clay, 1998). Utilization of the Fresnel approximations and assumption of small surface slopes results in the HKF integral (Medwin and Clay, 1998):

$$P(\boldsymbol{R_2}, \omega) = -\frac{iS(\omega)\Gamma\omega\cos\theta}{2\pi c R_1 R_2} e^{i\frac{\omega}{c}(R_1+R_2)} \int_{-\infty}^{\infty}\int_{-\infty}^{\infty} e^{\frac{i\omega}{cR}\left(x'^2\cos^2\theta + y'^2\right) + 2i\frac{\omega}{c}\cos\theta\,\zeta(x',y')}\, dx'dy', \tag{2.10}$$

where $R = 2R_1R_2/(R_1+R_2)$ and x' and y' are the integration variables in the x and y directions, respectively.

The expected value of the scattered field broadcast from a unit strength, omnidirectional point source is found by ensemble averaging Eq. (2.10) over surface realizations. For a zero-mean surface with Gaussian roughness profile and $\langle \zeta^2 \rangle \equiv h^2$, the ensemble average yields (Medwin and Clay, 1998)

$$\langle P(\boldsymbol{R_2}, \omega) \rangle = \Gamma \frac{e^{ik(R_1+R_2)}}{R_1+R_2} e^{-2(kh\cos\theta)^2}, \tag{2.11}$$

for wavenumber $k = \omega/c$. Equation (2.11) is the conventional Kirchhoff-approximated coherent field reflected from a random rough surface with a Gaussian height distribution. Substitution of Eq. (2.11) into Eq. (2.5) yields the in-band coherent reflection coefficient, which is exponentially diminishing as the square of $kh\cos\theta$,

$$\mathcal{R}_{coh} = e^{-2(kh\cos\theta)^2}. \tag{2.12}$$

2.2.3 Rough Surface Frequency-Difference Autoproduct

Inserting the HKF integral from Eq. (2.10) into Eqs. (2.1) and (2.2) yields the bandwidth-averaged autoproduct of the rough-surface reflected field:

$$\langle AP_\Delta(\boldsymbol{R_2}, \Delta\omega) \rangle_{BW} = \frac{|\Gamma|^2 \cos^2\theta}{\Omega_{BW}^\Delta 4\pi^2 c^2 R_1^2 R_2^2} e^{i\frac{\Delta\omega}{c}(R_1+R_2)} \int_{\Omega_C-\frac{1}{2}\Omega_{BW}^\Delta}^{\Omega_C+\frac{1}{2}\Omega_{BW}^\Delta} d\omega\, \omega_+\, \omega_- \tag{2.13}$$

$$\times \int_{-\infty}^{\infty}\int_{-\infty}^{\infty}\int_{-\infty}^{\infty}\int_{-\infty}^{\infty} e^{\frac{i}{cR}\cos^2\theta\left[\omega_+ x'^2 - \omega_- x''^2\right]} e^{\frac{i}{cR}\left[\omega_+ y'^2 - \omega_- y''^2\right]} e^{\frac{2i\cos\theta}{c}\left[\omega_+\zeta(x',y') - \omega_-\zeta(x'',y'')\right]} dx'dy'dx''dy''.$$

This is the general frequency-difference autoproduct for scattering from any randomly rough surface, $z = \zeta(x, y)$, subject to the Kirchhoff and Fresnel approximations. The quadruple integral over x', y', x'', and y'' represents a double surface integration in the orthogonal spatial directions x and y. Importantly, the bandwidth-averaging integral removes dependence on the source spectrum, leaving only features of the acoustic environment.

The expected value of the bandwidth-averaged frequency-difference autoproduct is found by surface-realization ensemble averaging of Eq. (2.13), the effect of which is isolated to the last exponential in the integrand. The expected value of the final exponential is the two-dimensional characteristic function of the random variable ζ. For a zero-mean normally-distributed variable, the two-dimensional characteristic function (Papoulis, 1984) is

$$\langle e^{\frac{2i\cos\theta}{c}[\omega_+\zeta(x',y')-\omega_-\zeta(x'',y'')]}\rangle = e^{-\frac{1}{2}v^2(\omega_+^2+\omega_-^2)}e^{v^2\omega_+\omega_-\Phi}, \tag{2.14}$$

where $v = 2(h/c)\cos\theta$, $\langle\ \rangle$ indicates an ensemble average over surface realizations, and Φ is the spatial correlation function of the rough surface. The surface correlation function is assumed Gaussian with isotropic correlation length L:

$$\Phi = \exp\left[-\frac{\alpha_x^2+\alpha_y^2}{L^2}\right], \tag{2.15}$$

where α_x and α_y are the difference coordinates in the *x* and *y* directions (Bozma and Kuc, 1991). Here the relevant sum and difference spatial coordinate transformations are defined by

$$\alpha_x = x' - x'', \tag{2.16a}$$

$$\alpha_y = y' - y'', \tag{2.16b}$$

$$\beta_x = x' + x'', \tag{2.16c}$$

$$\beta_y = y' + y'', \tag{2.16d}$$

$$d\alpha_x d\beta_x = 2dx'dx'', \tag{2.16e}$$

and

$$d\alpha_y d\beta_y = 2dy'dy''. \tag{2.16f}$$

Additionally, the factors preceding the first integration in Eq. (2.13) are identified for clarity in subsequent calculations as

$$\gamma = \frac{|\Gamma|^2\cos^2\theta}{4\pi^2c^2R_1^2R_2^2}e^{i\frac{\Delta\omega}{c}(R_1+R_2)}.$$

Substitution of Eqs. (2.14-2.16) into Eq. (2.13) and utilization of $\omega_{\pm} = \omega \pm \Delta\omega/2$ produces, after some manipulation,

$$\langle\langle AP_{\Delta}(\boldsymbol{R_2}, \Delta\omega)\rangle_{BW}\rangle = \frac{\gamma}{4\Omega_{BW}^{\Delta}} \int_{\Omega_C - \frac{1}{2}\Omega_{BW}^{\Delta}}^{\Omega_C + \frac{1}{2}\Omega_{BW}^{\Delta}} d\omega\, \omega_+\, \omega_-\, e^{-\frac{1}{2}v^2(\omega_+^2 + \omega_-^2)} \tag{2.17}$$

$$\times \int_{-\infty}^{\infty} d\alpha_x \int_{-\infty}^{\infty} d\alpha_y \exp\{v^2\omega_+\omega_-\Phi\} \exp\left\{\frac{i\Delta\omega\cos^2\theta}{4cR}\alpha_x^2\right\} \exp\left\{\frac{i\Delta\omega}{4cR}\alpha_y^2\right\}$$

$$\times \int_{-\infty}^{\infty} d\beta_x \exp\left\{\frac{i\cos^2\theta}{cR}\left[\alpha_x\beta_x\omega + \frac{\beta_x^2\Delta\omega}{4}\right]\right\} \int_{-\infty}^{\infty} d\beta_y \exp\left\{\frac{i}{cR}\left[\alpha_y\beta_y\omega + \frac{\beta_y^2\Delta\omega}{4}\right]\right\}.$$

The final two spatial integrands are Gaussian functions in β_x and β_y. Evaluation of the sum coordinate Gaussian integrals in Eq. (2.17) leads to

$$\langle\langle AP_{\Delta}(\boldsymbol{R_2}, \Delta\omega)\rangle_{BW}\rangle = \frac{i\gamma\pi cR}{\Omega_{BW}^{\Delta}(\Delta\omega)\cos\theta} \int_{\Omega_C - \frac{1}{2}\Omega_{BW}^{\Delta}}^{\Omega_C + \frac{1}{2}\Omega_{BW}^{\Delta}} d\omega\, \omega_+\, \omega_-\, e^{-\frac{1}{2}v^2(\omega_+^2 + \omega_-^2)} \tag{2.18}$$

$$\times \int_{-\infty}^{\infty} d\alpha_x \int_{-\infty}^{\infty} d\alpha_y \exp\{v^2\omega_+\omega_-\Phi\} \exp\left\{\frac{-i\alpha_x^2\omega_+\omega_-\cos^2\theta}{cR\Delta\omega}\right\} \exp\left\{\frac{-i\alpha_y^2\omega_+\omega_-}{cR\Delta\omega}\right\}.$$

Further evaluation of Eq. (2.18) requires asymptotic approximation of the remaining spatial integrand. A Taylor expansion of the correlation function about the origin of the difference coordinates was implemented following (Bozma and Kuc, 1991):

$$\Phi = \exp\left[-\frac{\alpha_x^2 + \alpha_y^2}{L^2}\right] \approx 1 - \frac{\alpha_x^2}{L^2} - \frac{\alpha_y^2}{L^2}.$$

Minimal asymptotic error is expected from this approximation as the correlation function appears only in an exponential, indicating that the major effects of scattering are contained near the specular point.

Substitution of the correlation function approximation results in standard Gaussian integrals in α_x and α_y. Interestingly, evaluation of the remaining spatial integrals eliminates

dependence on ω_+ and ω_-, leaving a trivial integration over angular frequency. However, the bandwidth-average is still an important step as averaging through the signal bandwidth improves robustness of the frequency-difference autoproduct. Replacement of γ and some algebraic effort yields an analytic result for the ensemble-averaged frequency-difference autoproduct scattered from a randomly-rough surface with Gaussian height distribution and Gaussian correlation function:

$$\langle\langle AP_{\Delta}(\boldsymbol{R_2}, \Delta\omega)\rangle_{BW}\rangle = |\Gamma|^2 \frac{e^{i\Delta k(R_1+R_2)}}{(R_1+R_2)^2} e^{-2(\Delta kh\cos\theta)^2} \times \left[\left(1 - i\Delta kh^2 \frac{4R}{L^2}\right)\left(1 - i\Delta kh^2 \frac{4R\cos^2\theta}{L^2}\right)\right]^{-1/2}, \tag{2.19}$$

where $\Delta k = \Delta\omega/c$. This result is analogous to Eq. (2.11) for the in-band field.

Aside from a modified boundary condition, $|\Gamma|^2$, and an extra factor of $1/(R_1 + R_2)$, the terms preceding the square brackets in Eq. (2.19) are reminiscent of the equivalent in-band field, Eq. (2.11), if it were evaluated at the difference frequency, $\Delta\omega$. These two features limit the autoproduct's exact mimicry of a genuine acoustic field at the difference frequency. They are inherent to the autoproduct's construction and are well-documented elsewhere (Worthmann and Dowling, 2017). Nevertheless, in Eq. (2.19), the Rayleigh roughness parameter in the exponential is dependent on Δkh. Thus, the apparent surface roughness may then become negligible for a sufficiently low difference frequency. As a result, $\mathcal{R}_{coh}$, as given by Eqs. (2.5) and (2.19),

$$\mathcal{R}_{coh} = e^{-2(\Delta kh\cos\theta)^2}\left[\left(1 - i\Delta kh^2 \frac{4R}{L^2}\right)\left(1 - i\Delta kh^2 \frac{4R\cos^2\theta}{L^2}\right)\right]^{-1/2}, \tag{2.20}$$

is governed by Δkh and may approach 1, regardless of the kh values of the constituent acoustic fields.

The terms in [ ]-brackets in Eqs. (2.19) and (2.20) are unique to the frequency-difference autoproduct and can also limit the recovery of coherent reflection. The form of these bracketed terms is such that nonzero imaginary components in each parenthesis leads to a reduction in $\mathcal{R}_{coh}$. Hence, the parameter combination, $4R\Delta kh^2/L^2$, is identified as the frequency-difference roughness parameter. For large values of the frequency-difference roughness parameter, coherent reflection will decrease. Conversely, for a given surface, the frequency-difference roughness parameter can be minimized, and coherent reflection restored, through judicious selection of the difference frequency.

The capability of the frequency-difference autoproduct to recover coherent reflection is predicted to depend exponentially on the Rayleigh roughness parameter and as an inverse square-root of a factored polynomial involving the frequency-difference roughness parameter. These findings were investigated numerically and experimentally by using underwater acoustic waves ensonifying a randomly rough, isotropic, pressure-release surface where $|\Gamma|^2 = 1$. However, this restriction is not general. The techniques outlined above are valid for acoustically hard boundaries, boundaries with near spatially-constant Γ, anisotropic surfaces, and any homogeneous acoustic medium.

2.3 Numerical Simulations

This section presents results of a numerical investigation into coherence recovery using simulated frequency-difference autoproducts. A description of the simulation strategy, including the numerical Helmholtz-Kirchhoff integral and random surface generation, precedes presentation of the simulated results.

2.3.1 Simulation Implementation

The specular plane of the simulated rough surface scattering environment is shown schematically in Figure 2.2. The omnidirectional source defines the origin of the x-coordinate and is located 0.20 m below the randomly rough, pressure-release surface ζ. The receivers are located 0.33 m in range from the source and sample 80 depths between 0.25-0.4 m, corresponding to 1.9 mm resolution. The sound speed, c, is 1480 m/s and the surface is interrogated with a signal pulse having bandwidth 40-110 kHz. The source spectrum is set to unity to simulate the Green's function. This simulation setup matches the geometry and experimental parameters of the water tank experiments described in Chapter 2.4.

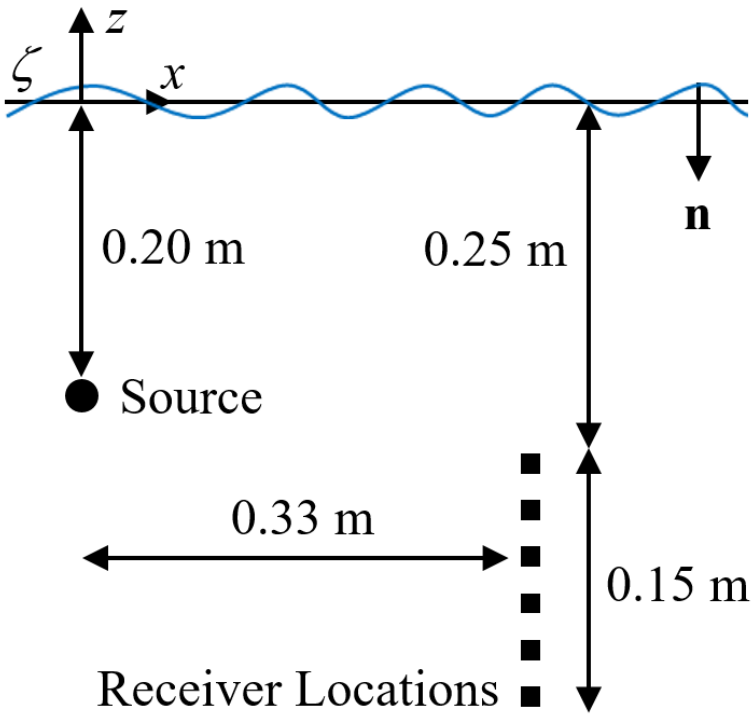

Figure 2.2: Specular plane schematic of nominal simulation and experimental geometry. The omnidirectional source at depth 0.20 m broadcasts to receiving locations at range 0.33 m. The receiving locations probe depths [0.25-0.4 m] with a spatial sampling interval of 1.9 mm (simulation) and 5 mm (experiment).

To simulate the rough surface scattering, the Kirchhoff-approximated Helmholtz-Kirchhoff integral in Eq. (2.9) is discretized. The Fresnel and small surface slope approximations utilized in the theoretical derivation to obtain Eq. (2.10) are therefore not utilized in the numerical evaluations. Using differential geometry identities for the normal derivative, $\partial/\partial n = n \cdot \nabla$, and the surface, $dS = \left(\zeta_x^2 + \zeta_y^2 + 1\right)^{1/2} dxdy$ where ζ_x and ζ_y are the partial spatial derivatives of the rough surface ζ, along with a directional sense of the impinging and diverging waves, the discrete Kirchhoff-approximated Helmholtz-Kirchhoff integral is

$$P(\boldsymbol{x}, \omega) = \frac{\Gamma}{4\pi} \int_X \int_Y \frac{e^{ik(r+r_s)}}{r r_s} \left[\left(ik - \frac{1}{r_s} \right) \hat{r_s} \cdot n - \left(ik - \frac{1}{r} \right) \hat{r} \cdot n \right] \left(\zeta_x^2 + \zeta_y^2 + 1 \right)^{\frac{1}{2}} dxdy, \quad (2.21)$$

where $\boldsymbol{x}$ is a generic field location in the coordinate system displayed in Fig. 2.2, hats denote unit vectors, and X and Y define the area of the rough surface projected onto the x-y plane. The geometrical unit vectors, $\hat{r_s}$ and $\hat{r}$, describe the directions from the source to an arbitrary (x,y)-point on the surface and from that (x,y) surface point to the receiver, respectively. Numerical evaluation of Eq. (2.21) is implemented via trapezoidal integration on a 1.25 m × 1.25 m surface patch sampled every 1.3 mm, corresponding to $\sim\lambda/15$ surface sampling with respect to the signal center frequency, 75 kHz.

In the limit of zero roughness, Eq. (2.21) should reduce to the Green's function given by the method of images:

$$G(\boldsymbol{x}, \omega) = \frac{P(\boldsymbol{x}, \omega)}{S(\omega)} = \Gamma \frac{e^{ik(R_1+R_2)}}{R_1 + R_2}. \quad (2.22)$$

Figure 2.3 provides an overview of this flat surface comparison. Theoretical fields are shown by the black curves and simulated fields by red dots in panels (a) and (b). Figure 2.3a) shows the real part of the pressure field evaluated at the center frequency, 75 kHz, along the receiving

depth locations. The complex cross-correlation coefficient, averaged through the signal bandwidth, confirms the excellent match; to five decimal places, $\chi = 1 + 0i$. Figure 2.3b) indicates slight magnitude discrepancies between theoretical and simulated fields not revealed by the cross-correlation coefficient. The RMSE between theoretical and simulated fields across the depth locations, as a percentage of the average theoretical receiver amplitude, is displayed by frequency in Fig. 2.3c). The RMSE is less than 1.5% across the signal bandwidth. Hence, the current numerical implementation accurately predicts phase and, within a few percent, amplitude of the in-band field.

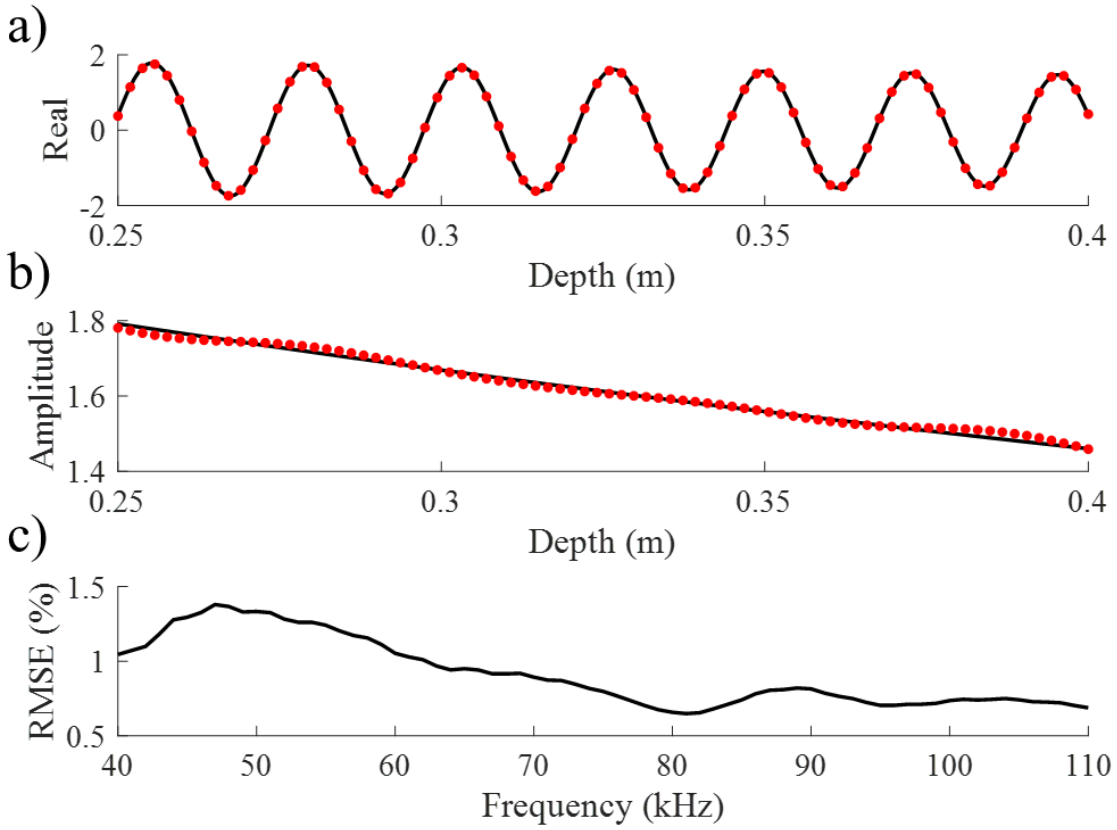

Figure 2.3: Zero roughness assessment of the numerical simulations. Panels (a) and (b) show the real part and amplitude of the received pressure vs. depth at 75 kHz. Theoretical Green's functions are shown in black and simulated fields are shown as red dots. Panel (c) displays the RMSE percentage between simulated and theoretical fields by frequency.

Randomly rough surfaces with Gaussian height distributions and Gaussian correlation functions were generated with open-source software in MATLAB (Bergström, 2012). Analysis was conducted on two statistically unique surfaces: (i) $h = 8$ mm and $L = 20$ mm (*short correlation length*) and (ii) $h = 8$ mm and $L = 45$ mm (*long correlation length*). The surface parameters were selected to reasonably satisfy and easily exceed, respectively, the validity requirements of the Kirchhoff approximation. Each surface type was generated 300 times. Slight statistical variation exists between the intended h and L and the values determined directly from the generated surfaces. Throughout this paper, surfaces are referred to by the intended statistical h and L values while calculations implement the actual post-surface-generation h and L values. A summary of the short correlation length surfaces is presented in Figs. 2.4a)-c), while the longer correlation length surfaces are shown in Figs. 2.4d)-f). The colormap (Auton, 2021) in figure panels 2.4a)-b) and 2.4c)-d) displays significantly negative (positive) surface height deviations in blue (red). Probability density functions (PDFs) of height deviation (with respect to $z = 0$) are shown in Figs. 2.4c) and 2.4f) and indicate the statistical variability. In each panel, the height deviation PDF of all 300 surface realizations is shown as a solid black curve while the 300 height deviation PDFs of individual surface realizations are shown in semitransparent red curves. Herein, the surfaces are distinguished by their relative correlation lengths. At each of the 80 receiver depth locations, the 600 randomly rough surfaces are integrated according to Eq. (2.21) for the 71 integer-kHz frequencies in the signal bandwidth, resulting in greater than 3.4 million simulated $P(\boldsymbol{x}, \omega)$'s.

To quantify statistical uncertainty, an additional 1200 surfaces (of each type) were integrated in the same manner. From this pool, ensembles of 300 surfaces were randomly

selected 500 times. The 95th percentile of the ensuing variation for both in-band and autoproduct results is indicated by error bars in Figs. 2.5 and 2.6.

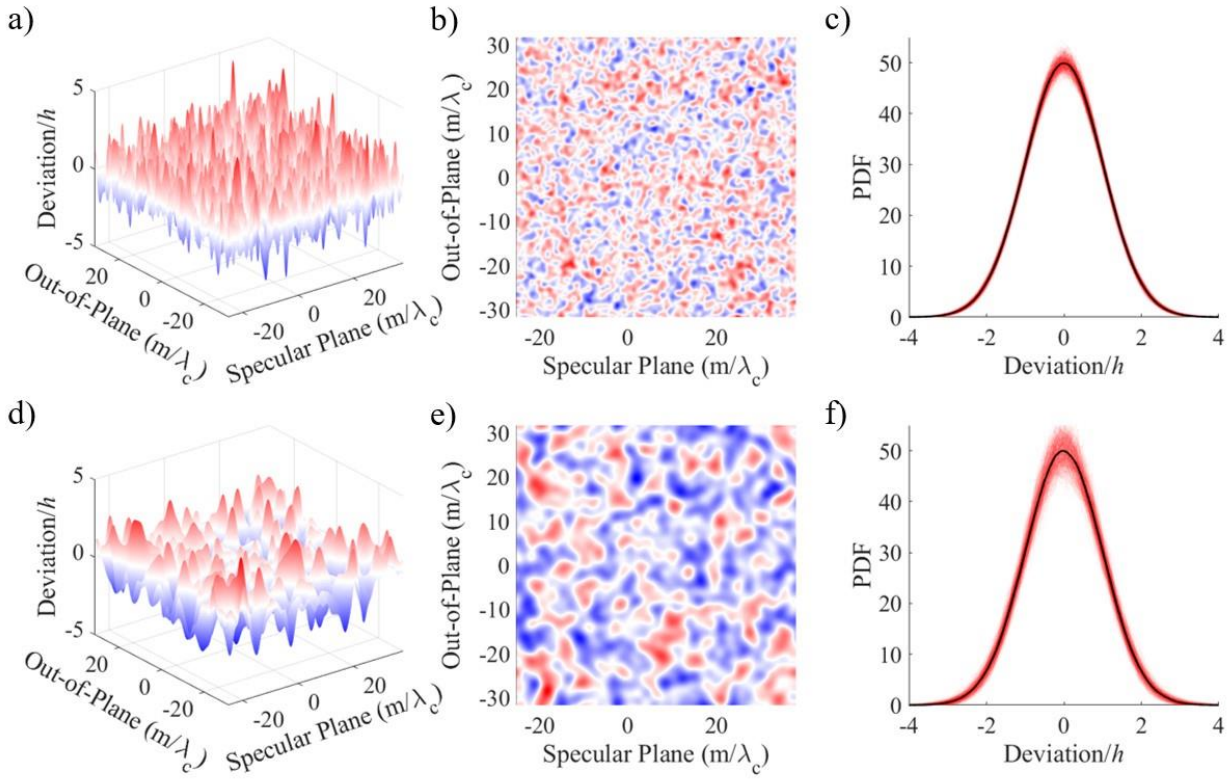

Figure 2.4: Overview of the randomly rough surfaces implemented in simulation. A sample realization with Gaussian height distribution, Gaussian correlation function, $kh = 2.55$ and $h/L = 0.40$ is shown in (a). The x- and y- axes are shown in center-frequency wavelength units, and the vertical deviation in units of rms height. A projection of (a) is shown in (b). PDFs of the height deviations are shown in (c). Each transparent red line indicates one surface realization and the black line is the PDF of all surfaces. Panels (d), (e), and (f) show equivalent information for a surface with $kh = 2.55$ and $h/L = 0.18$. For all panels, the incident wavelength is for the signal's center frequency, 75 kHz.

2.3.2 Results

Simulated frequency-difference autoproducts were computed from the numerical $P(\boldsymbol{x}, \omega)$'s and Eqs. (2.1) and (2.2) for both the shorter and longer correlation length surfaces. The theoretical

frequency-difference autoproducts were calculated from Eq. (2.19), with appropriate substitutions of h and L.

Figure 2.5 shows the real part of the theoretical and simulated frequency-difference autoproducts for the shorter [Figs. 2.5a) and 2.5b)] and longer [Figs. 2.5c) and 2.5d)] correlation length surfaces evaluated at two difference frequencies. In each plot, the theoretical autoproducts from Eq. (2.19) are shown by a solid black curve, simulated autoproducts from the numerical evaluation of Eq. (2.21) are shown by a dashed red line, and the horizontal axis is the receiver depth. The vertical axis limits are ± 1 for panels (a) and (b) and ± 2.75 for panels (c) and (d). The difference frequency and the cross-correlation coefficient between theoretical and simulated fields are shown in the bottom left of each panel.

The four plots in Fig. 2.5 verify the theory derived in Chapter 2.2 for two statistically unique surface ensembles. The cross-correlation coefficients, $\chi_{shorter}$ = 0.998+0.061i and χ_{longer} = 0.999-0.047i, indicate nearly perfect matching for $\Delta f = 5$ kHz autoproduct fields for both surface types. At $\Delta f = 15$ kHz, the real part of the cross-correlation coefficients for both surface types are greater than 0.96, but there is a non-negligible phase indicated by the imaginary component of χ. The cross-correlation phase increases with increasing difference frequency and can be attributed to the finite surface integration area and finite extent of ensemble averaging.

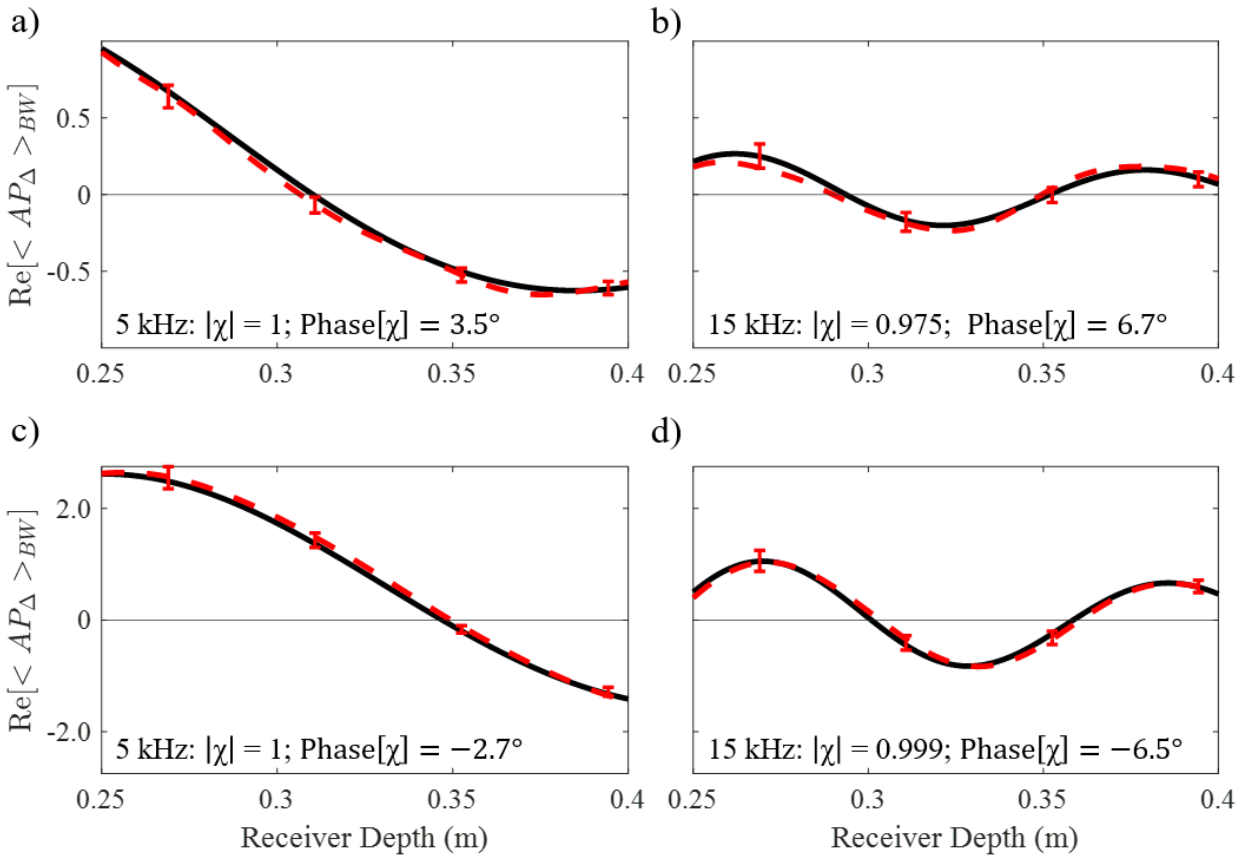

Figure 2.5: Simulated field plots of the real part of the frequency-difference autoproduct. Theoretical autoproducts are shown by the black curves and simulations by the dashed red lines. The plots all share the same *x*-axis (receiver depth) limits. The top (bottom) two panels display the fields scattered from the shorter (longer) correlation length surface shown in Fig. 4. The difference frequency and cross-correlation between theory and simulation is shown in each panel. Error bars every 0.04 m indicate the 95% confidence interval of the simulations.

From the ensemble-averaged acoustic and autoproduct fields, the coherent reflection coefficient may be calculated according to Eqs. (2.5), (2.12), and (2.20). Herein, the difference frequency bandwidth considered consisted of integer-kHz-values from 1-60 kHz. Although 60-70 kHz difference frequencies are available from the signal bandwidth, these difference frequencies were not investigated due to minimal bandwidth-averaging in Eq. (2.2). A systematic analysis of the significance of bandwidth averaging in rough surface scattering is outside of the

scope of this paper but is studied for a uniform half-space in (Lipa et al., 2018). On $|\mathcal{R}_{coh}|$ plots, the limiting behavior for $\Delta f = 0$ Hz is indicated as well.

The effect of the frequency-difference autoproduct on the recovery of coherent reflection is displayed in Fig. 2.6 for variable frequency and difference frequency. For sufficiently low difference frequencies, the coherent reflection coefficient can be arbitrarily close to 1. In each panel, the red (blue) dashed lines denote simulated out-of-band (in-band) frequencies and theoretical curves for out-of-band (in-band) frequencies are shown in black (green) solid lines. The theoretical in-band $|\mathcal{R}_{coh}|$'s are equivalent in panels (a) and (b) because the coherent acoustic field is independent of surface correlation length. The bumps at simulated in-band frequencies are due to imperfect statistical convergence to zero of a randomly-varying complex quantity. As the number of surfaces included in an ensemble average tends towards infinity, these discrepancies disappear.

The autoproduct field, however, includes a complicated dependence on the surface's correlation length through the frequency-difference roughness parameter. This effect is demonstrated by the concavity difference between panels (a) and (b) at the below-band frequencies. The shorter correlation length surface, with the larger frequency-difference roughness parameter, recovers coherent reflection only at significantly lower difference frequencies. For the longer correlation length surface, greater than 93% coherent reflection is recovered at 3 kHz whereas only 50% is recovered at this frequency for the short correlation length surface. Hence, the recovery of coherent information is limited by both Δkh and the correlation length, through the frequency-difference roughness parameter. The effect of correlation length may also be interpreted by the different vertical scales in Figs. 2.5a)-b) and 2.5c)-d).

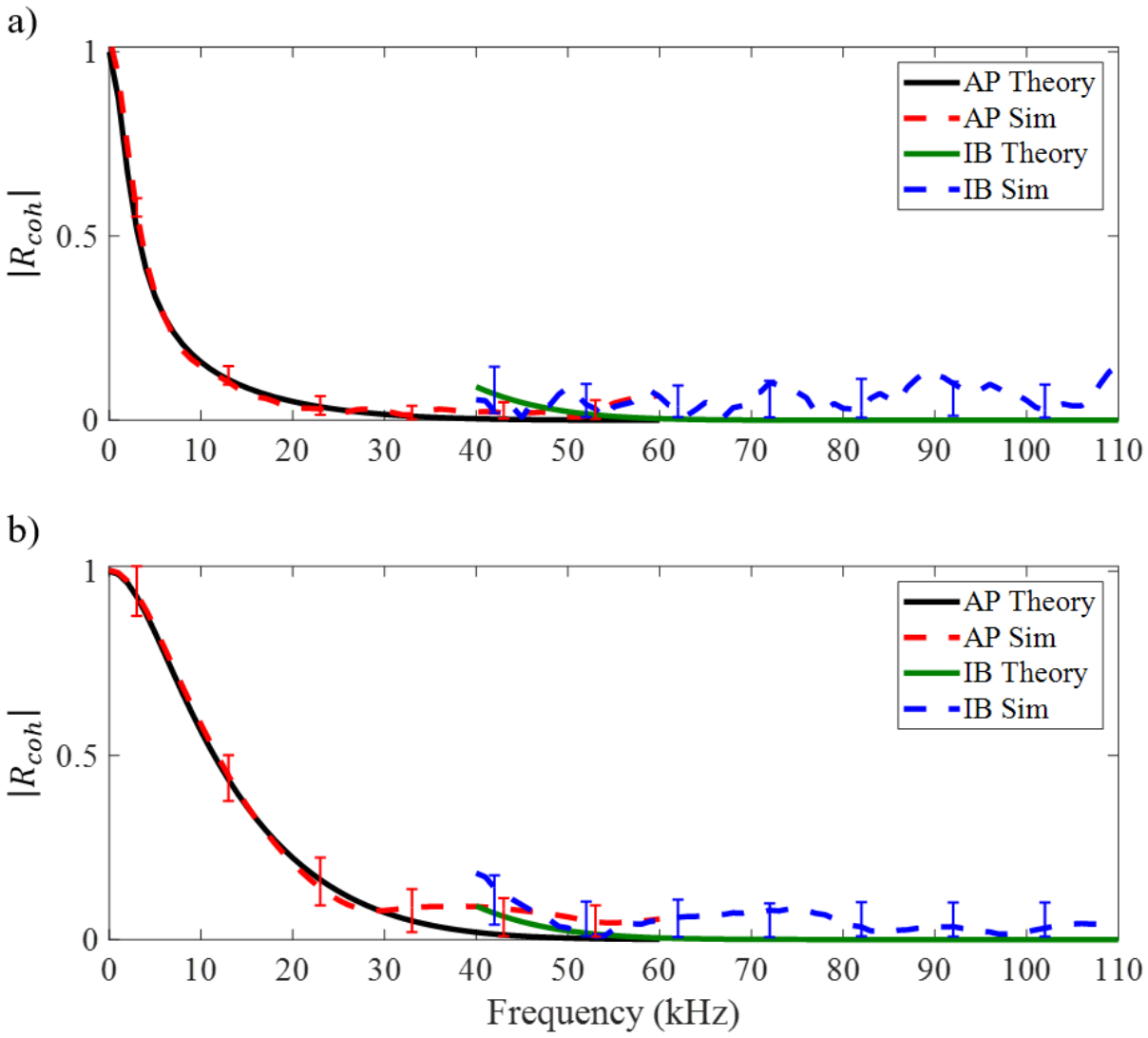

Figure 2.6: Simulated and theoretical coherent reflection coefficients, $\mathcal{R}_{coh}$, for in-band (IB) and out-of-band frequencies for (a) the shorter correlation and (b) the longer correlation length surfaces. In both panels, red (blue) dashed lines denote simulated out-of-band (in-band) frequencies. The theoretical curves for out-of-band (in-band) frequencies are displayed as black (green) solid curves. Error bars every 10 kHz indicate the 95% confidence interval of the simulations.

2.4 Experiment

This section discusses the results of a laboratory experiment probing the long correlation length limit of the theoretical autoproduct result, Eq. (2.19). This experiment was designed solely to test

the theoretical [Eqs. (2.19) and (2.20)] and simulation predictions; it is not directly relevant to any particular sea-surface or sea-floor scattering scenario. To compare experimental autoproduct fields to corresponding theoretical and simulated fields, the acoustic environment and experimental parameters must be sufficiently well-known. These details are presented next.

2.4.1 Experimental Design

Acoustic fields were generated and measured in a 1.20-m-diameter cylindrical water tank filled to an approximate depth of 0.90 m. An omnidirectional source, ITC-1042 (Gavial International Transducer Corporation - Santa Barbara, CA), broadcast a nominally 50-μs Gaussian-enveloped sinusoidal signal with center frequency 70 kHz from a fixed location. An omnidirectional receiver, Reson TC4013 (Teledyne Marine, Reson - Slangerup, Denmark), recorded acoustic pressure waveforms at a variable depth. The source depth, receiver range, and receiver depth limits match the simulations in Chapter 2.3 (see Fig. 2.2). Sampling of the pressure field, however, is coarser in experiment and occurs in 5 mm increments. By time-gating non-surface reflected arrivals, the cylindrical tank imitates a uniform half-space. Furthermore, the requisite temporal separation between the direct-path, surface-reflected, and tank-wall reflected signals was only possible over a finite range of receiver depths, 0.25 m to 0.40 m. For the given source depth (20 cm), these receiver depths correspond to specular incidence angles of $29° \leq \theta \leq 36°$.

Experimentally fabricating a surface with Gaussian statistics and sufficient roughness to scatter the underwater acoustic waves at frequencies of interest is a challenging task. Hence, a normal distribution of uniform height offsets to the tank water level (i.e. flat surfaces of different heights) was implemented to approximate an ensemble of rough surfaces with Gaussian correlation functions in the limit $L \to \infty$, even though each individual surface realization was not rough. Accurately sampling a normally distributed variable using an experimentally feasible

number of realizations was accomplished with an approach that shares features with Latin hypercube sampling [see e.g., (Helton and Davis, 2003)] while incorporating repeatability. For a specified rms surface height h and surface ensemble number N, the cumulative distribution function (CDF) for a normal distribution with standard deviation h was divided into N intervals. Then, N CDF values were selected to bisect the N intervals. Finally, the N height offsets were determined from the inverse distribution function for the probability values selected from the CDF. In this experiment, $h = 8$ mm and $N = 13$. The experimental height offset selections, superimposed as red crosses on a Gaussian distribution, are shown in Fig. 2.7a). The uniform height offsets were implemented by adding or extracting an appropriate volume of water from the tank. The 31 depth points were sampled for each surface realization using a sub-mm-resolution digital height gauge, the ME-HG-PRO-500 (Allendale Group Ltd, Machine-DRO – Hoddesdon, England). A total of 403 time domain pressure fields were recorded. A photograph of the experimental setup is shown in Fig. 2.7b).

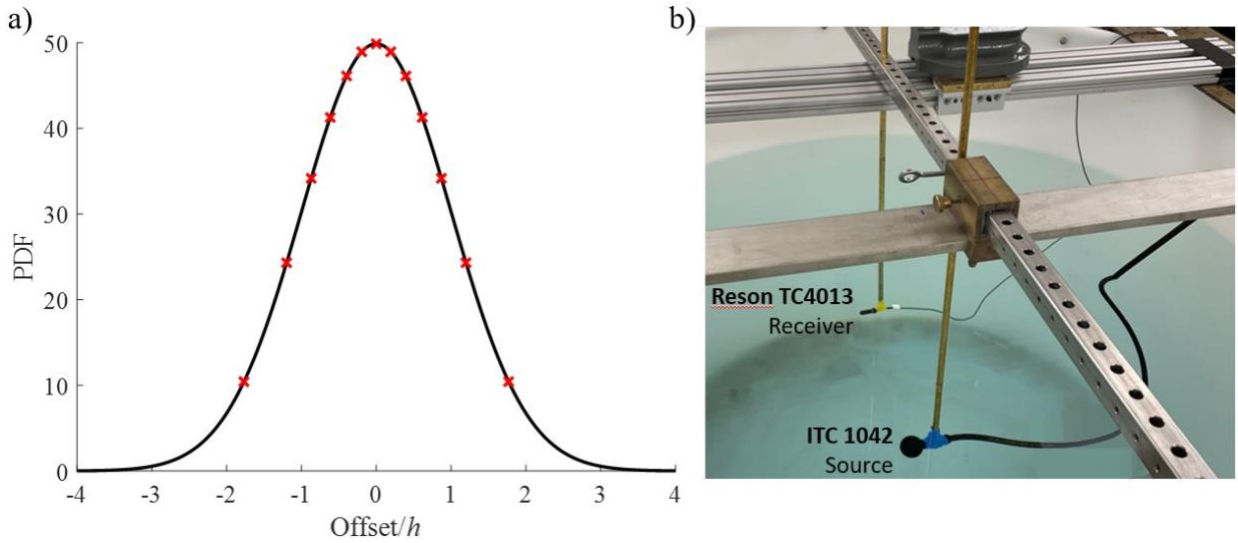

Figure 2.7: Long correlation length experiment design. Panel (a) shows the selected height offsets (red ×'s) on the underlying Gaussian PDF. The horizontal axis is reported in units of h. Panel (b) shows a photograph of the experimental setup at an oblique angle to the specular plane. The broadcast (receiving) transducer is shown in the foreground (background). Non-surface-reflected arrivals are time-gated from recorded signals.

2.4.2 Source Waveform and Environmental Characterization

To compute the bandwidth-averaged autoproducts defined by Eq. (2.2), the source waveform must be known and a signal bandwidth must be defined. Information may be obtained from the intended broadcast waveform, but imperfections in the frequency responses of the transducer pair altered the nominal waveform. Further, the noticeable distortion was directional. To mitigate unintended source waveform dependence, an experimental source waveform was determined for each receiver location.

Field recordings for a nominal surface height deviation of 0 m were measured for each depth location. To characterize the experimental waveform, a 175 μs interval, centered on the expected reflected-path arrival was isolated in the time domain. These recordings were then scaled by a factor proportional to the reflected path length, $R_1 + R_2$, to remove spherical spreading loss and shifted in time to maximize temporal cross-correlation with the intended source waveform. The outlined strategy and corresponding results for source waveform measurement was similar to previous studies using the ITC-1042 and Reson TC-4013 in a laboratory setting (Lipa et al., 2018).

The time- and frequency-domain source waveforms are displayed in Fig. 2.8. Recorded waveforms, shown as semitransparent red curves, are scaled to contain the same signal energy as the 50-μs-duration nominal waveforms, indicated by the dotted black curves. The experimental waveforms exhibit temporal spreading to approximately 75 μs. In the frequency domain, the spectral peak of 70 kHz was maintained, but the distribution of spectral energy was shifted to higher frequencies. The experimentally determined bandwidth, containing 99% of the signal energy, was $\Omega_L/2\pi$ = 40 kHz and $\Omega_H/2\pi$ = 110 kHz. Thus, the signal's center frequency shifted to 75 kHz, consistent with the resonant frequency of the ITC-1042 (79 kHz). A noticeable dip

near 90 kHz in Figure 2.8b) was attributed to imperfect transducer directionality. Moreover, the discrepancy in the frequency response of the semitransparent red curves near 65 kHz and 90 kHz provides the rationale for incorporating dependence on receiver location. Herein, analysis utilized the experimentally characterized source waveform to obtain Green's functions from pressure recordings.

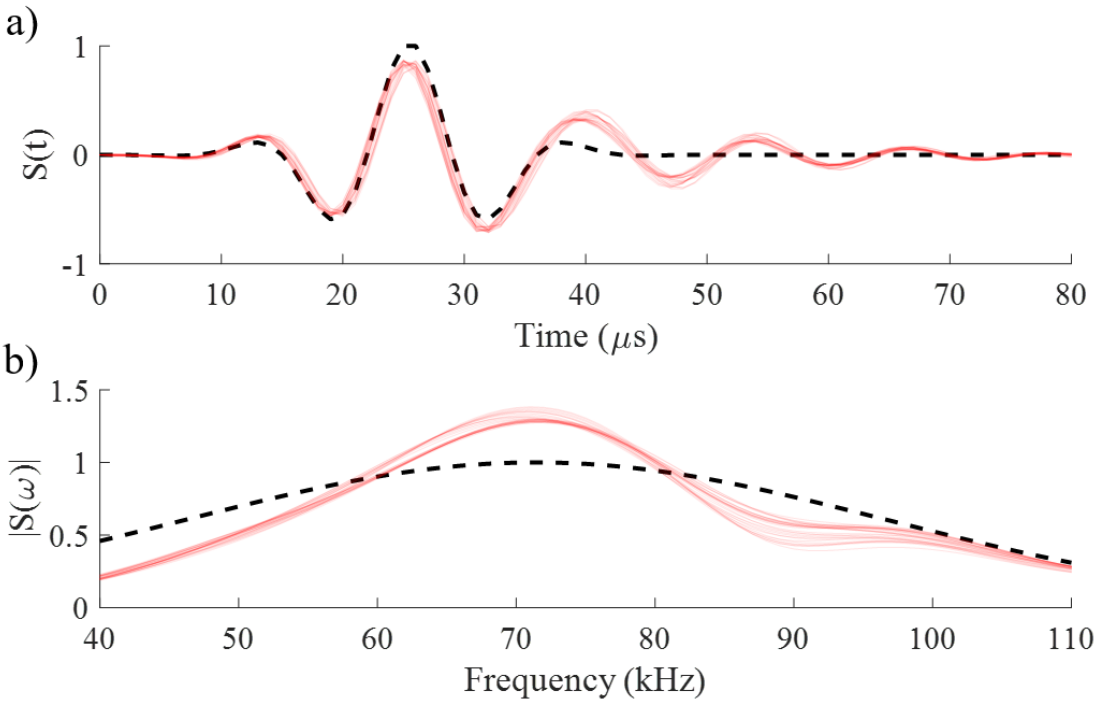

Figure 2.8: Measured source waveforms vs. time (a) and vs. frequency (b). In each panel, the black dotted curve is the nominal source waveform, while the semitransparent red curves are the measured source-broadcast waveforms, scaled to remove spherical spreading loss and temporally shifted to maximize cross correlation with the nominal source waveform. The red and black curves are scaled to contain the same signal energy.

The corresponding theoretical and simulated fields required values of four environmental parameters: source depth, receiver depth, source-receiver range, and sound speed. While the nominal values, schematically shown in Fig. 2.2, may be used, errors of less than 1% can significantly alter the predicted field values for the given signal bandwidth. Thus, to counteract

experimental uncertainty, the four experimental parameters were optimized in post-processing to maximize in-band theoretical-to-measured field correlation.

This parameter characterization produced optimized offsets to the nominal measured values. In the experiment, dimensions were measured according to the geometric center of the transducers. The optimized offsets then mitigate both experimental uncertainty and geometrical/acoustical center transducer discrepancy. Additionally, the sound speed offset improved the accuracy of the experimental sound speed, 1490.8m/s, obtained from the temperature of the fresh water (Kinsler et al., 2000). The nonlinear parameter optimization was performed in MATLAB by maximizing the real part of the complex cross-correlation between theoretical and measured in-band reflected-path Green's functions across the signal bandwidth. For a further discussion of the parameter optimization strategy, see (Lipa et al., 2018).

Prior to optimization, the magnitude of the cross-correlation coefficient averaged across the signal bandwidth, $\chi_{Unopt} = 0.64 + 0.72i$, indicated a strong match in theoretical and experimental fields. However, the presence of significant cross-correlation phase indicated a uniform phase offset between measured and theoretical reflected-field Green's functions. After optimization, the averaged cross-correlation coefficient, $\chi_{Opt} = 0.99 + 0.00i$, revealed a near perfect match in normalized magnitude and phase. The optimized offsets (1.1 mm source depth increase, 1.1 mm receiver depth increase, 1.56 mm range increase, and 0.44 mm/s sound speed decrease) were well within experimental uncertainties. Herein, optimized environmental parameters were utilized in all computations of theoretical and simulated autoproducts.

2.4.3 Long Correlation Length Results

The theory described in Chapter 2.2 was tested both experimentally and numerically in the limit of long correlation lengths. The in-band Green's functions were determined from measured data

as $P(\boldsymbol{x},\omega)/S(\omega)$. The simulated in-band Green's functions were calculated for each surface realization from the reflected-path Green's function of Eq. (2.22), rather than integrating Eq. (2.21). The theoretical frequency-difference autoproducts were computed from Eq. (2.19), with $L \to \infty$.

Figure 2.9 shows the real part of the theoretical, simulated, and measured frequency-difference autoproducts vs. depth for four difference frequencies. The theoretical autoproducts are shown by solid black curves, simulated autoproducts by a dashed green line, and measured autoproducts by red ×'s. In each plot, the horizontal-axis is the receiver depth (nominally 0.25-0.4 m) and the vertical-axis limits are set to accommodate the amplitude of a flat-surface reflected autoproduct. Error bars, reported at each depth as twice the RMSE between measured autoproducts and theoretical flat-surface reflected autoproducts for each surface offset, are visually insignificant for the difference frequencies and vertical-axis scale provided in panels (a) and (b). In Fig. 2.9 c) and d), the maximum error across the receiving locations is indicated by a single error-bar at the top right.

The four panels of Fig. 2.9 cover the range of available difference frequencies for the signal bandwidth and exhibit excellent matching of theory, experiment, and simulation. The real part of the cross-correlation coefficient, $\mathrm{Re}[\chi]$, is greater than 0.99 for difference frequencies less than 27 kHz and is greater than 0.95 for difference frequencies less than 36 kHz. At high difference frequencies, the larger apparent surface roughness causes incoherent scattering, leading to a significant reduction in autoproduct amplitude. For instance, in Fig. 2.9d), the $|\mathrm{Re}[AP]| < 0.12$, which is only a few percent of the flat-surface reflected amplitude. Thus, noise likely contaminates the match indicated by χ in this case.

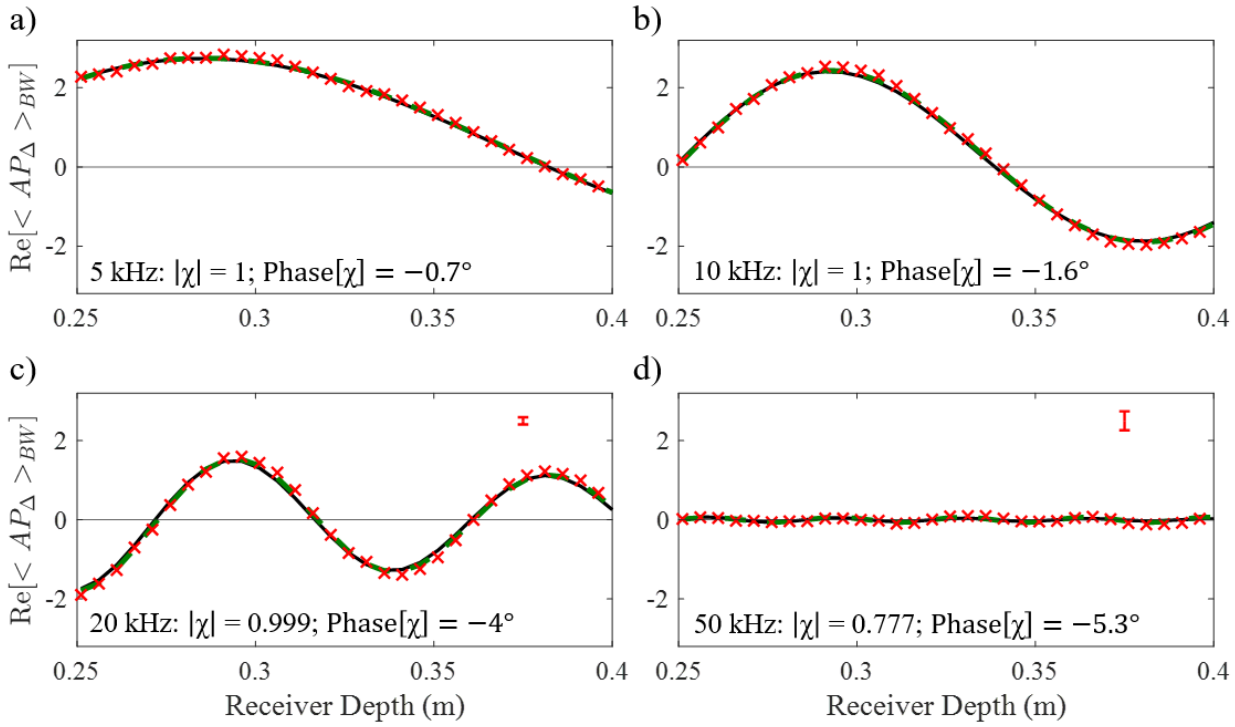

Figure 2.9: Field plots of the real part of the frequency-difference autoproduct. Theoretical autoproducts are shown by the black curves, simulations by the dashed green lines, and experimental results by the red ×'s. The plots all share the same horizontal (receiver depth) and vertical (autoproduct units) axis limits. In (a) and (b), error bars are omitted due to visual insignificance, and in (c) and (d), the maximum error across the depth points is displayed at the top right. The difference frequencies and cross-correlations between theory and experiment are shown at the bottom left of each panel.

The coherence recovery possible with the frequency-difference autoproduct is displayed in Fig. 2.10 which shows the coherent reflection coefficient computed according to Eqs. (2.5), (2.12), and (2.20) for frequency-difference autoproducts and in-band acoustic fields plotted against the difference frequency or signal frequency. The measured coherent reflection coefficient from frequency-difference autoproducts (in-band acoustic fields) is indicated by red (blue) ×'s (◊'s) while green (orange) dashed lines denote simulated coherent reflection coefficients. For $L \rightarrow \infty$, the coherent reflection coefficient in Eqs. (2.12) and (2.20) are identical for a single frequency. Hence, the theoretical coherent reflection coefficients are given

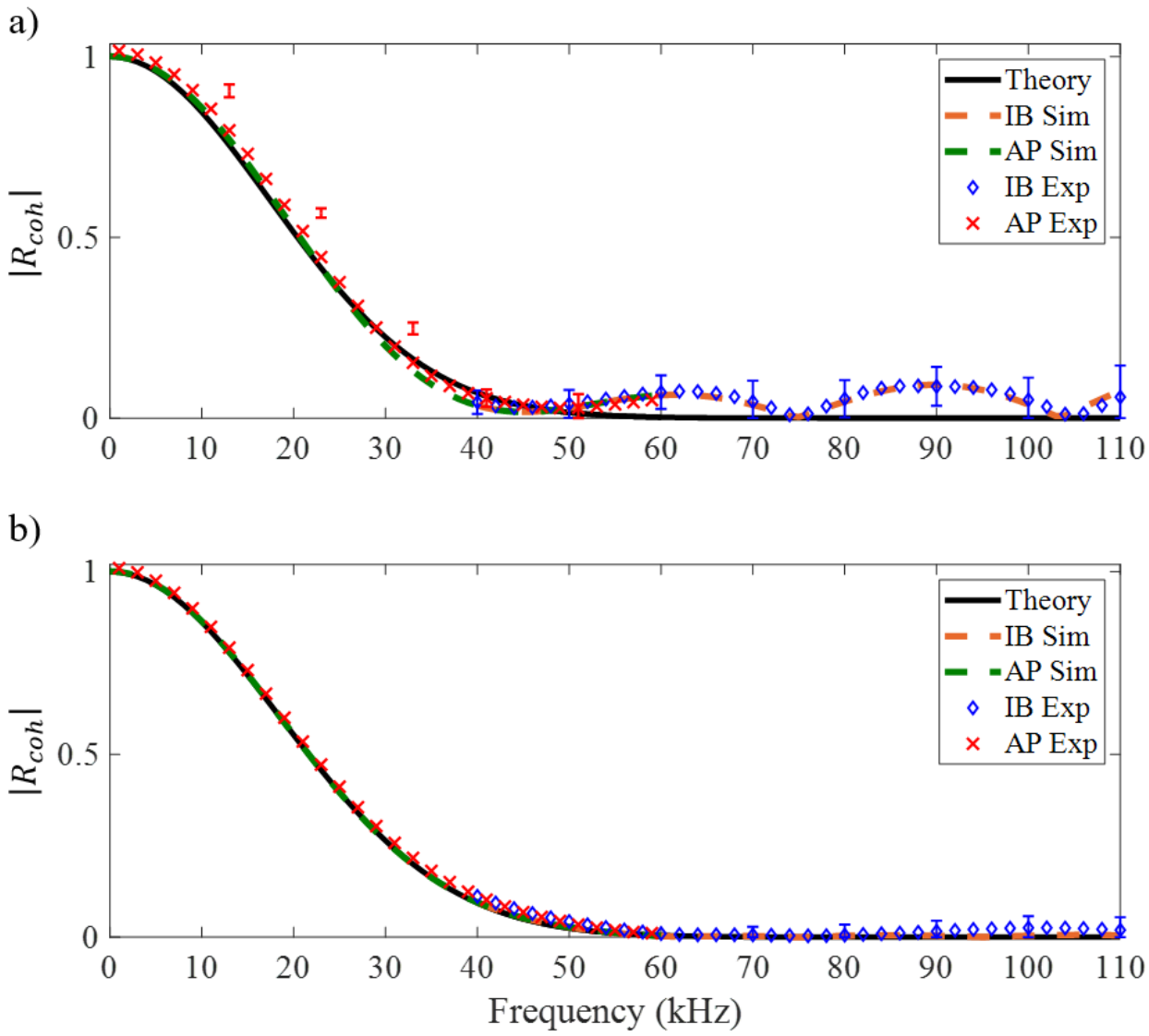

Figure 2.10: The coherent reflection coefficient from Eqs. (2.5), (2.12), and (2.20) for in-band (IB) and out-of-band frequencies: (a) N = 13 and (b) N = 150. In both panels, red (blue) ×'s (◊'s) and green (orange) dashed lines denote out-of-band (in-band) measured and simulated data, respectively. The theoretical prediction is displayed in black for all frequencies. Experimental error bars are indicated every 10 kHz when visually significant and are offset to the right of the data for low difference frequencies.

at all frequencies by a solid black curve. Excellent matching is exhibited between theoretical, simulated, and measured coherent reflection coefficients. Interestingly, the signal bandwidth is large enough to accommodate $\Delta\omega \geq \Omega_L$. In this region (40 to 60 kHz), the coherent reflection

coefficients from in-band fields and frequency-difference autoproducts overlap as expected. The measured coherent reflection coefficients are reported for odd- (even-) integer kHz out-of-band (in-band) frequencies. Further, error bars are displayed every fifth data point by propagating the real and imaginary RMSE between measured and theoretical fields (Taylor, 1997). For the lower frequencies in Fig. 2.10 a) and b), error bars are presented to the right of the data or are omitted when visually insignificant.

In Fig. 2.10a), the coherent reflection coefficient is generated from a single receiving depth (nominally 0.345 m) from the $N = 13$ experiments described above. The measured coherence recovery is evident for sufficiently low difference frequencies. Greater than 90% coherent reflection is found for difference frequencies less than 10 kHz and greater than 50% coherent reflection is expected for difference frequencies of 21 kHz or less. By contrast, the measured coherent reflection at in-band frequencies is consistently less than 10%. Similar features appear in equivalent plots of the other 30 depth points. The appearance of a coherent reflection coefficient slightly greater than unity at very low difference frequencies is a result of imperfect transducer reproducibility and a consequence of the experimental optimization strategy emphasizing normalized magnitude and phase matching via cross-correlation. The maxima of $|\mathcal{R}_{coh}|$ near 65 kHz and 90 kHz in Fig. 2.10a) are explained by interference patterns inherent in the experimental geometry and are an artifact of the choice of $N = 13$.

To explicitly address the latter experimental limitation, an $N = 150$ coherent reflection coefficient experiment was conducted for a single receiving depth location (nominally 0.25 m). Measured data were acquired through a nearly identical procedure to that described for the $N = 13$ experiment, and the results are shown in Fig. 2.10b). The general trends remain, and the recovery of coherent reflection by the frequency-difference autoproduct is accentuated. By

increasing the ensemble from $N = 13$ to $N = 150$, the prominence of the interference peaks at frequencies above 50 kHz are minimized and the in-band coherent reflection coefficient, averaged across the signal bandwidth, is reduced from 5.3% to 2.4%. Conversely, the coherent reflection coefficient computed from the frequency-difference autoproduct may become arbitrarily close to 1, for sufficiently low difference frequency even though the in-band field has lost coherence.

2.5 Conclusion

The frequency-difference autoproduct has been studied in a variety of environments including a uniform half-space (Lipa et al., 2018) and a refracting ocean environment (Geroski et al., 2021). The purpose of this study was to identify the behavior of the frequency-difference autoproduct after its constituent fields have reflected and scattered from a random rough surface. To investigate the interface scattering physics, the Kirchhoff approximation was utilized for both analysis and simulations. In addition, laboratory experiments relevant to the long-surface correlation-length limit were conducted and compared to the theoretical and simulation results. The theoretically-derived, numerically-simulated, and experimentally-measured results were all found to be in good agreement. The simulation ensembles of surfaces exhibiting two different correlation lengths when combined with the experiments test the theory at three different correlation lengths. In all cases, pressure-release surfaces with in-band $kh\cos\theta$ from 1 to 3 are used. Excellent correlation is found between theoretical, simulated, and measured genuine and autoproduct fields, and coherent reflection of the autoproduct is successfully recovered at sufficiently low frequencies.

The research presented here supports three conclusions. First, rough-surface-scattered frequency-difference autoproduct fields can be analytically derived, numerically simulated, and

experimentally measured (in the long surface-correlation length limit) for random rough surfaces with Gaussian height distributions and Gaussian correlation functions. The convergence of theoretical, simulated, and measured autoproducts was quantified here through a complex spatial cross-correlation coefficient which was found to approach unity in the circumstances of interest.

Second, and most important to the potential applications of this work, the frequency-difference autoproduct may provide a coherent reflection coefficient that approaches unity even when its constituent in-band complex fields provide coherent reflection coefficients that approach zero. The coherent acoustic field scattered from a rough surface exponentially diminishes as the square of $kh\cos\theta$. The frequency-difference autoproduct mitigates this detrimental effect by altering the dependence from $kh\cos\theta$ to $\Delta kh\cos\theta$ with a user-selectable $\Delta k = \Delta f/c$. Thus, the recovery of coherent reflection afforded by the frequency-difference autoproduct is controlled by the chosen difference frequency, Δf, the signal reception geometry, and the extent of surface roughness. In practice, this may lead to a trade-off for signal processing algorithms between the robustness of the autoproduct and the loss of resolution at lower (difference) frequencies [see (Dowling, 2018), or (Douglass and Dowling, 2019)]. Additional considerations may occur in seeking practical applications of the rough-surface scattered frequency-difference autoproduct. For instance, source-receiver motion, a small ensemble of realizations, non-Gaussian roughness spectrum, or incomplete knowledge of the source waveform limit the direct applicability of the results as discussed here. However, difficulties associated with low SNR may, in fact, be suppressed by bandwidth- and ensemble-averaging. Regardless, the coherence recovery afforded by the altered dependence from $kh\cos\theta$ to $\Delta kh\cos\theta$ remains a potential feature provided by the frequency-difference autoproduct to increase the robustness of remote sensing tasks.

Third, the autoproduct's recovery of coherent reflection does not exclusively depend on $\Delta khcos\theta$. As a result of the quadratic nature of the autoproduct construction, the rough surface's correlation length and other geometrical parameters also affect the autoproduct's coherent reflection. The combination of variables – the frequency-difference roughness parameter – is controlled by the difference frequency multiplied by the ratio of surface rms roughness height to correlation length. The autoproduct's recovery of coherent reflection is predicted to be more successful for longer surface correlation lengths. Interestingly, the presence of the frequency-difference roughness parameter may allow environmental inversion for both surface rms height and correlation length from a remotely-measured ensemble-averaged autoproduct field. Inversion for surface correlation length is not a possibility provided by an equivalent ensemble-averaged genuine acoustic field.

Chapter 3
Coherence of the Frequency-Difference Autoproduct in High Frequency Acoustic Sea Surface Scattering

High frequency acoustic interactions with the sea surface pose a challenging modeling problem, given the large roughness parameter for even modest waveheights. The coherent reflection coefficient, determined from an ensemble average, is studied for high frequency (30, 40 kHz) sound scattered from 50 independent realizations of a rough sea surface (root-mean-square height of 0.5 m). Using R/P FLIP, data was collected in deep waters off the coast of California in January 1992. The measurements were made from a single hydrophone, depth 66 m, 576 m in range from the source, depth 147 m. Owing to the large roughness parameter, $\chi > 20$, the recorded field was incoherent at the broadcast frequencies. Using the frequency-difference autoproduct, a quadratic product of complex fields at nearby frequencies, coherent reflection is recovered, albeit at lower effective frequency. An analytic formula for frequency-difference autoproduct coherent reflection coefficients, utilizing the Kirchhoff approximation and a Gaussian surface autocorrelation function, compares favorably with measurements. Better agreement with measurements is found by minor adjustments to the surface conditions, obtained from a curve-fitting procedure. Surface adjustments identified here from a single receiver match those determined from horizontal spatial coherence estimates made from the full eight element receiving array. The following chapter is a near reproduction of an in-progress manuscript. For clarity, formulas and figures repeated elsewhere in this thesis are maintained in this section.

3.1 Introduction

Reviews of rough surface scattering abound (Brekhovskikh and Lysanov, 1991; Darmon et al., 2020; Elfouhaily and Guérin, 2004; Medwin and Clay, 1998; Oglivy, 1991). Studies of rough surface scattering are germane to underwater acoustics, where the ocean surface incoherently scatters acoustic waves and limits sonar system performance through increased transmission loss and reverberation (Urick, 1983). The sea-surface-reflected path influences acoustic communications (Dowling and Jackson, 1993; Rawat et al., 2020) and is common in both shallow and deep water propagation (Dahl, 1996). Scattering effects typically scale with frequency, resulting in a challenging underwater transmission channel for high frequency acoustic energy.

One of the detrimental impacts of sea surface scattering is the loss of signal coherence. A common notion, valid in the Kirchhoff approximation (Eckart, 1953; Medwin and Clay, 1998), is that coherence exponentially diminishes as the Rayleigh roughness parameter $\chi = kh\cos\theta$ increases, where k is the acoustic wavenumber, h is the root-mean-square (rms) roughness of the surface, and θ is the incidence angle measured from the surface normal. Large values of the roughness parameter, indicative of significant incoherent scattering, are therefore more likely to occur in high frequency propagation. The coherence of the acoustic field in rough surface scattering scenarios is often quantified using the coherent reflection coefficient (Jones et al., 2009; Olson, 2023; Olson and Jackson, 2020; Thorsos, 1990; Williams et al., 2004). Prior studies demonstrated the capability of the frequency-difference autoproduct (Dowling, 2018; Worthmann and Dowling, 2017), a lower frequency pseudofield constructed from higher frequency acoustic fields, to recover coherent reflection from rough-surface-scattered acoustic fields in idealistic environments (Joslyn and Dowling, 2022) and in the ocean (Joslyn et al.,

2023). In both studies, coherent reflection was restored for genuine acoustic scattering of $1 < kh\cos\theta < 4$ by downshifting the frequencies to Δf, the difference frequency between constituent acoustic fields, such that $\Delta kh\cos\theta$ was negligible.

The primary purpose of this paper is to extend the regime of rough-surface-scattered frequency-difference autoproduct coherence recovery to higher frequencies and longer ranges. Theoretical and numerical results are compared to high frequency field data recorded by a single hydrophone off the coast of California on R/P FLIP in January 1992 (Dahl, 1996). In this experiment, narrowband pulses, 30 kHz and 40 kHz, were scattered by 50 independent realizations of the rough sea surface, $h = 0.5$ m, resulting in an exceedingly large roughness parameter ($\chi > 20$). The measured frequency-difference autoproduct coherent reflection coefficient approaches unity for sufficiently-low difference frequencies, even though the constituent fields themselves are incoherent. An analytic formula describing autoproduct-based coherence recovery, derived in (Joslyn and Dowling, 2022) using the Kirchhoff approximation and Gaussian surface autocorrelation function, compares favorably with experimental data. Monte Carlo sea surface scattering simulations, evaluated with the same assumptions, agree with measured data and quantify the expected variation of a 50-ping ensemble.

The secondary consideration of this work concerns surface characterization from remotely-measured acoustic fields at a single receiver. A numerical strategy, akin to one used to provide minor modifications of surface conditions in the Shallow Water ’06 experiment (Joslyn et al., 2023), was designed to identify the autocorrelation length that optimized agreement between theoretical and measured autoproduct coherent reflection coefficients. The autoproduct-based correction to surface autocorrelation length using a single receiver is nearly identical to the adjustment previously made using horizontal spatial coherence estimates from eight receivers

(Dahl, 1996). As a result, a potential parallel in rough surface scattering is discussed between the analytic form of the frequency-difference autoproduct and the spatial coherence of the acoustic field in the geometrical optics limit [see, e.g., (McDaniel, 2004), (Oglivy, 1991), or (Thorsos, 1988)].

The FLIP experiment was conducted in deep waters of the Pacific Ocean (depth ~4000 m). Horizontal spatial coherence measurements were first reported in (Dahl, 1996) and modeled using the Kirchhoff approximation. Later, analytic scaling relations for spatial coherence were examined (Dahl, 2004), and the time spreading of the surface-scattered signals has also been investigated (Dahl, 2001). Additionally, investigations of bubble backscattering(Dahl, 2003; Dahl and Plant, 1997) and bubble cloud evolution (Dahl and Jessup, 1995) during the experiment exist, but bubbles do not impact the forward scattered data analyzed here (Dahl, 1996).

Frequency-difference autoproduct studies employing field data principally address problems in remote sensing, by way of beamforming (Abadi et al., 2012; Douglass et al., 2017) and matched field processing (Geroski et al., 2023; Geroski and Dowling, 2019, 2021; Worthmann et al., 2017; Yuan et al., 2023). The success of the autoproduct in these cases is attributed to the greater robustness to mismatch at the difference frequencies than at the broadcast frequencies (Worthmann et al., 2015). This intuition is illustrated for beamforming through randomly-located scatterers in (Douglass and Dowling, 2019), where the deleterious effects of scattering were minimized at the difference frequency. Some work with field data explores the surrogate fields themselves, through cross correlations of measured autoproducts to predicted fields (Geroski et al., 2021), analysis of spatial coherence in bottom-reflected sound (Joslyn et al., 2022), and coherent reflection in mid-frequency sea-surface scattering (Joslyn et al., 2023). The current work constitutes further effort to explore the coherence of the

autoproduct, which is a key aspect of its success in array signal processing (Geroski and Dowling, 2019).

The remainder of this paper is organized into four sections. Section 3.2 summarizes the theoretical background and simulation details for rough-surface-scattered frequency-difference autoproducts. Section 3.3 highlights important features of the FLIP experiment. Section 3.4 presents the coherent reflection coefficients determined from theory, simulation, and measurements. Section 3.5 discusses the four conclusions drawn from this work.

3.2 Theory and Simulation

Given the previous works in the area (Joslyn et al., 2023; Joslyn and Dowling, 2022), only minimal context is provided here. Essential autoproduct formulas and coherence metrics are detailed, followed by a brief summary of the numerical Monte Carlo strategy.

3.2.1 Frequency-Difference Autoproduct and Coherent Reflection Coefficient

For a complex acoustic field $P(\boldsymbol{R_2}, \omega)$ at spatial location $\boldsymbol{R_2}$ and angular frequency ω, with bandwidth $\Omega_L \leq \omega \leq \Omega_H$, the bandwidth-averaged frequency-difference autoproduct is defined as

$$\langle AP_{\Delta}(\boldsymbol{R_2}, \Delta\omega)\rangle_{BW} = \frac{1}{\Omega_H - \Omega_L - \Delta\omega}\int_{\Omega_L+\Delta\omega/2}^{\Omega_H-\Delta\omega/2} P(\boldsymbol{R_2}, \omega_+)P^*(\boldsymbol{R}_2, \omega_-)\, d\omega\,. \qquad (3.1)$$

Here, the difference frequency $\Delta\omega$ denotes the separation between the constituent field frequencies $\omega_{\pm} = \omega \pm \Delta\omega/2$. The user-chosen difference frequency can, in general, exist below the recorded signal bandwidth, and the nonlinear pseudofield defined by Eq. (3.1) may mimic genuine acoustic fields at the out-of-band frequency (Lipa et al., 2018; Worthmann and Dowling, 2017). The $\langle\ \rangle_{BW}$ indicates autoproduct samples throughout the bandwidth have been averaged.

Scattered field coherence was determined by the coherent reflection coefficient (Medwin and Clay, 1998),

$$|\mathcal{R}_{coh}| = \left|\frac{\langle\psi_{rough}\rangle}{\psi_{flat}}\right|, \tag{3.2a}$$

where $\langle\ \rangle$ is an ensemble average over independent surface realizations and ψ is either the frequency-difference autoproduct or acoustic field. The emphasis of this work is assessment of the overall coherence, not phase, of high-frequency scattered fields and the frequency-difference autoproducts constructed from them. Thus, only magnitudes are reported, with values near 1 (0) indicative of coherent (incoherent) reflection. For measurements of the coherent reflection coefficient, the imperfectly-known source waveform is removed by

$$|\mathcal{R}_{coh}(f)| = \left|\frac{\langle P_{rough}(f)\rangle}{\langle|P_{rough}(f)|\rangle}\right|, \tag{3.2b}$$

for the acoustic field at frequency f and

$$|\mathcal{R}_{coh}(\Delta f)| = \left\langle\left|\frac{\langle P(r,\omega_+)P^*(r,\omega_-)\rangle}{\sqrt{\langle P(r,\omega_+)P^*(r,\omega_+)\rangle\langle P(r,\omega_-)P^*(r,\omega_-)\rangle}}\right|\right\rangle_{BW}. \tag{3.2c}$$

for the autoproduct at difference frequency Δf. Eqs. (3.2b) and (3.2c) were used to quantify reflected field coherence from an unknown source waveform in the Shallow Water ’06 experiment (Joslyn et al., 2023). A similar normalization strategy was implemented to estimate the horizontal spatial coherence of the FLIP data (Dahl, 1996).

Predictions of the coherent reflection coefficient are determined by analytic derivation. A common theoretical diagram of rough surface scattering is shown in Fig. 3.1. The mean value of the rough surface $\zeta(x,y)$ sets the x-y plane and the specular point defines the origin. The incidence angle, θ, is measured with respect to the surface normal in the x-z plane. Using the

Kirchhoff and Fresnel approximations, the scattered field received at $\boldsymbol{R_2}$ from an omnidirectional source at $\boldsymbol{R_1}$ is given by (Joslyn and Dowling, 2022; Medwin and Clay, 1998),

$$P(\boldsymbol{R_2}, \omega) = -\frac{i\Gamma\omega\cos\theta}{2\pi c R_1 R_2} e^{i\frac{\omega}{c}(R_1+R_2)} \int_{-\infty}^{\infty}\int_{-\infty}^{\infty} e^{\frac{i\omega}{cR}\left(x'^2\cos^2\theta + y'^2\right) + 2i\frac{\omega}{c}\cos\theta\,\zeta(x',y')}\, dx'dy', \qquad (3.3)$$

where $R = 2R_1R_2/(R_1+R_2)$, c is the sound speed, Γ is the reflection coefficient (-1 for ocean-air interface), and integration is performed over the x-y plane. Substituting Eq. (3.3) into Eqs. (3.1) and (3.2a) yields the coherent reflection coefficient for the frequency-difference autoproduct formed from rough-surface-scattered acoustic fields (Joslyn and Dowling, 2022):

$$\mathcal{R}_{coh} = e^{-2(\Delta k h\cos\theta)^2}\left[\left(1 - i\Delta k h^2\frac{4R}{L^2}\right)\left(1 - i\Delta k h^2\frac{4R\cos^2\theta}{L^2}\right)\right]^{-1/2}, \qquad (3.4)$$

where $\Delta k = \Delta\omega/c$ is the difference wavenumber, h is the rms roughness, and L is the (isotropic) surface correlation length.

In the derivation of Eq. (3.4), the surface height distribution and surface autocorrelation function were assumed Gaussian. The combination of high signal frequency and large surface roughness permitted replacement of the surface autocorrelation by the first two terms of its series expansion, equivalent to the geometric optics limit (McDaniel, 2004). Notably, Eq. (3.4) is independent of constituent field frequency, reminiscent of the frequency independence of the scattering cross section in the geometric optics limit (Dahl, 1996; Thorsos, 1988). The use of Eq. (3.4) for the field data examined herein is justified by the large surface roughness parameters in the FLIP experiment ($\chi > 20$). Furthermore, the geometric optics limit of the Kirchhoff approximation satisfactorily modeled the spatial coherence of the FLIP measurements (Dahl, 1996), rationalizing the modeling assumptions.

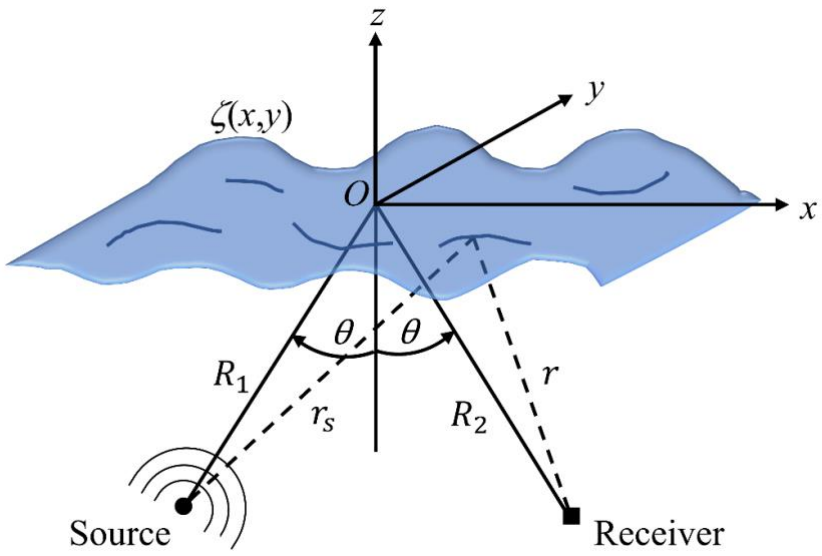

Figure 3.1: Reproduction of Fig. 1 from (Joslyn and Dowling, 2022) showing a typical scattering scenario from the rough surface ζ. The relevant features for Eqs. (3) and (4) are the source to specular point distance R_1, the specular point to receiver distance R_2, and the angle of incidence θ.

3.2.2 Monte Carlo Simulation

Stochastic treatment of the sea surface scattering was used to identify appropriate error bars. Following the Monte Carlo approach to quantify uncertainty of coherent reflection coefficients owing to a finite ensemble (Joslyn et al., 2023; Joslyn and Dowling, 2022), random surfaces with Gaussian roughness profile and roughness spectrum were generated using open-source software (Bergström, 2012). The rms height and autocorrelation length were chosen to match the FLIP experiment (surface conditions discussed in the next section). Ensembles of 50 independent surfaces were randomly selected 100 times from a pool of 1600 surface realizations (800 for each narrowband pulse in the experiment) and integrated following Eq. (3.3). Coherent reflection coefficients were then computed from Eqs. 3.2(b) and 3.2(c), and the 95th percentile of variation determined the error bars.

All numerical evaluations of Eq. (3.3) were conducted on a discretized, rectangular patch. The finite patch was 380 m by 120 m [selected to exceed the patch size of the prior ocean scattering autoproduct study (Joslyn et al., 2023)], with minor dimension orthogonal to the specular plane. The surface was sampled every 2.5 cm and the source spectrum set to unity. Trapezoidal integration was selected to perform numerical integration.

The efficacy of the numerical implementation was tested in the zero roughness limit. The well-known theoretical result for flat surface reflection, given by the method of images, was compared to evaluation of Eq. (3.3) with $\zeta = 0$. For the geometry and frequencies of the FLIP experiment, the complex cross correlation of simulated-to-theoretical results was ~1 and amplitude variations were 1% or less at all frequencies and difference frequencies. Thus, the numerical error bars are expected to satisfactorily provide nominal uncertainty estimates associated with limited-member ensembles.

3.3 FLIP Experiment Overview

Data collected from R/P FLIP was utilized to investigate autoproduct coherence recovery in high frequency sea surface scattering. Important details of the experiment are outlined in this section, including time and frequency domain representations of the recordings. Additional expedition information can be found elsewhere (Dahl, 1996; Dahl and Jessup, 1995).

3.3.1 Experiment Description

Measurements were obtained from the research platform FLIP off the southern coast of California in the Pacific Ocean (32 °N, 125 °W) during January 1992. The depth was ~4000 m, and the sound speed profile from a conductivity-temperature-depth unit resulted in negligible refraction-based adjustments to the nominal incidence angle. Thus, following previous work

(Dahl, 1996), the sound speed is set to $c = 1500$ m/s for computations. Bubbles, also investigated while at sea (Dahl, 2003; Dahl and Jessup, 1995; Dahl and Plant, 1997), did not influence the forward scattered data analyzed here, allowing for direct assessment of the surface scattering. The surface rms height was $h = 0.5$ m, owing to a large swell component, and the root-mean-square slope, determined from wind speed, was $s_L = 0.119$. By the equivalence of the mean-square slope, s_L^2, and the Laplacian of the surface autocovariance function evaluated at zero lag (Apel, 1994), the surface autocorrelation length was $L = 8.40$ m, consistent with the geometric optics limit.

The specular plane geometry is shown schematically in Fig. 3.2. The range between the acoustic source, depth 147 m, and receiver, depth 66 m, was 576 m, setting the incidence angle $\theta = 69.7°$. The source was deployed from a spar buoy tethered to FLIP, and the receiver analyzed was one channel of an eight element horizontal array attached the hull of the FLIP. The source and receiver are both ITC 1032 (Gavial International Transducer Corporation – Santa Barbara, CA) omnidirectional hydrophones.

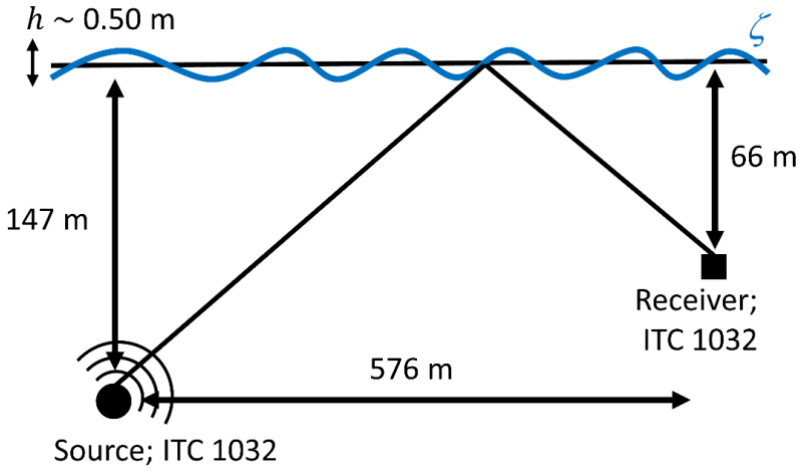

Figure 3.2: Specular plane diagram for field data collected in January 1992 off the coast of California. The omnidirectional source, depth 147 m, and omnidirectional receiver, depth 66 m, are separated by range 576 m.

The measurements studied herein, labeled as Set 3 in (Dahl, 1996), were one of five experimental runs. Each run used a different propagation geometry through range and source depth adjustments. The largest roughness parameter was obtained in Set 3, leading to its selection here. Further, the other sets had minor problems, including the potential for bubble scattering and attenuation (Set 1), temporal overlap between direct and reflected paths (Set 2), surface slicks (Set 4), and unexpectedly high spatial coherence estimates (Set 5). These issues did not preclude their spatial coherence analysis, but they do engender some hesitation for the frequency-difference autoproduct. Although the other sets could be investigated, for brevity only Set 3 was considered, and given the focus on coherent reflection recovery in large roughness parameter acoustic scattering, Set 3 is the natural choice.

3.3.2 Time and Frequency Domain Measurements

Narrowband signals with center frequencies of 30 kHz and 40 kHz were alternately broadcast from the source. In each case, the transmitted signal was a continuous wave pulse, approximately 12 ms in duration. The received signals were heterodyned to 5 kHz and sampled at 20 kHz, with the appropriate center frequencies recovered in post-processing. Interestingly, this is the first study in which autoproducts were constructed from heterodyned signals.

Signal transmission was repeated 50 times, resulting in 50 independent sea surface interactions for both the 30 and 40 kHz signals. Jitter was removed by aligning the direct path arrivals (Dahl, 2010; Joslyn et al., 2023). The time domain signals are shown in Fig. 3.3 with the direct path and surface-scattered path prominently apparent. The horizontal axis is reported in milliseconds relative to the direct path arrival and the vertical axis indicated ping number. The direct path is consistent in amplitude and temporal duration while the surface-scattered path

exhibits amplitude variation and time spreading expected of rough-surface-scattered signals. For coherence analysis, the surface-scattered path was isolated through time-gating.

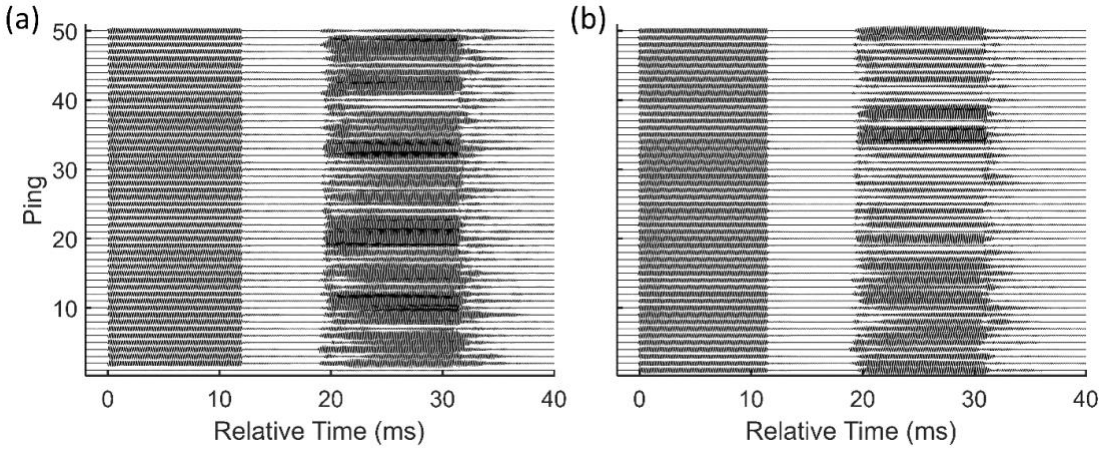

Figure 3.3: Time domain recordings of the direct and surface-scattered path for 50 pings of narrowband pulses with (a) 30 kHz and (b) 40 kHz center frequencies. The surface-scattered arrivals demonstrate significant amplitude variation and temporal broadening. The horizontal axis denotes time relative to the direct path arrival (~12 ms), and the ping numbers do not correlate between panels as pulses were alternately broadcast.

In Fig. 3.4, the average direct path amplitude, determined from an incoherent average of the direct path recordings at each frequency, is displayed for both center frequencies. Plotted against the recorded frequency (i.e. incorporating the apparent shift in frequency from the heterodyne), the normalized strength of the 30 kHz and 40 kHz pulses are shown in red and blue, respectively. Spectral components within approximately 100 Hz of the center frequency were selected for further analysis and are marked with crosses on Fig. 3.4. As the direct path is suggestive of the intended source waveform, maintaining more bins would introduce frequencies with trivial broadcast energy and maintaining fewer bins would result in an impractical difference frequency bandwidth. Thus, for the nominal frequency resolution (13 Hz), the autoproduct difference frequencies were $13 \leq \Delta f \leq 107$ Hz. The difference frequency range is shown schematically above Fig. 3.4.

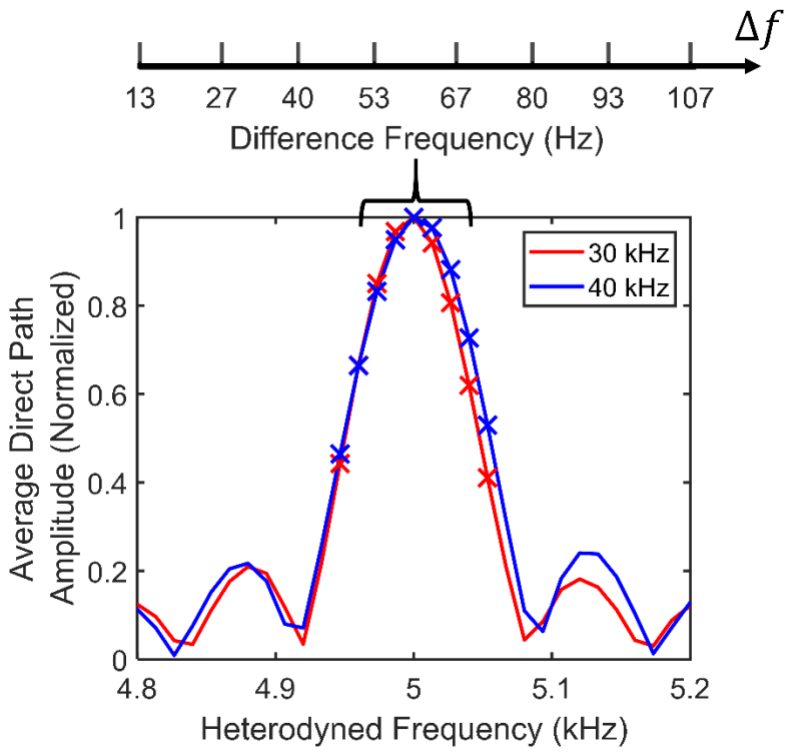

Figure 3.4: Approximate source waveform broadcast during the experiment. The average amplitude of the direct path, normalized to unity, is shown for 30 kHz (40 kHz) in red (blue). The apparent reduction in frequency from the heterodyne in data acquisition was removed in post-processing of the signals. Crosses superimposed on the pulses indicate the frequencies maintained in analysis, and the difference frequency range available from these frequencies is indicated above the main plot.

3.4 Coherent Reflection Coefficient in the FLIP Experiment

3.4.1 Recovery of Coherence

Theoretical autoproduct-based coherence recovery, described by Eq. (3.4), was assessed numerically and experimentally for high frequency acoustic sea surface scattering using the FLIP data. Although the narrowband signal limited measured difference frequencies, Eq. (3.4) was evaluated at difference frequencies of 10 Hz – 10 kHz, removing this restriction for the theory

curve. Using the strategy prescribed in Chapter 3.2.2, error bars were calculated for the experimental frequencies and difference frequencies. Measured coherent reflection coefficients were determined from the experimental recordings and Eqs. (3.2b) and (3.2c). For both the Monte Carlo simulations and the measured data, 30 kHz and 40 kHz pulses were processed separately, given their independent interactions with the sea surface.

Coherent reflection coefficients for the frequency-difference autoproduct and acoustic field are plotted against difference frequency and acoustic frequency on a logarithmic horizontal axis in Fig. 3.5. The measured 30 kHz acoustic coherent reflection coefficients are marked by red ◊'s, and the autoproduct coherent reflection coefficients generated from these acoustic fields are indicated by red asterisks. Equivalent markers for the 40 kHz measurements are shown in blue ◊'s and blue circles. The theoretical results from Eq. (3.4) are given by the black curve. Error bars encompassing the expected variation at the signal frequencies are noted by one error bar of the corresponding color. Difference frequency variation is captured by one error bar per difference frequency and attached to the theoretical curve.

Figure 3.5 shows the considerable recovery of coherent reflection afforded by the frequency-difference autoproduct for high-frequency-scattered acoustic fields in the FLIP experiment. Good agreement exists between theoretical, numerical, and experimental results. The measured acoustic field is incoherent, with an average coherent reflection coefficient value of 0.09 (0.11) for the 30 kHz (40 kHz) narrowband pulses. By contrast, the frequency-difference autoproducts generated from these fields register coherent reflection coefficients greater than 0.71 in all cases and exceed 90% recovery of coherent reflection for $\Delta f \leq 53$ Hz. The theory curve from Eq. (3.4) matches the measured autoproduct coherence well, particularly accounting for the finite ensemble error bars. Additionally, the theory curve indicates that for the FLIP

scattering environment more than 50% coherent reflection should be expected for difference frequencies up to 210 Hz.

Some discrepancy exists between the nominal theory curve and the measured autoproduct coherent reflection coefficients. The measurements tend to overestimate the expected coherent reflection coefficient. A minor surface correlation length modification, described in the next section, improves the agreement between theory and measurements and is shown in green. (Dahl, 1996) identified a similar adjustment to optimize the match between theoretical and measured spatial coherence in the FLIP data. Evaluation of Eq. (3.4) using that adjustment is indicated by orange dashes.

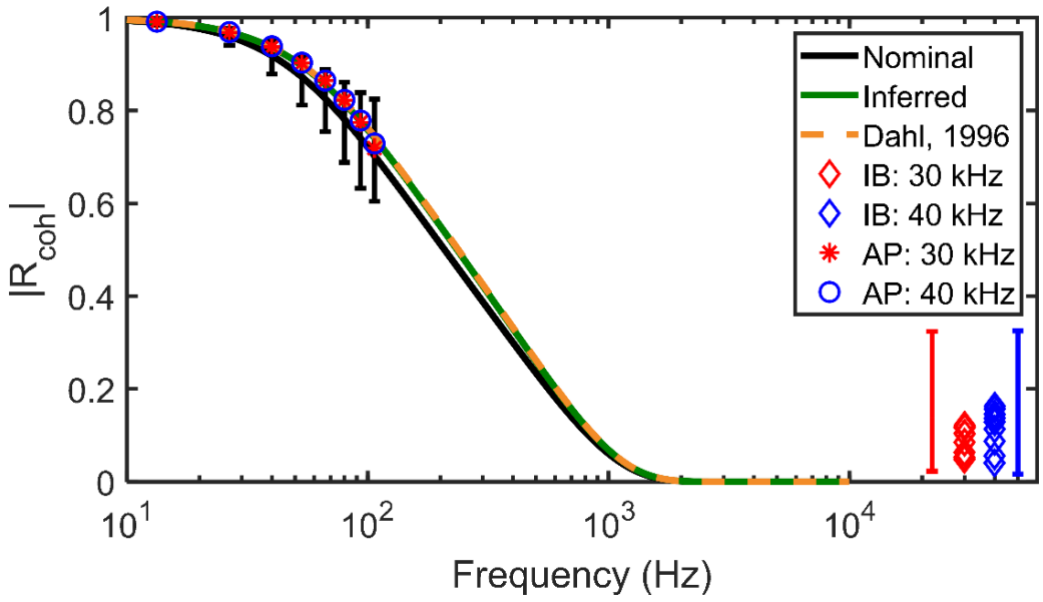

Figure 3.5: Coherent reflection recovery in the FLIP experiment using the frequency-difference autoproduct. Solid curves indicate theory while individual markers in red and blue denote measurements originating from 30 kHz and 40 kHz pings, respectively. The coherence of the measured autoproduct (left) is significantly greater than the coherence of the constituent high frequency fields (right). Error bars encompassing the 95th percentile of variation in Monte Carlo simulations are shown in the corresponding color. Theory curves using adjustments to the nominal correlation length from a numerical optimizer (green) and from spatial coherence analysis in (Dahl, 1996) (orange) show excellent agreement.

3.4.2 Inference of Surface Statistics

Predictions of autoproduct-based coherent reflection recovery using Eq. (3.4) require knowledge of the geometric environment and properties of the randomly-rough surface. In the FLIP experiment, the mean-square slope of the sea surface was estimated from recorded wind speed by the empirical formula (Phillips, 1977):

$$s_L^2 = 0.0046 \ln(2.1U^2), \tag{3.5}$$

where U is the wind speed (m/s) measured 10 m above the surface. Appendix A of (Dahl, 1996) provides additional details and comparisons to estimates of s_L from in-situ waveheight spectra measurements taken during the research expedition. As noted in Chapter 3.3.1, the mean-square slope is related to the isotropic surface autocorrelation function, $\Phi(\rho)$, by

$$s_L^2 = -\nabla^2 h^2 \Phi|_{\rho=0} = \frac{4h^2}{L^2}, \tag{3.6}$$

where the final equality is consistent with the geometrical optics limit.

Equations (3.4) – (3.6) define the relationship between autoproduct-based coherence recovery in high-frequency scattered acoustic fields and the environmental conditions (wind, mean-square slope, and autocorrelation length). A nonlinear curve-fitting scheme in MATLAB identified the autocorrelation length adjustment necessary to optimize the match between measured autoproducts and the theory given in Eq. (3.4). Reported adjustments are the average of the modifications obtained individually for the 30 kHz and 40 kHz data. Extensions to root-mean-square slope and wind speed by Eq. (3.5) and (3.6) are shown in Table 3.1.

The inferred environmental parameters are within the expected uncertainties of the FLIP experiment, especially given at sea wind speed measurement variability for the time ($\pm$2 m/s) (Apel, 1994). The autocorrelation length was increased by ~0.6 m, resulting in a wind speed decrease of 0.6 m/s. (Dahl, 1996) used a similar fitting strategy to maximize the match between

Table 3.1: Comparison of environmental characteristics nominally reported, inferred from autoproduct measurements, and identified from spatial coherence measurements in (Dahl, 1996).

	Autocorrelation Length (m)	Mean-Square Slope	Wind Speed (m/s)
Nominal	8.40	0.119	3.2
Inferred	9.03	0.111	2.6
(Dahl, 1996)	9.09	0.110	2.6

modeled and measured estimates of spatial coherence across the 8 element receiving array used in the FLIP experiment. Within rounding, those adjustments are identical to those identified here and are reproduced in the final row of Table 3.1. The surface autocorrelation functions, determined from an assumed Gaussian form, are shown in Fig. 3.6. The nominal (black), inferred (green), and (Dahl, 1996) (orange) autocorrelation functions are plotted against lag to 15 m. The inset panel focuses on the lag extent appropriately modeled under the geometric optics limit.

Equation (3.4) was evaluated for the surface modifications identified here and in (Dahl, 1996) and plotted in green and orange, respectively, in Fig. 3.5. The optimized theoretical curves are a great match to the measured data and to each other. The excellent agreement between the adjustments inferred from a single receiver here and those obtained by spatial coherence across 8 receivers is notable. Theoretical modeling was related only insofar as the Kirchhoff approximation and the geometrical optics limit were employed, suggestive of a parallel between the first moment of the quadratic field construct (autoproduct coherent reflection) and the second moment of the conventional field (acoustic spatial coherence).

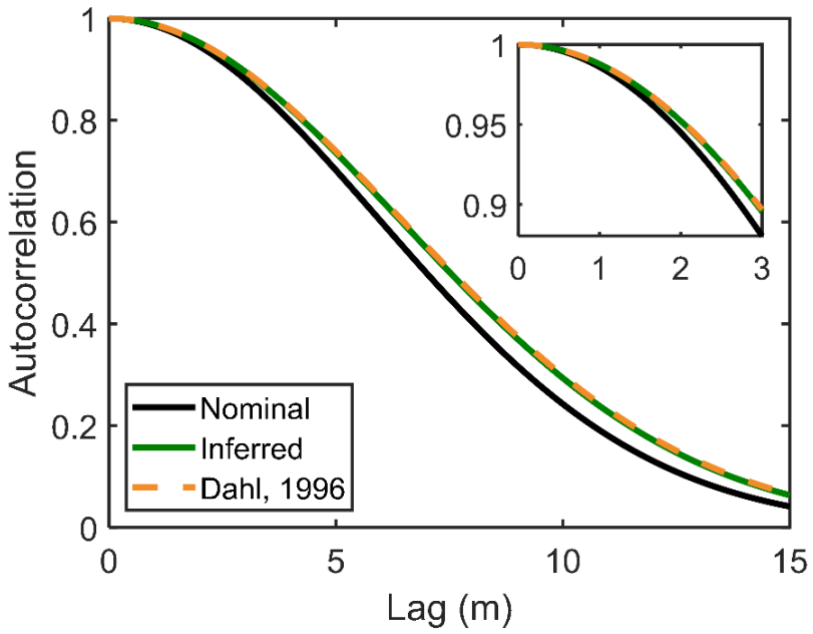

Figure 3.6: Comparison of sea surface autocorrelation functions with the inset figure zoomed in on the region significantly contributing to autoproduct coherence recovery in the geometric optics limit. The inferred corrections to rms height and autocorrelation length agree with those found in (Dahl, 1996). Note, the Gaussian form is not generated from a measured sea surface spectrum, but is a suitable assumption for the conditions reported during the experiment.

Given the error bars' coverage of the measured autoproducts in Fig. 3.5, surface corrections may be unnecessary for the present data. However, the surface adjustments identified previously (Dahl, 1996) were not strictly necessary either, given the size of spatial coherence error bars for a 50 ping ensemble. Importantly, the strategy outlined in this subsection details how Eq. (3.4) may be employed to extract environmental information from measured frequency-difference autoproducts, particularly if a larger ensemble is used.

3.5 Conclusion

Coherent reflection recovery using the frequency-difference autoproduct has been explored for moderately rough surfaces in both laboratory (Joslyn and Dowling, 2022) and ocean measurements (Joslyn et al., 2023). The major aim of this paper was to extend autoproduct-based

coherence recovery to high frequency acoustic scattering from very rough surfaces. For this purpose, sea-surface-scattered acoustic signals, where the roughness parameter $\chi = kh\cos\theta > 20$, collected from the R/P FLIP in the Pacific Ocean in 1992 were analyzed. The measured coherent reflection coefficients were incoherent across the 50 ping experiment at the broadcast frequencies, but > 71% coherent reflection was recovered for all autoproduct difference frequencies. Furthermore, autoproduct coherent reflection coefficients approached unity at the lowest available difference frequencies. Theoretical autoproduct coherent reflection coefficients, derived from the Kirchhoff approximation and a Gaussian form of the surface autocorrelation function, matched the measured data within the error bars determined from Monte Carlo simulations of a 50 ping ensemble. A numerical curve-fitting routine was provided to improve the match between theory and measurements.

The work here supports the following four conclusions. First, the frequency-difference autoproduct is capable of restoring reflected-field coherence in high frequency ocean-surface-scattered acoustic fields that are entirely incoherent. Greater recovery was reported at lower difference frequencies, where Δf was $O(f/1000)$. Thus, supporting contentions noted elsewhere (Douglass and Dowling, 2019; Dowling, 2018; Joslyn and Dowling, 2022), selection of the appropriate difference frequency in practice may require trade-offs between robustness and resolution. Second, autoproduct-based coherence recovery is possible at long ranges in the deep ocean. The prior sea-surface-scattering study (Joslyn et al., 2023) considered 14 – 20 kHz signals traversing 200 m range in a shallow channel. The extended range, greater depths, and higher frequencies used here result in a propagation distance of over ten thousand acoustic wavelengths, up to 8x further than the previous experiment. Third, a simple analytic formula (Joslyn and Dowling, 2022) can satisfactorily predict the recovery of coherent reflection offered

by the frequency-difference autoproduct in scattering characterized by large roughness parameters. Finally, optimization of the match between theoretical and measured autoproducts can provide estimates of environmental parameters. Surface characterization in this fashion identified values nearly identical to those made previously (Dahl, 1996) from comparing horizontal spatial coherence measurements to modeling based on the geometric optics limit. While it may be expected that equivalent approximations yield equivalent results, it is unexpected that corrections obtained from eight channels of a horizontal array are replicated with analysis from a single hydrophone.

Although the conclusions are positive, the predictability aspect of this study is limited by the assumption of a Gaussian autocorrelation function. The analytic formula, by way of the geometric optics limit in the derivation, naturally limits analysis to high frequency acoustic fields. However, given the motivation of the frequency-difference autoproduct to operate on high frequency fields, this may not be too restrictive in practice. Additionally, in light of other works considering the autocorrelation of natural surfaces to be effectively Gaussian at small lags (Darawankul and Johnson, 2007; Fung and Moore, 1966), as well as the analytic troubles of the exponential autocorrelation function (Oglivy, 1991), the applicability of the autoproduct formula may extend further than initially expected. In these cases, nevertheless, its utility for accurate inversion would need to be reassessed. Regardless of analytic predictability, the coherence of the frequency-difference autoproduct in rough surface scattering may be of appreciable importance in remote sensing tasks and array signal processing, where performance relies on consistent phase structure.

Chapter 4

Coherent Reflection Recovery in Scattering from the Ocean Surface Using the Frequency-Difference Autoproduct

Measurements and modeling of coherence of the frequency-difference autoproduct constructed from sea-surface-scattered acoustic fields are presented here. The frequency-difference autoproduct, a quadratic product of acoustic fields at nearby frequencies, mimics a genuine field at the difference frequency. In rough surface scattering, the lower effective frequency minimizes the apparent surface roughness, restoring coherent reflection. The recovery of coherent reflection in sea surface scattering via the frequency-difference autoproduct is examined for data collected off the coast of New Jersey during Shallow Water '06. An acoustic source, depth 40 m, and receiver, depth 24.3 m and range 200 m, interrogated 160 independent realizations of the ocean surface. The rms surface height h was 0.167 m and broadcast frequencies of 14 – 20 kHz are used, setting $2.5 \leq kh\cos\theta \leq 3.7$ for acoustic wavenumber k and incidence angle θ. Measured autoproducts, constructed from incoherent constituent fields, show significant coherent reflection at sufficiently low difference frequencies. Theoretical results, using the Kirchhoff approximation and a non-analytic surface autocorrelation function, agree with experimental findings. The match is improved using a numerical strategy, exploiting the relationship between autoproduct-based coherence recovery, the autocorrelation function, and the surface spectrum. Error bars computed from Monte Carlo scattering simulations support the assertions made herein. The following

chapter is a near reproduction of an in-progress manuscript. For clarity, formulas and figures repeated elsewhere in this thesis are maintained in this section.

4.1 Introduction

Field coherence is important in array signal processing as increased coherence typically improves the success of remote sensing tasks. Random rough surface scattering, a common means of coherence loss, has an extensive literature, with review articles (Darmon et al., 2020; Elfouhaily and Guérin, 2004; Fortuin, 1970) and textbooks (Bass and Fuks, 1979; Beckmann and Spizzichino, 1963; Brekhovskikh and Lysanov, 1991; Medwin and Clay, 1998; Oglivy, 1991) spanning both acoustics and electromagnetics. In underwater acoustics, the rough ocean surface is a primary mechanism for the random scattering of sound waves as forward scattering from the sea surface represents a prominent channel for shallow and deep water propagation (Dahl, 1996) and is important in underwater communications (Dowling and Jackson, 1993). The incoherent scattering of sound waves from the sea surface reduces both acoustic coherence (Gorodetskaya et al., 1999) and sonar system effectiveness (Urick, 1983) and the effects generally scale with the ratio of surface roughness to acoustic wavelength.

In this paper, theoretical and simulated recovery of reflected-field coherence afforded by the frequency-difference autoproduct (Worthmann and Dowling, 2017) is compared to ocean measurements collected off the coast of New Jersey during Shallow Water ’06 (Tang et al., 2007). A previous study (Joslyn and Dowling, 2022) investigated the capability of the frequency-difference autoproduct to restore coherence in acoustic waves, with wavenumber k and incidence angle from surface normal θ, scattered from two-dimensional (3-D scattering problem) pressure-release isotropic surfaces described by Gaussian height distributions, root mean square (rms) roughness h, and Gaussian autocorrelation functions, correlation length L. The work here

generalizes the analytical results to arbitrary surface autocorrelation functions and compares the modeled autoproduct coherent reflection coefficient to field data. The measured acoustic signals were scattered from a surface exhibiting both wind- and swell-wave systems for $2.5 \leq kh\cos\theta \leq 3.7$. Coherence recovery agrees well between all three methods and demonstrates the coherent reflection coefficient for the frequency-difference autoproduct may approach unity for sufficiently low difference frequencies, even when significant incoherent scattering exists at the broadcast acoustic frequencies. Furthermore, the nonlinearity of the frequency-difference autoproduct imparts a strong dependence on the surface autocorrelation function, thereby providing a means for acoustic identification of lateral and vertical statistics of a rough surface. The analytic relationship between autoproduct-based coherence recovery, surface autocorrelation function, and surface power spectrum is introduced and discussed. Through a curve-fitting optimization strategy, this relationship is used to infer characteristics about the experimental environment and the parameter estimates are found to be in agreement with experimental uncertainty.

This work primarily analyzes data collected off the coast of New Jersey as part of the Shallow Water ’06 experiment (Tang et al., 2007). The sea surface forward scattering experiment considered here consists of 160 measurements, recorded along a vertical array, of the sound reflected from the sea surface during a 6.5 hour period in August 2006. In studies of the spatial coherence of these measurements (Dahl, 2010; Dahl et al., 2013; Welton, 2015), refraction strongly influenced coherence results. Although full accounting of ray theory produced modeling results in agreement with measured data (Dahl, 2010; Dahl et al., 2013), appropriate adjustment of the specular incidence angle provided a suitable correction as well (Welton, 2015). The small slope approximation (Dahl, 2010; Dahl et al., 2013) and the Kirchhoff approximation (Welton,

2015) have both been used to model the surface scattering and the Kirchhoff approximation is found to be satisfactory here. The Kirchhoff approximation (Eckart, 1953; Medwin and Clay, 1998) is a common modeling choice and has been compared to other field data as well (Dahl, 1996).

Surface roughness is typically defined with respect to the incident acoustic wavelength by the Rayleigh roughness parameter, $\chi = kh\cos\theta$, with values greater than one suggestive of significant scattering. The large surface roughness parameter studied here (> 2.5) indicates significant incoherent scattering across the 160 independent realizations of the rough surface. The nominal surface spectrum (Dahl et al., 2013) was estimated by a combination of buoy-measured (low surface wavenumbers) and modeled (Plant, 2002) (high surface wavenumbers) spectrums. Minor modifications to the modeled region of the surface spectrum produced better agreement between theoretical and measured coherent reflection coefficients. Other studies employing the Kirchhoff approximation in ocean surface scattering (Dahl, 1996) and seafloor scattering (Berkson, 1980; Clay, 1966) have used the coherence of acoustic measurements to refine surface statistics. Unlike the previous works, however, the autoproduct-based strategy outlined herein allows for estimation of both vertical and lateral statistics from the recordings of only a single receiver.

In other studies of forward scattering from the ocean surface, coherence is interrogated within the broadcast bandwidth. Recent results suggest information at frequencies below the bandwidth may be synthetically estimated using the frequency-difference autoproduct (Dowling, 2018; Worthmann and Dowling, 2017). The physical implications of this unconventional claim have been investigated in a variety of environments (Geroski et al., 2021; Joslyn and Dowling, 2022; Lipa et al., 2018; Worthmann and Dowling, 2020b, 2020a), and the benefits for passive

remote sensing applications have been explored, including beamforming (Abadi et al., 2012; Douglass et al., 2017; Douglass and Dowling, 2019), matched field processing (Geroski et al., 2023; Geroski and Dowling, 2019, 2021; Worthmann et al., 2015; Yuan et al., 2023), and adaptive methods (Park et al., 2022; Wang et al., 2022; Worthmann et al., 2017; Xie et al., 2020; Yang et al., 2021). The positive remote sensing results can be attributed to the autoproduct's robustness against detrimental propagation effects that typically scale with frequency, such as seafloor scattering (Joslyn et al., 2022). Moreover, in the presence of strong, discrete scatterers randomly located in the acoustic propagation path, the autoproduct provides more reliable beamformed outputs, albeit at reduced resolution, by downshifting analysis to frequencies where the effects of scattering are not as strong (Douglass and Dowling, 2019). Analytic, numerical, and laboratory results extended this notion to regain coherent reflection from acoustic waves incoherently scattered randomly rough isotropic surfaces with Gaussian autocorrelation functions (Joslyn and Dowling, 2022). The main purpose of this study is to demonstrate the recovery of coherent reflection afforded by the frequency-difference autoproduct for acoustic scattering from realistic ocean surfaces with non-Gaussian autocorrelation functions. A secondary consideration of this work is prediction of the recovered coherence. Predictions are made from theoretical analysis and Monte Carlo simulations and compared to the measured data.

Section 4.2 details the mathematical formulation of autoproducts and rough surface scattering. Section 4.3 reviews relevant details of the Shallow Water '06 experiment and the highlights important sea surface conditions. Section 4.4 presents the modeling results and compares to ocean measurements. Section 4.5 summarizes the work and presents four conclusions.

4.2 Theory

This section reviews the previous formulation of the rough-surface-scattered frequency-difference autoproduct (Joslyn and Dowling, 2022) and presents the generalization to arbitrary surfaces. The frequency-difference autoproduct definition and the measure of coherence is presented prior to discussion of the relationship between coherence recovery, surface autocorrelation function, and surface spectra.

4.2.1 Autoproduct and Coherence Definitions

The frequency-difference autoproduct is a nonlinear acoustic pseudofield capable of mimicking genuine out-of-band acoustic fields (Dowling, 2018; Lipa et al., 2018; Worthmann and Dowling, 2017). Given a complex acoustic field, $P(\boldsymbol{R_2}, \omega)$, defined by the spatial coordinate $\boldsymbol{R_2}$ and angular frequency ω from an omnidirectional source with strength $S(\omega)$ at $\boldsymbol{R_1}$, a sample of the autoproduct, AP_Δ, is formed by multiplying the recorded signal at two different frequencies within the signal bandwidth:

$$AP_\Delta(\boldsymbol{R_2}, \omega, \Delta\omega) \equiv P(\boldsymbol{R_2}, \omega_+)P^*(\boldsymbol{R}_2, \omega_-)\,, \tag{4.1}$$

where the difference frequency, $\Delta\omega$, indicates the separation between the two frequencies $\omega_\pm = \omega \pm \Delta\omega/2$. For a signal with some bandwidth, $\Omega_L \leq \omega \leq \Omega_H$, there may be several $\omega_\pm$ satisfying the desired $\Delta\omega$. As shown in (Worthmann and Dowling, 2017) and discussed in other autoproduct studies (Dowling, 2018; Geroski et al., 2023; Geroski and Worthmann, 2021; Lipa et al., 2018), multipath cross terms arising from the quadratic product in Eq. (4.1) may be suppressed by a bandwidth average:

$$\langle AP_\Delta(\boldsymbol{R_2}, \Delta\omega)\rangle_{BW} = \frac{1}{\Omega_{BW}^\Delta}\int_{\Omega_C-\frac{1}{2}\Omega_{BW}^\Delta}^{\Omega_C+\frac{1}{2}\Omega_{BW}^\Delta} \frac{AP_\Delta(\boldsymbol{R_2}, \omega, \Delta\omega)}{S(\omega_+)\,S^*(\omega_-)}d\omega\,. \tag{4.2}$$

Here, the bandwidth available for averaging is given by $\Omega_{BW}^{\Delta} = \Omega_H - \Omega_L - \Delta\omega$ and the center frequency is $\Omega_C = (\Omega_L + \Omega_H)/2$. The assumed source spectrum knowledge in Eq. (4.2) provides a challenge to constructing bandwidth-averaged autoproducts for passive remote sensing, where source information may not be available. Previous studies avoid this limitation by averaging autoproduct cross-spectral density matrices (Geroski et al., 2023; Geroski and Dowling, 2021; Geroski and Worthmann, 2021; Worthmann et al., 2017) or even averaging Eq. (4.1) directly (Joslyn et al., 2022). Although the frequency-difference autoproduct formed from fields scattered by a surface exhibiting Gaussian vertical and lateral statistics is independent of constituent field frequency (Joslyn and Dowling, 2022), and the work here does not consider multipath propagation, bandwidth averages are included for completeness.

As in (Joslyn and Dowling, 2022), the reflected-field coherence was assessed by the coherent reflection coefficient $\mathcal{R}_{coh}$ (Medwin and Clay, 1998):

$$\mathcal{R}_{coh} = \frac{\langle \psi_{rough} \rangle}{\psi_{flat}}. \tag{4.3a}$$

Here, ψ is the acoustic field or the frequency-difference autoproduct and $\langle\ \rangle$ represents an ensemble average over realizations of the rough surface. The source spectrum used in data collection is imperfectly known, so a normalization, akin to that used for spatial coherence, is implemented for the acoustic field coherence at frequency f,

$$\mathcal{R}_{coh}(f) = \frac{\langle P_{rough}(f) \rangle}{\langle |P_{rough}(f)| \rangle}, \tag{4.3b}$$

and for the bandwidth-averaged autoproduct at difference frequency Δf,

$$\mathcal{R}_{coh}(\Delta f) = \left\langle \left| \frac{\langle P(r,\omega_+) P^*(r,\omega_-) \rangle}{\sqrt{\langle P(r,\omega_+) P^*(r,\omega_+) \rangle \langle P(r,\omega_-) P^*(r,\omega_-) \rangle}} \right| \right\rangle_{BW}. \tag{4.3c}$$

For omnidirectional sources and formal ensemble averages, the amplitude of Eqs. (4.3a) – (4.3c) are equivalent, due to the energy conservation inherent in the Kirchhoff approximation (Dahl, 1996; McDonald, 1974; Thorsos, 1984). The source-dependent phase of R_{coh} is not removed, but overall phase does not impact coherence (Joslyn and Dowling, 2022) and is not reported here. Perfectly coherent reflection is defined by $|\mathcal{R}_{coh}| = 1$ and totally incoherent scattering is given by $|\mathcal{R}_{coh}| = 0$.

4.2.2 Rough Surface Scattering

Generalization of rough-surface-scattered frequency-difference autoproducts to surfaces exhibiting non-Gaussian autocorrelation functions requires similar mathematical machinery to that shown in (Joslyn and Dowling, 2022). Given the existence of other works detailing preliminary analytic steps (Joslyn and Dowling, 2022; Medwin and Clay, 1998), only a terse overview of those are provided here.

Relevant rough surface scattering features are shown in Fig. 4.1. The origin of the Cartesian coordinate system is centered on the specular point between the omnidirectional source at $\boldsymbol{R_1}$ and omnidirectional receiver at $\boldsymbol{R_2}$. Two homogeneous media are divided by the arbitrary rough surface $\zeta(x, y)$, and the mean value of the interface determines the x-y plane. The x-z plane defines the plane of incidence, and the angle of incidence θ is measured from the surface normal.

The starting equation is Eq. (10) from (Joslyn and Dowling, 2022) for a unit strength, omnidirectional point source:

$$P(\boldsymbol{R_2}, \omega) = -\frac{i\Gamma\omega\cos\theta}{2\pi c R_1 R_2} e^{i\frac{\omega}{c}(R_1+R_2)} \int_{-\infty}^{\infty}\int_{-\infty}^{\infty} e^{\frac{i\omega}{cR}\left(x'^2\cos^2\theta + y'^2\right) + 2i\frac{\omega}{c}\cos\theta\,\zeta(x',y')}\, dx'dy'. \quad (4.4)$$

Here, the integration variables, x' and y', are in the x and y directions, Γ is the reflection

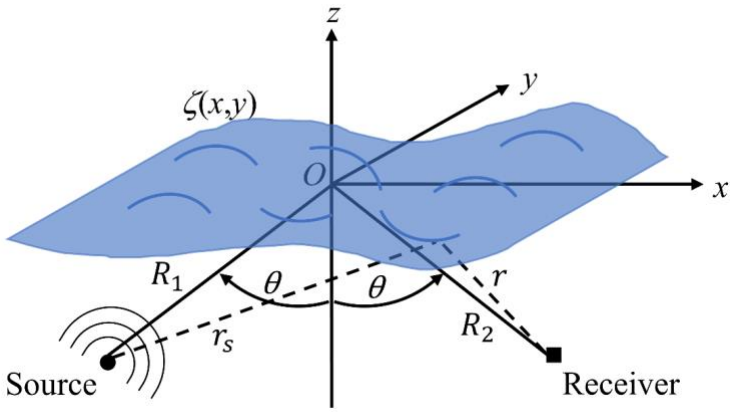

Figure 4.1: Mathematical features of a generic rough surface scattering environment. The specular point between the source at $\boldsymbol{R_1}$ and receiver at $\boldsymbol{R_2}$ defines the origin of the Cartesian coordinate system. The mean level of the arbitrary rough surface ζ defines the x-y plane and the angle of incidence θ is measured from the surface normal.

coefficient, and $R = 2R_1R_2/(R_1 + R_2)$. Also known as the Helmholtz-Kirchhoff-Fresnel integral (Medwin and Clay, 1998), Eq. (4.4) calculates the approximate pressure field at $\boldsymbol{R_2}$ reflected from an arbitrary rough surface. For a Gaussian distribution of surface heights, the in-band coherent reflection coefficient, found by a formal ensemble average of Eq. (4.4), exponentially decreases as the square of the roughness parameter,

$$\mathcal{R}_{coh} = e^{-2(kh\cos\theta)^2}. \tag{4.5}$$

The frequency-difference autoproduct at $\boldsymbol{R_2}$ reflected from an arbitrary rough surface is found by evaluating Eqs. (4.1) and (4.2) with the constituent pressure fields defined by Eq. (4.4),

$$\langle AP_\Delta(\boldsymbol{R_2}, \Delta\omega)\rangle_{BW} = \frac{|\Gamma|^2\cos^2\theta}{\Omega_{BW}^\Delta 4\pi^2c^2R_1^2R_2^2} e^{i\frac{\Delta\omega}{c}(R_1+R_2)} \int_{\Omega_C-\frac{1}{2}\Omega_{BW}^\Delta}^{\Omega_C+\frac{1}{2}\Omega_{BW}^\Delta} d\omega\, \omega_+\, \omega_- \tag{4.6}$$

$$\times \int_{-\infty}^{\infty}\int_{-\infty}^{\infty}\int_{-\infty}^{\infty}\int_{-\infty}^{\infty} e^{\frac{i}{cR}\cos^2\theta\left[\omega_+x'^2-\omega_-x''^2\right]} e^{\frac{i}{cR}\left[\omega_+y'^2-\omega_-y''^2\right]}$$

$$\times e^{\frac{2i\cos\theta}{c}\left[\omega_+\zeta(x',y')-\omega_-\zeta(x'',y'')\right]} dx'dy'dx''dy'',$$

where the quadruple spatial integral indicates a double surface integration. Unlike the acoustic field, the formal ensemble average of the frequency-difference autoproduct requires more mathematical details. The steps are shown in Eqs. (14) and (16) – (18) of the previous work (Joslyn and Dowling, 2022) and result in the ensemble-averaged frequency-difference autoproduct scattered from a rough surface with Gaussian roughness and arbitrary autocorrelation function, $\Phi(\alpha_x, \alpha_y)$:

$$\langle\langle AP_\Delta(\boldsymbol{R_2}, \Delta\omega)\rangle_{BW}\rangle = \frac{|\Gamma|^2 e^{i\frac{\Delta\omega}{c}(R_1+R_2)}}{(R_1+R_2)} \frac{i\cos\theta}{2\pi c R_1 R_2 \Omega_{BW}^{\Delta}(\Delta\omega)} \tag{4.7}$$

$$\times \int_{\Omega_C-\frac{1}{2}\Omega_{BW}^{\Delta}}^{\Omega_C+\frac{1}{2}\Omega_{BW}^{\Delta}} d\omega\, \omega_+\, \omega_-\, e^{-\frac{1}{2}v^2(\omega_+^2+\omega_-^2)}$$

$$\times \int_{-\infty}^{\infty} d\alpha_x \int_{-\infty}^{\infty} d\alpha_y \exp\{v^2\omega_+\omega_-\Phi(\alpha_x,\alpha_y)\} \exp\left\{\frac{-i\alpha_x^2\omega_+\omega_-\cos^2\theta}{cR\Delta\omega}\right\} \exp\left\{\frac{-i\alpha_y^2\omega_+\omega_-}{cR\Delta\omega}\right\}.$$

Here, $v = 2(h/c)\cos\theta$ and the spatial integration is performed over the difference coordinates, α_x and α_y, in the x and y directions, respectively. The first fraction in the coefficient preceding the integration is the flat-surface-reflected autoproduct. Hence, inserting Eq. (4.7) into Eq. (4.3a) removes the first coefficient, yielding the frequency-difference autoproduct coherent reflection coefficient,

$$\mathcal{R}_{coh} = \frac{i\cos\theta}{2\pi c R_1 R_2 \Omega_{BW}^{\Delta}(\Delta\omega)} \int_{\Omega_C-\frac{1}{2}\Omega_{BW}^{\Delta}}^{\Omega_C+\frac{1}{2}\Omega_{BW}^{\Delta}} d\omega\, \omega_+\, \omega_-\, e^{-\frac{1}{2}v^2(\omega_+^2+\omega_-^2)} \tag{4.8}$$

$$\times \int_{-\infty}^{\infty} d\alpha_x \int_{-\infty}^{\infty} d\alpha_y \exp\{v^2\omega_+\omega_-\Phi(\alpha_x,\alpha_y)\} \exp\left\{\frac{-i\alpha_x^2\omega_+\omega_-\cos^2\theta}{cR\Delta\omega}\right\} \exp\left\{\frac{-i\alpha_y^2\omega_+\omega_-}{cR\Delta\omega}\right\}.$$

While not immediately insightful, numerical evaluation of Eq. (4.8) determines the coherent reflection coefficient of the frequency-difference autoproduct scattered from a rough

surface with arbitrary rms height and autocorrelation function. Comparisons of Eq. (4.5) at the broadcast frequencies and Eq. (4.8) at the user-selectable difference frequency demonstrate the coherent reflection recovery available.

For surfaces exhibiting no discernable directionality, an isotropic version of Eq. (4.8) is possible. The Cartesian difference coordinate system, defined by α_x and α_y, is converted to polar coordinates using the standard transformation, namely $\alpha_x = \rho\cos\phi$, $\alpha_y = \rho\sin\phi$, and $da_x d\alpha_y = \rho d\rho d\phi$:

$$\mathcal{R}_{coh} = \frac{i\cos\theta}{2\pi cR_1R_2\Omega_{BW}^{\Delta}(\Delta\omega)}\int_{\Omega_C-\frac{1}{2}\Omega_{BW}^{\Delta}}^{\Omega_C+\frac{1}{2}\Omega_{BW}^{\Delta}} d\omega\,\omega_+\,\omega_-\,e^{-\frac{1}{2}v^2(\omega_+^2+\omega_-^2)} \tag{4.9}$$

$$\times\int_{-\infty}^{\infty} d\rho\,\rho\exp\{v^2\omega_+\omega_-\Phi(\rho)\}\int_0^{2\pi} d\phi\,\exp\left\{\frac{-i\omega_+\omega_-\rho^2}{cR\Delta\omega}\left(\cos^2\phi\cos^2\theta+\sin^2\phi\right)\right\},$$

where the autocorrelation function depends only on the radial coordinate, $\Phi(\rho)$. The corresponding angular integration is a known definite integral (Wolfram Research, 2022) and yields the isotropic coherent reflection coefficient for the frequency-difference autoproduct,

$$\mathcal{R}_{coh} = \frac{i\cos\theta}{cR_1R_2\Omega_{BW}^{\Delta}(\Delta\omega)}\int_{\Omega_C-\frac{1}{2}\Omega_{BW}^{\Delta}}^{\Omega_C+\frac{1}{2}\Omega_{BW}^{\Delta}} d\omega\,\omega_+\,\omega_-\,e^{-\frac{1}{2}v^2(\omega_+^2+\omega_-^2)} \tag{4.10}$$

$$\times\int_{-\infty}^{\infty} d\rho\,\rho\exp\{v^2\omega_+\omega_-\Phi(\rho)\}\,\exp\left\{\frac{-i\omega_+\omega_-\rho^2}{2cR\Delta\omega}(1+\cos^2\theta)\right\}J_0\left(\frac{-\omega_+\omega_-\rho^2}{2(\Delta\omega)cR}(-1+\cos^2\theta)\right),$$

where J_0 is the Bessel function of the first kind. As the spatial integration is the computationally limiting step, owing to the highly oscillatory nature of the difference coordinate integrands in both Eq. (4.8) and Eq. (4.10), the additional analytic effort provided simpler numerical implementation. The form of Eq. (4.10) is reminiscent of other Kirchhoff-approximated

expressions of intensity (Dahl, 1996; Oglivy, 1991), as expected, given the nonlinear nature of both.

4.2.3 Sea Surface Spatial Spectra

The autocorrelation function is related to the surface power spectrum by Fourier transform. Using notation similar to previous authors (Darawankul and Johnson, 2007; Olson, 2021), the forward and inverse transforms are defined as

$$h^2\Phi(\alpha_x,\alpha_y) = \mathcal{F}\{W(K_x,K_y)\} = \int_{-\infty}^{\infty}\int_{-\infty}^{\infty}[W(K_x,K_y)e^{-iK_x\alpha_x}e^{-iK_y\alpha_y}]dK_xdK_y\,, \qquad (4.11a)$$

$$W(K_x,K_y) = \mathcal{F}^{-1}\{h^2\Phi(\alpha_x,\alpha_y)\} = \frac{h^2}{(2\pi)^2}\int_{-\infty}^{\infty}\int_{-\infty}^{\infty}[W(K_x,K_y)e^{iK_x\alpha_x}e^{iK_y\alpha_y}]d\alpha_xd\alpha_y\,, \quad (4.11b)$$

where $W(K_x,K_y)$ is the surface power spectrum, K_x and K_y are the Cartesian surface wavenumbers, and $\mathcal{F}$ is the Fourier transform operator. The isotropic versions of Eq. (4.11) for radial wavenumber $K_\rho = \sqrt{K_x^2+K_y^2}$ are then given by

$$h^2\Phi(\rho) = \mathcal{F}\{W(K_\rho)\} = 2\pi\int_0^{\infty}K_\rho J_0(K_\rho\rho)W(K_\rho)dK_\rho\,, \qquad (4.12a)$$

$$W(K_\rho) = \mathcal{F}^{-1}\{h^2\Phi(\rho)\} = \frac{h^2}{2\pi}\int_0^{\infty}\rho J_0(K_\rho\rho)\Phi(\rho)d\rho\,. \qquad (4.12b)$$

Substitution of Eq. (4.11) or (4.12) into Eq. (4.8) or (4.10), respectively, reveals autoproduct-based coherence recovery depends directly on the surface power spectrum. The dependence is unexpectedly strong, for the autocorrelation function (power spectrum) appears in the exponential governing integrand magnitude in Eq. (4.8) and (4.10). Hence, maximizing the match between modeled and experimental coherent reflection coefficients may provide an effective means of remote acoustic identification of precise surface characteristics.

The power spectrum is the symmetric component of the more commonly reported spatial roughness description of the sea surface, the directional wave spectrum (Chapman, 1980). Thus, the sea surface autocorrelation function may be more appropriately estimated from

$$h^2\Phi(\alpha_x,\alpha_y) = \mathrm{Re}\left[\mathcal{F}\{F(K_x,K_y)\}\right] = \int_{-\infty}^{\infty}\int_{-\infty}^{\infty}\left[F(K_x,K_y)\cos(K_x\alpha_x + K_y\alpha_y)\right]dK_x dK_y\,, \quad (4.13a)$$

where $F(K_x,K_y)$ is the directional wave spectrum and Re[ ] denotes the real part of the quantity in brackets. Often, it is convenient for directional wave spectra to be expressed in polar wavenumber coordinates. In this case, the directionally-averaged wavenumber $F(K_\rho)$ is utilized, and defined (Dahl, 1999) with normalization as follows:

$$h^2\Phi(\rho) = \int_0^{\infty} K_\rho J_0(K_\rho\rho)F(K_\rho)dK_\rho\,. \quad (4.13b)$$

The anisotropic and isotropic forms of Eq. (4.13) may be inserted into Eq. (4.8) or Eq. (4.10), respectively, to calculate coherent reflection coefficients from the directional wave spectrum. The relationship between surface spectra and autoproduct-based coherence recovery was investigated numerically and experimentally for ocean surface acoustic scattering. Additionally, the relationship was inverted to estimate surface characteristics from the acoustic recordings. While sea surface scattering of $2.5 \leq kh\cos\theta \leq 3.7$ was studied here, the strategy is valid in other scattering regimes and propagation geometries, as long as the Kirchhoff and Fresnel approximations are satisfied.

4.3 Ocean Measurements

To address the general applicability of coherence recovery offered by the frequency-difference autoproduct, a subset of data collected during Shallow Water ’06 was analyzed. This section reviews relevant details of the experiment, including acoustic measurements and the ocean

surface spectrum. Additional information detailing data acquisition and the nominal environmental characteristics can be found in previous studies of the experiment (Dahl, 2010; Dahl et al., 2013).

4.3.1 Experiment Design

The acoustic measurements used here were collected from the research vessel R/V *Knorr* 100 km off the coast of New Jersey on 10 August 2006, 0830-1530 UTC. The experiment, designed to assess sea surface scattering, employed omnidirectional source and omnidirectional receivers in water channel depth of 80 m, which allowed isolation of the sea-surface reflected path through time-gating of the acoustic records. A schematic of the specular plane is shown in Fig. 4.2(a). A moored array receiving system (MORAY) was located at 39.0245°N, 73.0377°W, and defined the central position of the experiment. A 1.4 m vertical line array, consisting of four ITC-1042 (Gavial International Transducer Corporation – Santa Barbara, CA) hydrophones, was centered at 25 m depth. Only the shallowest receiver, depth of 24.3 m, is maintained here as processing of the other receivers produced analogous results and did not significantly adjust the geometry. At 200 m in range, the source, ITC-1007 (Gavial International Transducer Corporation – Santa Barbara, CA), was located 40 m below the stern of the R/V *Knorr*. By repositioning the R/V *Knorr*, measurements were conducted for four source-receiver bearing angles, separated by 90°. At each station, time domain recordings of acoustic scattering from 40 independent realizations of the ocean surface were collected, yielding a total of 160 recordings during the 6.5 hour experiment.

A conductivity-depth-temperature profile was made from the R/V *Knorr* during the experiment at 1107 UTC. The downward-refracting sound speed profile is shown in Fig. 4.2(b). The sound speed reaches a maximum of 1530 m/s near the surface and decreases to a minimum of 1485 m/s

at approximately 35 m depth. The depths of the source and receiver result in significant downward refraction in the surface-reflected path which increased the spatial coherence (Dahl, 2010). The incidence angle, $\theta = 74.8°$, increased by 2.6° from the incidence angle computed in an isospeed environment for the same geometry.

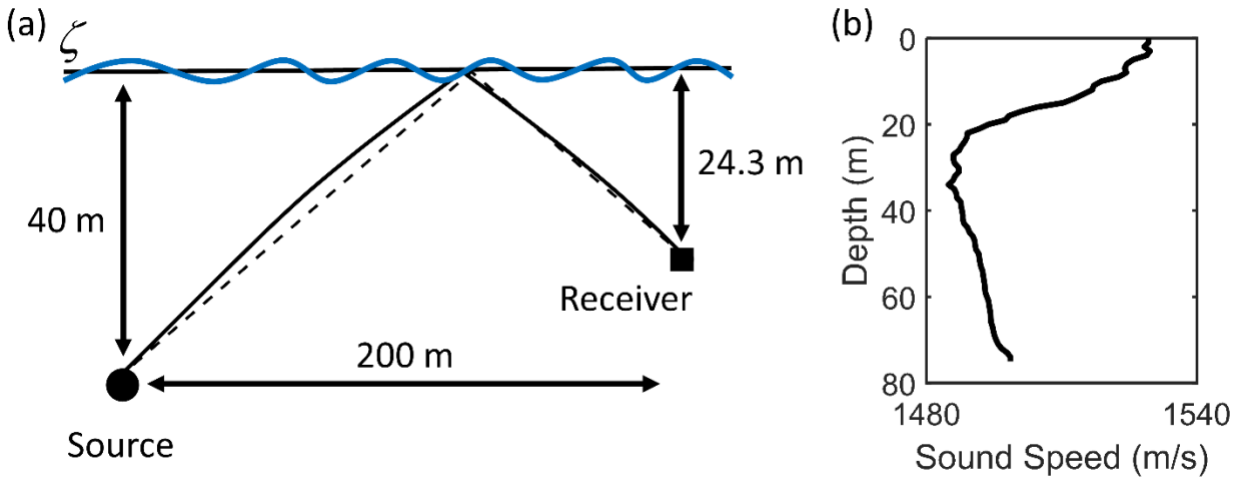

Figure 4.2: (a) Schematic of the SW06 specular plane geometry, including the surface-reflected path with (solid line) and without (dotted line) refraction. The omnidirectional receiver is positioned at depth 24.3 m and range 200 m from the omnidirectional source at depth of 40 m. (b) The nominal sound speed profile measured by a conductivity-depth-temperature (CTD) cast from the R/V *Knorr* during the experiment.

Transmitted signals were recorded at 50 kHz sample rate. The broadcast signal, a 3 ms continuous wave pulse, consisted of superimposed narrowband center frequencies of 4 – 20 kHz (every 2 kHz) transmitted simultaneously. In post-processing, the signals were time aligned to remove jitter, as was necessary in previous work (Dahl, 2010). Signals were time-gated to isolate the surface-reflected path from the earlier and later arrivals.

A representation of the source spectral content is shown in Fig. 4.3. The approximate source spectrum was computed by isolating the direct path recording, incoherently averaging the

magnitude, and normalizing the largest bin to unit amplitude. The frequencies studied here are indicated by red crosses. To ensure significant incoherent scattering from the sea surface, the roughness parameter was set to exceed 2.5, limiting analysis to center frequencies between 14 – 20 kHz. Spectral components within 200 Hz of each center frequency were also maintained, resulting in a complicated acoustic bandwidth non-uniformly sampling the frequency space. Consequently, two types of autoproduct difference frequencies are considered. Intrapulse autoproducts are constructed from spectral components of the same pulse while interpulse autoproducts are constructed from spectral components of pulses with different center frequencies. A graphical representation of intrapulse and interpulse autoproduct generation is superimposed on Fig. 4.3 in green and blue, respectively. Based on the nominal spectral resolution (7 Hz), the intrapulse difference frequency range was $7 \leq \Delta f_{intra} \leq 400$ Hz and the interpulse difference frequencies were contained near $\Delta f_{inter} \sim$ 2, 4, 6 kHz. Although the

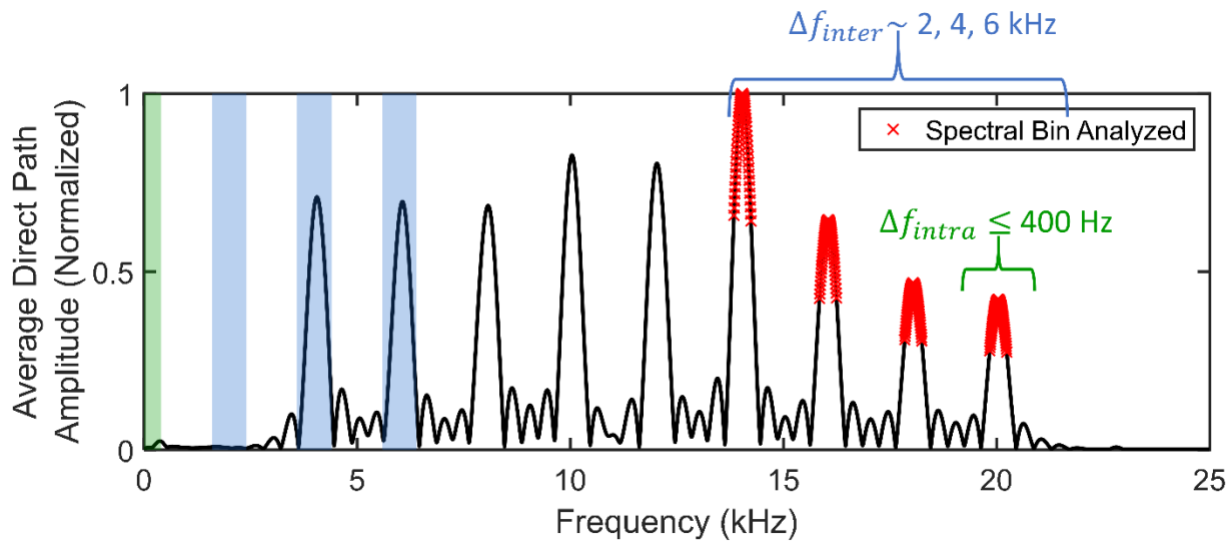

Figure 4.3: The transmitted signal broadcast during the SW06 experiment, approximated by the average magnitude of the direct path. Narrowband pulses were simultaneously broadcast with center frequencies between 4 – 20 kHz (every 2 kHz). Indicated by red crosses, the analyzed spectral components were selected to ensure strong surface scattering. The disjoint bandwidth offered the construction of intrapulse and interpulse autoproduct difference frequencies. The intrapulse (interpulse) autoproduct construction is schematically indicated in green (blue).

selected bandwidth around each narrowband pulse was arbitrary, 400 Hz was found to be suitable for autoproduct construction, and systematically investigating the tradeoffs of larger or smaller intrapulse bandwidth was irrelevant to studies of coherent reflection.

4.3.2 Sea Surface Conditions

Examination of realistic ocean surfaces is the major feature of this study. Importantly, bubbles negligibly influenced scattering and attenuation for the data studied here (Dahl, 2010; Dahl et al., 2008), permitting an assessment of scattering exclusively from the rough surface. The rough surface was modeled by the surface autocorrelation function and by stochastic generation of random surface realizations. Each method required environmental information collected during the experiment.

Directional wave measurements of the sea surface were made from two buoys in the area. A 0.9 m diameter TRIAXYS directional wave buoy was positioned 800 m from the MORAY and the Air-Sea Interaction Spar (ASIS) buoy was deployed 1.5 km from the MORAY. The wind speed, as recorded from the ASIS buoy, was 5.5 m/s ($\pm$1 m/s) at 10 m above the sea surface. The measured rms wave height was $h = 0.167$ m, varying by less than $\pm$10% during the collection period. Both buoy systems indicated the presence of swell and wind wave systems from the south (175°) and southwest (225°), respectively. The direction of the wave systems, with respect to the four transmit locations, are shown schematically in Fig. 4.4(a). Listed bearing angles indicate the compass heading direction of the source from the MORAY. Herein, rotated 2-D plots are used, where the x- (y-) component of the Cartesian coordinate system for scattering is aligned with 30° (300°). Following previous works (Dahl, 2010; Dahl et al., 2013), the directional wave spectrum of the TRIAXYS buoy is primarily used here and recorded $K_\rho < 1.45$. To highlight both the wind wave (northwest) and swell wave (southwest) fields, the normalized

logarithm of the spectrum, $\log_{10}\{F(K_x, K_y) \,/\, \max[F(K_x, K_y)]\}$, computed from the buoy data is shown in Fig. 4(b). This spectra is supplemented to higher wavenumbers not sensed by the buoy through a wind-wave model (Plant, 2002) based on wind speed and direction. Wavenumber information of $K_\rho \leq 12.4$ is maintained, and additional details are provided in (Dahl et al., 2013).

The autocorrelation function was computed from the directional wave spectrum using Eq. (4.13) and is shown in Fig. 4.4(c). Modeling sea surfaces described by non-analytic autocorrelation functions is an essential feature of this study. The autocorrelation function directly enters into numerical evaluation of the coherent reflection coefficient through Eq. (4.8). Notably, the wavelength associated with the spectral peak of the wind field (13.5 m) is evident along the northwest-southeast direction. The swell wave system contributes at larger lags unimportant to the modeling here.

Finally, from the directional wave spectra, random realizations of the rough surface may be generated [see Eq. (4) of (Dahl et al., 2013)] using the following formula:

$$\zeta(x, y) = \sum_{i=1}^{N} \sum_{j=1}^{N} A_{ij} \cos\left(K_x^i x + K_y^j y + \beta\right), \tag{4.14}$$

where N is the number of wavenumber samples, β is a random phase distributed between 0-2π, $A_{ij} = \eta \sqrt{F\left(K_x^i, K_y^j\right)}$, η is a Gaussian random variable with mean one and variance 0.04, and the desired value of h is enforced through an overall surface height normalization. Direct numerical evaluation of Eq. (4.14) is expensive for the scale and resolution necessary here and is sped up through the FFT2 function in MATLAB. The directional wave spectrum, recorded in polar coordinates, was interpolated on a Cartesian grid to appropriately utilize the 2-D fast Fourier transform for the desired size and resolution of the rough surface. A representative surface realization using this strategy is shown in Fig. 4.4(d). The wind wave effects at small spatial

scales and the swell wave from the southwest are both evident in the generated rough surface. For this resolution and spatial extent, direct numerical evaluation took approximately 2.8 h, while the FFT-based approach took 0.36 s. Because the Monte Carlo simulations use many rough surface realizations, this speed increase was necessary.

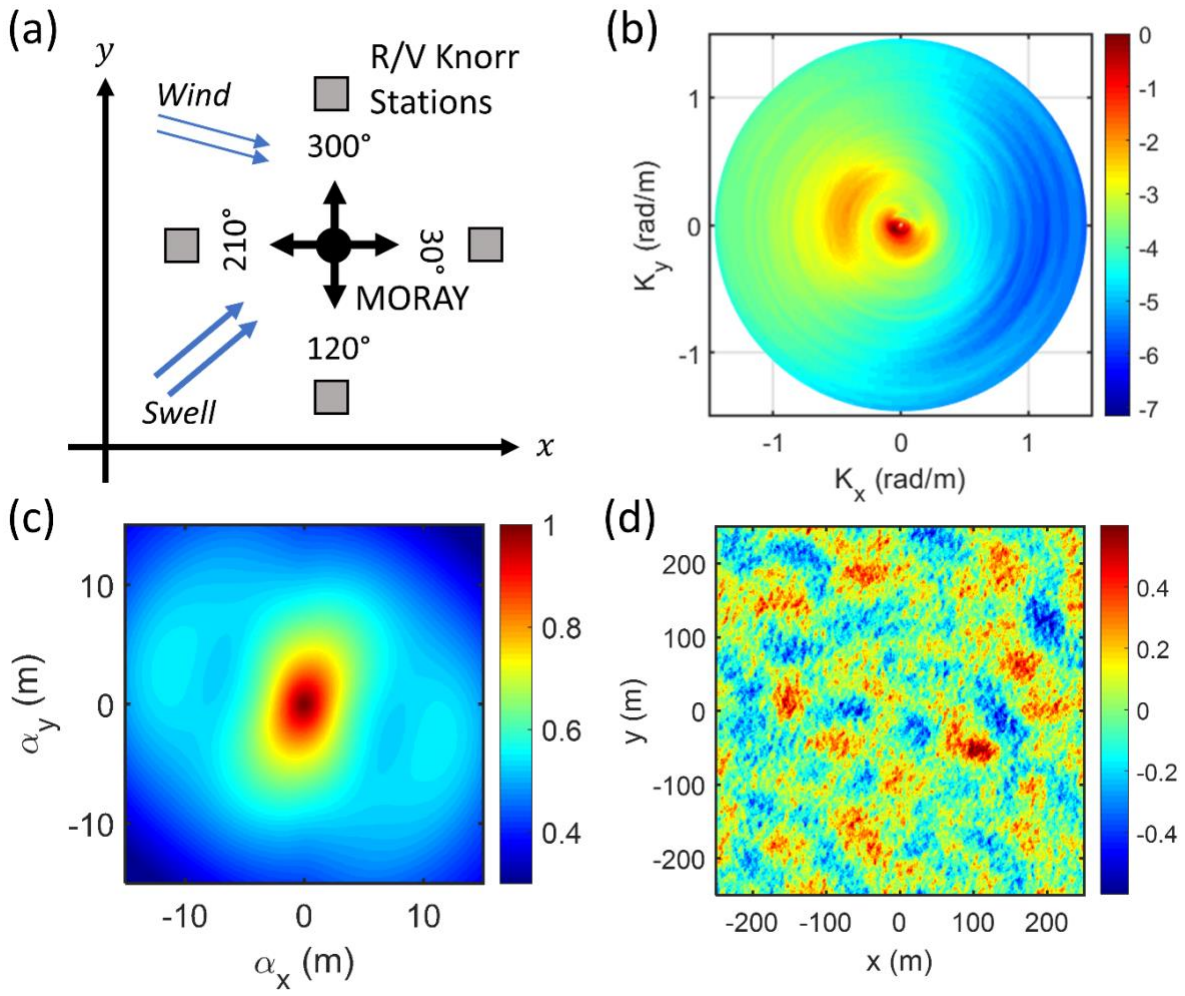

Figure 4.4: Overview of sea surface conditions important to the modeling efforts. The Cartesian coordinate system for modeling is shown aligned with 30° (x) and 300° (y). The other propagation angles were assessed by rotating the coordinate system. (a) Source (R/V *Knorr*) and receiver (MORAY) locations sampled four different propagation angles during the experiment. (b) The normalized spectrum (log scale) according to the TRIAXYS buoy measurements indicates swell ($|K_\rho|$~0.06) and wind wave ($|K_\rho|$~0.45) fields. The autocorrelation function (c) and a random rough surface realization (d), both computed from the directional wave spectrum, show the influence of wind waves originating from 225°. Both panels are representative; finer resolution and shorter spatial extent were implemented in the scattering calculations.

4.4 Recovery of Coherent Reflection

This section directly assesses the capability and predictability of autoproduct-based coherence recovery using the SW06 measurements discussed in the previous section. To suitably simulate the ocean surface scattering, appropriate numerical choices are made. Modeling details are shown next.

4.4.1 Numerical Modeling

Computational evaluations of the coherent reflection coefficient were determined for the geometry specified in Fig. 4.2(a) using two different approaches. The first, herein referred to as theory, required the autocorrelation function of the sea surface for direct numerical integration of Eq. (4.8). The second method, referred to as Monte Carlo simulation, simulates acoustic scattering by evaluating Eq. (4.4) and Eq. (4.3b)-(4.3c) with independent sea surface realizations generated from the directional wave spectrum. Primary emphasis was placed on the theoretical results while Monte Carlo simulations were used to determine error bars associated with limited-member ensemble averages.

In both strategies, the source spectrum was set to unity and the sound speed, c =1498 m/s, was the average of the measured profile shown in Fig 4.2(b). Owing to the symmetry of the scattering formulations, there is no numerical difference between bearings separated by 180°. Hence, results for bearing 30°/210° were calculated and the 120°/300° results were computed by rotating the sea surface representation by 90°. For theoretical curves, the sea surface autocorrelation function was discretized on a 4.5 m × 4.5 m rectangular patch sampled every ~0.5 mm. Large autocorrelation lags do not significantly contribute to the integral in Eq. (4.8), due to the rapidly oscillating and exponentially diminishing integrand. This asymptotic notion was used previously to justify the Taylor expansion replacement of the Gaussian autocorrelation

function (Joslyn and Dowling, 2022). For the Monte Carlo simulations, 300 m × 300 m surfaces with 2.5 cm resolution were stochastically produced according to the generation strategy prescribed for Eq. (4.14). A pool of 640 surfaces (320 in each major direction) was created. Computational load was reduced by performing integrations on a 300 m × 90 m patch of each rough surface, aligning the shorter dimension with the y-direction. Error bars are computed by randomly selecting 40-, 80-, or 160-surfaces from the pool 100 times and capturing the 95th percentile of the variation in ensemble averages. All integrals were numerically computed by trapezoidal integration.

Minor adjustments to the acoustic bandwidth shown in Fig. 4.3 were made in numerical implementation. The frequencies for Monte Carlo simulations matched the experiment but employed only every fourth experimental spectral bin for computational ease, setting the frequency resolution to ~27 Hz. For the theoretical results, frequencies between 13.8 kHz – 20.2 kHz (every 5 Hz) were utilized. A continuous bandwidth was selected, rather than a pulsed bandwidth, to assess autoproduct coherence recovery for all difference frequencies less than 6 kHz. Hence, the experimental restriction of intrapulse and interpulse difference frequencies was removed. Evaluation was expedited by limiting the bandwidth-averaging step to autoproduct samples spaced by 1 kHz.

For zero roughness, i.e. $h, \zeta = 0$, both methods ought to reduce to the method of images. The simulation results agreed well with Green's function for reflection, recording a cross correlation of ~1. Although the simulated coherent reflection coefficient amplitude exhibited some variation from the expected value of 1, due to evaluation of Fresnel integrals on a finite domain, the discrepancy did not extend to autoproducts, where the bandwidth-averaging tended to smooth these numerical errors. Further, these errors are negligible for the Monte Carlo

simulations as the ensemble average will also act to smooth the numerical errors. The theoretical approach, which evaluates autoproducts directly, registered correlation value of $0.97+0.1i$ with flat-surface-reflected autoproducts. Interestingly, the lack of rough surface effects is a hindrance to numerical accuracy as a specific autocorrelation function acts as an exponential taper on the amplitude of the integrand in Eq. (4.8). Hence, both strategies sufficiently predict the coherent reflection coefficient for the purposes here.

The theoretical derivations assumed an isospeed medium. In addition to setting a uniform sound speed, geometrical adjustments to the nominal geometry were required to account for refraction. Using BELLHOP (Porter and Bucker, 1987), corrections based on the sound speed profile in Fig. 4.2(b) were implemented. Importantly, the specular incidence angle was increased from 72.2° to 74.8°. The SW06 sound speed profile was shown to significantly increase spatial coherence predictions, due to the compression of vertical arrival angles (Dahl, 2010). Theoretical autoproduct coherent reflection coefficients computed with the SW06 sound speed profile (red) is compared to the isospeed results (black) in Fig. 4.5. Only the 30°/210° direction is shown, but the other direction is equivalent.

Refraction impacts coherent reflection by altering the surface roughness parameter, $\chi = kh\cos\theta$. The influence of the adjusted specular incidence angle on the frequency-difference autoproduct is modest and similar to that expected for the conventional coherent reflection coefficient given in Eq. (4.5). Notably, the influence of refraction on the coherent reflection coefficient is less pronounced than the effect on vertical spatial coherence in the same environment. This is attributed to the difference in coherence metrics. Refraction-based compression of vertical arrival angles acts to increase the spatial correlation of vertically-spaced receivers. The coherent reflection coefficient, a single receiver metric, does not inherit this

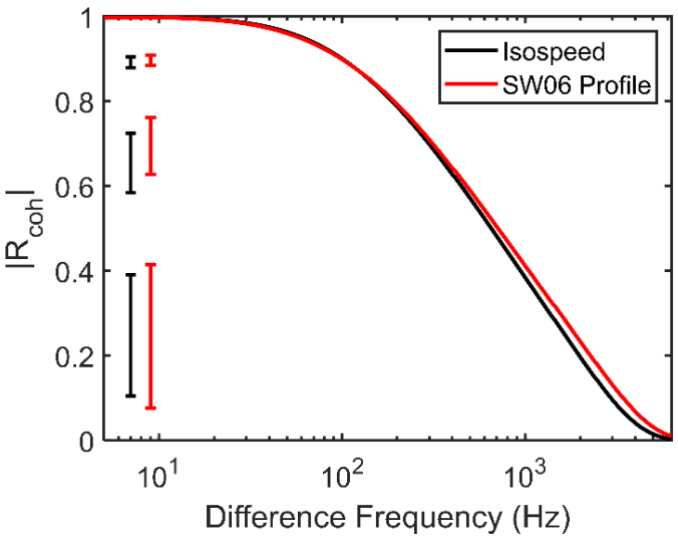

Figure 4.5: Modeled influence of the SW06 profile on the autoproduct coherent reflection coefficient using Eq. (8). The effect is mild, with more prominent effects limited to higher difference frequencies. Shown here is x axis aligned with 30°/210°.

additional coherence improvement mechanism. Error bars determined from 80-surface ensembles for Δf = 100 Hz, 400 Hz, and 2 kHz are reported on the left side of the figure to reduce visual clutter on the theoretical curves. Although refraction mildly increases the autoproduct coherent reflection coefficient, the adjustment is not experimentally realizable in light of the limited surface ensemble number in SW06. However, for completeness, refraction is accounted for herein using the BELLHOP corrections.

4.4.2 Directional Dependence

The SW06 sea surface conditions (see Fig. 4.4) exhibited a strong dependence on direction. For spatial coherence estimates in previous studies, directionality manifested only in the lower broadcast frequencies. Spatial coherence of the higher frequency pulses used here were independent of direction, due to the isotropy of the surface autocorrelation function at small lags (Dahl, 2010; Dahl et al., 2013). Thus, it is of interest to assess the directionality of the

autoproduct, a synthetic estimate of lower frequency field content from higher frequency constituent fields.

The coherent reflection coefficients determined from different source-receiver directions are plotted in Fig. 4.6 against difference frequency or acoustic frequency. In all coherence recovery plots, a representative subset of frequencies was selected to reduce visual clutter of the measured conventional and autoproduct coherent reflection coefficients. The measured coherent reflection coefficients are shown in orange (30°), green (300°), purple (210°), and red (120°), and theory/simulation results are shown in black (30°/210°) and blue (120°/300°). Plotted against a logarithmic frequency axis, the autoproduct results occupy the region $\Delta f \leq 6$ kHz and conventional results extend to $f \geq 14$ kHz. The gap between $\Delta f = 400$ and $\Delta f = 2$ kHz is due to the inability to construct difference frequencies from the recorded signal within this range. Autoproduct error bars are reported on the left side of the panel for coherent reflection coefficients determined from 40-member ensembles for Δf = 100 Hz, 200 Hz, 350 Hz, and 2 kHz. Equivalent error bars for conventional reflection coefficients capturing variation at the broadcast frequencies are indicated on the right side of the panel.

The recovery of coherence afforded by the frequency-difference autoproduct is evident in Fig. 4.6. The constituent acoustic field coherence is generally below 30%, with some samples significantly lower. However, at sufficiently low difference frequencies, the coherent reflection coefficient approaches unity, regardless of direction. In particular, the average acoustic field coherence for bearing angle 300° is 12%. Using Eqs. (4.1) – (4.3), greater than 90% of coherent reflection is recovered for autoproduct difference frequencies less than 200 Hz. Results are analogous in the other directions. Additionally, the measured data generally matches the shape of the theoretical curves, albeit uniformly increased at the intrapulse difference frequencies. This

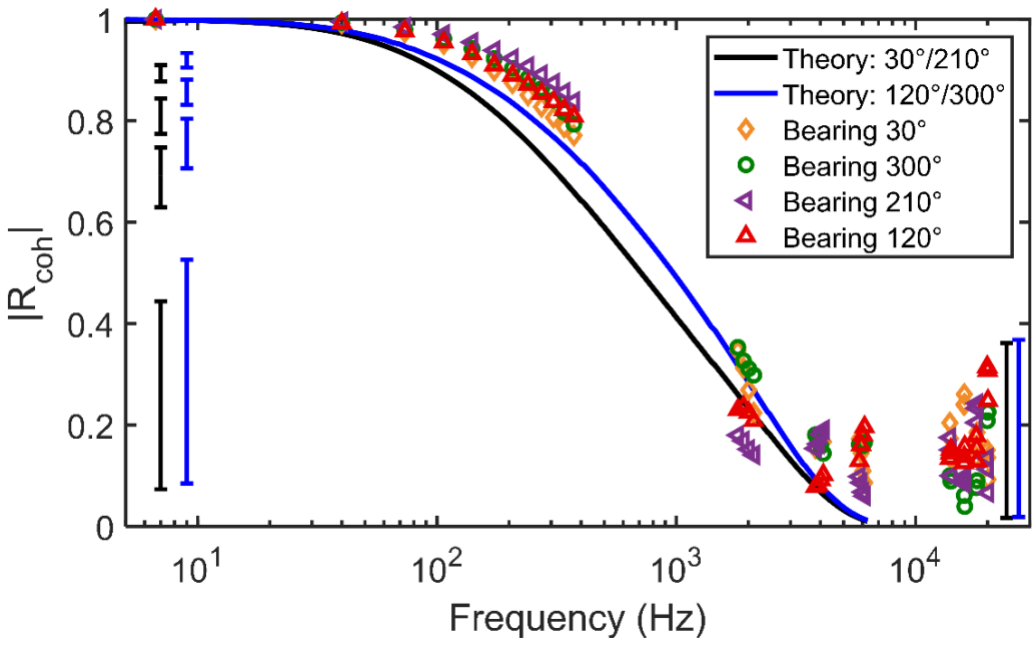

Figure 4.6: Directional dependence of measured and modeled coherent reflection coefficients. No statistical significance exists between directions for the measured difference frequencies. Error bars encapsulating 95% of the variation in 40-realization Monte Carlo simulations are shown for autoproducts (acoustic fields) at Δf = 100 Hz, 200 Hz, 350 Hz, and 2 kHz (f = 14 – 20 kHz) on the left (right) side of the figure.

discrepancy can be accounted for by minor alterations to the modeled sea surface spectrum and is studied further in Chapter 4.4.4.

The theoretical curves do offer some evidence of directional dependence. The autoproducts recover greater coherence in 120°/300° direction, owing to the slightly elongated surface autocorrelation function peak in this direction (shown as the y direction in Fig. 4.4). However, this effect is most prominent at difference frequencies not accessible from the signal bandwidth used in the experiment. Further, for most difference frequencies, the variation expected from a 40-surface ensemble was larger than the discrepancy between directions. Hence, the experimental restrictions of disjoint bandwidth and limited independent samples inhibit discernment of autoproduct directional dependence.

4.4.3 Coherent Reflection Coefficient

Herein, all directions are processed simultaneously to reduce uncertainty associated with a limited-number ensemble. Previous surface scattering work with the 14 – 20 kHz data also averaged across bearing angle (Dahl, 2010). The theoretical autoproduct curves were adjusted by averaging the coherent reflection coefficient from each direction prior to reporting its magnitude. The Monte Carlo simulations were expanded to ensembles of 160 surface realizations, drawn from the entire pool of surfaces. The measured coherent reflection coefficients were analyzed as one experiment with 160 independent samples.

The measured and modeled coherent reflection coefficients for the SW06 experiment are shown in Fig. 4.7 on a logarithmic frequency axis. The measured autoproduct (conventional) coherent reflection coefficients are shown by red (green) ×'s and the black curve denotes the theoretical autoproduct. Autoproduct error bars generated from Monte Carlo simulations are shown in black for $\Delta f = 80$ Hz, 150 Hz, 300 Hz, 2 kHz, 4 kHz, and 6 kHz. Uncertainty in Monte Carlo simulations of the conventional field frequencies are indicated on the right side of the figure.

Figure 4.7 demonstrates the significant coherence recovery possible via the frequency-difference autoproduct. The coherence of interpulse autoproducts generally increase with decreasing difference frequency, and the intrapulse autoproducts exhibit excellent coherence. For the autoproducts here, constructed from constituent fields with an average coherent reflection coefficient of 0.06, greater than 95% coherence is recovered at $\Delta f < 125$ Hz. Error bars associated with statistical uncertainty of a 160-surface ensemble are reduced from the 40-member size in Fig. 4.6, emphasizing the importance of the directional average.

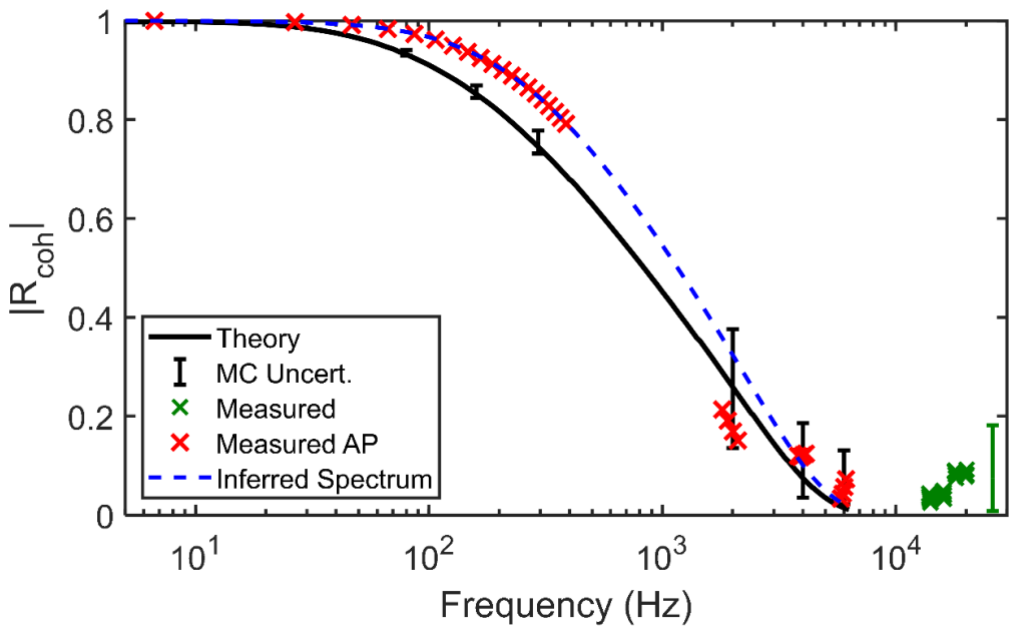

Figure 4.7: Measured and modeled coherent reflection coefficients averaged across all four propagation angles. Measurements are denoted by red (autoproduct) and green (conventional) ×'s and the nominal theoretical autoproduct prediction is shown in black. Error bars, based on uncertainty associated with 160-ping ensemble averages, accompany the conventional measurements and autoproduct theory. The dotted blue curve represents a best-fit theoretical autoproduct based on an adjusted sea surface wave spectrum.

Although coherence recovery is illustrated in Fig. 4.7, the measured data does not agree with the theoretical predictions, particularly at the intrapulse difference frequencies. In fact, modeled autoproducts uniformly underestimate the coherent reflection measured at the intrapulse difference frequencies. Reasonable corrections to surface statistics, outlined in the following subsection, remove this discrepancy and are demonstrated by the blue dashed line.

4.4.4 Surface Characterization

The theoretical autoproduct coherent reflection coefficient depends on the directional sea surface spectrum. The directional sea spectrum was determined through a combination of measured and modeled data, each with some level of uncertainty. The former through rms height uncertainty

($\pm$10%) and the latter through uncertainty in wind speed ($\pm$ 1 m/s) and the wind peak wavenumber. A numerical optimizer was used to identify the sea surface spectrum adjustments, within the uncertainty of the experiment, necessary to produce agreement between measured and theoretical autoproducts. Given the lack of directional dependence in the experiment and the computational load required by the optimizer, the isotropic form of the autoproduct coherent reflection coefficient was used. Evaluation of Eqs. (4.10) and (4.13b) required estimates of the directionally-averaged wave spectrum, $F(K_\rho)$.

The directionally-averaged wave spectrum implemented uses the buoy data shown in Fig. 4.4(b) supplemented by a modeled spectrum at higher wavenumbers. The D-spectrum (Plant, 2002) was multiplied by a Gaussian roll-off function. This adjustment is commonly employed to band-limit the exponential autocorrelation function in the radar community (Darawankul and Johnson, 2007; Li and Johnson, 2017). Hence, the modeled region abides by the following equation:

$$F(K_\rho) = D(K_\rho, K_{peak}, U) \exp\left[-\left(\frac{K}{K_{roll-off}}\right)^2\right], \tag{4.15}$$

where $D(K_\rho, K_{peak}, U)$ represents the (directionally-averaged) D-spectrum dependent on radial wavenumber, the wind peak wavenumber, and the wind speed, respectively. Spectrum-specific details are shown in (Plant, 2002). The wavenumber scale governing the roll-off function is $K_{roll-off}$. Using a nonlinear curve-fitting routine in MATLAB, adjustments to h, K_{peak}, U, and $K_{roll-off}$ were identified that maximize agreement between Eq. (4.10) and the measured autoproducts. Due to the relative statistical certainty of the intrapulse autoproducts, indicated by the small error bars in Fig. 4.7, the implementation was designed to optimize the match for $\Delta f \leq$ 400.

Results of the numerical optimization are shown in Table 4.1. The inferred parameters are within the uncertainties of the SW06 experiment, with the largest difference suggesting a reduction of the wind speed by ~0.5 m/s. The theoretical autoproduct coherent reflection coefficient was recomputed using the inferred directionally-averaged spectrum and superimposed in blue dashes on Fig. 4.7. The discrepancy between measured intrapulse autoproducts and the nominal theoretical predictions is removed and excellent agreement between measured and theoretical autoproducts from the inferred spectrum is shown.

Nominal (red) and inferred (blue) directionally-averaged wave spectra are shown in Fig. 4.8(a). The inferred spectrum differs only slightly from the nominal values until the roll-off function dominates near $K_\rho \sim 10$. The other directional wave buoy near the experimental site, ASIS, also measured surface spectral content. Data from the ASIS buoy, digitized (Rohatgi, 2022) from Fig. 6 in (Dahl, 2010), is shown in black and is lower than the other two spectra, supporting the inferred adjustments.

Table 4.1: Comparison of nominal and inferred environmental parameters. Autoproduct-based environmental characterization, computed by optimizing the match between theoretical and measured autoproduct coherent reflection coefficients, provides reasonable corrections within the uncertainty of the experiment.

	Rms roughness (m)	Wind Speed (m/s)	Wind Peak Wavenumber (rad/m)	Roll-off Wavenumber (rad/m)
Nominal	0.167	5.5	0.466	N/A[a]
Inferred	0.161	4.95	0.456	5.06

[a] Nominal spectrum does not include a roll-off parameter.

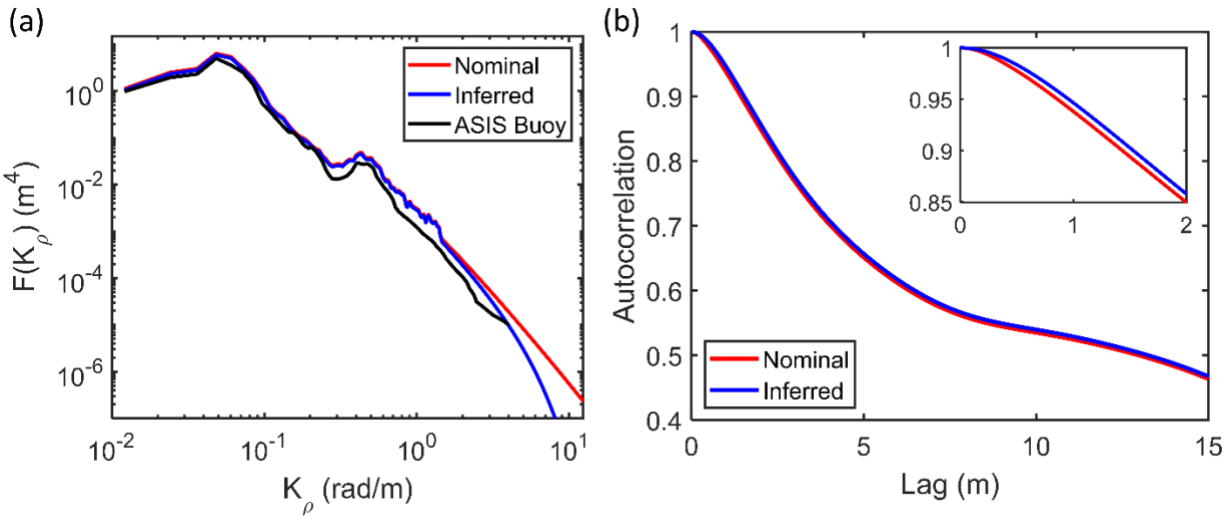

Figure 4.8: Effect of inferred parameter adjustments on isotropic representations of the SW06 sea surface. (a) Comparison of nominal and inferred directionally-averaged sea surface spectra. Data from the ASIS buoy, not used in analysis, is superimposed as well. (b) Nominal and inferred autocorrelation functions shown to 15 m lag. The inset figure shows the major effect of the inferred spectrum, increasing the correlation at small lag values.

Figure 4.8(b) shows the autocorrelation functions computed from Eq. (4.13b) using the nominal and inferred spectra. Plotted against lags up to 15 m, little discrepancy exists between the two curves. The root-mean-square percentage error was less than 1%. Inset in the panel is a zoomed-in view of the autocorrelation peak, out to 2 m lag. At small lags, the effect of the Gaussian roll-off function is evident in the curvature of the inferred autocorrelation function. This small increase in the autocorrelation function drives the difference in coherence recovery between nominal and inferred curves in Fig. 4.7. Hence, the autoproduct may only serve to refine estimates of the autocorrelation function at small lags (or, equivalently, the spectrum at higher wavenumbers). Although other surface wave spectrum models and more sophisticated optimization strategies exist, the current implementation was favored due to its simplicity. This subsection was developed to show how the remotely measured frequency-difference autoproduct

may assist environmental characterization efforts, not to exhaustively assess sea surface models and numerical optimizers.

4.5 Conclusion

The frequency-difference autoproduct constructed from rough-surface-scattered acoustic fields has been shown to recover coherent reflection in simulation and laboratory experiments for surfaces possessing Gaussian autocorrelation functions (Joslyn and Dowling, 2022). The goal of this work, therefore, was to examine the potential for autoproduct-based coherence recovery in acoustic scattering from realistic sea surfaces. Analytic and simulation results using the Kirchhoff approximation were generalized to account for arbitrary surface autocorrelation functions, and measured data collected during the SW06 experiment was compared to numerical predictions. In particular, the work here considered a pulsed signal, consisting of simultaneous high frequency narrowband transmissions, scattered from 160 independent realizations of the rough sea surface with $2.5 \leq kh \cos\theta \leq 3.7$. Coherent reflection is recovered in theory, simulations, and measured data. Moreover, with suitable corrections to the nominal sea surface wave spectrum, the recovery is in agreement between all methods. An autoproduct-based numerical strategy was presented to identify these minor sea surface spectrum adjustments.

The research here supports two minor and two major conclusions. The two minor conclusions concern attributes specific to the SW06 experiment. Refraction, shown previously to strongly influence vertical spatial coherence for the SW06 data (Dahl, 2010; Dahl et al., 2013), only modestly impacts the coherence recovery expected from frequency-difference autoproducts and can be accounted for with modifications to incidence angle and geometrical distances (R_1, R_2). Source-receiver bearing angle mildly influences theoretical autoproducts, exhibiting greater coherence in the 120°/300° direction than the in the 30°/210° direction. However, within

the variation expected from a 40-surface ensemble and the difference frequencies accessible from the transmitted signal, the discrepancy is not statistically significant.

The first major conclusion is that the frequency-difference autoproduct recovers coherent reflection in scattering from realistic sea surfaces. The significant recovery of coherence possible is evident in theory, simulation, and experiment. For the intrapulse difference frequencies studied here, the measured coherent reflection coefficient for autoproducts approached unity, even though the constituent acoustic fields were entirely incoherent. This effect is attributed to the frequency downshifting nature of the autoproduct, which causes the surface roughness, conventionally dependent on $kh\cos\theta$, to appear dependent on $\Delta kh\cos\theta$. Further, the expected variation in limited number ensembles, determined from Monte Carlo simulations, decreases as coherence increases, thereby eliminating the possibility of statistical fortuity in the measured data.

The second major conclusion concerns predictability of rough-surface-scattered autoproducts. Previous work noted the dependence of coherent reflection recovery on the surface autocorrelation function (Joslyn and Dowling, 2022). This notion is underscored as it appears that coherence recovery is strongly dependent on the autocorrelation function at small lag values, with greater coherent reflection expected from surfaces with larger autocorrelation values. In light of the Weiner-Khinchin theorem, autoproducts are then strongly influenced by the high wavenumber region of the sea surface spectrum, which is typically modeled and not measured in-situ through buoys. Hence, measured autoproducts may be inverted to estimate the sea surface spectrum from acoustic recordings at a single receiver. A nonlinear curve-fitting routine in MATLAB showed the feasibility of this strategy, identifying spectrum adjustments within

uncertainties noted in SW06. Theoretical autoproduct curves computed with the inferred sea surface spectrum showed excellent agreement with measured data.

Although the discontinuous bandwidth of the transmitted signal limited analysis to very small or large difference frequencies, this was a limitation of the SW06 experiment, not a general restriction. Experiments utilizing broadband transmissions are expected to create equivalent coherence recovery plots (Fig. 4.6 and Fig. 4.7) without the gaps in difference frequency. Additionally, the phase of the coherent reflection coefficient was not investigated here. While phase shifts are unimportant to overall coherence, optimizing the match in amplitude and phase between measured and theoretical autoproducts may enhance single receiver optimization strategies designed to fine-tune estimates of the sea surface spectrum.

Chapter 5

Spatial Coherence Comparisons between the Acoustic Field and Its Frequency-Difference and Frequency-Sum Autoproducts in the Ocean

The frequency-difference and frequency-sum autoproducts, quadratic products of complex acoustic field amplitudes at two frequencies, may mimic genuine acoustic fields at the difference and sum frequencies of the constituent fields, respectively. Autoproducts have proven useful in extending the useable frequency range for acoustic remote sensing to frequencies outside a recorded field's bandwidth. In array signal processing applications, the spatial coherence of the field often sets performance limits. This chapter presents results for the spatial coherence of the genuine field, the frequency-difference autoproduct, and the frequency-sum autoproduct as determined from data collected during the Cascadia Open-Access Seismic Transects (COAST 2012) experiment. In this experiment, an airgun array providing a 10 to 200 Hz signal was repeatedly fired off the coast of Washington state and the resulting acoustic fields were recorded by a nominally 8-km-long, 636-element towed horizontal array. Based on hundreds of airgun firings from a primarily shore-parallel transect, both autoproducts were found to extend field coherence to frequencies outside the genuine field's bandwidth and to produce longer coherence lengths than genuine fields, in most cases. When used for matched field processing, the same data illustrate the benefits of the autoproducts' extended coherence. The following chapter is a near reproduction of a journal article (Joslyn et al., 2022). For clarity, formulas and figures repeated elsewhere in this thesis are maintained in this section.

5.1 Introduction

Array signal processing techniques are used in a wide variety of underwater acoustic applications, including both active and passive remote sensing. Coherence between separated receivers is commonly needed for success in such applications with increased coherence leading to better outcomes. In general, the coherence between two points in space depends on the locations of the two points, the signal frequency, and the characteristics of the environment between the sound source and the two points. Coherence commonly increases with decreasing receiver separation and decreasing frequency, as well as with decreased environmental variability and complexity (Urick, 1983), although coherence in the presence of certain environmental characteristics has been shown to exhibit unintuitive behavior (Heaney, 2011). In addition, coherence measurements may be degraded when noise is present.

The distance over which a field exhibits coherence is known as the coherence length. Limited coherence length can be problematic for acoustic array signal processing in the ocean, especially for long arrays, when the array aperture exceeds the field's coherence length at the frequencies of interest. Coherence length is directly related to array gain (Carey, 1998; Carey and Moseley, 1991) and thus has important implications in beamforming (Cox, 1973; Morgan and Smith, 1990) and matched field processing applications (Baggeroer et al., 1993). When an array is nominally shorter than the field's coherence length, all of its elements should contribute positively to the achievable array gain; conversely, adding array elements that extend the array's aperture beyond the coherence length generally does not provide performance improvements and can potentially reduce the performance of array signal processing techniques. In particular, prior work has shown that for shallow water environments, spatial coherence length is a primary factor in predicting array performance (Rolt and Abbot, 1997). For a known finite coherence length, the

theoretical limitations of conventional beamforming methods with a linear array are understood and readily calculated (Cox, 1973; Morgan and Smith, 1990). Coherence length has been studied in a variety of simulation and experimental geometries and scenarios, including with both vertical and horizontal arrays (Wan et al., 2009), in the presence of internal waves (Duda et al., 2012; Finette and Oba, 2003; Lunkov and Petnikov, 2014), with varying channel depth (Carey, 1998), in the presence of multipath propagation (Carey and Moseley, 1991), and at long ranges (Andrew et al., 2005; Gorodetskaya et al., 1999), to understand the influence of various ocean environmental characteristics. The coherence of acoustic waves scattered from the ocean surface (Dahl, 2004, 2010; Dowling and Jackson, 1993) and floor sediment (Berkson, 1980; Brown et al., 2018) has also been investigated.

A shared characteristic of all existing work on coherence is the limitation to in-band signal frequencies, a typical feature of conventional signal processing methods. Interestingly, recent work has considered surrogate fields, the frequency-difference and frequency-sum autoproducts, as possible replacements for genuine acoustic fields at frequencies not broadcast by the source (Lipa et al., 2018; Worthmann and Dowling, 2017). Use of the autoproducts has been successful for beamforming (Abadi et al., 2012, 2013, 2018; Douglass et al., 2017) and matched field processing (Geroski and Dowling, 2019; Worthmann et al., 2015, 2017) at frequencies outside the broadcast signal's bandwidth. However, the coherence of autoproducts has yet to be directly examined, despite its importance in signal processing applications. Thus, the primary purpose of this paper is to report the spatial coherence properties of autoproducts computed from bottom-reflected acoustic recordings made during the Cascadia Open-Access Seismic Transects (COAST) experiment (Holbrook et al., 2012), conducted off the coast of Washington state on a varying bathymetry in July 2012. In particular, this chapter presents

results of spatial coherence and coherence lengths, as a function of frequency, for the frequency-difference and frequency-sum autoproducts and compares them to those of the genuine acoustic field – from which they are derived – in the same environment.

The autoproducts provide a means for processing signals at frequencies below and above the signal recording's bandwidth; thus, the coherence of the autoproducts relative to that of genuine in-band fields is critical for understanding their performance for various applications. In addition to signal processing at frequencies unavailable in the genuine field, information at in-band frequencies that is masked by low SNR, or other undesired features, can potentially be recovered by utilizing the autoproducts.

The remainder of this chapter is divided into three sections. Section 5.2 details the mathematical formulations for coherence, coherence length, and autoproducts; and overviews the COAST 2012 experiment and the specific data used for this study. Section 5.3 presents the coherence and matched field processing results for the genuine field, and for the frequency-difference and -sum autoproducts. The final section discusses this effort and presents the conclusions drawn from it.

5.2 Materials and Methods

The mathematical formulas for coherence, autoproducts, and matched field processing (MFP) used herein are described first, followed by an overview of the COAST 2012 experiment and the dataset used.

5.2.1 Coherence and Coherence Length

In general, for Q independent field samples recorded at locations $\boldsymbol{r}_m$ and $\boldsymbol{r}_n$, the complex coherence, Γ, of the field at angular frequency ω between these locations can be estimated from an ensemble-average (indicated by $\langle,\rangle$-brackets) of a product of normalized field amplitudes:

$$\Gamma(\boldsymbol{r_m}, \boldsymbol{r_n}, \omega) = \frac{\left\langle P_q(\boldsymbol{r_m}, \omega) P_q^*(\boldsymbol{r_n}, \omega) \right\rangle_Q}{\sqrt{\left\langle \left| P_q(\boldsymbol{r_m}, \omega) \right|^2 \right\rangle_Q \left\langle \left| P_q(\boldsymbol{r_n}, \omega) \right|^2 \right\rangle_Q}}, \tag{5.1}$$

where the asterisk indicates complex conjugation, $\boldsymbol{r_m}$ is the location of the reference receiver, $\boldsymbol{r_n}$ is the receiver a distance $\Delta r = |\boldsymbol{r_n} - \boldsymbol{r_m}|$ away from the reference receiver, and $P_q(\boldsymbol{r_j}, \omega)$ is the q^{th} field sample at angular frequency ω from the receiver located at $\boldsymbol{r_j}$ (Carter et al., 1973). The normalization in Eq. (5.1) ensures that the coherence value is bounded by the unit circle in the complex plane. The variance in phase of $P_q(\boldsymbol{r_m}, \omega) P_q^*(\boldsymbol{r_n}, \omega)$ for $1 \leq q \leq Q$ controls the coherence magnitude. Magnitudes of $\Gamma(\boldsymbol{r_m}, \boldsymbol{r_n}, \omega)$ near one indicate highly coherent fields while magnitudes near zero indicate poor coherence.

In this investigation, equally-spaced sample locations in the horizontal direction pointing away from a known-location source are of interest, so $\Delta \boldsymbol{r} = R\hat{\boldsymbol{e}}_{\boldsymbol{r}} = jd\hat{\boldsymbol{e}}_{\boldsymbol{r}}$, where j (≥ 0) is the sample location index relative to the reference receiver, d is the separation between neighboring receivers, $\hat{\boldsymbol{e}}_{\boldsymbol{r}}$ is the horizontal range unit vector pointing away from the source, and $R = jd$ is the total horizontal separation between any two receiver locations. The assumption of spatial homogeneity across the receiving array admits the following simplification to Eq. (5.1):

$$\Gamma(\Delta \boldsymbol{r}, \omega) = \Gamma(\boldsymbol{r_m}, \boldsymbol{r_n}, \omega), \tag{5.2}$$

where the spatial dependence is modified to receiver separation only. Approximate spatial homogeneity justification for a different ocean experiment is provided in (Andrew et al., 2005). Here, a further simplification is permitted as the coherence phase is not of interest. Thus,

$$\gamma(R,\omega) = |\Gamma(\Delta \boldsymbol{r},\omega)|, \tag{5.3}$$

defines the genuine acoustic field coherence function. The highest possible value of $\gamma(R,\omega)$ is unity (perfect coherence between field samples separated by R), while the minimum magnitude of $\gamma(R,\omega)$ is zero (complete lack of coherence between field samples separated by R).

The coherence length is the distance over which a predetermined level of coherence is maintained, though the exact mathematical definition of coherence length varies between scientific areas, applications, and authors. For the present purposes, the coherence length is determined from the decay of $\gamma(R,\omega)$ with increasing receiver-separation distance R. The normalization in Eq. (5.1) requires $\gamma(0,\omega) = 1$, and $\gamma(R,\omega)$ typically decreases monotonically with increasing R. Thus, the coherence length, $L(\omega)$, may then be defined as the receiver separation where $\gamma(R,\omega)$ falls below a specified threshold. No strict rules exist for this threshold value, but e^{-1} (≈ 0.368) is a common choice (Carey, 1998; Duda et al., 2012) and is used here as well.

5.2.2 Autoproducts

In prior work, coherence lengths have been determined from analysis, simulated data, and experimental measurements in a variety of acoustic environments and with a variety of signals. However, all such results consider only in-band signal frequencies. Recent work (Worthmann and Dowling, 2017) has shown that the frequency-difference and frequency-sum autoproducts constructed from nonzero-bandwidth acoustic field recordings may mimic genuine acoustic fields at (user-selectable) frequencies below and above, respectively, the recorded signal's

bandwidth. Further, the autoproducts can be used to obtain unique results in acoustic remote sensing (Dowling, 2018). The frequency-difference autoproduct, $AP_{\Delta,q}$, and frequency-sum autoproduct, $AP_{\Sigma,q}$, are defined from two frequencies of the q^{th} acoustic recording at the j^{th} element of a receiving array as

$$AP_{\Delta,q}(\boldsymbol{r_j}, \omega, \Delta\omega) = P_q(\boldsymbol{r_j}, \omega_+)P_q^*(\boldsymbol{r_j}, \omega_-), \tag{5.4a}$$

$$AP_{\Sigma,q}(\boldsymbol{r_j}, \omega, \Delta\omega) = P_q(\boldsymbol{r_j}, \omega_+)P_q(\boldsymbol{r_j}, \omega_-), \tag{5.4b}$$

where $\omega_\pm \equiv \omega \pm \Delta\omega/2$ denote the pair of recorded acoustic frequencies. Prior work has shown that $AP_{\Delta,q}$ and $AP_{\Sigma,q}$ may mimic genuine acoustic fields at the difference, $\Delta\omega$, and sum, $\Sigma\omega = 2\omega$, frequencies (Worthmann and Dowling, 2017). Equations (5.4a) and (5.4b) may be averaged through the recorded field's bandwidth, $\Omega_L \leq \omega \leq \Omega_H$, to determine the bandwidth-averaged autoproducts:

$$\langle AP_{\Delta,q}(\boldsymbol{r_j}, \Delta\omega)\rangle_{BW} = \frac{1}{\Omega_{BW}^{\Delta}} \int_{\Omega_C - \frac{1}{2}\Omega_{BW}^{\Delta}}^{\Omega_C + \frac{1}{2}\Omega_{BW}^{\Delta}} AP_{\Delta,q}(\boldsymbol{r_j}, \omega, \Delta\omega)\, d\omega\,, \tag{5.5a}$$

$$\langle AP_{\Sigma,q}(\boldsymbol{r}_j, \Sigma\omega)\rangle_{BW} = \frac{1}{\Omega_{BW}^{\Sigma}} \int_{0}^{\Omega_{BW}^{\Sigma}} AP_{\Sigma,q}(\boldsymbol{r_j}, \omega, \Delta\omega)\, d(\Delta\omega)\,, \tag{5.5b}$$

where $\Omega_C = (\Omega_L + \Omega_H)/2$ is the in-band center frequency. The signal bandwidths available to average $AP_{\Delta,q}$ and $AP_{\Sigma,q}$ are given by $\Omega_{BW}^{\Delta} = \Omega_H - \Omega_L - \Delta\omega$ and $\Omega_{BW}^{\Sigma} = \min[2\Omega_H - \Sigma\omega, \Sigma\omega - 2\Omega_L]$, respectively. The bandwidth averaging of Eq. (5.5) is advantageous in multipath environments because it suppresses cross terms incurred from the quadratic construction of the autoproducts, and enhances their mimicry of genuine difference- or sum-frequency acoustic fields (Lipa et al., 2018; Worthmann and Dowling, 2017). The implementation here differs slightly from bandwidth averages in previous work. Due to imperfect knowledge of the source

spectrum, autoproduct samples are averaged directly in Eq. (5.5), without explicit removal of the source spectrum.

The coherence definitions of the frequency-difference and frequency-sum autoproducts follow directly from Eqs. (5.1) - (5.3) with the bandwidth-averaged autoproducts replacing the genuine acoustic field:

$$\gamma_{\Delta}(R,\Delta\omega)=\frac{\left|\left\langle\left\langle AP_{\Delta,q}(\boldsymbol{r}_m,\Delta\omega)\right\rangle_{BW}\left[\left\langle AP_{\Delta,q}(\boldsymbol{r}_n,\Delta\omega)\right\rangle_{BW}\right]^{*}\right\rangle_{Q}\right|}{\sqrt{\left\langle\left|\left\langle AP_{\Delta,q}(\boldsymbol{r}_m,\Delta\omega)\right\rangle_{BW}\right|^{2}\right\rangle_{Q}\left\langle\left|\left\langle AP_{\Delta,q}(\boldsymbol{r}_n,\Delta\omega)\right\rangle_{BW}\right|^{2}\right\rangle_{Q}}}, \tag{5.6a}$$

$$\gamma_{\Sigma}(R,\Sigma\omega)=\frac{\left|\left\langle\left\langle AP_{\Sigma,q}(\boldsymbol{r}_m,\Sigma\omega)\right\rangle_{BW}\left[\left\langle AP_{\Sigma,q}(\boldsymbol{r}_n,\Sigma\omega)\right\rangle_{BW}\right]^{*}\right\rangle_{Q}\right|}{\sqrt{\left\langle\left|\left\langle AP_{\Sigma,q}(\boldsymbol{r}_m,\Sigma\omega)\right\rangle_{BW}\right|^{2}\right\rangle_{Q}\left\langle\left|\left\langle AP_{\Sigma,q}(\boldsymbol{r}_n,\Sigma\omega)\right\rangle_{BW}\right|^{2}\right\rangle_{Q}}}. \tag{5.6b}$$

Coherence lengths, $L_{\Delta}(\Delta\omega)$ and $L_{\Sigma}(\omega)$, for AP_{Δ} and AP_{Σ}, respectively, were then determined from the spatial decay of $\gamma_{\Delta}(R,\Delta\omega)$ and $\gamma_{\Sigma}(R,\Sigma\omega)$ in an equivalent manner to the calculation of $L(\omega)$ from $\gamma(R,\omega)$.

Uncertainty estimates for the γ's and L's are included to facilitate quantitative comparisons between acoustic field coherence and autoproduct coherence. The 95% confidence interval (Bendat and Piersol, 1980) for the coherence random error, ε_{γ}, reported here is:

$$\left[\left(1-2\varepsilon_{\gamma}\right)\gamma,\left(1+2\varepsilon_{\gamma}\right)\gamma\right], \tag{5.7a}$$

$$\varepsilon_{\gamma}=\frac{(1-\gamma^{2})}{\gamma\sqrt{2Q}}. \tag{5.7b}$$

These approximate error bounds rely exclusively on the number of field samples, Q, and the mean coherence value, γ. As such, Eq. (5.7) is used to generate error estimates for the genuine acoustic field coherence calculated from Eq. (5.3), and the frequency-difference and frequency-

sum autoproduct coherence calculated from Eq. (5.6a) and (5.6b). The error estimates of Eq. (5.7) have been used previously in ocean acoustic coherence studies (Dahl, 2004, 2010) and are expected to be a good approximation of the true variance for a large ensemble, Q (Carter et al., 1973). More exact confidence bound formulations exist (Carter, 1987; Carter et al., 1973) as well as iterative algorithms for confidence bound generation (Wang and Tang, 2004; Zoubir, 2005). However, Eq. (5.7) was used in favor of these alternatives because of its relative simplicity and the sufficiently large ensemble number, Q, provided by the COAST 2012 experiment.

5.2.3 Matched Field Processing

A field's coherence length has significant implications in array signal processing, and this is examined herein for the specific case of matched field processing (MFP) of the in-band field and its autoproducts. Previous work has considered the autoproducts for out-of-band MFP and has shown that they may provide improvements over conventional MFP when signal processing at in-band frequencies is problematic (Geroski and Dowling, 2019; Worthmann et al., 2015, 2017). Specifically, frequency-difference methods can suppress the negative impacts of array sparseness, random scattering, and wavefront mismatch, while frequency-sum methods can enhance resolution.

MFP is a common scheme to identify an unknown source location, in both range and direction, from a measured field. Computed replica fields (*aka* replicas), based on a modeled acoustic propagation environment, are generated for many potential source locations. The location of the source is then selected such that the replica field exhibits the highest correlation with the measured field at the recording locations. The first development of MFP in underwater acoustics can be found in Bucker (Bucker, 1976) and an overview of MFP is available in Jensen (Jensen et al., 2011).

The MFP strategy implemented is the Bartlett processor, which is a frequency domain spatial correlation between the measured field and computed replicas. Mathematically,

$$B_q(\boldsymbol{x},\omega) = \left| \sum_j^{N_L} P_q(\boldsymbol{r_j},\omega) w_j^*(\boldsymbol{x},\omega) \right|^2 , \tag{5.8}$$

where N_L is the number of array elements informed by the coherence length of the field, $\boldsymbol{x}$ is the search coordinate, and $w_j(\boldsymbol{x},\omega)$ is the weight vector based on the modeled propagation between $\boldsymbol{x}$ and the receiving location $\boldsymbol{r_j}$. The replicas here implement image theory for the surface and bottom reflections, which has been used recently in underwater shallow target localization using MFP (Hotkani et al., 2021). When plotted as a function of the search coordinate $\boldsymbol{x}$, B_q is normalized by its maximum value and presented as a decibel value: $10\log_{10}\{B_q(\boldsymbol{r},\omega)/\max[B_q(\boldsymbol{r},\omega)]\}$.

The out-of-band MFP formulation is identical to Eq. (5.8) with $P_q(\boldsymbol{r_j},\omega)$ replaced by $\langle AP_{\Delta,q}(\boldsymbol{r_j},\Delta\omega)\rangle_{BW}$ or $\langle AP_{\Sigma,q}(\boldsymbol{r}_j,\Sigma\omega)\rangle_{BW}$:

$$B_q(\boldsymbol{x},\Delta\omega) = \left| \sum_j^{N_L} \langle AP_{\Delta,q}(\boldsymbol{r_j},\Delta\omega)\rangle_{BW} w_j^*(\boldsymbol{x},\Delta\omega) \right|^2 , \tag{5.9a}$$

$$B_q(\boldsymbol{x},\Sigma\omega) = \left| \sum_j^{N_L} \langle AP_{\Sigma,q}(\boldsymbol{r}_j,\Sigma\omega)\rangle_{BW} w_j^*(\boldsymbol{x},\Sigma\omega) \right|^2 , \tag{5.9b}$$

with the weight vector evaluated at the difference or sum frequency, as appropriate.

5.2.4 COAST 2012 Experiment

The Cascadia Open-Access Seismic Transects (COAST) experiment (Holbrook et al., 2012) was conducted off the coast of Washington state in July 2012. The goal of this experiment was to

collect two-dimensional seismic reflection profiles and other geophysical data. In this experiment, the *R/V Marcus G. Langseth* towed an approximately 8-km-long streamer at 9 m depth that contained a receiver array with $N = 636$ hydrophone channels spaced $d = 12.5$ m apart. To minimize contributions from purely-horizontal-traveling energy, the recorded acoustic signal of each channel was an average of 14 hydrophones located along the horizontal array (Diebold et al., 2010). Herein, receiving groups are referred to as elements or individual hydrophones for simplicity. A further discussion of receiver subtleties exists in (Abadi and Freneau, 2019) or (Diebold et al., 2010). The output of the receiver nearest to the source exhibited behavior (low amplitude) inconsistent with neighboring receivers, and thus was removed from the data analysis so that $N = 635$ for the purposes of this manuscript.

An array of 36 airguns, towed 240 m behind the ship at either 9 m (used here) or 15 m depth (Tolstoy et al., 2009), was used as a single directional acoustic source with a total volume of 6600 cubic inches. The wideband impulsive signal was preferentially broadcast toward the ocean floor and the bandwidth spanned from below 10 Hz to above 200 Hz. The ship towed the airgun and receiving arrays at 4.5 knots along 11 separate transects, during which the airgun array was fired approximately every 50 m while the receiving array recorded for 16.384 s with a 500 Hz sampling rate. The timing of the source broadcasts and receiving array recording window provided ample time to record direct-path and multiple-reflected-path sounds at both the closest and furthest receivers. For the present study, the direct path is time-gated out and replaced with zeros in the time domain to emphasize reflected-path coherence. Further, no corrections for ship motion during the data recording interval were made in the data processing.

Figure 5.1(a) shows the layout of the experiment, with solid bold lines indicating each of the 11 transects. For the current study, data from the primarily shore-parallel transect number 10

(indicated in Fig. 5.1(a) by a white arrow) was used since the depth variation along this track was the smallest of the 11 available and the number of usable signal samples was far greater than the other primarily shore-parallel transect, number 11. Figure 5.1(b) shows the bathymetry of transect 10, which was traversed from north to south. To ensure array curvature and significantly distinct bathymetry did not influence the results, the first 200 and the last 483 airgun signal pulses along this track were not used in the analysis. The airgun was powered down for an additional 172 pulses due to marine life in the area. Hence, of the total 1684 airgun pulses on this transect, $Q = 829$ pulses were utilized here in this study. These data were collected on July 22, 2012 between 01:30:30 and 07:57:23 Greenwich Mean Time (GMT). The ship location, shown in Fig. 5.1(b), traversed 50 km from the first (10 km) to the last (60 km) analyzed signal pulses. The average water depth along the analyzed portion of the transect is slightly more than 1.9 km and varies by less than 200 m.

The airgun array was designed so that acoustic energy was primarily directed towards the ocean floor. Figure 5.2 shows a range-depth schematic with the nominal horizontal and vertical dimensions, corresponding to the experimental data used here. The bottom reflected (solid line) and bottom-surface reflected (dashed line) propagation paths to a single receiver are shown. These two paths convey most of the signal energy from the airgun array to the receivers. Although the nominal bathymetric depth is known along the transect, the actual reflection of bottom-reflected sound may include contributions from below the bathymetric depth. Reflection strength and phase is dependent on the geoacoustic properties of the ocean bottom and may contribute to coherence loss in the recorded sound along with the noted variations in bathymetry.

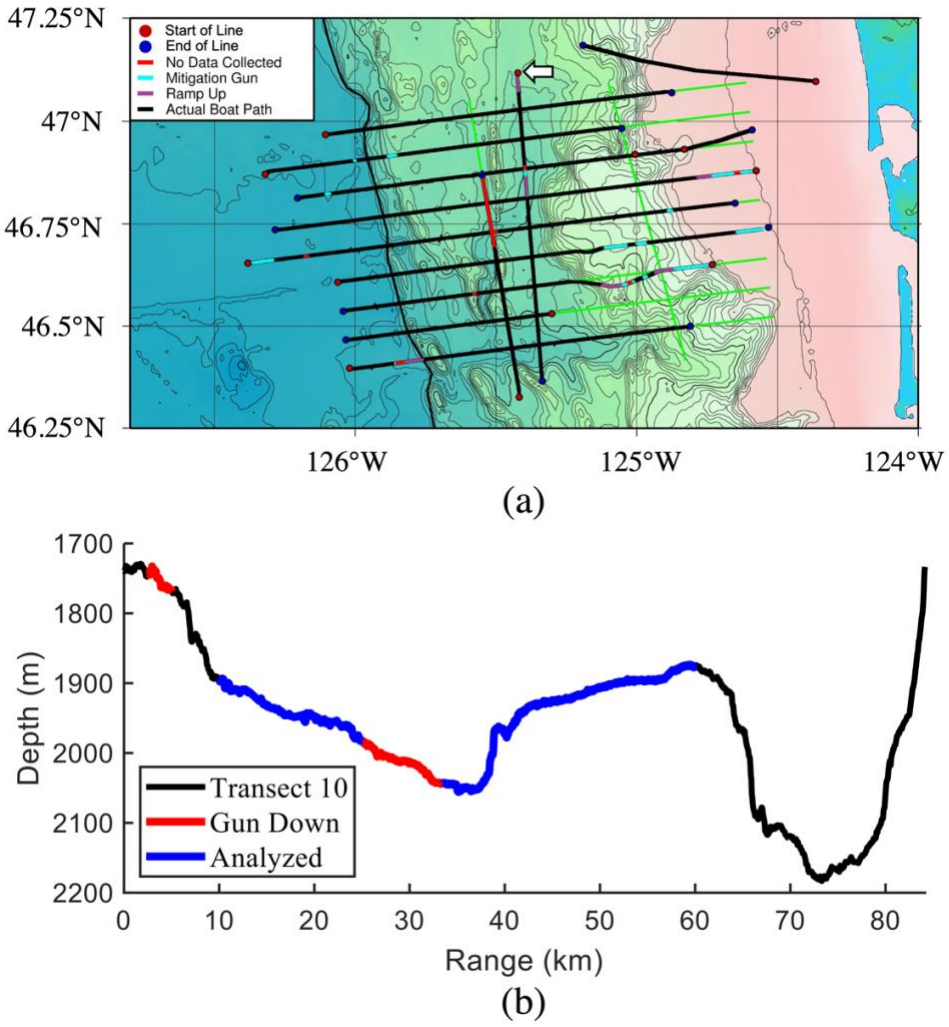

Figure 5.1: (a) Layout of the COAST experiment from (Holbrook et al., 2012), conducted off the coast of Washington state in July, 2012. Each line represents the ship's path while towing an ~8 km streamer with 636 receivers spaced 12.5 m and a source array of 36 airguns at 4.5 knots. The white arrow indicates the beginning of the analyzed transect. Data were collected by coordinated firing of the airgun array approximately every 50 m and recording for 16.384 s. (b) The bathymetry of transect 10 is shown here as a function of the ship location with blue indicating the ship location for the analyzed signal pulses.

As the receiving array is towed along transect 10, additional reductions in measured coherence arise from the varying bathymetry, ocean floor and surface roughness, and other propagation fluctuations along these paths.

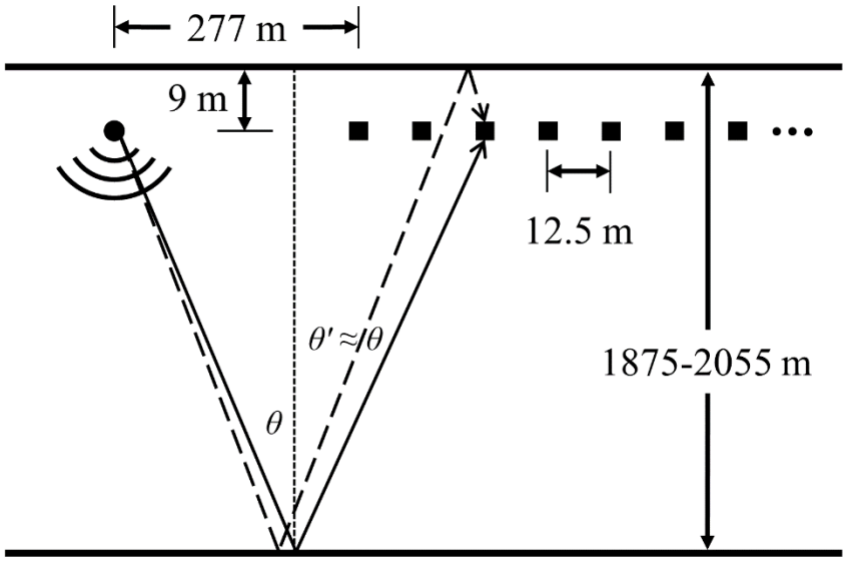

Figure 5.2: The approximate layout of COAST 2012 transect 10. The solid circle indicates the airgun array. The solid squares indicate receivers. The first bottom reflection (solid line) and bottom-surface reflection (dashed line) account for most of the signal energy recorded by each receiver of the array.

Figure 5.3(a) shows a waterfall plot of the receiver array output for one signal pulse taken at 06:36:16 GMT (only every 10th recorded waveform is shown for clarity), when the depth at the ship was roughly 1906 m. Here, receiver number 1 is closest to the airgun array and receiver number 635 is furthest from it. The strong signal arriving at the various receivers between 2.5 and 6.0 seconds is the first bottom reflection. A second bottom reflection and a faint third reflection are also evident in the recordings. The direct path is visible in the measurements of the nearest 50 receivers as a small-amplitude pulse arriving before the prominent reflections. Due to the absence of significant direct path energy further along the array, a half-second time-gate is applied herein to remove the expected direct path arrival at all receivers. Spectrograms for receivers 1 and 635 of the field sample in Fig. 5.3(a) are shown with a 256 ms Hamming window and 128 ms window overlap in Fig. 5.3(b) and Fig. 5.3(c), respectively. In the

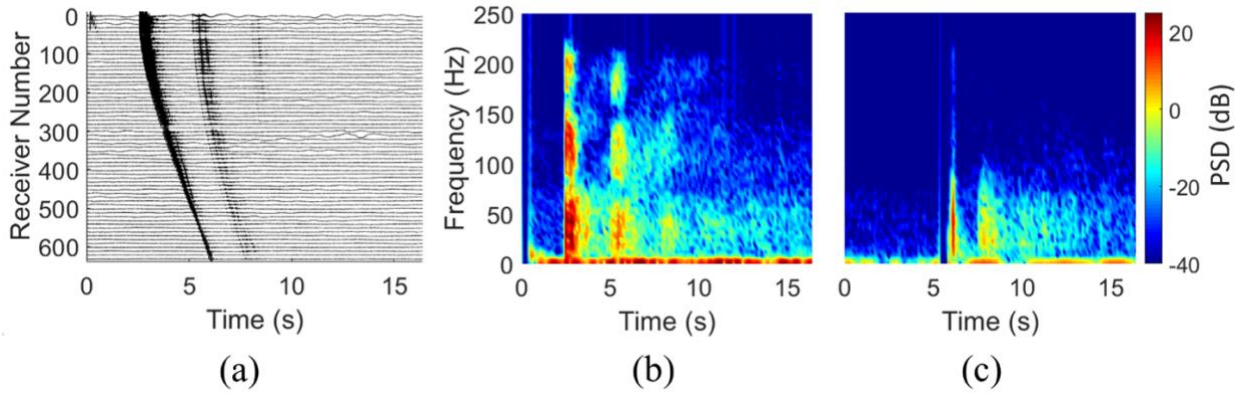

Figure 5.3: (a) Waterfall plot showing the time-series output of every 10th receiver for the ping recorded at 06:36:16 GMT on July 22, 2012. Spectrogram outputs with time-gated direct path, 256 ms Hamming window and 128 ms window overlap for the receivers closest to (b) and furthest from (c) the source.

spectrogram for the closest receiver, the first reflected path is visible (uneven red vertical stripe) near 2.5 s, followed by several bottom reflections with a time spacing of 2.5-3 s. For the farthest receiver, two bottom reflections are clearly apparent, with a possible third path indicated as well. In both spectrograms, the vertical blue bars are the result of the time-gated direct path.

The spectrograms demonstrate that substantial signal energy exists across most of the available frequency range, with noise being more prominent at lower frequencies. Additional dips in signal amplitude are apparent in Fig. 5.3(b) around 80 and 160 Hz. Spectrograms from other positions along the array are similar, and show the variations expected with increasing source-to-receiver range and variations in water column depth.

The dips in signal amplitude around 80 Hz and 160 Hz in Fig. 5.3(b) are predictable based on the experimental geometry and receiving array depth below the pressure-release ocean surface. Upward-propagating sea-floor reflected sound destructively interferes with downward-propagating sea-surface reflected sound in these frequency ranges, and this phenomenon causes variation in SNR across the frequencies of interest for this experiment. Figure 5.4 shows the

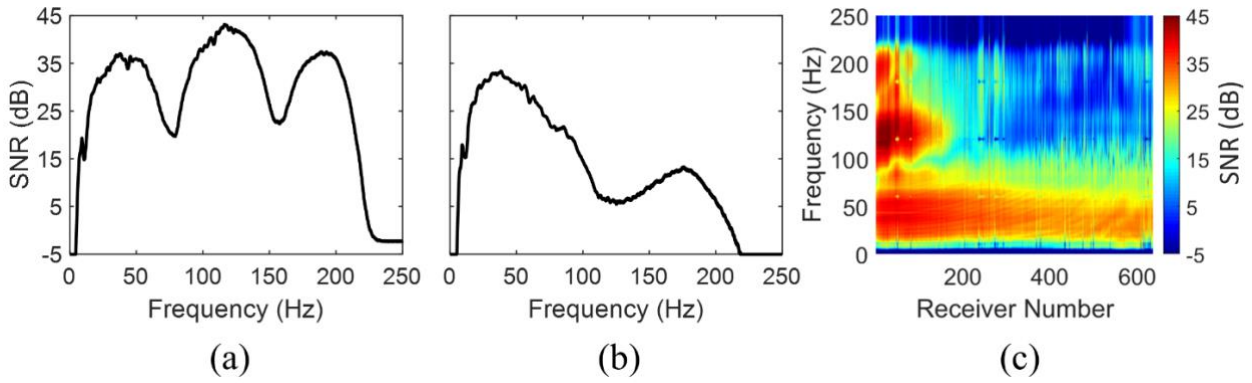

Figure 5.4: Signal-to-Noise Ratio (SNR) from (10) for the closest receiver (a) and halfway along the receiving array (b) for 829 signal pulses. SNR, plotted against both receiver number and frequency is shown in panel (c). The dips in SNR, particularly for the nearest receiver, occur at the frequencies predicted for destructive interference of upward- and downward-propagating sounds at the depth of the receiver array.

measured SNR for the nearest receiver to the source [Fig. 5.4(a)] and at a location halfway along the receiving array [Fig. 5.4(b)] as a function of frequency. In Fig. 5.4(c), the SNR is indicated for all frequencies and receiving locations. The SNR was calculated for each receiver at each frequency, $\omega = 2\pi f$, as the average recorded signal variance, $\left\langle \left| P_q(\boldsymbol{r}_j, \omega) \right|^2 \right\rangle_Q$, divided by the average noise variance, $\left\langle \left| N_q(\boldsymbol{r}_j, \omega) \right|^2 \right\rangle_Q$, for the 829 airgun pulses:

$$\mathrm{SNR}(\boldsymbol{r}_j, \omega) = 10 \log_{10} \left(\frac{\left\langle \left| P_q(\boldsymbol{r}_j, \omega) \right|^2 \right\rangle_Q}{\left\langle \left| N_q(\boldsymbol{r}_j, \omega) \right|^2 \right\rangle_Q} - 1 \right). \tag{5.10}$$

The '-1' within the logarithm ensures that $\mathrm{SNR}(\boldsymbol{r}_j, \omega)$ tends to the appropriate limit when the recorded complex field amplitudes, $P_q(\boldsymbol{r}_j, \omega)$, which contain signal and noise, become increasingly dominated by noise. Additionally, each value in Fig. 5.4 was averaged over multiple frequency samples with a 1 Hz sliding window to increase smoothness. To evaluate Eq. (5.10),

the complex field amplitudes, $P_q(\boldsymbol{r}_j, \omega)$, were determined from a 1.5 s time segment within each recording that started at the beginning of the first bottom reflection's arrival, while the noise-only amplitudes, $N_q(\boldsymbol{r}_j, \omega)$, were determined from a 1.5 s time segment at the end of each recording when no signal was apparent.

The dips in SNR seen in Fig. 5.4, particularly for the closest receiver, occur at the frequencies expected to produce destructive interference between bottom-reflected upward-propagating sound and bottom-surface-reflected downward-propagating sound for the COAST 2012 experimental geometry. A reduction in coherence length is expected at these SNR dips as well. In addition, the SNR drops below 0 dB for frequencies below roughly 5 Hz. Thus, at the lowest frequencies considered here, the genuine field's coherence is obscured by noise. A notable comparison between Fig. 5.4(a) and Fig. 5.4(b) is the prominence of the first major dip. For the further receiver, this SNR dip occurs at a frequency that is approximately 35 Hz higher than that for the close receiver and is much less prominent. This SNR-dip frequency variation arises from propagation angle variations in the experimental geometry that occur as receiver range increases. Additionally, in Fig. 5.4(c), the following receivers have been removed for poor SNR: 47, 53, 75, 188, 287, 415, 495, 539, 544, 606, and 626, resulting in N = 624 herein. This noise contamination was discussed in the cruise report, with most of these specific receivers identified as problematic for a different transect (Holbrook et al., 2012).

5.3 Results

5.3.1 Coherence

The coherence was calculated from the frequency domain data of COAST 2012 transect 10 as described in Chapter 5.2. Given that the results for in-band, frequency-difference, and frequency-

sum coherence all come from exactly the same data and that comparisons are the primary topic of this manuscript, no geometrical or environmental corrections based on the known experimental parameters were made to improve or alter any of the measured coherences. Furthermore, no signal-spectrum adjustments or frequency-dependent sea-floor reflection coefficient corrections were made to the data or the replicas. In all cases, the nearest receiver was used as the reference receiver. Additional reference receivers and reference receiver coherence averaging was not included, but similar results are expected if other reference receivers are chosen. Based on the sampling rate and time record duration, each signal pulse nominally provides 0.061 Hz frequency resolution. Herein, unless otherwise noted, the closest resolved frequency to the specified integer frequency was considered.

For simplicity and consistency, the signal bandwidth limits were defined as $\Omega_L/2\pi$ = 10 Hz and $\Omega_H/2\pi$ = 200 Hz for all the results provided here. Thus, the bandwidth-averaged frequency-difference autoproduct calculated from Eqs. (5.4a) and (5.5a) can probe difference frequencies from 0-190 Hz. Analogously, the frequency-sum autoproduct can achieve sum frequencies from 20-400 Hz. These three bandwidths overlap for 20-190 Hz, where coherences can be directly compared.

Figure 5.5 shows the three possible coherence curves for 60 Hz [Fig. 5.5(a)], 80 Hz [Fig. 5.5(b)], and 120 Hz [Fig. 5(c)]. The in-band coherence from Eq. (5.3) is shown in black, frequency-difference coherence from Eq. (5.6a) in red, and frequency-sum coherence from Eq. (5.6b) in blue. The confidence bounds from Eq. (5.7) are shown as semitransparent regions of the same color surrounding each coherence curve. The horizontal axis for all panels is the scaled receiver spacing R/λ, with limits of 0 and 40 wavelengths. Wavelengths were computed from the given frequency and a reference sound speed (1480 m/s) determined from the average of the

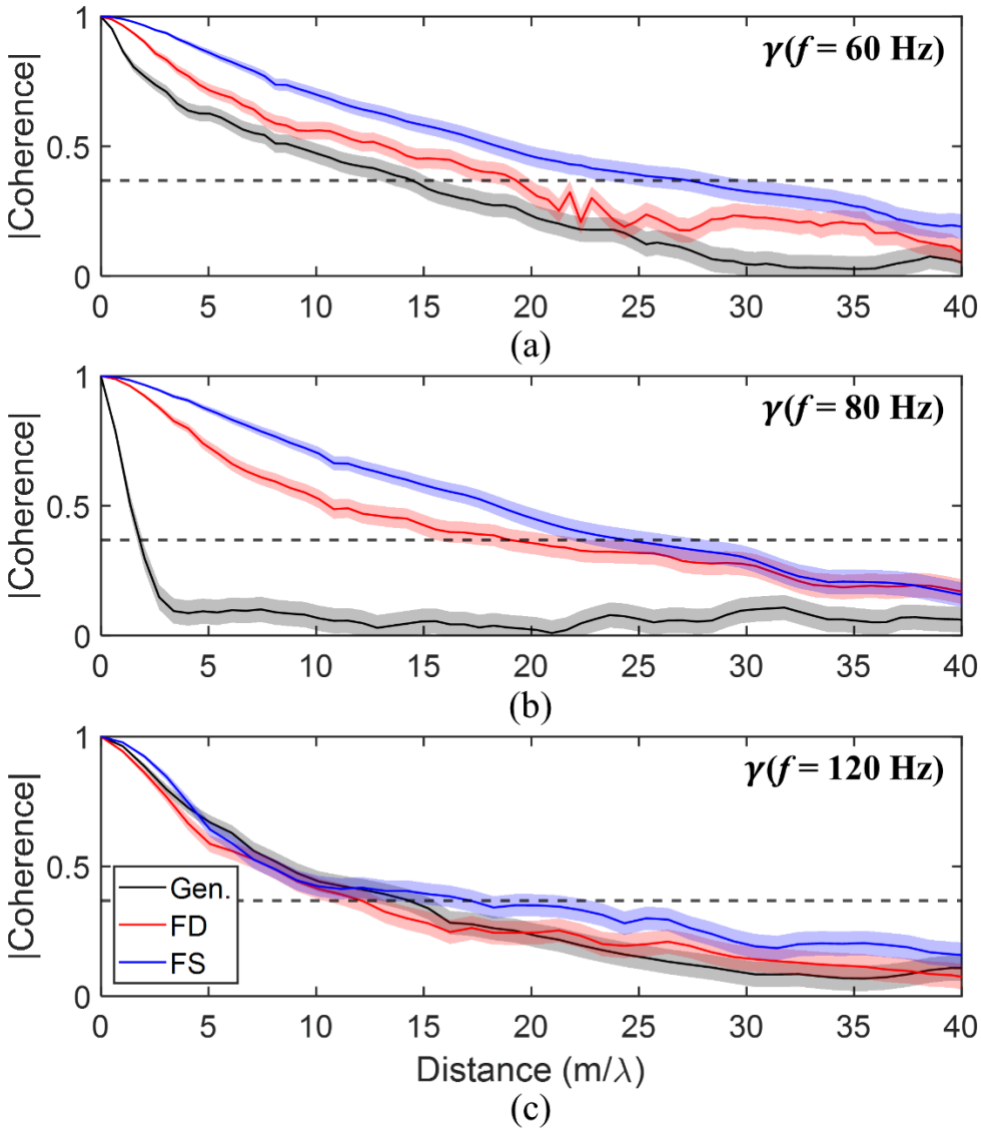

Figure 5.5: Coherence vs. distance (normalized by wavelength) comparison for frequencies obtainable by all three fields. The genuine in-band field is shown in black, the frequency-difference autoproduct is shown in red, and the frequency-sum autoproduct is shown in blue. The horizontal dotted black line is the $\exp[-1]$ threshold value for coherence length. Confidence intervals estimated from Eq. (5.7) are indicated as semitransparent regions and the frequency used is displayed in the upper right of each panel.

sound speed profiles recorded during the transect. The vertical axes are bounded from 0 to 1 and the horizontal dotted black line indicates the e^{-1} coherence length threshold. Figures 5.5(b) and

5.5(c) correspond to frequencies expected to exhibit destructive interference for the acoustic field and the autoproduct, respectively.

The three panels in Fig. 5.5 indicate that more coherence may be available from the autoproduct when the genuine field and both autoproducts can all be obtained at the same frequency. At 60 Hz, displayed in Fig. 5.5(a), the frequency-difference and frequency-sum autoproduct coherence exceeds the genuine field coherence by more than the estimated uncertainty. At 80 Hz, displayed in Fig. 5.5(b), the destructive interference pattern discussed in Chapter 5.2 significantly decreases the in-band field's coherence, but for the frequency-difference (frequency-sum) autoproduct, significant coherence is maintained for a horizontal receiver separation of nearly 20λ (25λ). This occurs because the quadratic character of the autoproducts causes them to respond to the ocean surface's pressure release boundary as if it were a hard boundary [see (Worthmann and Dowling, 2017)]. As a result, destructive interference occurs for autoproducts at 120 Hz, which is shown in Fig. 5.5(c). Interestingly, the effect of the destructive interference on the autoproducts' coherence is not as significant and can be attributed to the benefits of the bandwidth-averaging in Eq. (5.5). Within uncertainties, all three fields exhibit similar coherences at this frequency.

Either the frequency-difference or the frequency-sum autoproduct shares bandwidth with the genuine acoustic field in two other regions. Difference frequencies from 10-19 Hz and sum frequencies from 191-200 Hz overlap with the signal bandwidth. Figure 5.6 compares the genuine acoustic coherence to autoproduct coherence for 19 Hz [Fig. 5.6(a)] and 191 Hz [Fig. 5.6(b)]. Again, the coherence determined from the genuine acoustic field is shown in black, the frequency-difference autoproduct in red, and the frequency-sum autoproduct in blue. The confidence bounds are again indicated as semitransparent regions. For 19 Hz, the curves shown

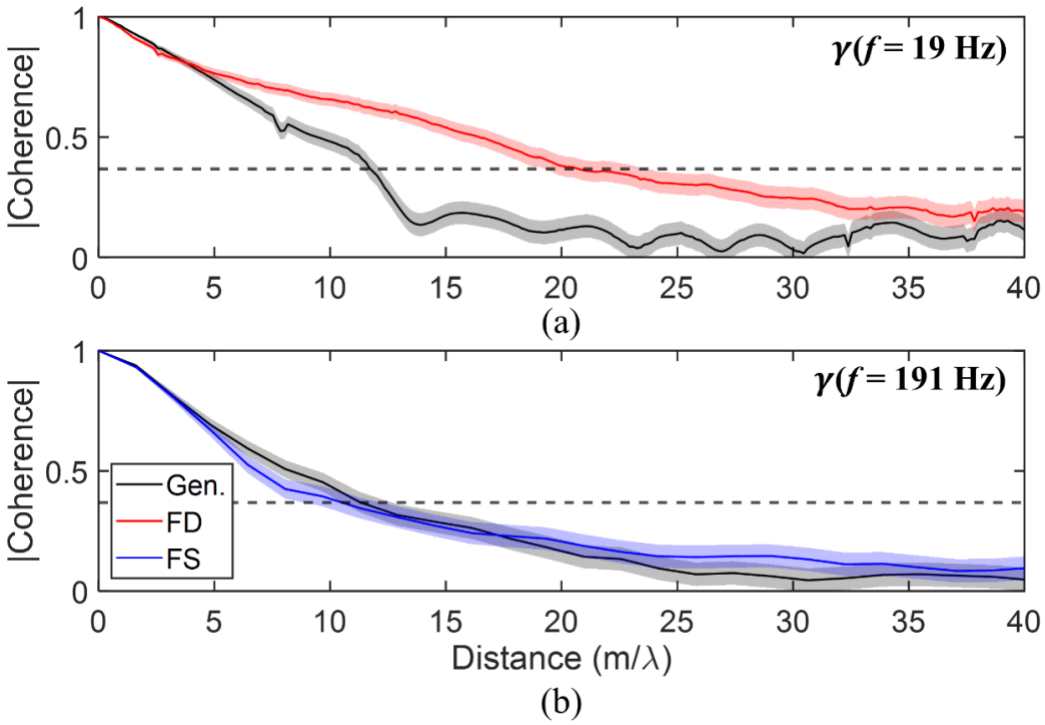

Figure 5.6: Coherence vs. distance (normalized by wavelength) comparison for frequencies within the signal bandwidth and obtainable by either the frequency-difference or frequency-sum autoproduct. Results for the genuine in-band field are shown in black, results for the frequency-difference autoproduct are shown in red, and results for the frequency-sum autoproduct are shown in blue. The horizontal dotted black line is the $\exp[-1]$ threshold value for coherence length. Confidence intervals determined from Eq. (5.7) are indicated as semitransparent regions and the frequency is displayed in the upper right of each panel.

in Fig. 5.6(a) indicate that the frequency-difference autoproduct provides a significantly greater coherence for $R = 5\lambda$ to 35λ. For the 191 Hz curves shown in Fig. 5.6(b), the frequency-sum autoproduct coherence and the acoustic field coherence are nearly identical. This is similar to the results shown in Fig. 5.5(c), as 191 Hz is expected to exhibit destructive interference for the frequency-sum autoproduct.

Finally, the autoproduct constructions allow for coherence calculation at frequencies both below and above the recorded signal bandwidth. For the data used here, the frequencies available to the frequency-difference (frequency-sum) autoproduct but unavailable to the in-band field are

1-9 Hz (201-400 Hz). Notably, the frequency-sum autoproduct provides coherence results above the signal bandwidth and above the Nyquist frequency limit (250 Hz) dictated by the experimental sampling rate. Coherence curves for two such frequencies, 1 Hz and 315 Hz, are shown in Fig. 5.7(a) and Fig. 5.7(b). The vertical axes are bounded from 0 to 1. The wavelength-scaled receiver-spacing horizontal axis in Fig. 5.7(a) spans the entire 8 km receiving array while the horizontal axis of Fig. 5.7(b) is limited to 40λ. Hence, for sufficiently low difference frequencies, the frequency-difference autoproduct is coherent along the entire receiving array, even if the constituent fields were not coherent themselves. Additionally, the frequency-sum autoproduct is coherent across a significant number of wavelengths, even at sum frequencies exceeding the Nyquist limit for the genuine acoustic field.

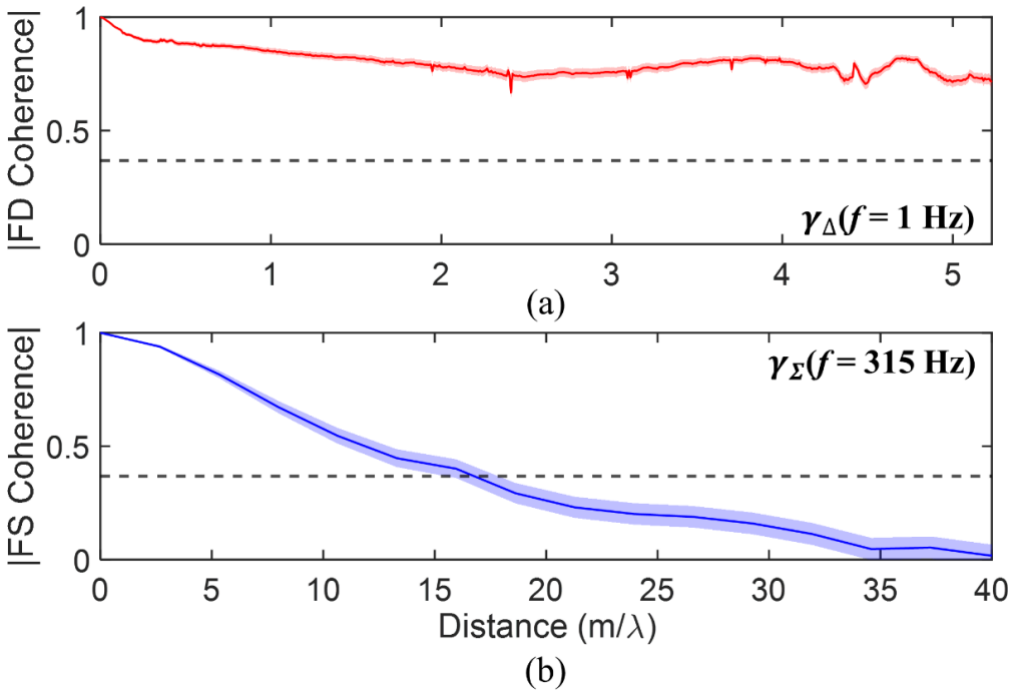

Figure 5.7: Coherence vs. distance (normalized by wavelength) comparison for frequencies obtainable only by the frequency-difference or frequency-sum autoproduct. The frequency-difference autoproduct is shown in red in (a) and the frequency-sum autoproduct is shown in blue in (b). The horizontal dotted black line is the $\exp[-1]$ threshold value for coherence length. Confidence intervals using Eq. (5.7) are indicated as semitransparent regions and the frequency used is displayed in the upper right of each panel.

5.3.2 Coherence Length

As described in Chapter 5.2, in-band, frequency-difference, and frequency-sum coherence lengths, $L(\omega)$, $L_{\Delta}(\Delta\omega)$, and $L_{\Sigma}(\Sigma\omega)$, were determined from identifying the e^{-1} length from the measured coherences, $\gamma(R,\omega)$, $\gamma_{\Delta}(R,\Delta\omega)$, and $\gamma_{\Sigma}(R,\Sigma\omega)$, respectively. Although the experiment provides 0.061 Hz frequency resolution, coherence lengths as functions of cyclic frequency (f) are reported here in 1 Hz increments. This was accomplished by averaging the coherence lengths for all resolved frequencies that round to the same integer-Hz frequency value. The upper and lower confidence-interval bounds of Eq. (5.7) (shown in Fig. 5.5, Fig. 5.6, and Fig. 5.7), were processed analogously to the mean coherences to provide confidence bounds on the coherence lengths at each resolved frequency. These upper and lower confidence bounds were then combined to produce an average bound for integer-Hz-averaged coherence lengths (Taylor, 1997).

Complete results for the three coherence lengths (divided by the nominal wavelength) are plotted vs. frequency in logarithmic coordinates in Fig. 5.8. Here, black dots indicate $L(f)$, red dots indicate $L_{\Delta}(\Delta f)$, blue dots indicate $L_{\Sigma}(\Sigma f)$, and the dashed black line represents the receiving array length. The error bars, shown between 5 Hz and 20 Hz for the three coherence lengths, represent the 95th percentile of the integer-Hz confidence-interval bounds.

For the in-band frequency range (10 to 200 Hz), both autoproduct coherence lengths generally exceed that of the in-band field and are less suppressed at the coherence dips seen at frequencies corresponding to destructive interference at the array depth. When averaged through their respective frequency ranges (provided in parentheses), the frequency-difference autoproduct's coherence length is 16.7 wavelengths (1 Hz $\leq \Delta f \leq$ 190 Hz), the genuine field's coherence length is 12.0 wavelengths (10 Hz $\leq f \leq$ 200 Hz), and the frequency-sum

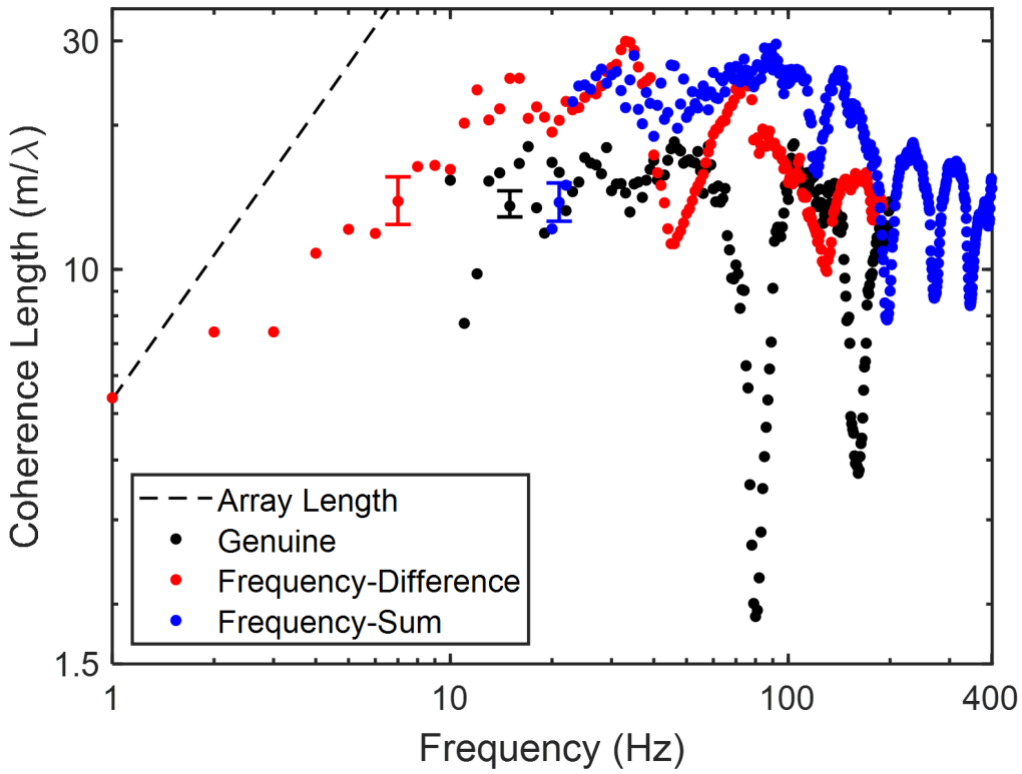

Figure 5.8: Coherence length (normalized by wavelength) vs. frequency comparison for the genuine and autoproduct fields on logarithmic axes. Genuine acoustic-field coherence lengths are indicated by black dots for f = 10-200 Hz while frequency-difference (-sum) coherence lengths are displayed in red (blue) for Δf = 1-190 Hz (Σf = 20-400 Hz). The receiving array length is indicated by a dashed black line and nominal error bars representing the 95th percentile for each data type are indicated between 5 and 20 Hz.

autoproduct's coherence length is 17.6 wavelengths (20 Hz $\leq \Sigma f \leq$ 400 Hz). In the below-band (1 Hz $\leq \Delta f \leq$ 10 Hz) and above-band (200 Hz $\leq \Sigma f \leq$ 400 Hz) frequency ranges, where the in-band coherence is either based on noise or cannot be calculated, the autoproducts provide coherence lengths of 5 to 18 wavelengths. Taken together, these results strongly suggest that the autoproducts might enhance coherent array signal processing when they can be calculated at in-band frequencies, and that they can extend coherent array signal processing to out-of-band frequencies. As a final note, at the lowest difference frequency, 1 Hz, the coherence length is

compromised by the finite length (8 km) of the COAST 2012 array as the coherence does not dip below the e^{-1} threshold.

As mentioned previously, the coherence length dips seen in the various curves on Fig. 5.8 are caused by destructive interference of upward- and downward-traveling sound at the depth of the receiving array. However, the frequencies of these dips differ between the genuine field and the autoproducts because of the modified boundary condition arising from the autoproducts' construction (Worthmann and Dowling, 2017). In addition, the depth of these coherence length dips is reduced for the autoproducts because they benefit from the bandwidth-averaging specified in Eq. (5.5) that does not appear in Eq. (5.1). A related phenomenon causes the coherence lengths from the lowest sum frequencies, near 20 Hz, to be reduced due to the minimal frequency averaging available from Eq. (5.5b) in that sum frequency range.

For comparative purposes, an overview of coherence length results from several experiments is provided in Table 5.1. This summary highlights the variability in the environments, experiments, and geometries in which coherence length has been studied. As a result of this variation, measured coherence lengths differ substantially across these studies, from less than 10 wavelengths, to over 400. All of these results utilize sub-1 kHz signals and some utilize frequencies or frequency ranges that overlap with the frequency range considered in this study. Both shallow and deep ocean results are provided, typically using horizontal line arrays (HLAs). Several notable differences exist between these experiments and the COAST 2012 experiment inhibiting a direct comparison. First, the horizontal distance between the source and the receiving elements is generally much shorter in the COAST 2012 experiment, ranging from 277 m to over 8 km, while in the experiments summarized in Table 5.1, much larger ranges were often investigated. Second, no experiments summarized in this table were designed such that a

Table 5.1: Summary of coherence lengths from a collection of other studies.

Reference	L/λ	Frequency (Hz)	Source-receiver range(s) (km)	Water column depth	Notes
(Duda et al., 2012)	7-25	100	19	80 m	21 day time scale
	7-40	200	19	80 m	< 3 hour averaging
	10-15	224	30	80 m	Studied internal waves
	10-15	400	30	80 m	HLA – 465 m
(Carey, 1998)*	94-450	400	137-963	Deep Ocean	Up to 1200 m sensor separation
	60-127	323; 337	300-800	Deep Ocean	Moving array, 640 m aperture
	31-234	300-600	500	1.6-4 km	Collection of deep ocean basin results
	10-54	200-800	4-100	65-1000 m	Collection of shallow water experiments
COAST 2012	2-18	10-200	0.3-8	1900 m	8 km aperture
	5-30	1-190 (Δf)	0.3-8	1900 m	12.5 m element spacing
	8-30	20-400 (Σf)	0.3-8	1900 m	6 hour time scale

* This reference contained a summary of results from many experiments.

near-surface source was broadcasting sound towards the ocean floor to measure the reflected path, which is expected to have significant impact on coherence length results. Third, the COAST 2012 experiment utilized a towed array, meaning the physical location of each snapshot was different, which is only true for one of the referenced results in Table 5.1. Interestingly, even though these experiments differ substantially from COAST 2012, many of these studies provide coherence lengths of the same order as those obtained here, with the experimental and environmental differences likely accounting for much of the coherence length differences.

5.3.3 Extension to Matched Field Processing

MFP is a well-known array signal processing technique for remote unknown source localization that is beneficially impacted by increased coherence length. Thus, it was chosen to illustrate the extended coherence afforded by the autoproducts. The results provided in the prior subsections suggest that the autoproducts typically provide longer coherence lengths than in-band fields while also providing useful coherence at above- and below-band frequencies. Therefore, the autoproducts may also provide a way to improve signal processing outcomes at low-coherence and low-SNR frequencies within and outside the signal bandwidth. However, the COAST 2012 experiment was not designed as a spatial coherence or source localization experiment; thus, some adjustments to the standard MFP implementation are needed. Nevertheless, the results presented here illustrate the benefits of the greater coherence possible with the autoproducts, particularly outside of the ordinary field's bandwidth.

To properly implement MFP within the COAST 2012 experimental scenario, the replica weight vector specified in Eq. (5.8) and Eq. (5.9) must account for the bottom-reflected and bottom-surface-reflected arrivals as well as the endfire location of the source with respect to the nominally-straight and horizontal array. The weight vector used herein took the following form:

$$w_j(\boldsymbol{x},\omega) = \frac{e^{-\frac{i\omega R_{b,j}}{c}}}{R_{b,j}} \pm \frac{e^{-\frac{i\omega R_{s,j}}{c}}}{R_{s,j}}, \tag{5.11}$$

where $\boldsymbol{x}$ is the search coordinate in range from the endfire array, $R_{b,j}$ is the bottom-reflected distance at receiver $\boldsymbol{r_j}$ from a source at $\boldsymbol{x}$, $R_{s,j}$ is the bottom-surface-reflected distance at receiver $\boldsymbol{r_j}$ from a source at $\boldsymbol{x}$, and the negative (positive) surface reflection coefficient is chosen for in-band (out-of-band) MFP. Here, the reflected path distances are calculated by using the depth of the ocean at the location of the tow vessel which may not be the ocean depth where the acoustic reflection occurs, so Eq. (5.11) introduces some mismatch. The $1/R_{b,j}$ and $1/R_{s,j}$ amplitude factor specified in Eq. (5.11) could have been changed to $1/R_{b,j}^2$ and $1/R_{s,j}^2$ when correlating with the autoproducts to compensate for their quadratic nature, but this change was not made for simplicity.

The final adjustment made to the standard MFP processor is a coherent average over 5 pings. Hence, $\langle P_q(\boldsymbol{r_j},\omega)\rangle_{\text{Five-Pings}}$ replaces $P_q(\boldsymbol{r_j},\omega)$ in Eq. (5.8) and the reflected path distances in Eq. (5.11) are calculated from the average depth at tow vessel for the five pings. Equation (5.9) is adjusted identically for the frequency-difference and frequency-sum autoproducts. Although coherent ping-averaging is uncommon, its implementation here directly reflects the coherence formulation defined in Chapter 5.2.

The MFP plots for single frequencies utilize an illustrative set of 5 pings sampled throughout the duration of the transect: 271, 777, 872, 1065, 1183. The first set of results are for the in-band frequency of 80 Hz. At this frequency, 3 receivers reside within the coherence length of the genuine field. Meanwhile, 29 and 37 receivers reside within coherence lengths of the frequency-difference and frequency-sum autoproduct coherence lengths, respectively. MFP results are shown in Fig. 5.9(a) for the genuine field in black, the frequency-difference

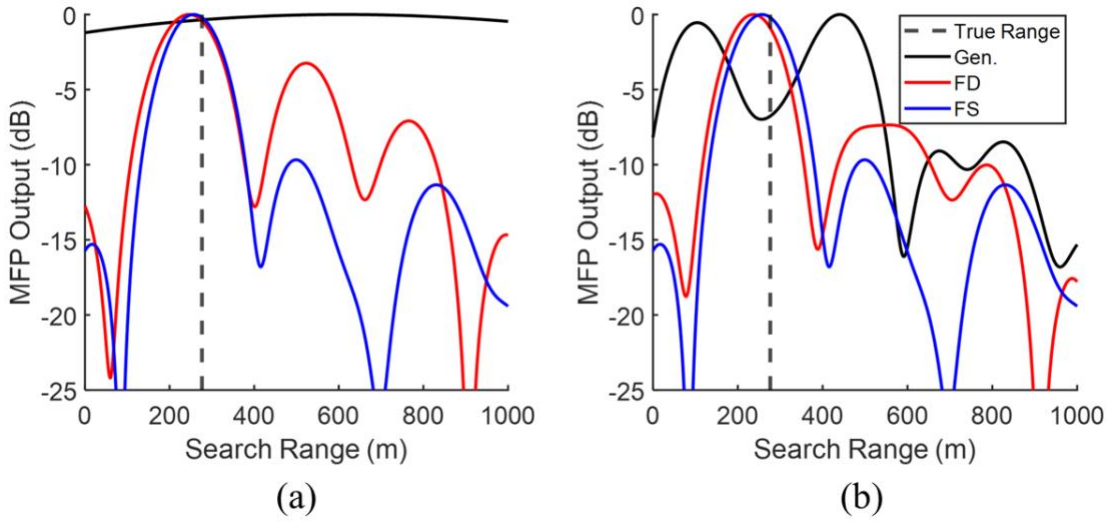

Figure 5.9: Matched-field processing results at 80 Hz for all three fields at the depth of the source along the line of the array. The genuine in-band field is shown in black, the frequency-difference autoproduct is shown in red, and the frequency-sum autoproduct is shown in blue. The vertical dashed black line indicates the true source range. (a) MFP calculations include receivers informed by each field's coherence length; (b) MFP calculations include receivers informed by the maximum coherence length.

autoproduct in red, and the frequency-sum autoproduct in blue. The plotted curves show the MFP output vs. search range (distance) at the depth of the source along the line of the array. The vertical dashed black line indicates the true source range. The results directly reflect the improved coherence of the autoproducts. Both the frequency-difference and frequency-sum approaches exhibit good source range estimation, whereas the 3-receiver-MFP approach of the in-band field is unable to confidently localize the source. Meanwhile, in Fig. 5.9(b), the number of receivers included in the calculation for each field is 37. As expected, increasing the number of receivers significantly beyond the genuine field's coherence length results in spurious peaks while the autoproduct-based results are largely unchanged.

The second set of MFP results are for frequencies below and above the signal bandwidth. Figure 5.10 shows frequency-difference MFP at 5 Hz and frequency-sum MFP at 315 Hz for the

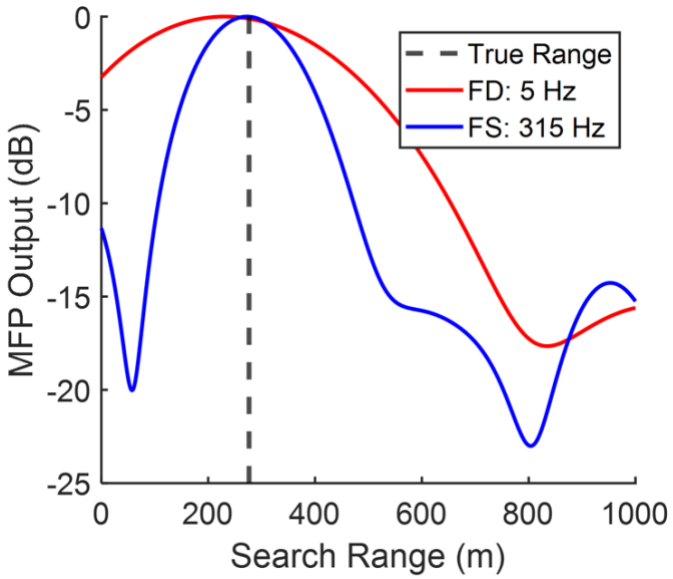

Figure 5.10: Matched-field processing results as in Fig. 5.9 for frequencies outside of the signal bandwidth. The vertical dashed black line indicates the true source range. The frequency-difference autoproduct at 5 Hz is shown in red, while the frequency-sum autoproduct at 315 Hz is shown in blue.

same set of pings. Both approaches exhibit good source range estimation, even though neither frequency was in the original broadcast signal's bandwidth. Further, the difference in the widths of the main lobes of each approach supports the unconventional claim that the frequency-difference and frequency-sum autoproducts are coherent at below and above band frequencies, respectively.

In-band, frequency-difference, and frequency-sum source range estimates were determined at each frequency by identifying the maximum MFP output across the search coordinates. Although there is 0.061 Hz frequency resolution in the experiment, only the closest resolved frequency to each integer frequency is considered for simplicity. This calculation was conducted for 100 randomly selected 5-ping-ensembles. Source range estimates within 100 m of the true target are deemed successful and the success fraction across the 100 trials is recorded in Fig. 5.11. Here, black dots indicate the in-band success fraction, red dots indicate the frequency-

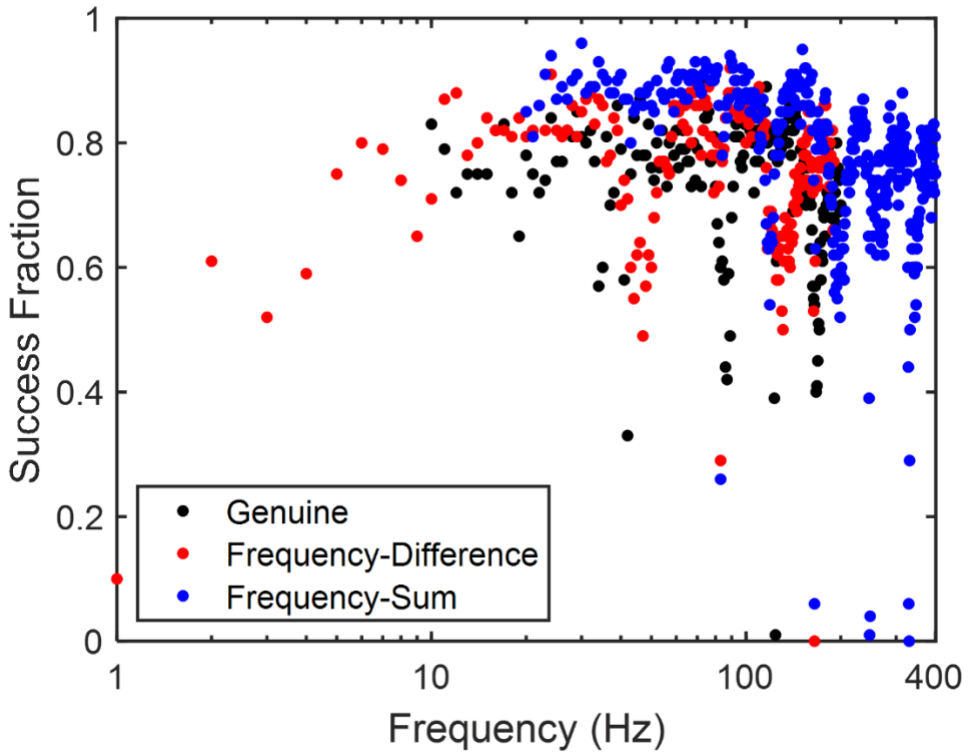

Figure 5.11: Source range estimation success fraction (across 100 trials) vs. frequency comparison for the genuine and autoproduct fields on logarithmic horizontal axes. Genuine acoustic field success fractions are indicated by black dots for f = 10-200 Hz while frequency-difference (-sum) coherence lengths are displayed in red (blue) for Δf = 1-190 Hz (Σf = 20-400 Hz).

difference success fraction, and blue dots indicate the frequency-sum success fraction. In all cases, the MFP calculations include receivers informed by the maximum coherence length across the three methods.

The complete results support the coherence length findings shown in Fig. 5.8. For the frequencies obtainable by all three methods (20 to 190 Hz), frequency-difference and in-band field approaches perform similarly, and frequency-sum outperforms them both. Within this frequency range, the frequency-difference autoproduct's average success fraction was 0.76, the genuine field's average success fraction was 0.74, and the frequency-sum autoproduct's average

success fraction was 0.84. Further, successful source range localization can be obtained at frequencies both below and above the signal bandwidth.

There exist a few unexpectedly low success fractions for the autoproducts in Fig. 5.11. The poor localization at 1 Hz is directly attributed to the large main lobe widths that results from processing at very low frequencies. Additionally, the destructive interference of upward- and downward-traveling sound at the depth of the receiving array is reflected in the dips of the various curves in Fig. 5.11, matching the coherence length dips in Fig. 5.8. Interestingly, a few blue and red dots with low success fraction occur at 80 and 160 Hz, frequencies of constructive interference for autoproducts. Since the autoproducts are coherent at these frequencies, poor localization success suggests that MFP processor could be improved by adjusting the weight vectors for autoproduct processing. Systematically altering the weight vectors is outside of the scope of the paper, but replica field adjustments have recently been done to improve performance in long range ocean source localization using autoproducts (Geroski and Dowling, 2019, 2021).

5.4 Discussion

Prior work has shown that autoproduct-based methods can be effective for mitigating array-signal-processing problems associated with array sparseness, unknown random scattering, and wavefront mismatch (Dowling, 2018). Given that such improvements require coherent fields, the goals of this investigation were to determine and compare the spatial coherences of the acoustic field, its frequency-difference autoproduct, and its frequency-sum autoproduct from ocean recordings collected on a north-to-south transect during the COAST 2012 experiment. In particular, this investigation considered 829 airgun pulses recorded by 624 receivers (nearly) uniformly spaced along an 8-km-long horizontal array towed at a depth of 9 m where the ocean

depth was approximately 1.9 km. Variations in water depth, surface reflections, and acoustic propagation along the 50-km-long tow path led to coherence loss between the first and any subsequent receiver along the array. The nominal frequency range of the airgun signals was 10 Hz to 200 Hz. Nevertheless, coherence results were obtained for frequencies from 1 Hz to 400 Hz, including a substantial range (20 to 190 Hz) where all three types of coherence and coherence lengths could be determined. The claims of coherence were then illustrated with a simple matched field processing approach to source range estimation.

The work presented here supports five conclusions. First, the frequency-difference autoproduct has substantial coherence at frequencies below the signal band, where signal energy is insignificant and noise dominates the recorded field. In the current investigation, the frequency-difference autoproduct provided coherence lengths of 5.4 to 30 difference frequency wavelengths, $\Delta\lambda$, for 1 Hz $\leq \Delta f \leq$ 190 Hz. Second, the frequency-sum autoproduct is similarly coherent at frequencies above the signal band and above the Nyquist frequency set by the sampling rate. In the current investigation, the frequency-sum autoproduct provided coherence lengths of 7.8 to 30 sum frequency wavelengths, $\Sigma\lambda$, for 20 Hz $\leq \Sigma f \leq$ 400 Hz. Third, destructive interference from surface reflections at the 9 m depth of the receiving array in the COAST 2012 experiment reduced coherence lengths for all three fields at predictable frequencies, but more modest coherence suppression occurred for the autoproducts. Fourth, the autoproducts maintain coherence at frequencies where the genuine field suffers from destructive interference and reduced coherence length. This happens because the quadratic nature of the autoproducts rectifies the ocean surface reflection coefficient so that the ocean surface appears as a rigid boundary, and this alters the autoproducts' interference pattern at the COAST 2012 receiver depth. However, to successfully localize in these interference patterns, an alternate

replica field scheme may be required in matched field applications. Fifth, and perhaps most important, the coherence lengths of the autoproducts are generally greater than that of the corresponding genuine acoustic field from which they are derived and can support coherent array signal processing. In this investigation, the frequency-averaged coherence lengths were 12.0, 16.7, and 17.6 wavelengths for the genuine field, frequency-difference autoproduct, and frequency-sum autoproduct, respectively. The increased coherence lengths possible with the autoproducts are believed to result from utilizing the full signal bandwidth for frequency averaging to produce each autoproduct sample prior to determining coherence.

Chapter 6

Cubic Extensions to Autoproduct Theory and the Utility of Cubic Frequency-Difference in Noisy Direction of Arrival Estimation

Autoproducts are quadratic products of acoustic fields that can mimic genuine fields at frequencies outside the recorded bandwidth. While the applications of autoproduct-based signal processing are substantial, the nonlinear construction of the autoproduct has been limited to quadratic order. This paper presents the cubic extension to autoproduct theory and emphasizes the cubic frequency-difference autoproduct, which mimics field content at frequencies within the recorded bandwidth. Field equations, originating from the inhomogeneous Helmholtz equation, and analytical results in single- and two-path environments justify the pseudofield interpretation and underscore the similarities to the quadratic autoproduct. For nonzero signal bandwidth, many frequency triplets satisfy the cubic autoproduct relationship. The serendipitous noise suppression therefore inherent in the bandwidth average is shown to facilitate significant phase structure recovery in free space simulations corrupted by Gaussian noise. Cubic autoproduct-based direction of arrival estimation in noisy environments is investigated using acoustic recordings and *in situ* noise measurements collected in the ocean. The cubic autoproduct results are generally more accurate, maintaining 60% success rate across the 160 snapshots until the signal-to-noise ratio (SNR) was -14 dB, while conventional processing crossed the 60% threshold at SNR of -9 dB. Similar improvements in peak-to-sidelobe ratio are discussed as well. The

following chapter is a near reproduction of an in-progress manuscript. For clarity, formulas and figures repeated elsewhere in this thesis are maintained in this section.

6.1 Introduction

There exists an increasing body of work on the frequency-difference and frequency-sum autoproducts (Dowling, 2018; Worthmann and Dowling, 2017), quadratic products of complex field amplitudes satisfying approximate Helmholtz wave mechanics at the difference and sum frequencies of the constituent fields. Some studies consider the autoproducts themselves, examining spatial cross correlations with genuine fields (Geroski et al., 2021; Lipa et al., 2018; Worthmann and Dowling, 2020b, 2020a) or exploring the coherence (Joslyn et al., 2022; Joslyn and Dowling, 2022), but most investigations focus on improved array signal processing performance in beamforming (Abadi et al., 2012; Douglass et al., 2017; Douglass and Dowling, 2019) and matched field processing (Geroski et al., 2023; Geroski and Dowling, 2019, 2021; Worthmann et al., 2017). Although the frequency-sum autoproduct provides increased resolution in remote sensing applications (Abadi et al., 2018), the robustness to mismatch offered by the frequency-difference autoproduct (Worthmann et al., 2015) has thus far been favored in sonar signal processing. Regardless of frequency-difference or frequency-sum, the emphasis of most studies is the quadratic autoproduct in acoustics. Some initial works (Dowling, 2018; Worthmann and Dowling, 2017) in the area, however, posited other autoproduct-based constructions, and while the domain has been expanded recently to include seismic waves (Neo et al., 2022) and electromagnetic simulations (Geroski, 2021), higher-order autoproducts are yet to be examined, apart from a preliminary investigation of fourth-order frequency-sum beamforming in underwater acoustics (Abadi et al., 2013).

This chapter presents the mathematical formulation of cubic autoproducts and investigates the remote sensing benefits of the cubic frequency-difference autoproduct in low signal-to-noise ratio (SNR) environments. Unlike previous autoproduct constructions, the cubic frequency-difference autoproduct synthetically estimates field content at frequencies within the bandwidth of the constituent field. Discussion of cubic frequency-sum and higher-order autoproducts accompanies the analytical development of the cubic frequency-difference autoproduct, including derivations of the governing field equations and genuine acoustic field mimicry in simple environments. Owing to the many different combinations of constituent field frequencies satisfying the cubic frequency-difference autoproduct relationship, the bandwidth-averaging step may provide an unconventional approach to reducing noise. This fortuitous noise suppression mechanism was explored both numerically and experimentally. In simulation, free space fields were contaminated with Gaussian noise, and in experiment, *in situ* noise measurements were added to the ocean acoustic recordings. Results from both simulation and experiment support the ability of the cubic frequency-difference autoproduct to significantly suppress noise.

Remote sensing performance of the cubic frequency-difference autoproduct is primarily assessed with ocean measurements from the Shallow Water ’06 (Tang et al., 2007) experiment in the Atlantic Ocean. Obtained off the coast of New Jersey along a vertical line array in August 2006, the data studied here has been examined in several previous works. The spatial coherence of high frequency surface scattering was the subject of several of these studies (Dahl, 2010; Dahl et al., 2013; Welton, 2015), as well as bubble-based attenuation in moderate to high frequencies (Dahl et al., 2008) and the frequency-difference autoproduct in rough surface scattering (Joslyn et al., 2023). Although the experiment was designed to target surface-scattering physics, not

remote sensing capabilities, the temporal separation between propagation paths and the 160 snapshots allowed for an effective beamforming scenario. Single snapshot direction of arrival finding of the direct path was computed by both conventional and cubic autoproduct-based plane-wave beamforming for SNR between –25 to 10 dB. Independent measurements of *in situ* noise were made after each broadcast pulse, allowing for manual adjustment of the ambient ocean noise power. While potentially important in remote sensing applications and available in the time domain recordings, multipath effects and surface/bottom scattering are not considered here for brevity.

The benefit of quadratic autoproduct-based processing is attributed to the manufacturing of out-of-band information from a band-limited signal when lower or higher frequencies may offer advantageous information. Interestingly, the cubic frequency-difference autoproduct generates cubic difference frequencies within the original bandwidth. Use of this synthetically-constructed pseudofield then may appear entirely academic. However, as shown here, the bandwidth average suppresses noise, thereby improving remote sensing outcomes. Additionally, the information provided by the cubic autoproduct, just like its quadratic counterpart, is complementary to the original recordings. No additional data acquisition effort is required, as the construction of the cubic frequency-difference autoproduct occurs in the post-recording signal processing, using only a digital Fourier transform and multiplication.

Third-order moments of a recorded field are not especially common, particularly in underwater acoustics where the second (intensity) and fourth (scintillation index) moments command more attention [see, for instance, the recent work done in the Beaufort Sea (Kucukosmanoglu et al., 2022)]. The triple autocorrelation function and the bispectrum, by Fourier transform (Lohmann and Wirnitzer, 1984), are the most notable cubic products of a

recorded field. Since the bispectrum of a Gaussian process is zero, it has been employed for signal detection in underwater acoustics (Morelia, 1994; Richardson and Hodgkiss, 1994). The bispectrum can also be used to identify phase coupling between frequency components. Bispectrum detectors have been implemented in underwater acoustics (Richardson and Hodgkiss, 1994), ocean wave analysis (Hasselmann et al., 1963), and astronomical turbulence studies of the interstellar medium (O'Brien et al., 2022). Just as the quadratic autoproducts are reminiscent of other second-order signal processing methods (Dowling, 2018; Geroski and Worthmann, 2021; Worthmann and Dowling, 2017), the cubic frequency-difference autoproduct does share some features with the bispectrum, particularly the triplet frequency dependence. Importantly, though, the cubic autoproduct was developed as a logical extension of the quadratic autoproduct, not as a generalization and reinterpretation of a third-order correlation function. Further, similar to its quadratic counterpart, and unlike better-known third-order moments, the cubic frequency-difference autoproduct does not require an ensemble average, utilizes a unique bandwidth average of frequency triplets, and may under appropriate circumstances mimic a genuine acoustic field at the cubic autoproduct difference frequency.

The remainder of this chapter is organized as follows. Section 6.2 details the mathematical formulations of cubic autoproducts, including their governing field equations and analytical results in a uniform half-space. Section 6.3 presents an explicit formula to compute the number of cubic autoproduct samples within a discretized signal bandwidth and discusses the impact on noise suppression in a free space environment. Section 6.4 investigates the unexpected remote sensing benefits offered by the cubic frequency-difference autoproduct with noisy recordings obtained in the ocean during Shallow Water '06. Section 6.5 summarizes the work and provides three conclusions.

6.2 Cubic Autoproduct Theory

6.2.1 Definition and Field Equation

The natural starting point for frequency domain analysis is the inhomogeneous Helmholtz equation with a single point source. The Fourier transform of the signal is $S(\omega)$ and c is the sound speed of the isospeed medium:

$$\left(\nabla^2 + \frac{\omega^2}{c^2}\right) P(\boldsymbol{r},\, \omega) = -S(\omega)\delta(\boldsymbol{r} - \boldsymbol{r_s}), \tag{6.1}$$

where $P(\boldsymbol{r}, \omega)$ defines the complex pressure field at angular frequency ω and spatial coordinate $\boldsymbol{r}$. The source location is at $\boldsymbol{r_s}$ and the bandwidth of the source spectrum is $\Omega_L \leq \omega \leq \Omega_H$.

The cubic frequency-difference autoproduct is generated from a cubic product of complex pressure field amplitudes, with one conjugated field factor:

$$AP_{III}(\boldsymbol{r}, \omega_1, \omega_2, \Delta\omega) = P(\boldsymbol{r}, \omega_1)P(\boldsymbol{r}, \omega_2)P^*(\boldsymbol{r}, \omega_3) = P_1 P_2 P_3^*, \tag{6.2}$$

where the cubic difference frequency, $\Delta\omega = \omega_1 + \omega_2 - \omega_3$, ranges from $\max[0, 2\Omega_L - \Omega_H] \leq \Delta\omega \leq 2\Omega_H - \Omega_L$. The constituent field frequencies lie within the signal bandwidth and are defined by the triplet $\omega_1 = \omega - \Delta\omega_1/2$, $\omega_2 = \omega + \Delta\omega_1/2$, and $\omega_3 = 2\omega - \Delta\omega$. The final equality is Eq. (6.2) denotes a notation for clarity where subscripts indicate frequency components. The cubic difference frequency range encompasses the entire signal bandwidth and thus, the cubic frequency-difference autoproduct may be processed for remote sensing tasks at the broadcast frequencies. Such is the most interesting consequence of the cubic frequency-difference autoproduct, and the cubic difference frequency range is set to $\Omega_L \leq \Delta\omega \leq \Omega_H$ herein. Note, if $\Delta\omega = 0$, such that the triplet is defined by $\omega_3 = \omega_1 + \omega_2$, Eq. (6.2) defines a single sample of the bispectrum at ω_1 and ω_2, which is then used in an ensemble average to estimate the bispectrum (Richardson and Hodgkiss, 1994).

The field equation governing the cubic frequency-difference autoproduct may be formed from Eqs. (6.1) and (6.2). Begin with Eq. (6.1) evaluated at ω_1, ω_2, and ω_3 with a complex conjugation, cross-multiply by the P-fields from the other two equations and add all three equations together:

$$P_2P_3^*\nabla^2P_1 + P_1P_3^*\nabla^2P_2 + P_1P_2\nabla^2P_3^* + \left(\frac{\omega_1^2 + \omega_2^2 + \omega_3^2}{c^2}\right)P_1P_2P_3^* \tag{6.3}$$

$$= -(P_2P_3^*S_1 + P_1P_3^*S_2 + P_1P_2S_3^*)\delta(\boldsymbol{r} - \boldsymbol{r_s}).$$

From the vector calculus identity, $\nabla^2(P_1P_2P_3^*) = P_2P_3^*\nabla^2P_1 + P_1P_3^*\nabla^2P_2 + P_1P_2\nabla^2P_3^* + 2[P_1(\nabla P_2 \cdot \nabla P_3^*) + P_2(\nabla P_1 \cdot \nabla P_3^*) + P_3^*(\nabla P_1 \cdot \nabla P_2)]$, and setting $\Delta k = \Delta\omega/c$, $\Delta k_1 = \Delta\omega_1/c$, and $k = \omega/c$, rearrangement of terms in Eq. (6.3) yields the field equation for the cubic frequency-difference autoproduct:

$$(\nabla^2 + (\Delta k)^2)(P_1P_2P_3^*) = -(P_2P_3^*S_1 + P_1P_3^*S_2 + P_1P_2S_3^*)\delta(\boldsymbol{r} - \boldsymbol{r_s}) \tag{6.4}$$

$$+2\left[P_1(\nabla P_2 \cdot \nabla P_3^*) + P_2(\nabla P_1 \cdot \nabla P_3^*) + P_3^*(\nabla P_1 \cdot \nabla P_2) + \left(2k\Delta k - 3k^2 - \frac{(\Delta k_1)^2}{4}\right)P_1P_2P_3^*\right].$$

Hence, the cubic frequency-difference autoproduct, $AP_{III}(\boldsymbol{r}, \omega_1, \omega_2, \Delta\omega) = P_1P_2P_3^*$ abides by an inhomogeneous Helmholtz equation when the terms in the square brackets are 0. The linear Helmholtz operator at the cubic difference frequency acts on the cubic frequency-difference autoproduct on the left side of Eq. (6.4) and on the right side is a source term and a cross term in square brackets, where the relative amplitude of the cross term will control the autoproduct mimicry of the genuine acoustic field at the difference frequency. A field equation analogous to Eq. (6.4) was derived previously for the quadratic autoproducts (Worthmann and Dowling, 2017). Continuing the analogue with that work (Worthmann and Dowling, 2017), it is illustrative to consider the field equation for the two simplest propagating waves: plane and spherical.

For a plane wave complex pressure field given by $P = A\exp[ik\hat{\boldsymbol{s}}\cdot\boldsymbol{r}]$, where $\hat{\boldsymbol{s}}$ is the unit vector in the propagation direction, the bracketed term on the right side of Eq. (6.4) can be found simply. Using $\nabla P = ik\hat{\boldsymbol{s}}P$,

$$P_1(\nabla P_2\cdot\nabla P_3^*)+P_2(\nabla P_1\cdot\nabla P_3^*)+P_3^*(\nabla P_1\cdot\nabla P_2)=\left(-2k\Delta k+3k^2+\frac{(\Delta k_1)^2}{4}\right)P_1P_2P_3^*, \quad (6.5)$$

and the bracketed term in Eq. (6.4) is identically 0. Thus, in scenarios where the received pressure field is adequately modeled by a plane wave, the cubic frequency-difference autoproduct is a solution to the Helmholtz equation at the cubic difference frequency,

$$(\nabla^2+(\Delta k)^2)(P_1P_2P_3^*)=0. \quad (6.6)$$

Finally, consider the spherical waves emanating from a point source: $P = (A/r)\exp[ikr]$. Evaluation of Eq. (6.4) for the point source response ($r \neq 0$) yields

$$(\nabla^2+(\Delta k)^2)(P_1P_2P_3^*)=(\Delta k)^2\left(\frac{6}{(\Delta kr)^2}-\frac{4i}{\Delta kr}\right)(P_1P_2P_3^*). \quad (6.7)$$

When $\Delta kr \gg 1$, the contributions of the right-hand side of Eq. (6.4) become negligible, and the cubic frequency-difference autoproduct ought to mimic a genuine acoustic field. This is not unexpected given the similarity of spherical waves and plane waves at large distances. Eqs. (6.6) and (6.7) are analogous to the results derived for the quadratic autoproduct (Worthmann and Dowling, 2017).

These analytic findings are also demonstrated by directly applying Eq. (6.2) to plane waves:

$$AP_{III}(\boldsymbol{r},\omega_1,\omega_2,\Delta\omega)=P_1P_2P_3^*=A_1A_2A_3^*\exp[i\Delta k\hat{\boldsymbol{s}}\cdot\boldsymbol{r}], \quad (6.8a)$$

and spherical waves:

$$AP_{III}(\boldsymbol{r},\omega_1,\omega_2,\Delta\omega)=P_1P_2P_3^*=\left(\frac{A_1A_2A_3^*}{r^3}\right)\exp[i\Delta kr]. \quad (6.8b)$$

It is clear that Eq. (6.8a) is an exact solution to the Helmholtz equation at the cubic difference frequency, and that the non-vanishing right side of Eq. (6.7) comes from the $1/r^3$ amplitude in Eq. (6.8b). The amplitude dependence on the cubic power of the radial coordinate is expected from the nonlinear construction of the cubic frequency-difference autoproduct. The limitations associated with the $1/r^2$ amplitude dependence of quadratic autoproducts are well-understood (Lipa et al., 2018; Worthmann and Dowling, 2017) and are amplified for the cubic autoproduct.

6.2.2 Bandwidth Average

For a source with nonzero signal bandwidth, multiple frequency triplets may satisfy $\omega_1 + \omega_2 - \omega_3 = \Delta\omega$. To accommodate all such combinations, the cubic frequency-difference autoproduct sample defined in Eq. (6.2) must be averaged through the signal bandwidth by the following double integration:

$$\langle AP_{III}(\boldsymbol{r}, \Delta\omega)\rangle_{BW} = \frac{1}{\beta_H^{\Delta} - \beta_L^{\Delta}} \int_{\beta_L^{\Delta}}^{\beta_H^{\Delta}} d(\omega) \left[\frac{1}{\alpha_{BW}^{\Delta}} \int_0^{\alpha_{BW}^{\Delta}} \frac{AP_{III}(\boldsymbol{r}, \omega_1, \omega_2, \Delta\omega)}{S(\omega_1)S(\omega_2)S^*(\omega_3)} d(\Delta\omega_1) \right]. \qquad (6.9)$$

Here, the inner limit of integration $\alpha_{BW}^{\Delta} = \min[2\omega - 2\Omega_L,\ 2\Omega_H - 2\omega]$ and the outer limits of integration are $\beta_L^{\Delta} = \max[\Omega_L,\ (\Omega_L + \Delta\omega)/2]$ and $\beta_H^{\Delta} = \min[\Omega_H,\ (\Omega_H + \Delta\omega)/2]$. For the cubic difference frequency range studied here, $\Omega_L \leq \Delta\omega \leq \Omega_H$, $\beta_{L,H}^{\Delta}$ take the second values of their argument. The dependence on source characteristics is removed by the divisor in the integrand, which is of some consequence in passive remote sensing applications where the source spectrum may not be known a priori. Bandwidth-averaging of quadratic autoproducts requires a single integration and suppresses cross terms in multipath environments, thereby improving autoproduct mimicry of genuine fields (Lipa et al., 2018; Worthmann and Dowling, 2017). Further, even without multipath, the bandwidth average increases robustness of the

autoproduct (Joslyn et al., 2023). Similar benefits are expected here for the cubic frequency-difference autoproduct.

The double integration defined in Eq. (6.9) is a combination of quadratic-type bandwidth-averaging integrals. The inner integration averages all pairs $\omega_1 + \omega_2 = 2\omega$, like a frequency-sum bandwidth average, for the ω_3 defined by the outer integral, like a frequency-difference bandwidth average. The selection of appropriate frequency triplets is shown schematically in Fig. 6.1(a), with blue and red showing the inner and outer integration steps, respectively. In Fig. 6.1(b), the number of frequency triplets available to average is illustrated for an arbitrary signal bandwidth (see Chapter 6.3). The horizontal axis encompasses all available cubic difference frequencies, while the shaded region highlights cubic difference frequencies that lie within the original bandwidth.

Hence, Eqs. (6.2) and (6.9) define the cubic extension to the frequency-difference autoproduct. The cubic frequency-difference autoproduct mimics a genuine acoustic field at the

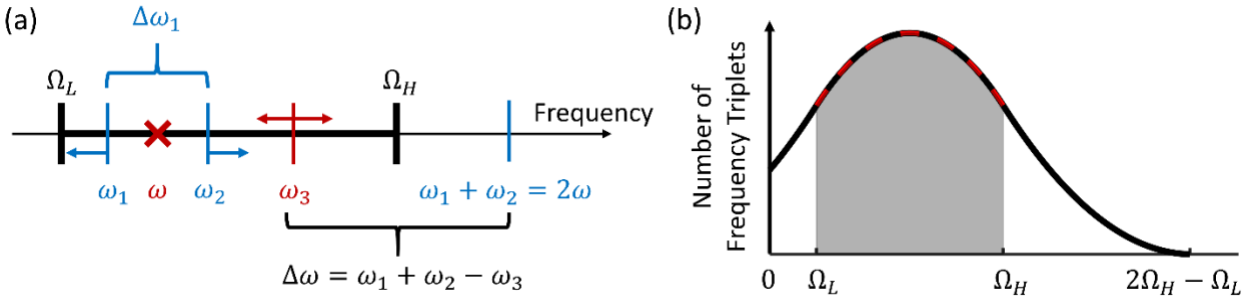

Figure 6.1: Representation of the bandwidth-averaging step of the cubic frequency-difference autoproduct. (a) On the frequency axis in black, the inner (blue) and outer (red) integrations of Eq. (6.9) are shown schematically by arrows of the corresponding color. By increasing the separation between ω_1 and ω_2 or by an overall shift on ω_3, all frequency triplets appropriately summing to the cubic difference frequency are averaged. (b) The relative number of frequency triplets for an arbitrary bandwidth. All possible cubic difference frequencies are shown by the solid black curve and the shaded gray region highlights cubic difference frequencies within the signal bandwidth. Red dashes indicate computation of triplets using Eq. (6.14) from the analytical approach of Chapter 6.3.

cubic difference frequency, which lies within the broadcast bandwidth, but the mimicry is limited by the field equation derived in Eq. (6.4). Additionally, the large number of triplets available to bandwidth average may provide remote sensing benefits unique to the cubic frequency-difference autoproduct and will be investigated in Chapter 6.3 and Chapter 6.4.

6.2.3 Cubic Frequency-Difference Autoproduct in a Lloyd's Mirror Environment

The simplest multipath environment to assess the cubic frequency-difference autoproduct is the uniform half-space with a constant reflection coefficient at the surface. Lloyd's mirror was used previously to quantify quadratic autoproduct mimicry of genuine acoustic fields, and thus is a good comparison for the work here (Lipa et al., 2018). The theoretical Green's function is

$$G(\boldsymbol{r},\omega) = \frac{P(\boldsymbol{r},\omega)}{S(\omega)} = \frac{e^{i\omega\tau_1}}{r_1} - \frac{e^{i\omega\tau_2}}{r_2}, \tag{6.10}$$

where $r_{1,2}$ are the direct and reflected path distances and $\tau_{1,2} = r_{1,2}/c$. The constant reflection coefficient of –1 for the water-air interface is the coefficient of the second term.

Using Eqs. (6.2) and (6.10), a single cubic frequency-difference autoproduct sample is formed:

$$\begin{aligned} AP_{III}(\boldsymbol{r},\omega_1,\omega_2,\Delta\omega) &= \frac{e^{i\Delta\omega\tau_1}}{r_1^3} - \frac{e^{i\Delta\omega\tau_2}}{r_2^3} \\ &- \frac{1}{r_1^2 r_2}\left[e^{-2i\omega\Delta\tau}e^{i\Delta\omega\tau_2} + 2e^{i\omega\Delta\tau}e^{i\Delta\omega\tau_1}\cos\left(\frac{\Delta\omega_1\Delta\tau}{2}\right)\right] \\ &+ \frac{1}{r_1 r_2^2}\left[e^{2i\omega\Delta\tau}e^{i\Delta\omega\tau_1} + 2e^{-i\omega\Delta\tau}e^{i\Delta\omega\tau_2}\cos\left(\frac{\Delta\omega_1\Delta\tau}{2}\right)\right], \end{aligned} \tag{6.11}$$

where $\Delta\tau = \tau_2 - \tau_1$. The cubic autoproduct sample in Eq. (6.11) exhibits two notable features. First is the presence of both self and cross terms. The first two terms are the self terms which, aside from a modified power in the denominator, match the Green's function in Eq. (6.10) at the

cubic difference frequency. Hence, the self terms should correlate well with a genuine acoustic field. Second, an altered reflection coefficient, i.e. $|\mathcal{R}|^2$, is a common consideration of the quadratic frequency-difference autoproduct. For the cubic version, the modified reflection coefficient is $\mathcal{R}|\mathcal{R}|^2$, which in the case of Lloyd's mirror is equivalent to the genuine reflection coefficient of –1.

The cross terms in the square brackets of Eq. (6.11) limit the mimicry of a genuine acoustic field, but can be mitigated through a bandwidth average of cubic autoproduct samples. To suppress the cross-term impact, substitute Eq. (6.11) into Eq. (6.9). After some effort, for $\Omega_L \leq \Delta\omega \leq \Omega_H$:

$$\langle AP_{III}(\boldsymbol{r}, \Delta\omega)\rangle_{BW} = \frac{e^{i\Delta\omega\tau_1}}{r_1^3} - \frac{e^{i\Delta\omega\tau_2}}{r_2^3} + \frac{1}{\left(\beta_H^{\Delta} - \beta_L^{\Delta}\right)\Delta\tau}\left[\frac{\gamma_1}{r_1^2 r_2} + \frac{\gamma_2}{r_1 r_2^2}\right]. \tag{6.12}$$

Here, γ_1 and γ_2 are the cross terms contributions, each consisting of 8 terms, 6 of which asymptotically tend to zero for a large signal bandwidth. Explicit enumeration of γ_1 and γ_2 are provided in the Appendix, as well as a brief summary of the algebraic derivation of Eq. (6.12). The coefficient of the square bracket indicates a large signal bandwidth, by $\left(\beta_H^{\Delta} - \beta_L^{\Delta}\right)$, or a large difference in arrival times, by $\Delta\tau$, minimizes the cross-term contributions. Significant bandwidth size and temporal separation of arrivals were necessary for the quadratic autoproduct to mimic a genuine acoustic field (Lipa et al., 2018), but given the third-order nature of the nonlinearity here, the cross terms are more consequential for the cubic autoproduct. However, given a sufficiently large signal bandwidth, Eq. (6.12) may correlate well with Eq. (6.10) evaluated at the difference frequency.

To visualize and quantitatively assess the cubic frequency-difference autoproduct, Eq. (6.12) was compared to Eq. (6.10). The geometry, schematically detailed in Fig. 6.2(a), was selected to nominally reflect the Lloyd's mirror laboratory study (Lipa et al., 2018) of quadratic

autoproducts. The source was located 20 cm below the pressure-release surface and the receivers, at range 50 cm, sampled 40 cm in depth, with 1 mm spacing. The frequency bandwidth was bounded by $\Omega_L = 40$ kHz and $\Omega_H = 110$ kHz, and the cubic difference frequency was $\Delta\omega = 75$ kHz. To assess a different propagation scenario and to test the suppression of cross terms from bandwidth-averaging, an additional geometry and a larger signal bandwidth were investigated as well. The altered geometry, with increased source and receiver depths and greater receiver range, is indicated in blue in Fig. 6.2(a), and the expanded signal bandwidth set $\Omega_L = 20$ kHz and $\Omega_H = 250$ kHz.

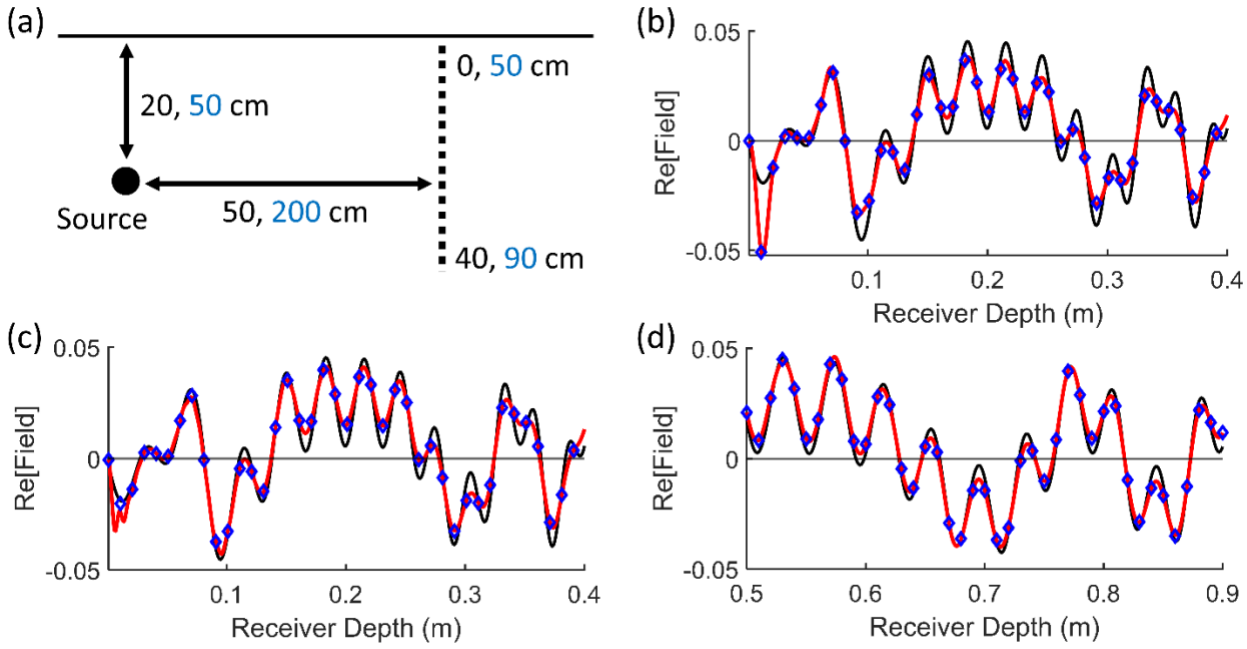

Figure 6.2: Comparisons of theoretical cubic frequency-difference autoproducts and genuine acoustic fields at the cubic difference frequency. Genuine acoustic field Green's functions are shown in black, the theoretical bandwidth-averaged autoproduct is shown in red, and discrete evaluation of cubic autoproducts are marked in blue. (a) The geometry for panels (b) and (c) is shown in black, and the geometry for panel (d) is shown in blue. The bandwidth for panels (b) and (d) is 40 – 110 kHz and panel (c) uses 20 – 250 kHz bandwidth. All field plots are normalized and computed for 75 kHz.

Panels (b) – (d) of Fig. 6.2 compare bandwidth-averaged cubic autoproducts from Eq. (6.12) to Green's functions of the acoustic field from Eq. (6.10), both at 75 kHz. Panel (b) was created from the nominal geometry and signal bandwidth, panel (c) utilized a larger signal bandwidth with the original geometry, and panel (d) used the original signal bandwidth with the altered geometry. In Fig. 6.2(b) – (d), the real component of genuine acoustic fields, computed from Eq. (6.10) at $f = 75$ kHz, are shown with a solid black curve and the real component of theoretical bandwidth-averaged cubic frequency-difference autoproducts, computed from Eq. (6.12) at Δf = 75 kHz, are shown in red. Blue diamonds, providing a direct assessment of the analytic derivation of Eq. (6.12) from Eqs. (6.9) and (6.11), denote simulated cubic frequency-difference autoproducts generated from discrete evaluation of Eqs. (6.2), (6.9), and (6.10). Discrete evaluation of Eq. (6.10) was computed every 1 kHz and sampled every 1 cm in depth. A normalization strategy, as outlined in (Lipa et al., 2018) was implemented to facilitate comparison between fields with different units.

The excellent agreement exhibited between the black and red curves in Fig. 6.2(b) – (d) verifies the mimicry of genuine acoustic fields possible from the cubic frequency-difference autoproduct. Furthermore, the discrepancies between the curves are well-explained from the aforementioned autoproduct considerations. In panel (b), the most glaring difference occurs near the surface, where arrival times between the two paths are very close, and while some discrepancies persist in panel (c), the larger signal bandwidth resolves much of the difference. Finally, in panel (d), the greater depths and longer ranges alleviated $\Delta\tau$ and $1/r^3$ concerns, respectively, leading to a good match of fields.

The mimicry of genuine acoustic fields can be explicitly quantified by a spatial cross correlation, χ [for instance, see (Lipa et al., 2018)]. Values of the spatial cross correlation

coefficient near 1 (0) represent well-correlated (poorly-correlated) fields and the imaginary component captures any phase shifts between fields. The spatial cross correlations between theoretical cubic frequency-difference autoproducts and genuine acoustic fields were 0.91 (b), 0.97 (c), and 0.99 (d), with negligible imaginary components in each case. The increased cross correlation value between Fig. 6.2(b) and Fig. 6.2(c) underscores the importance of a large signal bandwidth for genuine acoustic field mimicry, and the nearly perfect cross correlation in Fig. 6.2(d) highlights the mimicry possible in judicious propagation scenarios. In all cases, the spatial cross correlation between theoretical and simulated cubic autoproducts was $\chi = 1 + 0i$ to three decimal places, confirming the accuracy of the analytical derivation of Eq. (6.12).

The presence of reflecting boundaries and multipath arrivals limit quadratic autoproduct-based mimicry of genuine acoustic fields, and while the same concerns exist for the cubic construction, mimicry is still possible through bandwidth-averaging. Although accounting for more complicated multipath is clearly possible, it is not pursued here, and given the complexity of the uniform half-space results, theoretical treatment of more complicated environments may be prohibitive. Regardless of tractability, the analytical form of Eq. (6.12), indicating a large signal bandwidth or significant arrival time difference enhances acoustic field mimicry, and the practical utility of the quadratic autoproduct, whose field mimicry depends on the same two features, suggests that the cubic frequency-difference autoproduct may provide remote sensing benefits in scenarios beyond the single-path environments considered herein.

6.2.4 Other Autoproduct Constructs

Although potential remote sensing benefits of the cubic frequency-difference autoproduct are the primary focus herein, other extensions to conventional autoproduct theory are readily available.

Two other third-order autoproducts can be constructed, corresponding to differing numbers of conjugated field factors, and higher-than-cubic order autoproducts can also be formed.

Another type of cubic frequency-difference autoproduct, utilizing two conjugated field factors, exists but is of little practical utility. The synthetically-generated frequency content ranges between $(0, \max[0, \Omega_H - 2\Omega_L])$, which may be trivial in many narrow-bandwidth practical scenarios. Furthermore, the quadratic frequency-difference autoproduct will always superset the same difference frequencies, and owing to its merely second-order nonlinearity, will likely be more advantageous in signal processing tasks.

The cubic frequency-sum autoproduct is constructed from Eq. (6.2) with no conjugated constituent fields. The generated sum frequencies, $\Sigma\omega$, range from $3\Omega_L \leq \Sigma\omega \leq 3\Omega_H$, which may be of interest in array signal processing, owing to the higher resolution offered at higher frequencies. Equivalent results to those derived in Chapter 6.2.1 and Chapter 6.2.2 for a cubic frequency-sum autoproduct are provided here. The cubic frequency-sum autoproduct sample is defined as

$$AP_{III\Sigma}(\boldsymbol{r}, \omega_I, \omega_{II}, \Sigma\omega) = P_I P_{II} P_{III}, \tag{6.13a}$$

where $\omega_I = \omega - \Delta\omega_2 - \Delta\omega_3$, $\omega_{II} = \omega + \Delta\omega_2$, $\omega_{III} = \omega + \Delta\omega_3$, and $\Sigma\omega = 3\omega$, and numeral subscripts were used to differentiate from the cubic frequency-difference autoproduct development. The cubic frequency-sum bandwidth average is, therefore,

$$\langle AP_{III\Sigma}(\boldsymbol{r}, \Sigma\omega)\rangle_{BW} = \frac{1}{\beta_H^\Sigma}\int_0^{\beta_H^\Sigma} d(\Delta\omega_3)\left[\frac{1}{\alpha_H^\Sigma - \alpha_L^\Sigma}\int_{\alpha_L^\Sigma}^{\alpha_H^\Sigma} \frac{AP_{III\Sigma}(\boldsymbol{r}, \omega_I, \omega_{II}, \Sigma\omega)}{S(\omega_I)S(\omega_{II})S(\omega_{III})}\, d(\Delta\omega_2)\right], \tag{6.13b}$$

where $\alpha_L^\Sigma = -\Delta\omega_3/2$, $\alpha_H^\Sigma = \min[\Delta\omega_3, \Sigma\omega/3 - \Omega_L - \Delta\omega_3]$, and $\beta_H^\Sigma = \min[\Omega_H - \Sigma\omega/3, 2(\Sigma\omega/3 - \Omega_L)]$.

The field equation governing the cubic frequency-sum autoproduct, derived equivalently to Eq. (6.4), is

$$(\nabla^2 + (\Sigma k)^2)[P_I P_{II} P_{III}] = -(P_{II}P_{III}S_I + P_I P_{III}S_{II} + P_I P_{II}S_{III})\delta(\boldsymbol{r} - \boldsymbol{r_s}) \qquad (6.13c)$$
$$+2[P_I(\nabla P_{II} \cdot \nabla P_{III}) + P_{II}(\nabla P_I \cdot \nabla P_{III}) + P_{III}(\nabla P_I \cdot \nabla P_{II})$$
$$+ (3k^2 - \Delta k_2 \Delta k_3 - (\Delta k_2)^2 - (\Delta k_3)^2) P_I P_{II} P_{III}],$$

where $\Sigma k = \Sigma\omega/c$, $\Delta k_{2,3} = \Delta\omega_{2,3}/c$. Hence, like the cubic frequency-difference autoproduct, the cubic frequency-sum autoproduct is an exact solution of a Helmholtz equation at the sum frequency, $\Sigma\omega$, when the quantity in square brackets is zero. Under assumption of plane wave pressure fields, this happens identically as

$$P_I(\nabla P_{II} \cdot \nabla P_{III}) + P_{II}(\nabla P_I \cdot \nabla P_{III}) + P_{III}(\nabla P_I \cdot \nabla P_{II}) \qquad (6.13d)$$
$$= -(3k^2 - \Delta k_2 \Delta k_3 - [\Delta k_2]^2 - [\Delta k_3]^2) P_I P_{II} P_{III}.$$

For a spherical wave response, Eq. (6.13c) reduces to:

$$(\nabla^2 + (\Sigma k)^2)(P_I P_{II} P_{III}) = (\Sigma k)^2 \left\{\frac{6}{(\Sigma kr)^2} - \frac{4i}{\Sigma kr}\right\}(P_I P_{II} P_{III}). \qquad (6.13e)$$

which matches Eq. (6.7) for the sum frequency. When $\Sigma kr \gg 1$, the contributions of the right-hand side of Eq. (6.13e) are minimized, and the cubic frequency-sum autoproduct should correlate well with a genuine acoustic field at the cubic sum frequency. The matching of frequency-sum and frequency-difference field equations for spherical wave pressure fields was found for quadratic autoproducts as well (Worthmann and Dowling, 2017).

Higher-order autoproducts (i.e. quartic or greater) are clearly possible, but analytic prescription of their formulation is rather cumbersome, and as a result, provides little benefit. Given the abundance of programming languages with functions that rapidly identify all desired combinations of a set, investigation of quartic-or-higher autoproducts should be pursued numerically. However, some guiding intuition is available. The N-th order frequency-sum

autoproduct samples will target sum frequencies between $N\Omega_L$ and $N\Omega_H$, as noted for fourth order (Abadi et al., 2013). Interestingly, $N-1$ versions of N-th order frequency-difference autoproducts are possible, depending on the number of conjugated field factors. As noted for the cubic frequency-difference autoproduct with two conjugations, though, higher-than-cubic-order frequency-difference autoproducts may not find much use in practice, as their difference frequency range overlaps, or entirely subsets, lower-order frequency-difference autoproduct ranges. Finally, the negative impacts of cross terms associated with the quadratic autoproduct (Geroski and Worthmann, 2021; Lipa et al., 2018; Worthmann and Dowling, 2017) are exacerbated for higher-order autoproducts and may entirely restrict the utility of nonlinear constructions beyond the cubic order studied here.

Further examination of higher-order autoproducts is beyond the scope of this work. Herein, the potential remote sensing benefits of the cubic frequency-difference autoproduct with a single conjugated factor are investigated. For compactness, cubic autoproduct and cubic difference frequency are used in lieu of the full terminology: cubic frequency-difference autoproduct with one conjugation and its associated difference frequency.

6.3 Noise Suppression

The previous section largely considered the mathematical apparatus and pseudofield nature of the cubic autoproduct. To illustrate the potential utility of the cubic frequency-difference autoproduct, the capability of the cubic bandwidth average to reduce noise is examined. Simulations in free space follow analytic development.

6.3.1 Discrete Bandwidth Average

In practice, acoustic recordings are sampled discretely. Hence, consider a discretized signal bandwidth of N bins between f_L and f_H, setting the frequency resolution $\delta f = (f_H - f_L)/(N - 1)$. For a non-trivial bandwidth, many Fourier bins may exist such that $\omega_1 + \omega_2 - \omega_3 = \Delta\omega$. The number of triplets satisfying this constraint for a given cubic difference frequency $\Delta\omega$, $\eta(\Delta\omega)$, is determined from:

$$\eta(\Delta\omega) = \sum_{\substack{\Sigma f = f_L + \Delta f; \\ \Sigma f \text{ is multiple of } \delta f}}^{f_H + \Delta f} \text{Min}\left[\sigma, N - \sigma + 1 - \text{rem}\left(\frac{\Sigma f - 2f_L}{\delta f}, 2\right)\right], \tag{6.14a}$$

where

$$\sigma = \text{floor}\left(1 + \frac{\Sigma f - 2f_L}{2\delta f}\right). \tag{6.14b}$$

Here, $\text{Min}[x, y]$ takes the minimum of the two arguments, $\text{floor}(x)$ rounds x down, and $\text{rem}(x, y)$ is the remainder from division of x by y. The summand in Eq. (6.14a) computes the number of combinations of $f_1 + f_2 = \Sigma f$, corresponding to the inner integration in Eq. (6.9). In Fig. 6.1(b), evaluation of Eq. (6.14) is superimposed with red dashes.

The influence of the recorded field's bandwidth on the number of independent cubic frequency-difference autoproduct samples is evident in Eq. (6.14). Without loss of generality, consider the frequency limits of the previous section, $f_L = 40$ kHz and $f_H = 110$ kHz, with varying frequency resolution. Computations of Eq. (6.14) with these limits is shown in Fig. 6.3 against increasing number of spectral bins, N. To maintain the target difference frequency, $\Delta f = 75$ kHz, specific values of N were necessary and are marked by circles.

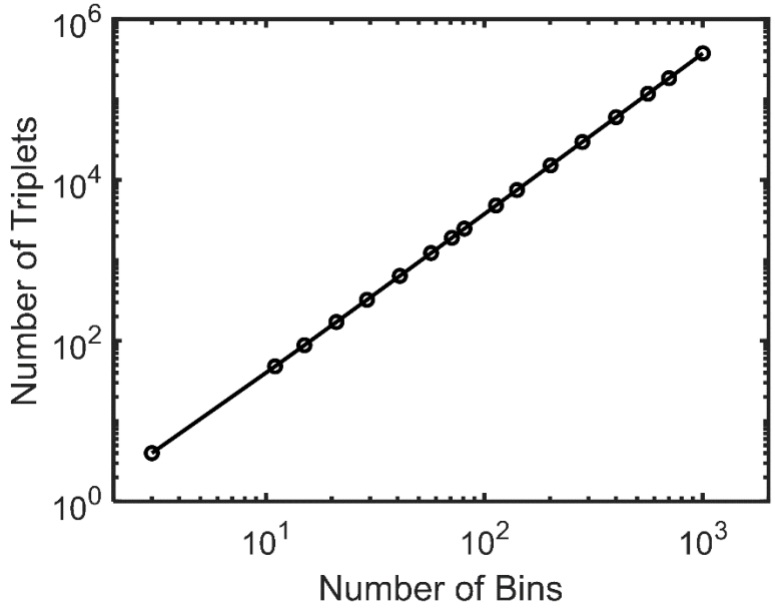

Figure 6.3: Number of cubic autoproduct samples available from a discretized signal bandwidth. The logarithmic horizontal axis indicates the number of frequency bins comprising the signal bandwidth while the logarithmic vertical axis indicates the number of frequency triplets that satisfy the cubic autoproduct relationship. Computed from Eq. (6.14), the signal bandwidth limits were 40 – 110 kHz and the cubic difference frequency was 75 kHz. Circle markers represent specific values of N such that the cubic difference frequency was obtainable.

Figure 6.3 demonstrates the significant number of cubic autoproduct samples available from a discretized signal bandwidth. The horizontal and vertical axes are both logarithmic, leading to the inference $\eta \propto N^2$. In fact, for the data in Fig. 6.3, a nonlinear power law curve-fitting routine in MATLAB found the best fit was $\eta = 0.38N^2$. The cubic frequency-difference bandwidth average, specified by Eq. (6.9), may therefore provide an unexpected means for suppressing noise by averaging (potentially) many cubic autoproduct samples, each containing noise components.

Consider a recorded pressure field $P(\boldsymbol{r}, \omega) = s(\boldsymbol{r}, \omega) + n(\boldsymbol{r}, \omega)$, where $s(\boldsymbol{r}, \omega)$ is the signal at location $\boldsymbol{r}$ and frequency ω and $n(\boldsymbol{r}, \omega)$ is the noise. The coherent average of Γ snapshots reduces the noise amplitude by $1/\sqrt{\Gamma}$. A similar principle underlies the cubic

bandwidth average, and since $\eta \propto N^2$, a natural expectation is noise reduction of $1/N$. Each cubic autoproduct sample, however, does not independently sample the noise field, so $1/N$ noise suppression is an overestimate. Regardless, increasing the temporal recording duration, i.e. increasing N, can enhance cubic autoproduct-based noise suppression in practice.

6.3.2 Free Space

To provide evidence of noise suppression, simulations were conducted in a free space environment with Gaussian noise. The spectral content ranged from $f_L = 40$ kHz and $f_H = 110$ kHz, and $N = 281$ bins, setting the frequency resolution to 250 Hz. Free space acoustic fields were computed for ranges 1.95 to 2.05 m from the source and 0.15 to 0.25 m in depth below the source, corresponding to the direct path response nominally aligned with the secondary geometry in Fig. 6.2(a). The real part of the genuine acoustic field at 75 kHz is shown in Fig. 6.4(a).

Noise was added to all computed free space fields such that the SNR was –10 dB. The SNR calculation used here includes an average across space and frequency:

$$\text{SNR} = 10\log_{10}\left(\frac{\langle|P(\boldsymbol{r},\omega)|^2\rangle_{\boldsymbol{r},\omega}}{\langle|n(\boldsymbol{r},\omega)|^2\rangle_{\boldsymbol{r},\omega}}\right), \tag{6.15}$$

where $\langle\,\rangle_{\boldsymbol{r},\omega}$ indicates the average. Gaussian white noise was enforced by adding random phasors with uniform phase distributions and Rayleigh-distributed amplitude. In Fig. 6.4(b), the noisy acoustic field at 75 kHz is shown. The strong noise content corrupts the phase and amplitude structure of the acoustic signal. Consequently, the spatial cross correlation of panel (b) to the noise-free field in panel (a) was poor: $\chi = 0.30$. Gaussian noise does not impart any overall phase structure into the field, so the lack of a significant imaginary component of the spatial cross correlation was expected.

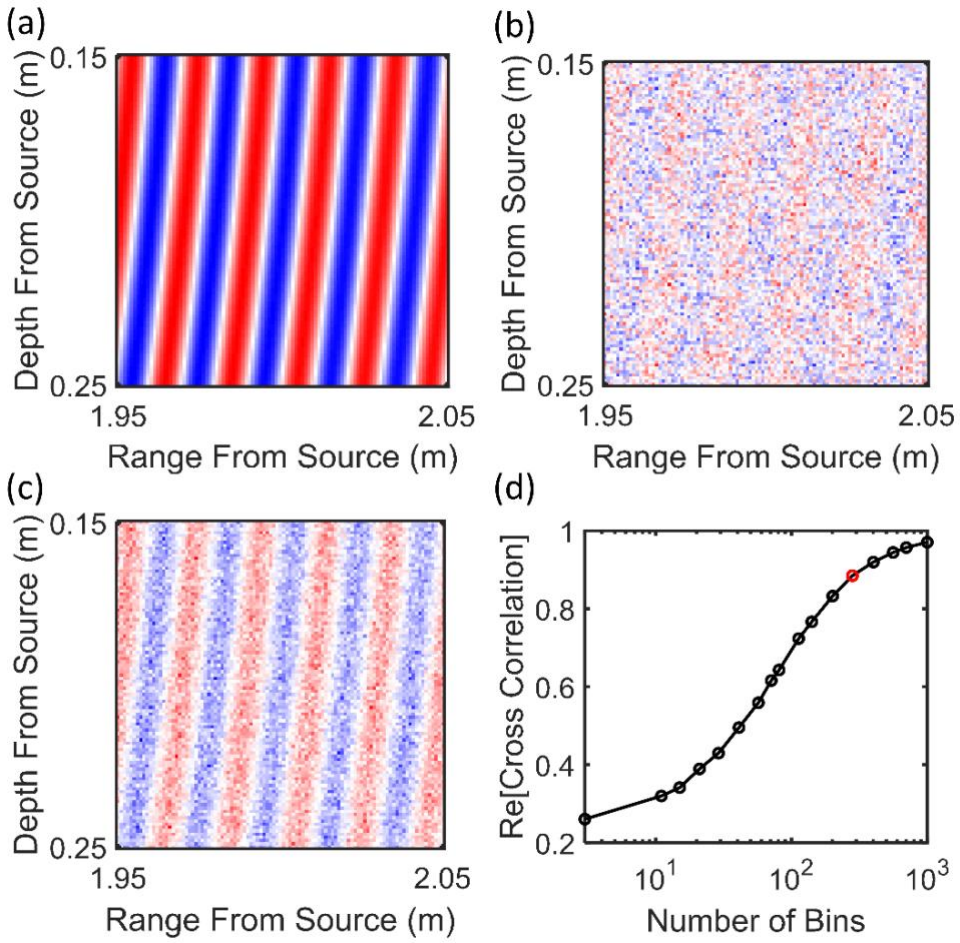

Figure 6.4: Noise suppression from the cubic frequency-difference autoproduct in free space propagation. Panels (a)–(c) show the normalized real part of the complex field at 75 kHz on depth and range axes. The color scale ranges from +1 (red) to -1 (blue). (a) The genuine acoustic field in free space at 75 kHz. (b) Acoustic field at 75 kHz with noise added to -10 dB SNR. (c) The bandwidth-averaged cubic autoproduct at 75 kHz computed from 40 – 110 kHz (250 Hz resolution) constituent fields, each with -10 dB SNR. Spatial cross correlation to panel (a) increases from 0.30 in (b) to 0.88 in (c). (d) Real part of the spatial cross correlations between bandwidth-averaged cubic autoproducts, generated from -10 dB SNR fields, and free space fields at 75 kHz vs. increasing number of bins within the 40 – 110 kHz bandwidth. The red circle indicates the correlation of panel (c) to panel (a).

The bandwidth-averaged cubic frequency-difference autoproduct at 75 kHz, computed from Eq. (6.2) and Eq. (6.9) with constituent field SNR of –10 dB, is shown in Fig. 6.4(c). The phase structure of the noise-free acoustic field, shown in Fig 6.4(a), is nearly entirely recovered, which is impressive given that the constituent fields, as shown in Fig. 6.4(b), lack predictable

phase structure. The phase variation, demonstrated by red-to-blue changes in the colormap, is not as sharp as the genuine field shown in panel (a), indicative of noise that was not totally suppressed by the bandwidth average. The visual inferences are quantitatively supported by the high value of the spatial cross correlation coefficient between panel (c) and panel (a): $\chi = 0.88$.

The effectiveness of cubic autoproduct-based noise suppression is further demonstrated in Fig. 6.4(d). The logarithmic horizontal axis indicates the number of bins within $f_L = 40$ kHz and $f_H = 110$ kHz used to construct the bandwidth-averaged cubic autoproduct. The vertical axis displays the real part of the spatial cross correlation between bandwidth-averaged cubic autoproducts, generated from -10 dB SNR fields, and free space fields at 75 kHz. Cross correlations were computed across the range and depth axes used in panels (a)–(c). The same values of N from Fig. 6.3 were used to generate Fig. 6.4(d), and the red circle denotes the correlation of panel (c), $N = 281$ bins, to panel (a). Overall, panel (d) provides confirmation of the relationship between the number of bins and the success of cubic autoproduct-based noise reduction. As evidenced by the correlation to a noiseless field, increasing the number of bins, thereby generating more cubic autoproduct samples, allows for enhanced noise suppression through the bandwidth average. In fact, for the largest value of N considered here (1001 bins), the cross correlation of the bandwidth-averaged cubic autoproduct with the genuine free space acoustic field was 0.97, reflective of the nearly entirely suppressed noise field.

In Fig. 6.4, normalization (Lipa et al., 2018) was implemented to compare genuine fields and autoproducts, and the colomaps (Auton, 2021) were normalized to a maximum value of one. In the two orthogonal directions of field plots, 1 mm spatial resolution was used. The noise suppression shown in this section may prove beneficial in remote sensing where noise can reduce array signal processing performance. However, the Gaussian noise was uncorrelated in both

space and frequency, which may be unrealistic in practical applications. An example with ambient ocean noise measurements is presented next.

6.4 Direction of Arrival Finding in Noisy Ocean Recordings

To investigate the utility of the noise suppression afforded from the cubic frequency-difference autoproduct, remote sensing performance with ocean measurements was assessed. Relevant experimental details, including acoustic measurements and ambient noise recordings, precede analysis of cubic autoproduct-based beamforming results. Additional details of the Shallow Water '06 experiment studied here is found in previous works (Dahl, 2010; Dahl et al., 2013).

6.4.1 SW06 Experimental Description

Measurements made from the research vessel R/V *Knorr* were collected on 10 August 2006, 0830-1530 UTC. The experimental geometry is nominally shown in Fig. 6.5(a). A 1.4 m nonuniform vertical line array was stationed at 39.0245° N, 73.0377° W, approximately 100 km off the coast of New Jersey. Four omnidirectional ITC-1042 hydrophones (Gavial International Transducer Corporation – Santa Barbara, CA) with inter-element spacing of 0.2, 0.3, and 0.9 m constituted the receiving array, which was located 200 m in range from the acoustic source. The omnidirectional source, an ITC-1007, was located 40 m in depth below the stern of the R/V *Knorr*. A downward-refracting sound speed profile, shown to impact the spatial coherence of surface-reflected sound (Dahl, 2010; Dahl et al., 2013), was measured during the data collection. However, along the direct path, refraction effects are negligible (less than 1°) and were ignored in favor of an isospeed environment, where $c = 1498$ m/s was determined from the average of the sound speed profile. Hence, the direct path angle of arrival, as measured from the broadside of the array, was $\theta' = -4.3°$.

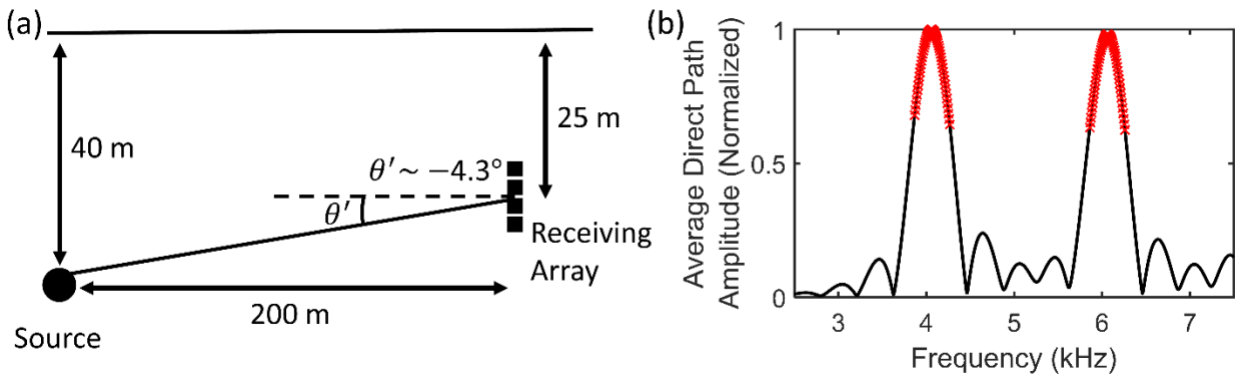

Figure 6.5: Overview of the relevant SW06 experimental details. (a) Schematic indicating omnidirectional source and four-element vertical receiving array of omnidirectional hydrophones. The angle of arrival, with respect to the broadside of the array was $-4.3°$. (b) Broadcast frequency content, approximated by the incoherent average of the direct path recorded at the shallowest receiver. The red ×'s denote spectral components within the signal bandwidth. By construction, the red crosses also represent the cubic difference frequency bandwidth.

During the 6.5-hour data collection, 160 signal broadcasts were recorded at 50 kHz sampling rate. Continuous wave pulses with center frequencies of 4 and 6 kHz were transmitted simultaneously. Higher frequency pulses were superimposed as well, but not selected for analysis due to their poor direct path phase consistency throughout the 160 snapshots. The water channel, 80 m depth, provided prominent secondary arrivals from surface- and bottom-reflected sound, but multipath and scattering effects are not considered here. The 3 ms signal afforded sufficient temporal separation for isolation of the direct path, and, like other studies with this dataset (Dahl, 2010; Joslyn et al., 2023), the signals were time-aligned to remove jitter.

Four different source-receiver bearing angles, separated by 90°, were sampled from the 160 signal transmissions. Due to the surface anisotropy, directional effects were important in the surface-reflected path (Dahl et al., 2013), but are unimportant here for two reasons. First, phase variation during the experiment is minimal for the lower frequencies analyzed here. The direct transmission coefficient, determined from the amplitude of the normalized coherent average

across pings, exceeded 0.80 for all analyzed frequencies. Second, the direction of arrival estimation strategy considered in the next section does not exploit ping-to-ping coherence. Instead, single snapshot performance is compared between conventional and cubic autoproduct approaches.

A proxy for the imperfectly-known source spectrum is shown in Fig. 6.5(b). The incoherent average of the direct path amplitude, normalized to a maximum bin amplitude of unity, was determined from the shallowest receiver. The nominal frequency resolution was $\delta f = 7$ Hz, and spectral components within 200 Hz of the peak of each pulse, marked by red $\times$'s, were maintained, in agreement with previous autoproduct work using this experiment (Joslyn et al., 2023). Because the cubic autoproduct mimics genuine fields within the signal bandwidth, the red crosses indicate the cubic difference frequency bandwidth as well. Since the signal bandwidth was disjoint, Eq. (6.14) is not directly applicable, but a significant noise suppression was still expected for each cubic difference frequency as $N = 122$ spectral bins were within the signal bandwidth.

Transmissions for other experiments were alternately broadcast with the multi-frequency pulse. In particular, a 16 kHz narrowband pulse was transmitted and is used here to artificially adjust the experimental SNR in post-processing. At the lower frequencies of interest, measurements of the 16 kHz transmission were effectively a recording of *in situ* ocean noise. The remote sensing results from this dataset therefore directly assess the performance capabilities of the cubic autoproduct in the presence of ambient ocean noise.

Designed as a surface scattering experiment, relatively little noise exists in the recorded data. The nominal SNR, computed from Eq. (6.15), where $P(\boldsymbol{r}, \omega)$ is the direct path signal and $n(\boldsymbol{r}, \omega)$ is the *in situ* ocean noise recording, was $\mathrm{SNR}_0 = 31$ dB. For the SW06 measurements,

an additional average in Eq. (6.15) over the 160 snapshots was performed to concisely report a single SNR metric. To increase noise in the measurements, noise was added to the acoustic recordings:

$$P'(\boldsymbol{r},\omega) = P(\boldsymbol{r},\omega) + \alpha n(\boldsymbol{r},\omega). \tag{6.16a}$$

The SNR of the added-noise acoustic fields is therefore

$$\mathrm{SNR}(\alpha) = 10\log_{10}\left(\frac{\langle|P(\boldsymbol{r},\omega)|^2\rangle_{\boldsymbol{r},\omega,Q}}{\alpha^2\langle|n(\boldsymbol{r},\omega)|^2\rangle_{\boldsymbol{r},\omega,Q}}\right) = \mathrm{SNR}_0 - 10\log_{10}(\alpha^2)\,, \tag{6.16b}$$

where the additional average over Q =160 snapshots is specified. The noise-enhancement strategy of Eq. (6.16) is used to assess cubic autoproduct-based direction of arrival finding in the presence of varying levels of noise.

6.4.2 Direction of Arrival Results

Direction-of-arrival estimation is a common remote sensing task, and plane-wave beamforming is a spatial filtering process often used to provide an estimate [see, for instance, (Jensen et al., 2011)]. The simplest implementation is the linear Bartlett processor, computed by

$$B_{conv}(\omega,\theta) = \left|\sum_{k=1}^{K} P(\boldsymbol{r_k},\omega)\, w^*(\boldsymbol{r_k},\omega)\right|^2, \tag{6.17}$$

where θ is the steering angle, K is the number of receivers and the weighting vector is given by

$$w(\boldsymbol{r_k},\omega) = \exp\,(i\omega\hat{\boldsymbol{e}}_{\boldsymbol{s}}\cdot\boldsymbol{r_k}/c). \tag{6.18}$$

Here, $\hat{\boldsymbol{e}}_{\boldsymbol{s}}$ is the unit vector in the search direction specified by θ. For the vertical line array shown in Fig. 6.5(a), $\hat{\boldsymbol{e}}_{\boldsymbol{s}}\cdot\boldsymbol{r_k} = d_k\sin\theta$ where d_k is the depth from the shallowest receiver ($d_1 = 0$). Equation (6.17) may be incoherently averaged through the signal bandwidth to produce one beamformed output from the recorded signal:

$$B_{conv}(\theta) = \langle B_{conv}(\omega,\theta)\rangle_{\omega}. \tag{6.19}$$

Quadratic frequency-difference beamforming can be performed by replacing the acoustic field in the summand of Eq. (6.17) by the autoproduct and incoherently averaging through both the signal bandwidth and the difference frequency bandwidth (Abadi et al., 2012; Douglass et al., 2017). Cubic autoproduct-based beamforming is formulated in a similar manner, but the bandwidth-averaged cubic autoproduct replaces the acoustic field in the Bartlett processor, rather than conducting the bandwidth average incoherently, as was done for the quadratic form. Notably, this decision requires knowledge of the source spectrum in order to compute the bandwidth average in Eq. (6.9). For the imperfectly-known source waveform of the SW06 experiment, cubic autoproduct samples were bandwidth-averaged without removal of the source waveform. This approach, which assumes source phase linearity, has been used in a previous quadratic autoproduct study with array signal processing of ocean measurements (Joslyn et al., 2022). The cubic autoproduct counterparts of Eqs. (6.17) – (6.19) are:

$$B_{III}(\Delta\omega,\theta) = \left|\sum_{k=1}^{K} \langle AP_{III}(\boldsymbol{r_k},\Delta\omega)\rangle_{BW}\, w^*(\boldsymbol{r_k},\Delta\omega)\right|^2, \tag{6.20}$$

$$w(\boldsymbol{r_k},\Delta\omega) = \exp(i\Delta\omega\hat{\boldsymbol{e}}_{\boldsymbol{s}}\cdot\boldsymbol{r_k}/c), \tag{6.21}$$

$$B_{III}(\theta) = \langle B_{III}(\Delta\omega,\theta)\rangle_{\Delta\omega}. \tag{6.22}$$

Equations (6.19) and (6.22) are typically normalized by their maximum value and shown on a decibel scale. The cubic autoproduct beamformer produces outputs at the same frequencies as conventional acoustic beamforming. Hence, similar resolution may be achieved, unlike the quadratic frequency-difference autoproduct which sacrifices resolution in favor of robustness (Dowling, 2018).

Conventional (blue), computed from Eq. (6.19), and cubic autoproduct (red), computed from Eq. (6.22), beamformed outputs of a single representative SW06 snapshot are shown in Fig.

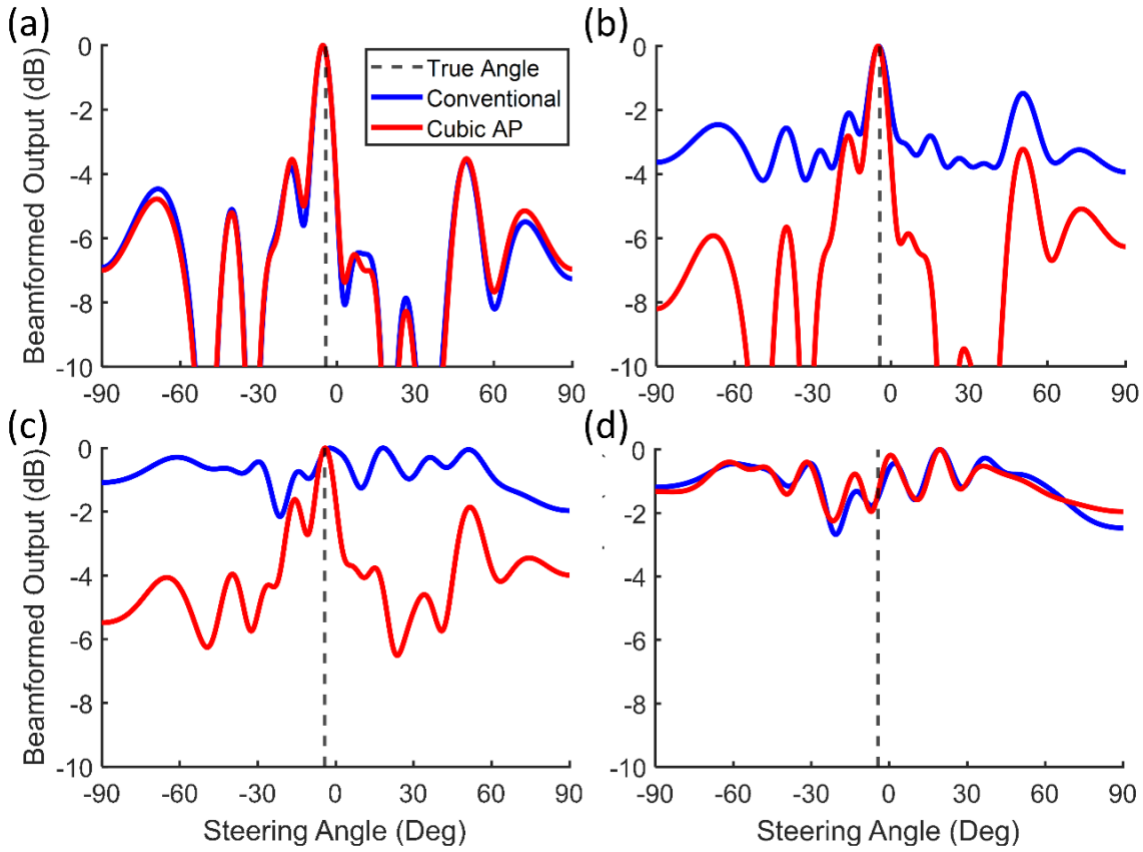

Figure 6.6: Comparisons of SW06 beamformed outputs in the presence of increasing noise. Beamforming using conventional and cubic autoproduct processing are shown in blue and red, respectively. The true angle of arrival is denoted by the dashed black line. In (a), no noise was added to the measured signal. Noise was added to an SNR of –5 in (b), –12.5 in (c), and –25 in (d). The dynamic range shown covered 10 dB and the same signal snapshot was used in all panels.

6.6 with increasing amounts of added noise. In all plots, the target search vector, θ swept between $-90°$ and $90°$ in $0.01°$ step size, the true angle is noted by the vertical dashed black line, and the vertical axis covers 10 dB. Panel (a) shows beamformed outputs of the recorded acoustic field with no added noise. Both approaches perform well, adequately identifying the direction of arrival and exhibiting peak-to-sidelobe ratios greater than 3.5 dB. In panels (b) – (c), beamforming computations were performed on enhanced-noise measurements with SNR values, according to Eq. (6.16), of -5 dB, -12.5 dB, and -25 dB. At SNR = -5, both approaches

successfully determined the direction of arrival, but the peak-to-sidelobe ratio was greater for the cubic autoproduct (2.8 dB) than for conventional processing (1.5 dB). For SNR = -12.5 dB, conventional beamforming incorrectly localizes the direction of arrival and several sidelobes are prominent. Meanwhile, the cubic autoproduct beamformed output correctly indicates the true direction of arrival and the peak-to-sidelobe ratio is 1.6 dB. At SNR = -25 dB, neither approach performs successfully, due to the significant noise power. The improved single-snapshot performance in direction-of-arrival estimation and peak-to-sidelobe ratio may be further assessed by computing average results across all 160 SW06 acoustic recordings.

Figure 6.7 compares success fractions and average peak-to-sidelobe ratios from the 160 acoustic measurements obtained during the SW06 experiment with added *in situ* noise. Success fraction, determined by the percentage of direction of arrival estimates within $\pm 3°$ of the true angle $\theta' = -4.3°$, was computed for SNR values between –25 dB and 10 dB in half-dB steps. Average peak-to-sidelobe ratio, determined from the mean difference between the largest and second largest peaks in beamformed outputs, was computed for the same SNR values. In both panels, conventional beamforming results are marked by blue crosses and red circles indicate cubic autoproduct results.

Overall accuracy improvement offered by the cubic autoproduct is demonstrated in Fig. 6.7(a). The curves from both approaches follow a similar form, but the cubic autoproduct maintains accuracy in the presence of significantly more noise. Direction of arrival estimates from cubic autoproduct processing maintain 60% success until SNR = -14 dB, while the equivalent threshold for conventional processing was maintained until SNR = -9 dB. The maximum success increase offered by the cubic autoproduct occurred at SNR = -13 dB. At this

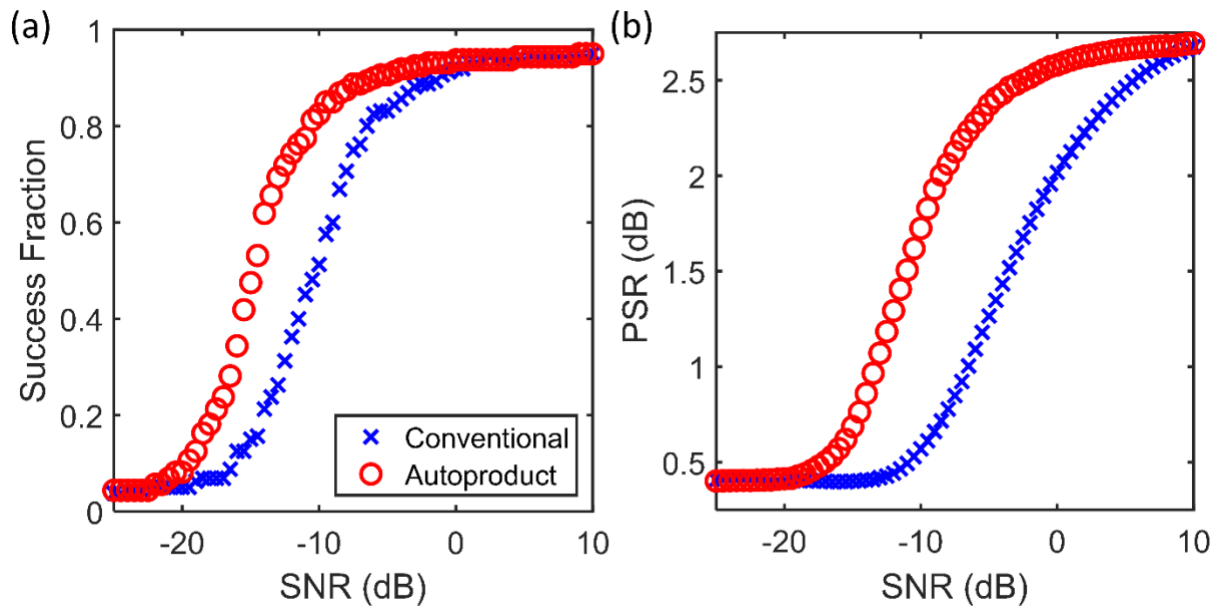

Figure 6.7: Success fraction (a) and average peak-to-sidelobe ratio (b) vs. SNR from the 160 SW06 experimental snapshots. Results from conventional beamforming are shown by blue ×'s and results from cubic autoproduct beamforming are marked with red circles. The power of measured ambient noise added to the acoustic recordings prior to beamforming corresponded to SNR values between –25 and 10 dB, in half–dB steps.

noise level, conventional success fraction was 0.26 and cubic autoproduct success fraction was 0.69, reflecting a 43% success increase.

Increased robustness, quantified by the average peak-to-sidelobe ratio, is illustrated in Fig. 6.7(b). The separation, and therefore performance improvement, between conventional and cubic autoproduct curves is similar to those shown in Fig. 6.7(a). Here, an average cubic autoproduct peak-to-sidelobe ratio of 2 dB was maintained until SNR = -8.5 dB. The noise level for the corresponding average conventional peak-to-sidelobe ratio was SNR = 0 dB. Additionally, the maximum average peak-to-sidelobe ratio increase afforded by the cubic autoproduct was 1.3 dB when SNR = -8.5 dB. For SNR = -8.5 dB, conventional peak-to-sidelobe ratio was 0.7 dB, while the cubic autoproduct peak-to-sidelobe ratio was 2.0 dB.

Together, Fig. 6.6 and Fig. 6.7 support the claims made in Sec. III that the cubic autoproduct may be a promising method for remote sensing in noisy environments. The improved performance, attributed to the noise suppression inherent in Eq. (6.9), encompassed both direction of arrival estimation accuracy and peak-to-sidelobe ratio. Additionally, the added noise was not artificially manufactured. Instead, the noise was recorded in the propagation environment, representing realistic ambient ocean noise. The complicated signal bandwidth, an artifact of the experiment, contained 122 spectral bins, which is directly related to the noise suppression possible from the cubic autoproduct. For a signal bandwidth with more (less) bins, the curves in Fig. 6.7 are expected to exhibit greater (less) separation between the two approaches.

6.5 Conclusion

Quadratic products of the recorded field, termed autoproducts, have been explored for over a decade with the remote sensing benefits owing to the autoproducts' mimicry of genuine acoustic fields outside the recorded signal bandwidth. The primary purpose of this paper was to extend autoproduct theory to a cubic product of the recorded fields, of which the cubic frequency-difference autoproduct may be considered a pseudofield for the broadcast frequencies. Mathematical analysis justifying the pseudofield interpretation is provided, including the governing field equations and results in a Lloyd's mirror environment. The secondary goal of this work was to identify practical utility of the cubic frequency-difference autoproduct. Due to the large number of cubic frequency-difference autoproduct samples within the signal bandwidth of a digitized recording, cubic autoproduct processing can provide an unexpected avenue for remote sensing in noise environments. Direction of arrival estimates of noisy signal recordings

measured during Shallow Water ’06 highlight the improved performance offered by the cubic autoproduct.

Three conclusions are drawn from this research effort. First, cubic extensions to autoproduct theory are possible and generally follow the same intuition built for quadratic autoproducts. Under appropriate circumstances, the field equations governing cubic autoproducts resemble the Helmholtz equation, with a modified source term, evaluated at the cubic autoproduct frequency. In the simplest multipath environment, Lloyd’s mirror, bandwidth-averaged cubic frequency-difference autoproduct mimicry of a genuine acoustic field is only possible for a sufficiently-large signal bandwidth and/or sufficiently-large temporal differences in path arrivals, both of which also limit quadratic autoproduct mimicry in the same environment (Lipa et al., 2018). Second, the bandwidth-averaging step of the cubic autoproduct may offer serendipitous noise suppression. The number of cubic autoproduct samples entering into the bandwidth average was determined explicitly and found to be approximately proportional to the square of the number of spectral bins within the signal bandwidth. Simulations in a free space environment with Gaussian noise support the unconventional noise suppression capabilities. Third, in the presence of significant ambient ocean noise, remote sensing may be more accurate with the cubic autoproduct than with the genuine acoustic field. Across 160 recordings of both signal and *in situ* noise in the SW06 experiment, direction of arrival estimates using the cubic autoproduct were more robust against low SNR than processing with the conventional field.

Although the experimental results are positive, some practical aspects require attention. Multipath cross terms, correlated noise, and the signal spectrum each could limit the utility of the cubic autoproduct processing presented here. The latter two, correlated noise and signal spectrum, were components of the SW06 experiment as ambient ocean noise was recorded and

the source waveform was not explicitly removed. Given the successful performance here, these two considerations may not be too restrictive in sonar signal processing applications. Cross terms, arising in multipath environments for all autoproduct constructions, are naturally more insidious for cubic autoproducts than their quadratic counterparts due to the higher-order nonlinearity. The analytic result for the cubic autoproduct in a Lloyd's mirror environment, however, suggests that sufficient bandwidth averaging may alleviate this concern as well. Regardless, the bandwidth average offered by the cubic autoproduct is a unique means of suppressing incoherent noise at a single receiver while retaining remote sensing resolution, thereby improving array signal processing outcomes. Interestingly, since the cubic frequency-difference autoproduct is a pseudofield constructed from recordings at a single receiver, common considerations, including array gain (Cox et al., 1987), and more advanced techniques, such as compressive sensing (Lee et al., 2023) or other adaptive methods (Park et al., 2022; Worthmann et al., 2017), may be used in concert with the cubic autoproduct to further enhance remote sensing capabilities.

Chapter 7
Target Localization in Forested Environments Using the Electromagnetic Frequency-Difference Autoproduct

Forests provide a complicated channel for electromagnetic wave propagation. Absorption and scattering from foliage, branches, and tree trunks result in signal attenuation and coherence loss as propagation distance increases through the random medium. Consequently, remote sensing in forested environments remains a challenging and salient task. This chapter introduces the electromagnetic frequency-difference autoproduct, the outer product of the electric field vector with itself at nearby frequencies, and describes its capacity to improve target localization in random scattering media. The electromagnetic frequency-difference autoproduct, a generalization of the scalar frequency-difference autoproduct in underwater acoustics, is a dyadic quantity that synthetically estimates electric field content at the difference frequency of the two constituent electric fields. Properties of the pseudofield are numerically examined for plane waves and perfectly conducting cylinders. Experiments are conducted in dense wooded areas on the University of Michigan campus using TDSR P440 Ultra Wideband radio transceivers and BroadSpec linearly polarized antennas. The 3-5 GHz frequency content is recorded along a linear receiving array in *vv*-polarization (TM) configuration. Beamforming demonstrates the advantages of autoproduct-based active target localization of a metallic reflector at 12 m transmitter-to-target distance. While the lower effective frequency reduces resolution of signal processing algorithms, robustness against scattering is increased.

7.1 Introduction

Recent research in acoustics suggests that a quadratic product of complex fields at nearby frequencies, termed the frequency-difference autoproduct, may resemble a genuine field at the difference frequency between the two constituent fields (Dowling, 2018; Worthmann and Dowling, 2017). The autoproduct, a pseudofield quantity, has been investigated in a variety of remote sensing applications, including beamforming (Abadi et al., 2012; Douglass et al., 2017; Douglass and Dowling, 2019) and matched field processing (Geroski et al., 2023; Geroski and Dowling, 2019; Worthmann et al., 2015, 2017; Yuan et al., 2023). In the aforementioned studies, the success of autoproduct-based processing is attributed to the mimicry of a genuine lower frequency field, where array signal processing is more robust. The genuine field mimicry has been investigated in a uniform half-space (Lipa et al., 2018), in scattering from a rough surface (Joslyn and Dowling, 2022), and in the presence of diffraction (Worthmann and Dowling, 2020b, 2020a). Although not strictly limited to acoustic analysis, the autoproduct has seldom been utilized in other fields. Backprojection of earthquakes using seismic waves (Neo et al., 2022) and preliminary electromagnetic simulations in random media (Geroski, 2021) are the only non-acoustic autoproduct works.

This chapter presents theoretical, numerical, and experimental investigations of the electromagnetic frequency-difference autoproduct, a dyadic pseudofield quantity. Mathematical formulations accompany examination of the frequency-difference autoproduct constructed from electric fields scattered by a perfectly conducting infinite cylinder. The ability of the frequency-difference autoproduct to provide useful remote sensing results was determined by target localization in a forested environment. Results from both the modeling and target localization experiments highlight the capability of the frequency-difference autoproduct to mimic a genuine

electric field at the difference frequency. In all cases, only a single element of the autoproduct dyadic is studied, the vv-polarization.

Generally, the effects of random media scale with frequency [see, for instance, (Ishimaru, 1978)]. Hence, the synthetic estimation of lower frequency field content offered by the frequency-difference autoproduct allows for array signal processing at difference frequencies where the effects of the random media are minimized. The random media selected here for target localization experiments was forested areas on the University of Michigan campus. Due to the relevance for both defense and civilian applications, electromagnetic propagation through forested areas is an active area research [see the review articles in (Meng et al., 2009) and (Meng and Lee, 2010)]. Significant work considers propagation modeling, encompassing physics-based statistical models (Wang and Sarabandi, 2007), empirical and site-specific models (Zhang et al., 2019), and using a 3-D digital map with Foldy-Lax multiple scattering theory (Chee et al., 2014), among many others. Remote sensing tasks, such as target detection (Zhao et al., 2018) and localization (Ziadé et al., 2008), are common in this environment as well.

Constructed from recorded fields, the frequency-difference autoproduct requires significant bandwidth in the transmitted signal. To provide sufficient bandwidth, the PulsON 440 Ultra Wideband Radio (TDSR - Petersburg, TN) was obtained. The P440 (or earlier iterations) has been used in myriad of applications from target detection in forested environments (Zhai and Jiang, 2013, 2014) to tomographic imaging (Beck et al., 2016) to localization (Mu and Song, 2019) and thus is an excellent module for the target localization experiments conducted here. Broadspec linearly polarized antennas were used to isolate desired polarization.

The notion of a dual-field quantity is not unique to autoproduct theory. In electromagnetics, Δk or two-frequency radar (Popstefanija et al., 1993; Weissman, 1973),

interferometric synthetic aperture radar (Sarabandi and Member, 1997) and the frequency correlation function (Sarabandi et al., 1999) share features with the frequency-difference autoproduct. However, the frequency-difference autoproduct differs from these related concepts in that the pseudofield does not require an ensemble average, retains phase information, and has field properties associated with a genuine field at the difference frequency. Importantly, the frequency-difference autoproduct was developed independently to solve problems associated with passive remote sensing in underwater acoustics, not as an extension or generalization of other dual-field formulations.

The remainder of this chapter is organized as follows. Section 7.2 introduces the frequency-difference autoproduct concept, including mathematical formulations and results in simple modeling environments. Section 7.3 provides experimental details of the target localization scenario, and Section 7.4 investigates the corresponding beamforming results. Section 7.5 summarizes the study and discusses three conclusions.

7.2 Theory and Modeling

7.2.1 Frequency-Difference Autoproduct

The frequency-difference autoproduct may be constructed from any time domain recording using a digital Fourier transform and multiplication. No specific experimental design or preprocessing is necessary. Much of the mathematical apparatus defined in this subsection was first formulated in (Geroski, 2021).

Here, the complex (frequency domain) electric field vector, $\vec{E}(\vec{x}, \omega)$, at spatial location $\vec{x}$ is defined as,

$$\vec{E}(\vec{x},\omega) = \begin{bmatrix} 0 \\ E_h \\ E_v \end{bmatrix} \tag{7.1}$$

where ω is the angular frequency. In this generic form, the horizontal and vertical transverse components, E_h and E_v respectively, are defined based on the propagation scenario, and the zero element indicates the lack of a compressional component in the direction of propagation.

The frequency-difference autoproduct is formed by an outer product of electric field vectors at two different frequencies with one conjugation:

$$\overline{\overline{AP}}(\vec{x},\omega,\Delta\omega) = \vec{E}^{*,T}(\vec{x},\omega_-)\vec{E}(\vec{x},\omega_+) = \begin{bmatrix} 0 & 0 & 0 \\ 0 & AP_{hh} & AP_{hv} \\ 0 & AP_{vh} & AP_{vv} \end{bmatrix}, \tag{7.2}$$

where the asterisk indicates complex conjugation, T represents the vector transpose operation, $\Delta\omega$ is the difference frequency between constituent fields, and $\omega_\pm \equiv \omega \pm \Delta\omega/2$. The premise of Eq. (7.2), extending the claims made for the scalar wavefield (Dowling, 2018; Worthmann and Dowling, 2017), is that the frequency-difference autoproduct is a pseudofield for the genuine electromagnetic field at the difference frequency $\Delta\omega$. Synthetic estimation of lower frequency field content from higher frequencies may be useful in remote sensing applications where the recorded field is corrupted by random media effects (scattering, jitter, lack of coherence) unlikely to significantly impact lower frequency propagation. Notably, the formulation in the rightmost equality of Eq. (7.2) resembles a scattering matrix [see, for instance, (Huynen, 1965; Singh et al., 2019)], which represent incident and scattered polarizations at the same frequency. The matrix in Eq. (7.2), however, indicates a dyadic product of measured polarizations at different frequencies.

To improve the mimicry of a genuine electric field, an additional mathematical step is conducted on the frequency-difference autoproduct. For a transmitter with nontrivial signal bandwidth, $\Omega_L \leq \omega \leq \Omega_H$, Eq. (7.2) equally-spaced frequency pairs are averaged by

$$\left\langle \overline{\overline{AP}}(\vec{x},\ \Delta\omega) \right\rangle_{BW} = \frac{1}{\Omega_{BW}^{\Delta}} \int_{\Omega_C - \frac{1}{2}\Omega_{BW}^{\Delta}}^{\Omega_C + \frac{1}{2}\Omega_{BW}^{\Delta}} \overline{\overline{AP}}(\vec{x}, \omega, \Delta\omega)\, d\omega = \begin{bmatrix} 0 & 0 & 0 \\ 0 & \langle AP_{hh} \rangle_{BW} & \langle AP_{hv} \rangle_{BW} \\ 0 & \langle AP_{vh} \rangle_{BW} & \langle AP_{vv} \rangle_{BW} \end{bmatrix}, \quad (7.3)$$

where $\Omega_C = (\Omega_L + \Omega_H)/2$ is the transmission center frequency and $\Omega_{BW}^{\Delta} = \Omega_H - \Omega_L - \Delta\omega$. The bandwidth average is an important step as it increases robustness of the autoproduct estimate (Joslyn and Dowling, 2022). Furthermore, the bandwidth average suppresses multipath cross terms inherited from the quadratic autoproduct construction that are not present in the genuine difference frequency field (Geroski et al., 2023; Geroski and Worthmann, 2021; Lipa et al., 2018; Worthmann and Dowling, 2017). In passive remote sensing, the unknown source spectrum limits the applicability of Eq. (7.3) as shown and bandwidth-averaging cross-spectral density matrices is more prudent (Geroski et al., 2023; Geroski and Dowling, 2021; Geroski and Worthmann, 2021; Worthmann et al., 2017). However, in active remote sensing, the source spectrum may be removed prior to Eqs. (7.2) and (7.3). Removal of the transmitted waveform did not significantly alter the experimental results studied here, so Eqs. (7.2) and (7.3) are used as shown, like in (Joslyn et al., 2022).

The rest of this study is restricted to the vv-polarized element in the bottom right of the matrix shown in Eq. (7.3), $\langle AP_{vv} \rangle_{BW}$. Extensions to other nonzero elements of Eq. (7.3) are clearly possible, but outside the scope of this chapter. In (Geroski, 2021), both co-polarized elements were reported for numerical simulations of bistatic propagation through random scattering media. There, both co-polarized autoproducts mitigated the effects of randomly-located scattering metallic cylinders, but the horizontally-polarized autoproduct, $\langle AP_{hh} \rangle_{BW}$, was

more robust than the vertically-polarized autoproduct, $\langle AP_{vv}\rangle_{BW}$, when the cylinder axis was in the vertical direction. Thus, results for $\langle AP_{hh}\rangle_{BW}$, equivalent to those presented here for $\langle AP_{vv}\rangle_{BW}$, are expected to further mitigate the impacts of scattering.

7.2.2 Plane Wave

To assess the frequency-difference autoproduct, consider the simplest electric field: a plane wave. The plane wave convention used here is

$$\vec{E}(\vec{x},\omega) = \hat{z}\exp[ikx]\,, \tag{7.4}$$

where $k = \omega/c$ is the wavenumber, c is the speed of light, and the amplitude is set to unity. The x-coordinate corresponds to the propagation direction and the electric field oscillates in the z-direction.

Matching the transmitted experimental frequencies (see Chapter 6.3), Fig. 7.1(a) and Fig. 7.2(b) show the real component of Eq. (7.4) evaluated at 3 and 4 GHz, respectively. In Fig. 7.3(c), the real part of the electric field at a lower frequency, 1 GHz, is plotted. The real component of the frequency-difference autoproduct at 1 GHz, constructed from applying Eq. (7.3) to the constituent electric fields in panels (a) and (b), is shown in panel (d). The horizontal axis of each panel is aligned with the propagation direction and covers 30 cm in extent, and the red-to-blue color scale applies to the entire figure.

Figure 7.1 illustrates the mimicry offered by the frequency-difference autoproduct. Generated from 3 GHz and 4 GHz fields in the same environment, the frequency-difference autoproduct synthetically estimates field content at the difference frequency of 1 GHz. The plots in Fig. 7.1(c) and Fig. 7.1(d) are identical, as shown by substituting Eq. (7.4) into Eq. (7.2) (with z-direction corresponding the vertical transverse component),

$$\langle AP_{vv}\rangle_{BW} = \exp[i\Delta kx]\,, \tag{7.5}$$

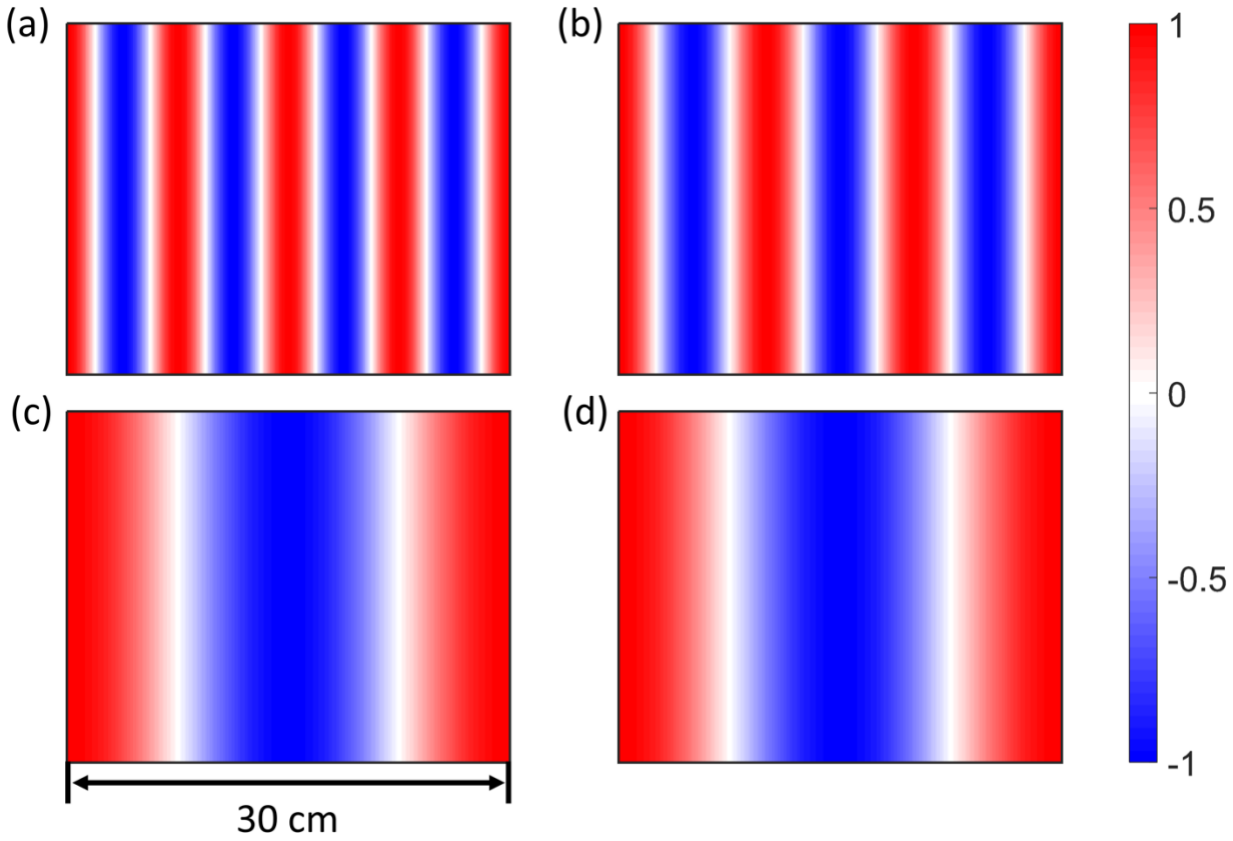

Figure 7.1: Frequency-difference autoproduct mimicry of a genuine lower-frequency electric field for plane waves. In panels (a), (b), and (c), the real component of the electric field is shown at 4 GHz, 3 GHz, and 1 GHz, respectively. The real part of the frequency-difference autoproduct at 1 GHz, determined from Eq. (7.2) with panels (a) and (b) as constituent fields, is shown in panel (d). Constructed from higher frequency content, the frequency-difference autoproduct (d) perfectly mimics the genuine electric field at the difference frequency (c) when plane waves sufficiently describe the field. The horizontal axes covers 30 cm in the propagation direction and the red-to-blue colorbar applies to all panels.

where $\Delta k = \Delta\omega/c$ is the difference wavenumber. Although the match between the frequency-difference autoproduct and the genuine electric field at the difference frequency is perfect for plane waves, the autoproduct should not be considered a genuine field that propagates through the environment. Rather, the frequency-difference autoproduct is a pseudofield, capable of

mimicking lower frequency content, and in the simplifying limit of plane wave propagation, the mimicry is perfect (Worthmann and Dowling, 2017).

7.2.3 Single Perfectly Conducting Infinite Cylinder

While many investigations consider the combined effects of canopy and tree trunks (Lin et al., 1999; Sarabandi and Lin, 2000; Zhang et al., 2019), the experimental work here specifically assessed autoproduct remote sensing performance for electromagnetic propagation through tree trunks. Hence, a simple modeling strategy was designed to build autoproduct intuition using perfectly conducting infinite cylinders ensonified by an incident plane wave.

The scattering of a plane wave from a perfectly conducting infinite cylinder is analytically tractable and the solution, determined by matching coefficients of a Bessel function expansion, is well known. Following (Jin, 2010), the scattered field for a TM-polarized (electric field aligned with cylinder axis) plane wave incident on a cylinder of radius a centered at the origin is given by

$$E_z^{sc} = -\sum_{n=-\infty}^{\infty} j^{-n} \frac{J_n(ka)}{H_n^{(2)}(ka)} H_n^{(2)}(k\rho) e^{jn\phi} \tag{7.6}$$

where J_n is the Bessel function of the first kind, $H_n^{(2)}$ is the Hankel function of the second kind, ρ is the radial spatial coordinate, and ϕ is the angular spatial coordinate. Summation limits of ± 50 were sufficient for the numerical implementation here. Thus, the total field is given by

$$E_z^{tot} = E_z^{inc} + E_z^{sc} = e^{-jkx} - \sum_{n=-50}^{50} j^{-n} \frac{J_n(ka)}{H_n^{(2)}(ka)} H_n^{(2)}(k\rho) e^{jn\phi}\,. \tag{7.7}$$

In Fig. 7.2, genuine electric fields scattered by perfectly conducting infinite cylinder and the frequency-difference autoproduct constructed from the scattered fields are compared.

Horizontal and vertical axes cover 1.5 m in the plane orthogonal to the cylinder axis, and the cylinder, radius 7.5 cm, is indicated by the white circle at the origin. Each panel with 2 mm

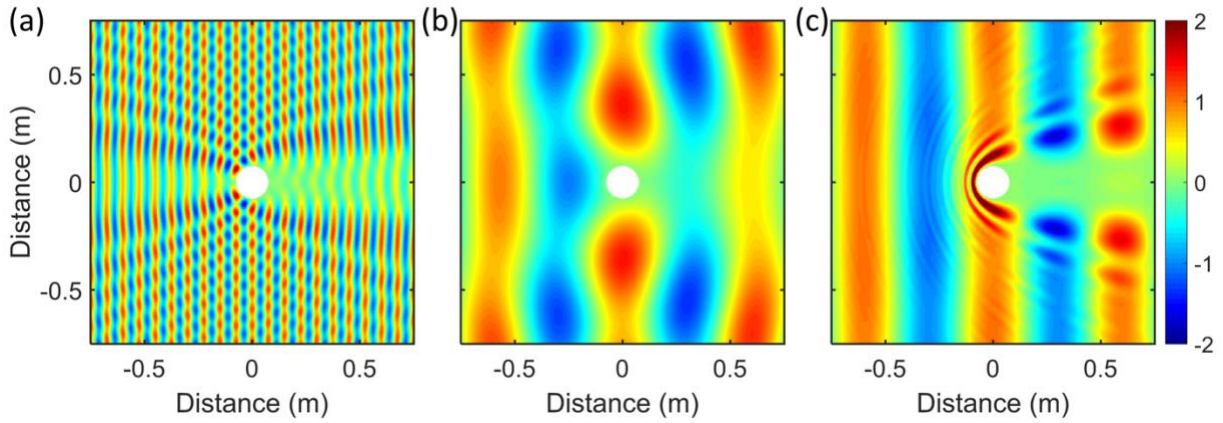

Figure 7.2: Scattering by a perfectly conducting infinite cylinder for a TM-polarized incident plane wave. The real part of the total electric field is shown at (a) 4 GHz and (b) 500 MHz. (c) The real part of the frequency-difference autoproduct at 500 MHz, constructed from constituent fields between 3 GHz and 5 GHz, mimics the genuine difference frequency field in (b) and, outside of the shadow zone, retains much of the phase structure of a plane wave at the difference frequency. The white circle denotes the cylinder of radius 7.5 cm (the wavelength at 4 GHz) and the horizontal and vertical axes cover ± 0.75 m.

resolution and the color scale extends from -2 to +2 (corresponding to total constructive interference of the incident and scattered waves).

Evaluation of Eq. (7.7) at 4 GHz and 500 MHz is shown in panels (a) and (b), respectively. The effects of scattering are less noticeable for 500 MHz, evidenced by the lack of a prominent shadow zone behind the cylinder in (b), but not entirely removed as the phase variation does not uniformly vary from red-to-blue like the incident plane wave. Equation (7.7) was evaluated for 3 – 5 GHz (every 50 MHz), and the frequency-difference autoproduct was computed by inserting these constituent fields into Eq. (7.2) and Eq. (7.3). The frequency-difference autoproduct at 500 MHz is shown in panel (c).

Several interesting autoproduct features, not present in Fig. 7.1, emerge in Fig. 7.2. The mimicry of the genuine difference frequency field [panel (b)] offered by the frequency-difference autoproduct [panel (c)] is not perfect. A significant shadow zone behind the cylinder, owing to the shadow zones of the constituent fields, exists for the frequency-difference autoproduct that does not appear so prominently in the genuine electric field at the difference frequency. Related, areas of constructive (and destructive) interference between the constituent incident and scattered fields persist through the autoproduct construction and manifest as brightly- (dimly-) colored regions around the shadow zone. Minor parabolic ripples in the field, centered on the cylinder, exist for the autoproduct, but not for the genuine field. These high frequency variations are artifacts of the autoproduct construction and are suppressed (become more prominent) by increasing (decreasing) the number of frequency pairs within the bandwidth average. Lastly, outside of the shadow zone, the effects of scattering are much more minimal for the autoproduct. The phase structure of the autoproduct, indicated by the red-to-blue color variation, is nearly identical to a plane wave at the difference frequency. Generally, these findings match those found for the acoustic frequency-difference autoproduct for Mie scattering from a sphere (Worthmann and Dowling, 2020a), which is not particularly surprising given the similarity of these two wave propagation scenarios.

Although the mimicry of panel (b) by panel (c) is not perfect, it is compelling and indicates the potential advantages of autoproduct-based array signal processing. Synthetically estimated from higher frequency field content, like that shown in panel (a), the frequency-difference autoproduct may provide an avenue for successful remote sensing when scattering effects corrupt the signal and lower frequencies were not transmitted. Additionally, the nearly

complete removal of scattering effects outside of the shadow zone may lead to more robust remote sensing performance, even if the genuine difference frequency field was accessible.

7.2.4 Multiple Perfectly Conducting Infinite Cylinders

To further assess the utility of the frequency-difference autoproduct, multiple perfectly conducting infinite cylinders were placed in the propagation medium. The single scattering approximation was implemented to model the scattering,

$$E_z^{tot} = E_z^{inc} + \sum_{q=1}^{Q} E_z^{sc}\,, \tag{7.8}$$

where Q is the number of scatterers. The individual contributions to the summation are determined from Eq. (7.6), with an appropriate phase offset to account for the location of the cylinder. The results of this section were computed similarly to those of the single perfect conducting infinite cylinder. To accommodate multiple cylinders, the horizontal and vertical extent was expanded to $\pm$1.25 m, cylinder radius was reduced to 5 cm, and the grid was computed at 4 mm resolution.

In Fig. 7.3, genuine electric fields are compared to the frequency-difference autoproduct for scattering of a TM-polarized incident wave by five perfectly conducting infinite cylinders, subject to the single scattering approximation. The total electric fields at 4 GHz and 500 MHz, determined from Eq. (7.6) and Eq. (7.8), are shown in panel (a) and panel (b), respectively, and the frequency-difference autoproduct at 500 MHz is shown in panel (c). As in the previous section, the bandwidth-averaged frequency-difference autoproduct was computed by inserting 3 – 5 GHz (every 50 MHz) constituent fields, computed from Eq. (7.6) and Eq. (7.8), into Eq. (7.2) and Eq. (7.3). The frequency-difference autoproduct at 500 MHz is shown in panel (c).

Figure 7.3 further demonstrates the conclusions obtained from analysis of the single scatterer. Originating in the higher frequency constituent fields, a pronounced shadow zone is maintained by the frequency-difference autoproduct. Moreover, shadow zones appear behind

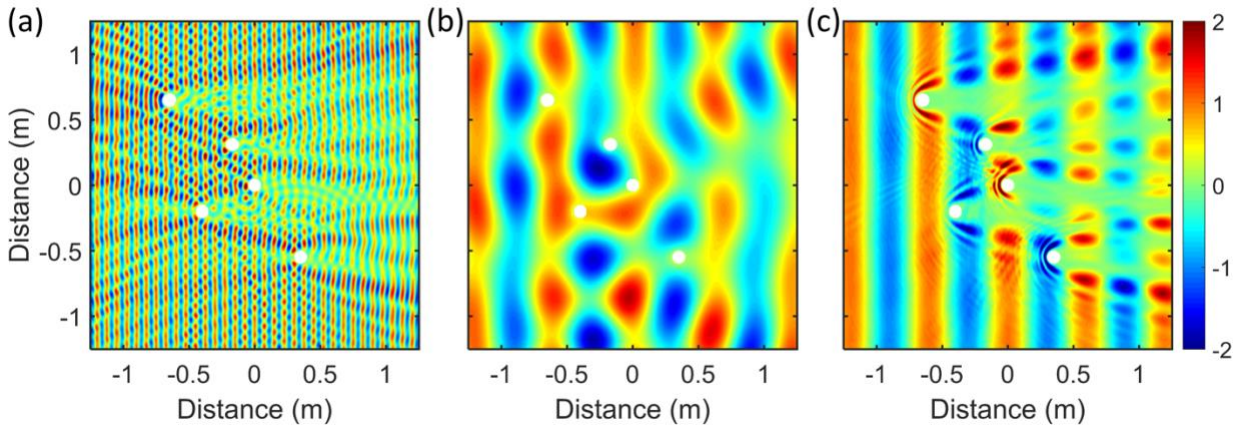

Figure 7.3: Scattering of a TM-polarized plane wave by five perfectly conducting infinite cylinders. The cylinders, each of radius 5 cm and denoted by the white circles, were placed throughout the medium, and the single scattering approximation was used to model the field. As in Fig. 7.2, the real part of the total electric field at 4 GHz and 500 MHz is shown in (a) and (b), respectively. The real part of the frequency-difference autoproduct at 500 MHz, computed from constituent 3 – 5 GHz fields, is shown in (c). The horizontal and vertical axes cover $\pm$1.25 m.

each individual cylinder. In the genuine difference frequency field, these shadow zones do not exist. For the autoproduct, both the minor parabolic ripples emanating from cylinder centers, suppressible by additional bandwidth averaging, and the regions of constructive/destructive interference surrounding the shadow zone persist to the multiple scatterer scenario of this section. Outside of these features, however, the frequency-difference autoproduct resembles a plane wave at the difference frequency, unlike the genuine field in Fig. 7.3(b). Hence, even with multiple scatterers, the frequency difference autoproduct shown in Fig. 7.3(c) may provide more

useful remote sensing outputs than conventional processing of its constituent fields, i.e. the field shown in Fig. 7.3(a).

The frequencies and difference frequencies assessed in this section were selected to mimic the nominal experimental values. However, some modifications were made to avoid the aesthetic challenges of presenting field plots of drastically different frequencies on equal axes. As described in the next section, experimental difference frequencies were lower than those used in this section, effectively increasing the autoproduct's ability to minimize scattering impacts. Although more complicated modeling strategies could be pursued with commercial software or more advanced analytical forms [for instance, the scattering of a plane wave from a dielectric cylinder (Jin, 2010)], single scattering approximation for perfectly conducting cylinders provided sufficient intuition to design the target localization experiment.

7.3 Experiment

To assess the remote sensing capabilities of the frequency-difference autoproduct, a target localization experiment was designed and performed on the University of Michigan campus. Equipment and design details are provided prior to discussion of the random propagation medium.

7.3.1 Equipment and Design

A key feature of the frequency-difference autoproduct is the bandwidth-averaging step defined in Eq. (7.3). Thus, unlike many radar schemes, a large transmitted (and receiver) bandwidth was desirable. The TDSR P440 Ultra Wideband radio transceivers [see (Petroff, 2012) or (Petroff, 2014) for an overview] were used with BroadSpec linearly polarized antennas to isolate the desired vertical polarization of the transmitter and receiver. The P440 modules were mounted to

tripods as was done in previous work using the P440 (Edgar et al., 2012; Mu and Song, 2019). An overview of the experiment is provided in Fig. 7.4.

The default waveform of the P440 system was used. Sampled every 61 ps (16.38 GHz sample rate), a laboratory recording of the waveform, away from reflective surfaces, is shown in Fig. 7.4(a). A secondary peak, occurring here near 2 ns, can be seen in other studies (Mu and Song, 2019; Petroff, 2014) and may be due to the tripod or the battery (Petroff, 2014). The frequency content of this pulse, by Fourier transform of Fig. 7.4(a), is shown by the black curve

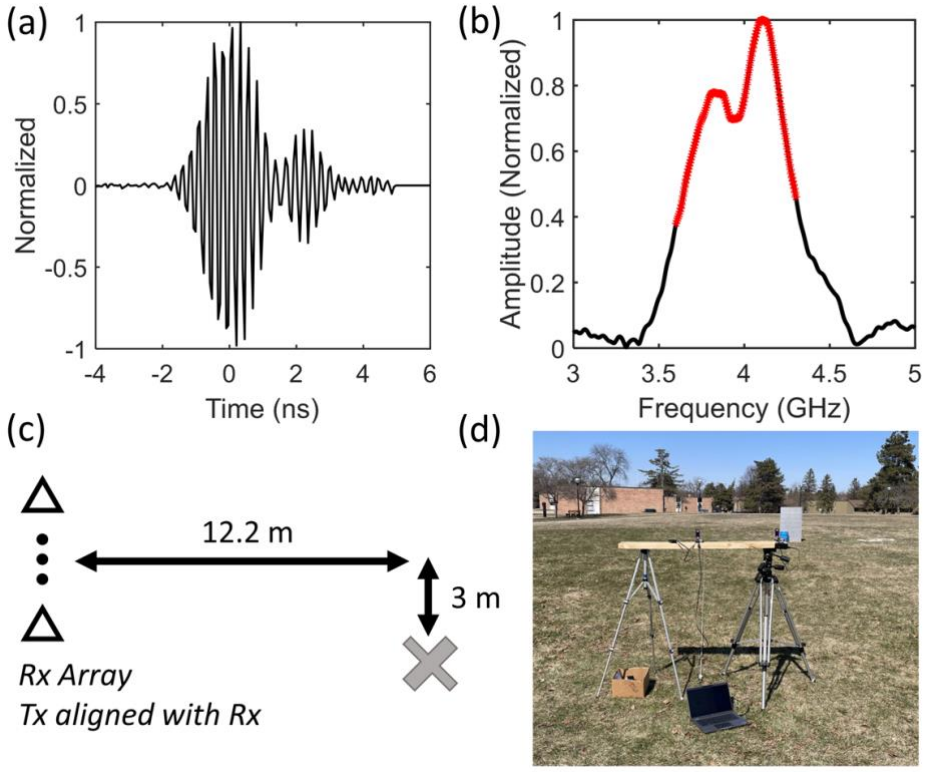

Figure 7.4: Overview of the target localization experiment. The default PulsON 440 waveform as recorded in laboratory environment in the time (a) and frequency (b) domain. The red crosses in panel (b) indicate the frequencies selected to constitute the signal bandwidth. A schematic of the localization experiment is shown in (c). For the same target location, the receiving array was designed as both a 1 m aperture array with 5 cm channel spacing and a 11 m aperture array with 1.8 m channel spacing. The smaller array design is shown in panel (d) with the target reflector in the background. The park shown in (d) functions as the no-scatterer environment.

in Fig. 7.4(b). To ensure sufficient transmitted energy within the signal bandwidth, frequencies between 3.6 GHz and 4.3 GHz (nominal frequency resolution of 5.5 MHz) were maintained in processing and are denoted by red ×'s on Fig. 7.4(b). Hence, autoproduct difference frequencies only exist below 700 MHz. In practice, difference frequency selection must balance robustness and resolution concerns (Dowling, 2018), but quantitatively assessing that tradeoff is beyond the scope of the work. The difference frequency bandwidths used are presented in Chapters 7.4.1 and 7.5.1.

The experimental geometry is diagrammed in Fig. 7.4(c). The target, a 74.5 cm × 121.5 cm aluminum plate shown in the background of Fig. 7.4(d), was located 12.2 m (40 ft) in range and 3 m (10 ft) in cross range from the center of the receiving array. Due to naturally-occurring obstructions in the forested environment (rocks, branches, trees), minor adjustments to the stated geometry were occasionally necessary. These modifications are not listed but were accounted for in the data processing. Two different receiving array designs were implemented. The first configuration, nominally well-designed for the transmitted frequencies, was a 1 m array aperture with 5 cm channel spacing. This 21-element array is used in Chapter 7.4 for direction-of-arrival finding. The second design, extremely sparse for the transmitted frequencies, was an 11 m array aperture with 1.8 m channel spacing. This 7-element array is implemented in Chapter 7.5 for localization in both direction and range. Importantly, only a single transmitter-receiver pair was used. For both designs, the full array was synthetically created by moving the receiver to the appropriate spatial location and combining all recordings.

A picture of data collection is shown in Fig. 7.4(d). In the foreground, the transmitting and receiving antennas were located on a wooden plank marked with the spatial locations for the small-aperture array configuration. For the sparse array, transmitter and receiver were mounted

directly to the tripod. The location, a park on the University of Michigan campus, was a relatively quiescent environment free of scatterers used to assess remote sensing performance of the frequency-difference autoproduct no scatterers are present.

7.3.2 Forested Environment

The utility of the frequency-difference autoproduct is robustness against random media effects that corrupt remote sensing performance. By shifting analysis to lower frequencies, these negative effects may be minimized. Thus, the experiment reviewed in Fig. 7.4 was also conducted in randomly-scattering environments. Three different locations in forested areas on the University of Michigan campus, shown in Fig. 7.5, were selected to provide varying levels of scattering.

The three areas shown in Fig. 7.5 are herein described as “light forest” and “dense forest.” The light forest, shown in panel (a), is characterized by skinny tree trunks and relatively clean line-of-sight to the target reflector and was used only for the small-aperture array design.

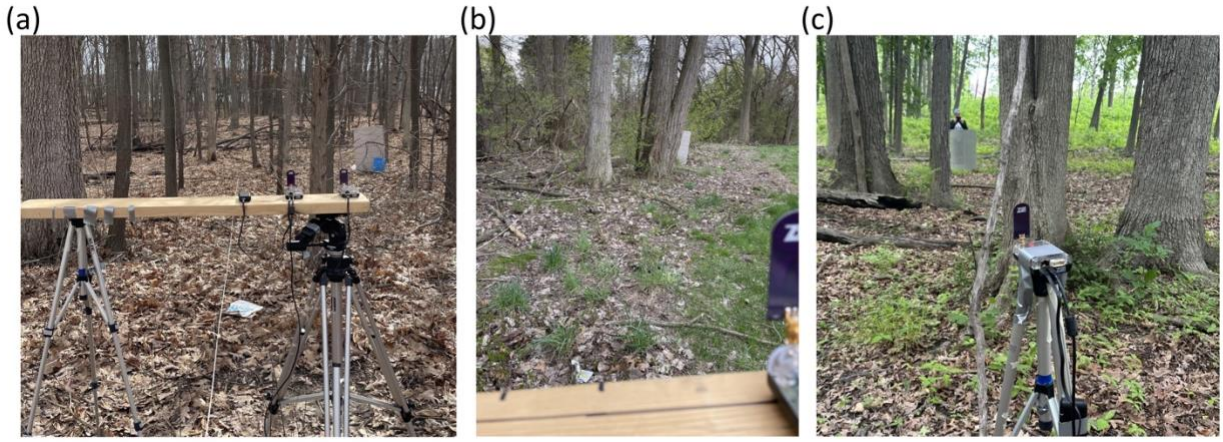

Figure 7.5: Random forested environments used in the target localization experiments. A lightly scattering forest, indicated by skinny tree trunks and clean line-of-sight to the target, is shown in (a). A dense forest, indicated by thick tree trunks significantly corrupting line-of-sight to the target, is shown for the small-aperture array design in (b) and the sparse array design in (d).

The dense forest is characterized by thick tree trunks and poor line-of-sight to the target. Both the small-aperture and sparse array designs recorded in the dense forest and the locations are shown in panel (b) and panel (c), respectively. Notably, no effort was made to understand the electrical properties of the random medium. While such an endeavor would likely improve results, this step was avoided to investigate autoproduct-based remote sensing performance when very little is known about the propagation environment.

Figure 7.6 compares sparse array time domain recordings in the park and in the dense forest. On the same horizontal time axis, the waterfall plots show the time domain recording of each receiver. The receiver axis is aligned with the diagram in Fig. 7.4(c). In panel (a), the park recordings show clean target reflections. In panel (b), the dense forest recordings include scattered arrivals throughout the time record and corruption of the target reflection envelope, as expected for the stronger scattering environment.

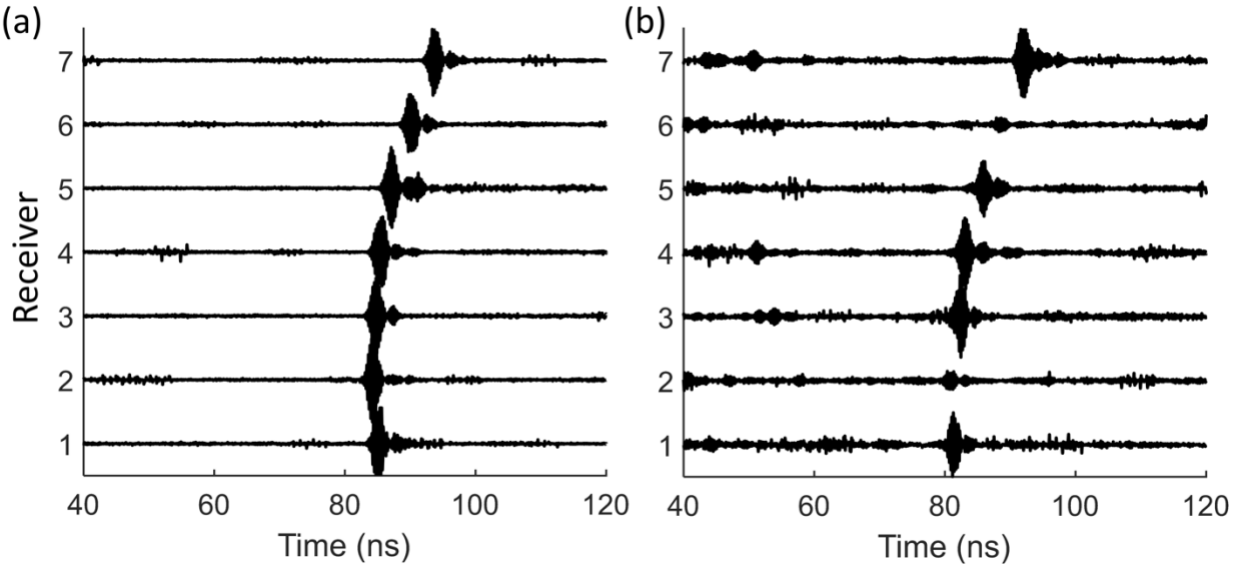

Figure 7.6: Comparison of sparse array time domain recordings in the (a) park and (b) the dense forest. In both panels, the horizontal axis is time (in ns) from signal transmission and the receiver number increases along the vertical axis. The target reflection is prominent and clean for all park recordings, while the dense forest recordings exhibit both scattered arrivals and corruption of the target reflection envelope.

7.4 Direction of Arrival Finding

The first set of target localization results utilize the small-aperture array configuration discussed in Chapter 7.3 to estimate direction of arrival from the recorded signals. Prior to presentation of the results, conventional and autoproduct-based planewave beamforming is discussed.

7.4.1 Plane-Wave Beamforming

Beamforming is a ubiquitous task in remote sensing [see, for instance, (Van Veen and Buckley, 1988)]. Here, a broadband frequency domain plane-wave beamformer is used to estimate direction of arrival from recorded signals:

$$B_{Conv.}(\theta) = \left\langle \left| \sum_{j=1}^{21} E_v(\vec{r}_j, \omega) w_j^*(\vec{r}_j, \omega) \right|^2 \right\rangle_{f=3.6-4.3\ \mathrm{GHz}}, \tag{7.9}$$

where θ is the steering angle with respect to array broadside, $\vec{r}_j$ is the receiver spatial location, and the summation is taken over the 21-element receiving array. The angular brackets indicate an incoherent average through the signal bandwidth. The weight vector is the phase delay associated with the steering angle,

$$w_j(\vec{r}_j, \omega) = \left(\frac{i\omega d_j \sin\theta}{c} \right), \tag{7.10}$$

where d_j is the distance from receiver 1 ($d_j = 0$).

Beamforming with the frequency-difference autoproduct is performed by replacing the genuine electric field with the bandwidth-averaged frequency-difference autoproduct of Eq. (7.3) and summing over difference frequencies:

$$B_{AP}(\theta) = \left\langle \left| \sum_{j=1}^{21} \langle AP_{vv}(\vec{r}_j, \Delta\omega) \rangle_{BW} w_j^*(\vec{r}_j, \Delta\omega) \right|^2 \right\rangle_{\Delta f=105-325\ \mathrm{MHz}}, \tag{7.11}$$

where the weight vector is evaluated at the difference frequency. The difference frequency bandwidth, 105 MHz $\leq \Delta f \leq$ 325 MHz, was chosen to be significantly lower than the transmitted frequency content, but not so low in frequency that the results would be uninteresting, given the array size. In several underwater acoustics studies (Abadi et al., 2012; Douglass et al., 2017; Douglass and Dowling, 2019), the bandwidth average is performed incoherently, rather than inside the summation, to remove dependence on the source waveform. This is motivated by the emphasis on passive remote sensing in acoustics and is unnecessary here.

7.4.2 Results

In all beamforming plots, Eqs. (7.9) and (7.11) were evaluated for -90°$\leq \theta \leq$ 90°, in step size of 0.01°. Additionally, the beamformed outputs are reported in dB, normalized to the largest value. The true angle of arrival was approximately 14°.

The plane wave beamforming results for recordings in the park, light forest, and dense forest are shown in Fig. 7.7(a), Fig. 7.7(b), and Fig. 7.7(c), respectively. Dynamic range is reported on the vertical axis and the horizontal axis indicates the steering angle of the beamformer. The conventional (frequency-difference autoproduct) curve is shown in red (blue), and the true angle is denoted by the black vertical dashed line. In panel (a), both beamforming approaches accurately identify the direction of arrival and generally perform as expected. The autoproduct, owing to its effectively lower frequency content, exhibits a much larger lobe shape than the conventional method using the recorded electric field. The mild scattering effects of the light forest are illustrated in panel (b). Although both approaches identify the correct direction of arrival, dynamic range of the conventional approach is significantly reduced compared to the park results. Interestingly, the autoproduct curve is mostly unaltered from panel (a) to panel (b),

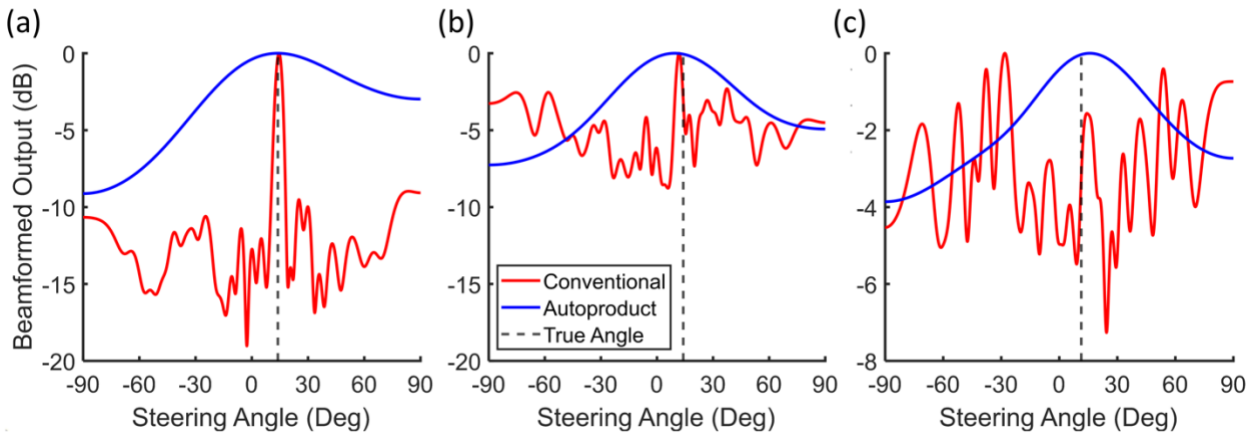

Figure 7.7: Direction of arrival estimation comparison between conventional (red) and autoproduct-based (blue) approaches in varying levels of scattering. Results from recordings collected in a scatterer-free park (a), light forest (b), and dense forest (c). Panels (a) and (b) share the same vertical limits, while vertical extent in panel (c) is much smaller. In all plots, the true angle is indicated by the vertical dashed line.

underscoring the autoproduct's ability to minimize the impacts of scattering. In panel (c), the scattering of the dense forest, shown in Fig. 7.5(b), completely corrupts the conventional plane wave beamforming strategy. Several local maxima exist within and the global peak incorrectly determines the direction of arrival by nearly 40°. Meanwhile, the frequency-difference autoproduct approach, computed from the same time domain recordings, currently identifies (4.4° error) the direction of arrival within its main lobe. The effects of scattering are not entirely removed, however, as the dynamic range of the autoproduct curve is reduced in panel (c) compared to panels (a) and (b).

Figure 7.7 demonstrates the robustness to scattering offered by the frequency-difference autoproduct. To further assess the lower-frequency field mimicry of the autoproduct, simulated free space fields at the difference frequencies, determined only from spherical spreading emanating from the target location, were computed. Conventional plane-wave beamforming on the simulated difference frequency data is shown in blue in Fig. 7.8. The autoproduct curves

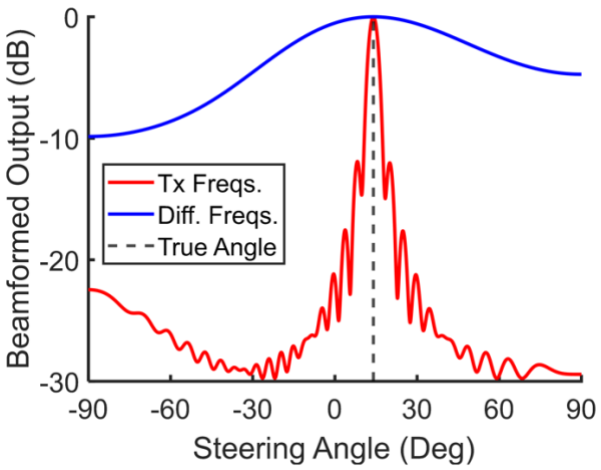

Figure 7.8: Direction of arrival estimation from simulated data of spherical spreading at the transmitted frequencies (red) and the difference frequencies (blue). The central lobe and overall dynamic range of the transmitted and difference frequencies generally match the conventional and autoproduct-based beamforming of experimental data in Fig. 7.7, respectively.

shown in Fig. 7.7, particularly in panels (a) and (b), match the beamformed outputs from conventional processing at the lower frequencies in free space. Hence, the autoproduct appears to be robust to scatterers in the propagation path and mimic lower frequency field content, as expected from the modeling in Chapter 7.2. Conventional plane-wave beamforming of simulated free space fields at the transmitted frequencies is shown in red in Fig. 7.8 as well and generally agrees with the experimental park result in Fig. 7.7(a).

7.5 Sparse Array Target Localization

The second set of target localization results implement the sparse array design introduced in Chapter 7.3 to estimate target location from the recorded signals. Prior to presentation of the results, conventional and autoproduct-based spherical wave beamforming is discussed.

7.5.1 Spherical Wave Beamforming

Spherical wave beamforming may be used when the array aperture is large enough to accommodate wavefront curvature. The implementation is similar to Eq. (7.9),

$$B_{Conv.}(\vec{r_s}) = \left\langle \left| \sum_{j=1}^{7} E_v(\vec{r_j}, \omega) w_j^*(\vec{r_j}, \omega) \right|^2 \right\rangle_{f=3.6-4.3\ \text{GHz}}, \tag{7.12}$$

where $\vec{r_s}$ is the search grid of potential target locations, and the summation is taken over the 7-element sparse receiving array. The weight vector for spherical wave beamforming is the spherical spreading phase associated with the search location, $\vec{r_s}$,

$$w_j(\vec{r_s}, \omega) = \exp\left(\frac{i\omega|\vec{r_s} - \vec{r_j}|}{c}\right). \tag{7.13}$$

Again, the autoproduct-based beamforming approach substitutes the genuine electric field with the bandwidth-averaged frequency-difference autoproduct and sums over difference frequencies:

$$B_{AP}(\vec{r_s}) = \left\langle \left| \sum_{j=1}^{7} \langle AP_{vv}(\vec{r_j}, \Delta\omega) \rangle_{BW} w_j^*(\vec{r_j}, \Delta\omega) \right|^2 \right\rangle_{\Delta f=85-260\ \text{MHz}}, \tag{7.14}$$

where difference frequency bandwidth, 85 MHz $\leq \Delta f \leq$ 260 MHz, is indicated.

7.5.2 Results

In all spherical wave beamforming plots, Eqs. (7.12) and (7.14) were evaluated on a 30 m × 30 m grid with 5 cm resolution. As with the plane-wave beamforming results, outputs are reported in dB, normalized to the maximum value. In each plot, the true target location is indicated by a white circle and the beamformed estimate is shown by a sideways, black-outlined triangle.

Sparse receiving array locations are marked by black-outlined triangles along the left of each plot.

Spherical wave beamforming outputs for recordings made in the park are shown in Fig. 9. The red-to-blue colormap covers 15 dB of dynamic range, and conventional and autoproduct-based outputs are shown in (a) and (b), respectively. Both approaches correctly determine the target location, and although the conventional approach identifies a slightly closer position, significant sidelobes populate the beamformed output due to the sparseness of the receiving array at the transmitted frequencies. For autoproduct beamforming, side lobes are entirely removed, owing to the effectively lower frequency content processed. As a result, the frequency-difference autoproduct may be an unconventional means of overcoming array sparsity. The claim of (effectively) lower frequency field content is further supported by examining Fig. 7.9(c). Conventional spherical wave beamforming of free space simulations at the difference

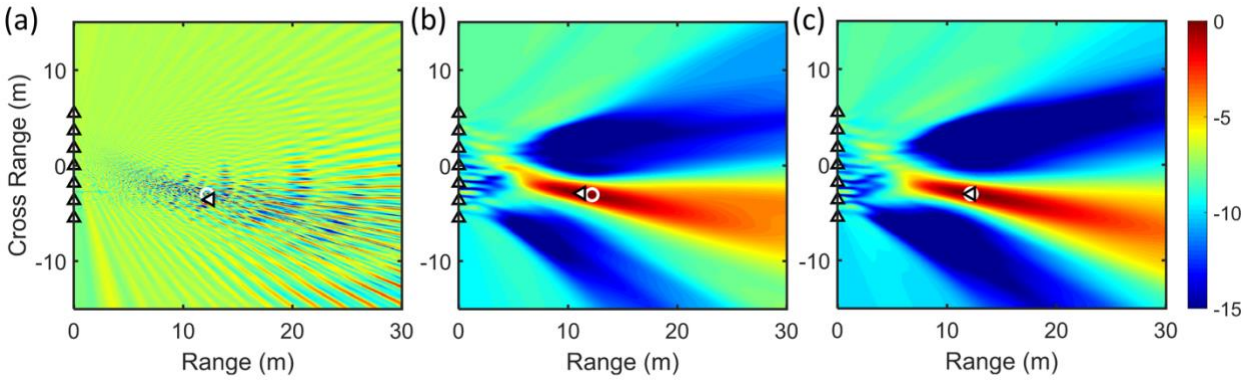

Figure 7.9: Comparisons of sparse array target localization in the park. Spherical wave beamforming outputs are shown with 15 dB dynamic range on range (horizontal) and cross range (vertical) axes, each 30 m extent. Conventional processing of the transmitted frequencies is shown in (a) and processing of the frequency-difference autoproduct is shown in (b). In (c), conventional processing of simulated free space fields at the difference frequencies are shown. The true target location is indicated by the white circle and the beamformed estimate is shown by the sideways triangle. Triangles on the left of the figure denote the receiving array.

frequencies, akin to the computations to produce Fig. 7.8, are shown in panel (c). Again, the lobe shapes and sizes correlate excellently with panel (b), autoproduct-based beamforming of higher frequency recorded signals.

In Fig. 7.10, the conventional (a) and frequency-difference autoproduct (b) spherical wave beamforming outputs are shown for recordings made in the dense forest. The random scattering caused by the dense forest, evident in the time domain recordings of Fig. 7.6(b), persists through the beamforming calculations. Both approaches incorrectly localize the target, but the autoproduct-based error (1.7 m) is a near miss and may be sufficient for some applications. Additionally, the autoproduct beamformed output is characterized by one major lobe, providing robustness in the estimated location. The shape of the lobe, although with reduced dynamic range, generally matches the plots shown in Fig. 7.9(b) and Fig. 7.9(c), indicative of mitigation of scattering effects. Meanwhile, many spurious peaks exist for the

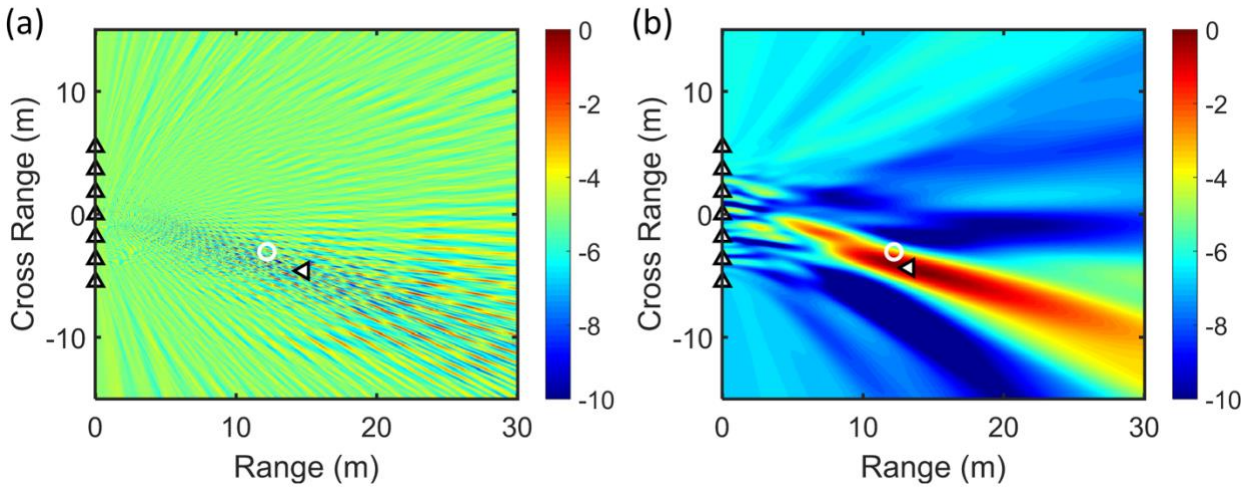

Figure 7.10: Comparisons of sparse array target localization for recordings in dense forest. Spherical wave beamforming outputs are shown with 10 dB dynamic range on range (horizontal) and cross range (vertical) axes, each 30 m extent. Conventional processing of the transmitted frequencies is shown in (a) and processing of the frequency-difference autoproduct is shown in (b). The true target location is indicated by the white circle and the beamformed estimate is shown by the sideways triangle. Triangles on the left of the figure denote the receiving array.

conventional processing approach, and the error (3 m) associated with the estimate is greater.

In wave propagation through random media, noise and timing jitter are common considerations. To assess autoproduct performance in the presence of these concerns, random noise and time delays were added in post-processing to the recorded signals shown in Fig. 7.6(b). Gaussian noise was added to the signal to reduce the signal-to-noise ratio (SNR) from ~20 dB to ~3 dB. Here, the approximate SNR was determined from a single receiver by isolating 10 ns near the target reflection and 10 ns near the end of the time record (where only noise exists). The SNR was then reported as one number by averaging across the signal bandwidth (in the frequency domain). Timing jitter was added by inserting random time delays to recorded signals with standard deviation of 0.4 ns. A 0.4 ns timing delay corresponds to spatial offset of 12 cm along the entire path length, well within experimental errors of transmitter, receiver, and target position. Computed from the same noisy, time-delayed signals, the conventional and frequency-difference autoproduct beamformed outputs are compared in Fig. 7.11.

Figure 7.11 demonstrates the benefit of the robust processing offered from the lower frequencies accessed by the frequency-difference autoproduct. Processing of the genuine electric field in panel (a) is nearly entirely useless. Poor localization (4 m error) is accompanied by a complete lack of dynamic range. On the other hand, a prominent main lobe exists in the autoproduct-based beamformed output of panel (b). Although the localization accuracy is not perfect (2 m error), the autoproduct approach suppresses spurious peaks and maintains 6 dB of dynamic range.

Finally, for some propagation scenarios, the random media may vary in time and/or the scatterers may not be stationary. In these cases, averaging the beamformed outputs from individual snapshots may improve localization performance. The sparse array target localizations

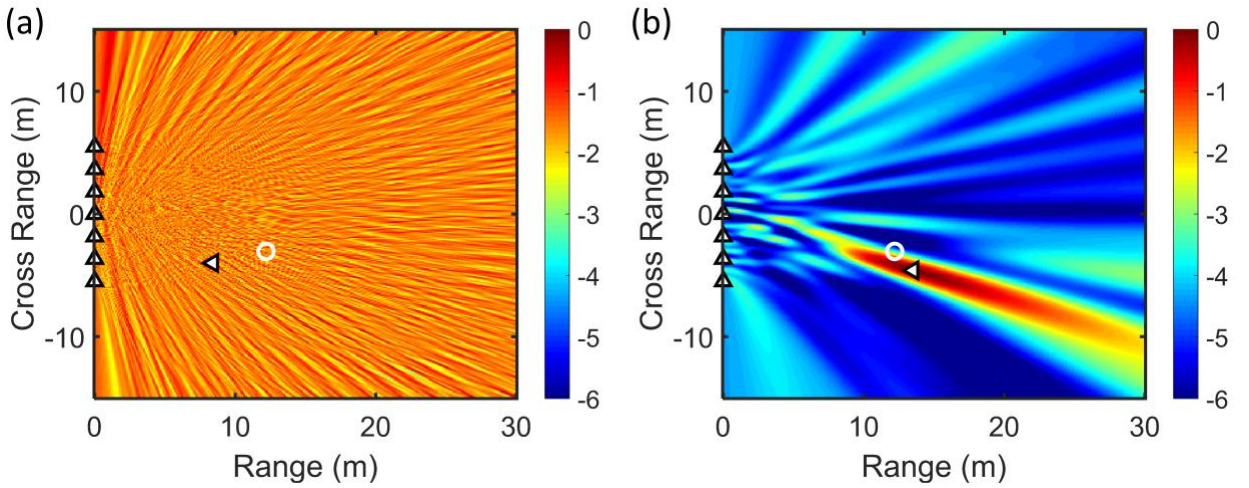

Figure 7.11: Comparisons of sparse array target localization for recordings in dense forest with added noise and timing jitter. Gaussian noise was added in the time domain to reduce the signal-to-noise ratio by 16.5 dB and the recorded signals were randomly time delayed with standard deviation of 0.4 ns. Spherical wave beamforming outputs are shown with 6 dB dynamic range on range (horizontal) and cross range (vertical) axes, each 30 m extent. Conventional processing of the transmitted frequencies is shown in (a) and processing of the frequency-difference autoproduct is shown in (b). The true target location is indicated by the white circle and the beamformed estimate is shown by the sideways triangle. Triangles on the left of the figure denote the receiving array.

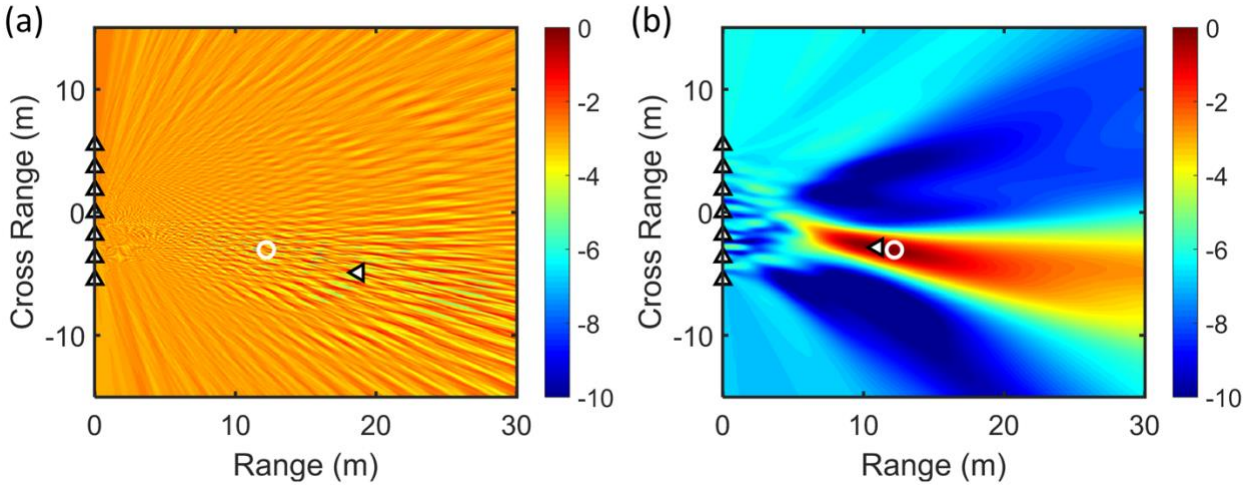

Figure 7.12: Average beamforming outputs for four target localization experiments in the park and in the dense forest. Conventional processing of the transmitted frequencies is shown in (a) and processing of the frequency-difference autoproduct is shown in (b). The true target location is indicated by the white circle and the beamformed estimate is shown by the sideways triangle. Triangles on the left of the figure denote the receiving array.

were conducted twice in both the park and the dense forest to imitate this scenario. Results from incoherently averaging the four beamformed outputs, two in the park and two in the forest, are shown in Fig. 7.12. When averaged, the highly varying conventional beamformed outputs significantly reduce the dynamic range of panel (a) and lead to a false localization result (6.8 m error). Meanwhile, the individual frequency-difference beamforming outputs contain a single lobe near the target location, see Figs. 7.9(b) and 7.10(b). Thus, averaging produces one central lobe, exhibiting 10 dB of dynamic range, with an accurate localization estimate (1.2 m).

7.6 Conclusion

The frequency-difference autoproduct is a pseudofield that synthetically estimates lower frequency field content through a quadratic product of higher frequency complex field amplitudes (Dowling, 2018). Generally investigated in acoustic propagation in ocean environments (Abadi et al., 2012; Douglass et al., 2017; Geroski et al., 2023; Joslyn et al., 2022; Worthmann et al., 2015), the frequency-difference concept has recently been used in seismic wave backprojection (Neo et al., 2022) and numerically-studied for electromagnetics (Geroski, 2021). The purpose of this work was to establish the electromagnetic frequency-difference autoproduct, a dyadic quantity constructed from the outer product of the electric field vector with itself at different frequencies, and explore its potential to enhance conventional electromagnetic remote sensing capabilities. Lower frequency field mimicry, critical to the success of autoproduct-based array signal processing, is assessed for plane wave propagation and scattering of plane wave by perfectly conducting infinite cylinders. Target localization experiments were conducted with and without scatterers in the propagation path, and the scattering strength of the randomly-located scatterers was varied by performing experiments in both lightly and densely forested areas on the University of Michigan campus. In simulations and experiments, only the

vertically-polarized element of the electric field, and therefore only the vertically-vertically polarized element of the dyadic autoproduct quantity, was considered.

Three conclusions are supported by the work presented here. First, the electromagnetic frequency-difference autoproduct is a measurable pseudofield quantity, capable of synthesizing lower frequency field content from higher recorded frequencies. The mimicry offered by the frequency-difference autoproduct is perfect for plane waves, but exhibits some caveats in more complicated environments. In particular, the frequency-difference autoproduct constructed from TM-polarized waves scattered from perfectly conducting infinite cylinders shares some features with the genuine electric field at the difference frequency, but mimicry is limited in the shadow zones, as expected from a scattering study of the acoustic autoproduct (Worthmann and Dowling, 2020a).

Second, the frequency-difference autoproduct provides a unique means of dealing with sparse arrays. Array configurations, sparse at the transmitted frequencies, may no longer be sparse for sufficiently low difference frequencies. As shown herein, by downshifting the recorded frequencies, prominent sidelobes in conventional spherical wave beamforming ambiguity surfaces were entirely removed in corresponding plots using frequency-difference autoproduct processing.

The third conclusion is that the frequency-difference autoproduct provides robust remote sensing performance in the presence of random scattering. By mimicking lower frequency field content where the impacts of scattering are less severe, the frequency-difference autoproduct minimizes the deleterious scattering effects and may be used in array signal processing tasks, even when the constituent fields contain significant scattering. Both direction of arrival and localization estimates, computed by beamforming signals recorded in forests with randomly-

located tree trunks of varying size, were improved from estimates obtained by conventional processing of the electric field. Moreover, random noise and timing jitter appear to be mitigated by the frequency-difference autoproduct as well, but further study is required.

Overall, the results presented here are positive. The electromagnetic frequency-difference autoproduct appears to be a genuine, meaningful quantity capable of enhancing array signal processing methodologies. Furthermore, the findings obtained here generally agree with acoustic autoproduct theory. Although this study was limited to the vv-element of the autoproduct dyadic, the conclusions should apply to the hh-element as well.

Chapter 8
Conclusions and Future Work

8.1 Conclusions

Broadly, this thesis covers two main objectives: recovery of coherence facilitated by the autoproduct and extensions to standard autoproduct theory. The thesis supports seven major conclusions related to these objectives. The listed conclusions require synthesis of contributions from several chapters or generalize beyond the work of any individual chapter. Chapter-dependent conclusions may be found in the final sections of Chapter 2 – 7.

1. Autoproduct coherence exists, and it is a theoretically-predictable and experimentally-measurable quantity. The increased coherence offered by the autoproduct underlies all previous remote sensing studies [i.e. (Douglass and Dowling, 2019; Geroski and Dowling, 2019; Worthmann et al., 2015)], yet, outside of (Douglass, 2019), actual measures of the coherence had not been reported. This thesis contains the first published work on autoproduct coherence itself (in Chapter 5), rather than its impact on array signal processing. Further, the theoretical development of autoproduct coherence, by way of the coherent reflection coefficient in Chapters 2 – 4, is unique to this thesis.

2. Recovery of coherent reflection in acoustic signals scattered from a randomly rough surface is possible by the frequency-difference autoproduct. Quantified by the coherent reflection coefficient, the first moment of the scattered field, much of Chapters 2 – 4 examine this concept. Important for array signal processing applications, the coherent reflection coefficient of the frequency-difference autoproduct can approach unity (ideal coherence) even when the coherent reflection coefficient of the constituent scattered fields is near zero (total incoherence). Coherent reflection recovery is shown for measurements collected in a laboratory water tank, the Pacific Ocean, and the Atlantic Oceans in Fig 2.10, Fig. 3.5, and Fig 4.7, respectively.

3. Recovery of coherent reflection is predictable from analytic equations. Equation (4.8) details a (numerically evaluated) formula relating an arbitrary surface autocorrelation function to the frequency-difference autoproduct coherent reflection coefficient. Under the assumption of a Gaussian surface autocorrelation function, an analytic formula, indicated in Eq. (2.20) and Eq. (3.4) may be derived, as shown in Chapter 2.2.3. Discussed in Chapter 4.2.3, the Fourier pair relationship between autocorrelation and power spectrum admits dependence of autoproduct formulas on the surface-height-fluctuation power spectrum. Theoretical predictions accompany the measurements of coherent reflection coefficients in Fig 2.10, Fig. 3.5, and Fig 4.7.

4. The predictability of autoproduct-based coherent reflection recovery provides a mechanism for environmental inversion from surface-scattered acoustic signals recorded by a single receiver. Provided a representation of the surface fluctuations (autocorrelation

or power spectrum) exists, refinements to the nominal surface characteristics may be made. Chapter 3 and Chapter 4 explore this possibility for an ocean surface well-described by a Gaussian autocorrelation function and an ocean surface possessing a non-analytic power spectrum, respectively. In both chapters, minor modifications within noted experimental uncertainties produced better agreement between theoretical and measured autoproducts. Interestingly, the adjustments found in Chapter 3 match those determined 25 years ago from analysis of spatial coherence with multiple receivers in the same environment (Dahl, 1996).

5. Extensions to the standard quadratic autoproduct used in acoustics are possible and follow the intuition built from quadratic autoproduct theory. Chapter 6 investigates higher-order autoproducts in underwater acoustics, with the primary focus on the cubic frequency-difference autoproduct. The cubic frequency-difference autoproduct is formulated and the governing field equation shows similarities to the quadratic autoproduct field equation determined in (Worthmann and Dowling, 2017). In Chapter 7, the electromagnetic frequency-difference autoproduct, initially studied in (Geroski, 2021), is investigated numerically and experimentally. The dyadic autoproduct quantity, formed from an outer product of the recorded electric field vector, is formulated and the numerically-evaluated autoproduct in scattering from a perfectly conducting infinite cylinder shares features with the acoustic autoproduct in Mie scattering from a sphere (Worthmann and Dowling, 2020a).

6. The bandwidth-averaged cubic frequency-difference autoproduct provides an unconventional means of noise suppression within the signal bandwidth. The large number of cubic autoproduct samples possible, detailed in Eq. (6.14) and discussed in Chapter 6.3, reduce the impact of noise when averaged together. As the cubic frequency-difference autoproduct is a pseudofield representation of frequencies within the signal bandwidth (see field comparisons in a uniform half-space in Chapter 6.2.3), the cubic frequency-difference autoproduct may be used in array signal processing to reduce noise and maintain resolution. Using acoustic measurements collected in the Atlantic Ocean (of both signal and ambient noise), the cubic frequency-difference autoproduct was able to determine the direction of arrival, even when the noise power corrupted direction of arrival estimates computed from the recorded field. Comparisons of conventional and cubic autoproduct-based processing for direction of arrival estimation are shown in Fig. 6.6 and Fig. 6.7.

7. The electromagnetic frequency-difference autoproduct may be employed to mitigate two common problems in array signal processing: array sparsity and random scattering. At sufficiently-low difference frequencies, any array configuration is no longer sparse and the effects of random scattering are less prominent. Active localization of a metallic target (located approximately 12.2 m from the transmitting and receiving antennas) positioned in a randomly-scattering forested area supported these claims. Direction of arrival estimates, computed from recordings made by a small aperture array, are shown in Fig. 7.7. Spherical wave beamforming plots, computed from recordings made by a sparse array, are shown in Figs. 7.9 – 7.12.

8.2 Future Work

This thesis provides the groundwork for several further investigations. In particular, many remote sensing avenues are possible given the formal establishment of the cubic frequency-difference autoproduct and the electromagnetic frequency-difference autoproduct. Additionally, the work on rough surface scattering has natural extensions. A few possibilities are outlined below.

Frequency-difference autoproducts constructed from acoustic fields scattered by a randomly-varying ocean surface were investigated thoroughly in Chapters 2 – 4. Extensions to surfaces defined by power spectra not explored here, for instance the popular Pierson-Moskowitz spectrum (Thorsos, 1990), are clearly possible. For signal processing tasks reliant on surface reflection, autoproduct formulas for additional power spectra may lead to improved outcomes. Also, given the ability to perform surface inversion (see Chapters 3 and 4), additional power spectra may provide better environmental characterization. For Pierson-Moskowitz, the autocorrelation function shown in (Yang et al., 2020) may be a good place to start.

Given the existence of Eq. (4.8), which numerically predicts the frequency-difference autoproduct coherent reflection coefficient for scattering from a surface with arbitrary autocorrelation function, perhaps the more fruitful avenue of research in this area concerns scattering from the seafloor. Unlike the sea surface, a constant reflection coefficient (of –1) cannot be assumed as sound incident on the ocean floor is both transmitted and reflected. Furthermore, the seafloor is not time-varying, so the ensemble average utilized in derivations of coherent reflection coefficients cannot be directly applied. However, obtaining recordings of

sound scattered from different bottom locations and averaging may be equivalent (Clay, 1966). Seafloor scattering is a popular area of current research (Brown et al., 2018; Olson, 2023; Olson and Jackson, 2020), and autoproduct studies could proceed with theory, simulation, or experiment.

Several directions exist for future research using the cubic frequency-difference autoproduct. Multipath arrivals can cause issues for quadratic autoproducts, due to the proliferation of cross terms, and this problem is amplified for the cubic autoproduct, as shown in Chapter 6.2.3. Thus, assessing the performance of cubic autoproduct-based array signal processing algorithms, i.e. matched field processing, in multipath environments is a critical next step. Experimental geometries with longer ranges, propagation through more complicated environments, or the presence of a genuine noise source, rather than artificially inflating the ambient noise as in Chapter 6, are potential future directions as well.

Similarly, the establishment of the electromagnetic frequency-difference autoproduct opens many exciting areas of research. For the experiment discussed in Chapter 7, selection of an omnidirectional target reflector, i.e. a curved metallic surface, ensonifies more scatterers in the propagation path, thereby increasing the random scattering strength. Assessment of the three other nonzero elements of the frequency-difference autoproduct dyadic represents the most interesting future research. Simulations conducted in (Geroski, 2021) demonstrated the hh-polarized element was more robust to vertical scatterers than the vv-polarized element. Hence, a target localization experiment, equivalent that of Chapter 7, using horizontally-polarized electric fields may provide even more compelling autoproduct remote sensing performance. The cross-

polarized elements have no analogue to acoustics (a scalar wave field), and thus would provide an entirely new avenue of autoproduct-based research.

As a final possibility, the work of Chapters 2 – 4 and Chapter 7 provide the basis for studying the frequency-difference autoproduct constructed from rough-surface-scattered constituent electric fields. In electromagnetics, scattering matrices are dyadic quantities themselves, so the mathematics may become tedious. However, the recovery of coherent reflection at sufficiently-low difference frequencies is likely to persist to electromagnetics, which may be of interest to practitioners in the area.

Appendix

Bandwidth-Averaged Cubic Frequency-Difference Autoproduct in a Two-Path Environment

This appendix provides auxiliary information for the analytical derivation of *Chapter 6.2.3: Cubic Frequency-Difference Autoproduct in Lloyd's Mirror Environment*. Lloyd's mirror, a uniform half-space with a constant reflection coefficient at the surface, is the simplest multipath environment to assess the bandwidth-averaged cubic frequency-difference and was used in a previous study of quadratic autoproducts (Lipa et al., 2018). In this environment, the bandwidth-averaged cubic frequency-difference autoproduct is a lengthy combination of self-path terms and cross-path terms. Much of this clutter was removed in Eq. (6.12) through use of γ_1 and γ_2. An overview of the derivation producing Eq. (6.12) accompanies enumeration of these variables.

The theoretical Green's function for Lloyd's mirror is

$$G(\boldsymbol{r},\omega) = \frac{P(\boldsymbol{r},\omega)}{S(\omega)} = \frac{e^{i\omega\tau_1}}{r_1} - \frac{e^{i\omega\tau_2}}{r_2}, \tag{A1}$$

where $r_{1,2}$ are the direct and reflected path distances, $\tau_{1,2} = r_{1,2}/c$, and the reflection coefficient of –1 for the water-air interface is the coefficient of the second term. The cubic frequency-difference autoproduct [Eq. (6.2)], $AP_{III}(\boldsymbol{r},\omega_1,\omega_2,\Delta\omega) = P(\boldsymbol{r},\omega_1)P(\boldsymbol{r},\omega_2)P^*(\boldsymbol{r},\omega_3)$, may be bandwidth averaged as shown in Eq. (6.9) and reproduced here,

$$\langle AP_{III}(\boldsymbol{r},\Delta\omega)\rangle_{BW} = \frac{1}{\beta_H^{\Delta}-\beta_L^{\Delta}}\int_{\beta_L^{\Delta}}^{\beta_H^{\Delta}} d(\omega)\left[\frac{1}{\alpha_{BW}^{\Delta}}\int_0^{\alpha_{BW}^{\Delta}}\frac{AP_{III}(\boldsymbol{r},\omega_1,\omega_2,\Delta\omega)}{S(\omega_1)S(\omega_2)S^*(\omega_3)}d(\Delta\omega_1)\right]. \quad \text{(A2)}$$

Analytical evaluation of Eq. (A2) requires careful consideration of the limits of integration. The selection of the inner limit, $\alpha_{BW}^{\Delta} = \min[2\omega - 2\Omega_L,\ 2\Omega_H - 2\omega]$, depends on the outer integration variable, ω, and may take on either value of the argument. In fact, for $\Omega_L \le \Delta\omega \le \Omega_H$, the emphasis of this work, analytical evaluation of Eq. (A2) requires breaking the integral into two parts,

$$\langle AP_{III}(\boldsymbol{r},\Delta\omega)\rangle_{BW} = \frac{1}{\beta_H^{\Delta}-\beta_L^{\Delta}}\left\{\begin{array}{l}\displaystyle\int_{\beta_L^{\Delta}}^{\Omega_C} d(\omega)\left[\frac{1}{\alpha_{BW}^{\Delta}}\int_0^{\alpha_{BW}^{\Delta}}\frac{AP_{III}(\boldsymbol{r},\omega_1,\omega_2,\Delta\omega)}{S(\omega_1)S(\omega_2)S^*(\omega_3)}d(\Delta\omega_1)\right] \\ \displaystyle+\int_{\Omega_C}^{\beta_H^{\Delta}} d(\omega)\left[\frac{1}{\alpha_{BW}^{\Delta}}\int_0^{\alpha_{BW}^{\Delta}}\frac{AP_{III}(\boldsymbol{r},\omega_1,\omega_2,\Delta\omega)}{S(\omega_1)S(\omega_2)S^*(\omega_3)}d(\Delta\omega_1)\right]\end{array}\right\}, \quad \text{(A3)}$$

where the first integral sets $\alpha_{BW}^{\Delta} = 2\omega - 2\Omega_L$ and the second integral sets $\alpha_{BW}^{\Delta} = 2\Omega_H - 2\omega$. Since $\Delta\omega$ resides within the signal bandwidth, $\beta_L^{\Delta} = (\Omega_L + \Delta\omega)/2$ and $\beta_H^{\Delta} = (\Omega_H + \Delta\omega)/2$.

Substitution of Eq. (6.11) (a cubic autoproduct sample in Lloyd's mirror environment) into the first integration term of Eq. (A3) yields a double integration of the six terms constituting a single cubic autoproduct sample. While the inner integration is rather mundane, the outer integral requires an integration by parts and integral tabulations (i.e. Mathematica). Hence,

$$\int_{\beta_L^{\Delta}}^{\Omega_C} d(\omega)\left[\frac{1}{\alpha_{BW}^{\Delta}}\int_0^{\alpha_{BW}^{\Delta}}\frac{AP_{III}(\boldsymbol{r},\omega_1,\omega_2,\Delta\omega)}{S(\omega_1)S(\omega_2)S^*(\omega_3)}d(\Delta\omega_1)\right] = \left(\Omega_C - \beta_L^{\Delta}\right)\left\{\frac{e^{i\Delta\omega\tau_1}}{r_1^3} - \frac{e^{i\Delta\omega\tau_2}}{r_2^3}\right\} \quad \text{(A4)}$$

$$+\frac{1}{\Delta\tau}\left\{\frac{ie^{i\Delta\omega\tau_2}}{2r_1^2r_2}\left(e^{-2i\beta_L^{\Delta}\Delta\tau} - e^{-2i\Omega_C\Delta\tau}\right) + \frac{ie^{i\Delta\omega\tau_1}}{2r_1r_2^2}\left(e^{2i\beta_L^{\Delta}\Delta\tau} - e^{2i\Omega_C\Delta\tau}\right)\right\}$$

$$-\frac{2e^{i\Delta\omega\tau_1}}{r_1^2r_2\Delta\tau}\left[-\frac{ie^{i\Omega_L\Delta\tau}}{2}\left(-\mathrm{Ei}\left[2i\left(\beta_L^{\Delta}-\Omega_L\right)\Delta\tau\right] + \mathrm{Ei}[2i(\Omega_C-\Omega_L)\Delta\tau] + \ln\left[\frac{\beta_L^{\Delta}-\Omega_L}{\Omega_C-\Omega_L}\right]\right)\right]$$

$$+\frac{2e^{i\Delta\omega\tau_2}}{r_1r_2^2\Delta\tau}\left[\frac{ie^{-i\Omega_L\Delta\tau}}{2}\left(-\mathrm{Ei}\left[-2i\left(\beta_L^{\Delta}-\Omega_L\right)\Delta\tau\right] + \mathrm{Ei}[-2i(\Omega_C-\Omega_L)\Delta\tau] + \ln\left[\frac{\beta_L^{\Delta}-\Omega_L}{\Omega_C-\Omega_L}\right]\right)\right],$$

where $\mathrm{Ei}(x)$ is the exponential integral function of argument x and $\ln(x)$ is the natural logarithm of argument x. Evaluation of the second integration term in Eq. (A3) proceeds similarly. However, the difference in sign of ω in the upper limit of the inner integral produces a slightly different result:

$$\int_{\Omega_C}^{\beta_H^\Delta} d(\omega)\left[\frac{1}{\alpha_{BW}^\Delta}\int_0^{\alpha_{BW}^\Delta}\frac{AP_{III}(\boldsymbol{r},\omega_1,\omega_2,\Delta\omega)}{S(\omega_1)S(\omega_2)S^*(\omega_3)}\,d(\Delta\omega_1)\right] = \left(\beta_H^\Delta-\Omega_C\right)\left\{\frac{e^{i\Delta\omega\tau_1}}{r_1^3}-\frac{e^{i\Delta\omega\tau_2}}{r_2^3}\right\} \quad \text{(A5)}$$

$$+\frac{1}{\Delta\tau}\left\{\frac{ie^{i\Delta\omega\tau_2}}{2r_1^2r_2}\left(e^{-2i\Omega_C\Delta\tau}-e^{-2i\beta_H^\Delta\Delta\tau}\right)+\frac{ie^{i\Delta\omega_2\tau_1}}{2r_1r_2^2}\left(e^{2i\Omega_C\Delta\tau}-e^{2i\beta_H^\Delta\Delta\tau}\right)\right\}$$

$$-\frac{2e^{i\Delta\omega\tau_1}}{r_1^2r_2\Delta\tau}\left[\frac{ie^{i\Omega_H\Delta\tau}}{2}\left(\mathrm{Ei}[2i(\Omega_C-\Omega_H)\Delta\tau]-\mathrm{Ei}\left[2i\left(\beta_H^\Delta-\Omega_H\right)\Delta\tau\right]+\ln\left[\frac{\Omega_H-\beta_H^\Delta}{\Omega_H-\Omega_C}\right]\right)\right]$$

$$+\frac{2e^{i\Delta\omega\tau_2}}{r_1r_2^2\Delta\tau}\left[-\frac{ie^{-i\Omega_H\Delta\tau}}{2}\left(\mathrm{Ei}[-2i(\Omega_C-\Omega_H)\Delta\tau]-\mathrm{Ei}\left[-2i\left(\beta_H^\Delta-\Omega_H\right)\Delta\tau\right]+\ln\left[\frac{\Omega_H-\beta_H^\Delta}{\Omega_H-\Omega_C}\right]\right)\right].$$

Insertion of Eq. (A4) and Eq. (A5) into Eq. (A3) produces, after grouping of like terms and simplification, the bandwidth-averaged cubic frequency-difference autoproduct in a Lloyd's mirror environment for $\Omega_L \le \Delta\omega \le \Omega_H$:

$$\langle AP_{III}(\boldsymbol{r},\Delta\omega)\rangle_{BW} = \frac{e^{i\Delta\omega\tau_1}}{r_1^3}-\frac{e^{i\Delta\omega\tau_2}}{r_2^3}+\frac{1}{\left(\beta_H^\Delta-\beta_L^\Delta\right)\Delta\tau}\left[\frac{\gamma_1}{r_1^2r_2}+\frac{\gamma_2}{r_1r_2^2}\right] \quad \text{(A6)}$$

where γ_1 and γ_2 are determined from terms with a $1/r_1^2r_2$ and a $1/r_1r_2^2$ coefficient, respectively. Thus,

$$\gamma_1 = \frac{ie^{i\Delta\omega\tau_2}}{2}\left(e^{-2i\beta_L^\Delta\Delta\tau}-e^{-2i\beta_H^\Delta\Delta\tau}\right) \quad \text{(A7)}$$

$$-e^{i\Delta\omega\tau_1}\left\{ie^{i\Omega_H\Delta\tau}\left(\mathrm{Ei}[2i(\Omega_C-\Omega_H)\Delta\tau]-\mathrm{Ei}\left[2i\left(\beta_H^\Delta-\Omega_H\right)\Delta\tau\right]+\ln\left[\frac{\Omega_H-\beta_H^\Delta}{\Omega_H-\Omega_C}\right]\right)\right.$$

$$\left.-ie^{i\Omega_L\Delta\tau}\left(-\mathrm{Ei}\left[2i\left(\beta_L^\Delta-\Omega_L\right)\Delta\tau\right]+\mathrm{Ei}[2i(\Omega_C-\Omega_L)\Delta\tau]+\ln\left[\frac{\beta_L^\Delta-\Omega_L}{\Omega_C-\Omega_L}\right]\right)\right\}$$

and

$$\gamma_2 = \frac{ie^{i\Delta\omega\tau_1}}{2}\left(e^{2i\beta_L^{\Delta}\Delta\tau} - e^{2i\beta_H^{\Delta}\Delta\tau}\right) \tag{A8}$$

$$+e^{i\Delta\omega\tau_2}\left\{ ie^{-i\Omega_L\Delta\tau}\left(-\mathrm{Ei}\left[-2i\left(\beta_L^{\Delta}-\Omega_L\right)\Delta\tau\right] + \mathrm{Ei}[-2i(\Omega_C-\Omega_L)\Delta\tau] + \ln\left[\frac{\beta_L^{\Delta}-\Omega_L}{\Omega_C-\Omega_L}\right]\right)\right.$$

$$\left. - ie^{-i\Omega_H\Delta\tau}\left(\mathrm{Ei}[-2i(\Omega_C-\Omega_H)\Delta\tau] - \mathrm{Ei}\left[-2i\left(\beta_H^{\Delta}-\Omega_H\right)\Delta\tau\right] + \ln\left[\frac{\Omega_H-\beta_H^{\Delta}}{\Omega_H-\Omega_C}\right]\right)\right\}$$

The symmetry between γ_1 and γ_2 is expected due to their encapsulation of cross terms arising from one reflected-path field factor and two reflected-path field factors, respectively. Interestingly, of the 8 terms captured by $\gamma_{1,2}$, 6 of these terms, shown in curly braces, asymptotically tend to 0 with increasing bandwidth. As the bandwidth increases, the combinations of Ei terms approach 0 and the argument of the logarithmic terms approaches unity. The remaining two terms feature no suppression mechanisms. However, as noted in Chapter 6.2.3, all eight terms are preceded by $1/(\beta_H^{\Delta}-\beta_L^{\Delta})\Delta\tau$ factor in the full formula in Eq. (A6), corresponding to additional cross term suppression for large bandwidths or large arrival time differences.

Analytical formulas for $\Delta\omega < \Omega_L$ and $\Delta\omega > \Omega_H$ are obtainable by direct evaluation of Eq. (A2) with appropriate selection of the limits, $\left[\alpha_{BW}^{\Delta} = 2\omega - 2\Omega_L;\ \beta_L^{\Delta} = \Omega_L;\ \beta_H^{\Delta} = (\Omega_H + \Delta\omega)/2\right]$ and $\left[\alpha_{BW}^{\Delta} = 2\Omega_H - 2\omega\ ;\ \beta_L^{\Delta} = (\Omega_L + \Delta\omega)/2\ ;\ \beta_H^{\Delta} = \Omega_H\right]$, respectively. Due to the focus of the cubic frequency-difference autoproduct on mimicking frequency content within $\Omega_L \leq \Delta\omega \leq \Omega_H$, those forms were not pursued here.

Bibliography

Abadi, S. H., and Freneau, E. (**2019**). "Short-range propagation characteristics of airgun pulses during marine seismic reflection surveys," J. Acoust. Soc. Am., **146**, 2430–2442. doi:10.1121/1.5127843

Abadi, S. H., Haworth, K. J., Mercado-Shekhar, K. P., and Dowling, D. R. (**2018**). "Frequency-sum beamforming for passive cavitation imaging," J. Acoust. Soc. Am., **144**, 198–209. doi:10.1121/1.5045328

Abadi, S. H., Van Overloop, M. J., and Dowling, D. R. (**2013**). "Frequency-sum beamforming in an inhomogeneous environment," Proc. Meet. Acoust., doi:10.1121/1.4799027. doi:10.1121/1.4799027

Abadi, S. H., Song, H. C., and Dowling, D. R. (**2012**). "Broadband sparse-array blind deconvolution using frequency-difference beamforming," J. Acoust. Soc. Am., **132**, 3018–3029. doi:10.1121/1.4756920

Andrew, R. K., Howe, B. M., and Mercer, J. A. (**2005**). "Transverse horizontal spatial coherence of deep arrivals at megameter ranges," J. Acoust. Soc. Am., **117**, 1511–1526. doi:10.1121/1.1854851

Apel, J. R. (**1994**). "An improved model of the ocean surface wave vector spectrum and its effects on radar backscatter," J. Geophys. Res., **99**, 269–291. doi:10.1029/94jc00846

Auton, A. (**2021**). *Red Blue Colormap*, Available: https://www.mathworks.com/matlabcentral/fileexchange/25536-red-blue-colormap.

Baggeroer, A. B., Kuperman, W. A., and Mikhalevsky, P. N. (**1993**). "An overview of matched field methods in ocean acoustics," IEEE J. Ocean. Eng., **18**, 401–424. doi:10.1109/48.262292

Bass, F. G., and Fuks, I. M. (**1979**). *Wave Scattering from Statistically Rough Surfaces*, Pergamon, Oxford.

Beck, B., Ma, X., and Baxley, R. (**2016**). "Ultrawideband tomographic imaging in uncalibrated networks," IEEE Trans. Wireless Comm., **15**, 6474–6486. doi:10.1109/TWC.2016.2585141

Beckmann, P., and Spizzichino, A. (**1963**). *The Scattering of Electromagnetic Waves from Rough Surfaces*, MacMillan, New York.

Bendat, J. S., and Piersol, A. G. (**1980**). *Engineering Applications of Correlation and Spectral Analysis*, Wiley and Sons, New York.

Bergström, D. (**2012**). *MySimLabs*, Available: http://www.mysimlabs.com/index.html

Berkson, J. M. (**1980**). "Measurements of coherence of sound reflected from ocean sediments," J. Acoust. Soc. Amer., **68**, 1436–1441. doi:10.1121/1.385110

Bozma, Ö., and Kuc, R. (**1991**). "Characterizing pulses reflected from rough surfaces using ultrasound," J Acoust Soc Am, **89**, 2519–2531. doi:10.1121/1.400692

Brekhovskikh, L. M., and Lysanov, Y. P. (**1991**). *Fundamentals of Ocean Acoustics*, Springer-Verlag, New York.

Brown, D. C., Brownstead, C. F., Lyons, A. P., and Gabrielson, T. B. (**2018**). "Measurements of two-dimensional spatial coherence of normal-incidence seafloor scattering," J. Acoust. Soc. Am., **144**, 2095–2108. doi:10.1121/1.5056168

Bucker, H. P. (**1976**). "Use of calculated sound fields and matched-field detection to locate sound sources in shallow water," J. Acoust. Soc. Am., **59**, 368–373. doi:10.1121/1.380872

Carey, W. M. (**1998**). "Determination of signal coherence length based on signal coherence and gain measurements in deep and shallow water," J. Acoust. Soc. Am., **104**, 831–837. doi:10.1121/1.423357

Carey, W. M., and Moseley, W. B. (**1991**). "Space-Time Processing Environmental-Acoustic Effects," IEEE J. Ocean. Eng., **16**, 285–301.

Carter, G. C. (**1987**). "Coherence and time delay estimation," Proceedings of the IEEE, **75**, 236–255. doi:10.1109/PROC.1987.13723

Carter, G. C., Knapp, C. H., and Nuttall, A. H. (**1973**). "Statistics of the Estimate of the Magnitude-Coherence Function," IEEE Trans. Audio Electroacoust., **21**, 388–389. doi:10.1109/TAU.1973.1162487

Chapman, D. M. F. (**1980**). "The directional nature of attenuation of sound due to scattering at a rough ocean surface," J. Acoust. Soc. Am., **68**, 1475–1481. doi:10.1121/1.385071

Chee, K. L., Catalán, F., Torrico, S. A., and Kürner, T. (**2014**). "Modeling tree scattering in rural residential areas at 3.5 GHz," Radio Sci, **49**, 44–52. doi:10.1002/2013RS005173

Clay, C. S. (**1966**). "Coherent reflection of sound from the ocean bottom," J. Geophys. Res., **71**, 2037–2046. doi:10.1029/jz071i008p02037

Cohen, L. (**1989**). "Time-Frequency Distributions-A Review," Proc. IEEE, **77**, 941–981.

Cox, H. (**1973**). "Line array performance when the signal coherence is spatially dependent," J. Acoust. Soc. Am., **54**, 1743–1746. doi:10.1121/1.1914473

Cox, H., Zeskind, R. M., and Owen, M. M. (**1987**). "Robust Adaptive Beamforming," IEEE Trans. Acoust., **ASSP-35**, 1365–1376.

Dahl, P. H. (**1996**). "On the spatial coherence and angular spreading of sound forward scattered from the sea surface: Measurements and interpretive model," J. Acoust. Soc. Am., **100**, 748–758.

Dahl, P. H. (**1999**). "On bistatic sea surface scattering: Field measurements and modeling," J Acoust. Soc. Am., **105**, 2155–2169. doi:10.1121/1.426820

Dahl, P. H. (**2001**). "High-Frequency Forward Scattering from the Sea Surface: The Characteristic Scales of Time and Angle Spreading," IEEE J. Ocean. Eng., **26**, 141–151.

Dahl, P. H. (**2003**). "The contribution of bubbles to high-frequency sea surface backscatter: A 24-h time series of field measurements," J. Acoust. Soc. Am., **113**, 769–780. doi:10.1121/1.1532029

Dahl, P. H. (**2004**). "Forward scattering from the sea surface and the van Cittert–Zernike theorem," J. Acoust. Soc. Am., **115**, 589–599. doi:10.1121/1.1635417

Dahl, P. H. (**2010**). "Observations and modeling of angular compression and vertical spatial coherence in sea surface forward scattering," J. Acoust. Soc. Am., **127**, 96–103. doi:10.1121/1.3268594

Dahl, P. H., Choi, J. W., Williams, N. J., and Graber, H. C. (**2008**). "Field measurements and modeling of attenuation from near-surface bubbles for frequencies 1–20kHz," J. Acoust. Soc. Am., **124**, EL163–EL169. doi:10.1121/1.2963096

Dahl, P. H., and Jessup, A. T. (**1995**). "On bubble clouds produced by breaking waves: an event analysis of ocean acoustic measurements," J. Geophys. Res., **100**, 5007–5020. doi:10.1029/94JC03019

Dahl, P. H., and Plant, W. J. (**1997**). "The variability of high-frequency acoustic backscatter from the region near the sea surface," J. Acoust. Soc. Am., **101**, 2596–2602. doi:10.1121/1.419307

Dahl, P. H., Plant, W. J., and Dall'Osto, D. R. (**2013**). "Vertical coherence and forward scattering from the sea surface and the relation to the directional wave spectrum," J. Acoust. Soc. Am., **134**, 1843–1853. doi:10.1121/1.4817846

Darawankul, A., and Johnson, J. T. (**2007**). "Band-limited exponential correlation function for rough-surface scattering," IEEE Trans. Geo. Rem. Sens., **45**, 1198–1206. doi:10.1109/TGRS.2007.893817

Darmon, M., Dorval, V., and Baqué, F. (**2020**). "Acoustic Scattering Models from Rough Surfaces: A Brief Review and Recent Advances," Appl. Sci., **10**, 1–27. doi:10.3390/app10228305

Diebold, J. B., Tolstoy, M., Doermann, L., Nooner, S. L., Webb, S. C., and Crone, T. J. (**2010**). "R/V Marcus G. Langseth seismic source: Modeling and calibration," Geochem., Geophys., Geosys. doi: 10.1029/2010GC003216. doi:10.1029/2010GC003216

Douglass, A. (**2019**). *Beamforming and Source Quantification in Complex Environments Using In-Band and Out-of-Band Methods*, Ph.D. dissertation, Univ. of Mich., Ann Arbor, MI.

Douglass, A. S., and Dowling, D. R. (**2019**). "Frequency-difference beamforming in the presence of strong random scattering," J. Acoust. Soc. Am., **146**, 122–134. doi:10.1121/1.5114811

Douglass, A. S., Song, H. C., and Dowling, D. R. (**2017**). "Performance comparisons of frequency-difference and conventional beamforming," J. Acoust. Soc. Amer., **142**, 1663–1673. doi:10.1121/1.5003787

Dowling, D. R. (**2018**). "Revealing hidden information with quadratic products of acoustic field amplitudes," Phys. Rev. Fluids 3, 110506. doi: 10.1103/PhysRevFluids.3.110506.

Dowling, D. R., and Jackson, D. R. (**1993**). "Coherence of acoustic scattering from a dynamic rough surface," J. Acoust. Soc. Amer., **93**, 3149–3157. doi:10.1121/1.405699

Duda, T. F., Collis, J. M., Lin, Y.-T., Newhall, A. E., Lynch, J. F., and DeFerrari, H. A. (**2012**). "Horizontal coherence of low-frequency fixed-path sound in a continental shelf region with internal-wave activity," J. Acoust. Soc. Amer., **131**, 1782–1797. doi:10.1121/1.3666003

Eckart, C. (**1953**). "The Scattering of Sound from the Sea Surface," J. Acoust. Soc. Am., **25**, 566–570. doi:10.1121/1.1907123

Edgar, M., Aw, J., Dudley, J., Marley, R., Reid, A., Smith, Z., Taylor, A., et al. (**2012**). "Characterization of a UWB Transceiver for Mining Applications," Australian Mining Tech. Conf., 125–140.

Elfouhaily, T. M., and Guérin, C. A. (**2004**). "A critical survey of approximate scattering wave theories from random rough surfaces," Waves Rand. Med. 14, R1-R40. doi:10.1088/0959-7174/14/4/R01

Finette, S., and Oba, R. (**2003**). "Horizontal array beamforming in an azimuthally anisotropic internal wave field," J. Acoust. Soc. Am., **114**, 131–144. doi:10.1121/1.1582441

Fortuin, L. (**1970**). "Survey of Literature on Reflection and Scattering of Sound Waves at the Sea Surface," J. Acoust. Soc. Am., **47**, 1209–1228. doi:10.1121/1.1912022

Fung, A. K., and Moore, R. K. (**1966**). "The correlation function in Kirchoff's method of solution of scattering of waves from statistically rough surfaces," J. Geophys. Res., **71**, 2939–2943. doi:10.1029/jz071i012p02939

Geroski, D. (**2021**). *Wave Propagation and Source Localization in Random and Refracting Media,* Ph.D. dissertation, Univ. Mich., Ann Arbor, MI.

Geroski, D. J., and Dowling, D. R. (**2019**). "Long-range frequency-difference source localization in the Philippine Sea," J. Acoust. Soc. Am., **146**, 4727–4739. doi:10.1121/1.5138124

Geroski, D. J., and Dowling, D. R. (**2021**). "Robust long-range source localization in the deep ocean using phase-only matched autoproduct processing," J. Acoust. Soc. Am., **150**, 171–182. doi:10.1121/10.0005477

Geroski, D. J., Dzieciuch, M. A., and Dowling, D. R. (**2021**). "Measurements of the correlation of the frequency-difference autoproduct with acoustic and predicted-autoproduct fields in the deep ocean," J. Acoust. Soc. Am., **149**, 853–865. doi:10.1121/10.0003377

Geroski, D. J., Johnson, J. R., and Dowling, D. R. (**2023**). "Localization of a remote source in a noisy deep ocean sound channel using phase-only matched autoproduct processing," J. Acoust. Soc. Am., **153**, 2223–2237. doi:10.1121/10.0017786

Geroski, D. J., and Worthmann, B. M. (**2021**). "Frequency-difference autoproduct cross-term analysis and cancellation for improved ambiguity surface robustness," J. Acoust. Soc. Am., **149**, 868–884. doi:10.1121/10.0003383

Gorodetskaya, E. Y., Malekhanov, A. I., Sazontov, A. G., and Vdovicheva, N. K. (**1999**). "Deep-water acoustic coherence at long ranges: theoretical prediction and effects on large-array signal processing," IEEE J. Ocean. Eng., **24**, 156–171. doi:10.1109/48.757268

Gulin, E. P. (**1975**). "Reflection of pulse signals from a rough surface," Sov. Phys. Acoust., **20**, 332–337.

Harper, E. Y., and Labianca, F. M. (**1975**). "Perturbation theory for scattering of sound from a point source by a moving rough surface in the presence of refraction," J. Acoust. Soc. Am., **57**, 1044–1051. doi:10.1121/1.380572

Hasselmann, K., Munk, W., and MacDonald, G. J. (**1963**). "Bispectra of Ocean Waves," Proc. Symp. Time Series Analysis, 125-139.

Heaney, K. D. (**2011**). "Shallow water narrowband coherence measurements in the Florida Strait," J. Acoust. Soc. Amer., **129**, 2026–2041. doi:10.1121/1.3557048

Helton, J. C., and Davis, F. J. (**2003**). "Latin hypercube sampling and the propagation of uncertainty in analyses of complex systems," Reliab. Eng. Syst. Saf., **81**, 23–69. doi:10.1016/S0951-8320(03)00058-9

Holbrook, S., Kent, G., Keranen, K., Johnson, P., Trehu, A., Tobin, H., Caplan-Auerbach, J., et al. (**2012**). "COAST: Cascadia Open-Access Seismic Transects," GeoPRISMS News. Issue No. 29.

Hotkani, M. M., Bousquet, J. F., Seyedin, S. A., Martin, B., and Malekshahi, E. (**2021**). "Underwater Target Localization Using Opportunistic Ship Noise Recorded on a Compact Hydrophone Array," Acoust., **3**, 611–629. doi:10.3390/acoustics3040039

Huynen, J. R. (**1965**). “Measurement of the target scattering matrix,” Proc. IEEE, **53**, 936–946.

Ishimaru, A. (**1978**). *Wave Propagation and Scattering in Random Media*, New York: Academic Press, Vol. 2.

Jensen, F. B., Kuperman, W. A., Porter, M. B., and Schmidt, H. (**2011**). *Computational Ocean Acoustics*, Springer, New York, 2nd ed.

Jin, J.-M. (**2010**). *Theory and Computation of Electromagnetic Fields*, John Wiley & Sons, Inc.

Jones, A. D., Sendt, J., Duncan, A. J., Clarke, P. A., and Maggi, A. (**2009**). “Modelling the acoustic reflection loss at the rough ocean surface,” Proc. Acoust., 1–8.

Joslyn, N., Dahl, P. H., and Dowling, D. R. (**2023**). “Coherent reflection recovery in scattering from the ocean surface using the frequency-difference autoproduct,” J. Acoust. Soc. Am. **In Progress.**

Joslyn, N. J., Douglass, A. S., and Dowling, D. R. (**2022**). “Spatial Coherence Comparisons between the Acoustic Field and Its Frequency-Difference and Frequency-Sum Autoproducts in the Ocean,” Acoust., **4**, 764–782. doi:10.3390/acoustics4030046

Joslyn, N. J., and Dowling, D. R. (**2022**). “Recovery of coherent reflection from rough-surface scattered acoustic fields via the frequency-difference autoproduct,” J. Acoust. Soc. Am., **151**, 620–633. doi:10.1121/10.0009318

Kinsler, L. E., Frey, A. R., Coppens, A. B., and Sanders, J. V. (**2000**). *Fundamentals of Acoustics*, Wiley and Sons, New York.

Kucukosmanoglu, M., Colosi, J. A., Worcester, P. F., Dzieciuch, M. A., Olson, D. R., Richards, E. L., and Miller, C. W. (**2022**). “Beaufort Sea observations of 11 to 12.5 kHz surface pulse reflections near 50 degree grazing angle from summer 2016 to summer 2017,” J. Acoust. Soc. Am., **151**, 106–125. doi:10.1121/10.0009164

Lee, J.-H., Park, Y., and Gerstoft, P. (**2023**). “Compressive frequency-difference direction-of-arrival estimation,” J. Acoust. Soc. Am., **154**, 141–151. doi:10.1121/10.0020053

Li, H., and Johnson, J. T. (**2017**). “On the Amplitude Distributions of Bistatic Scattered Fields from Rough Surfaces,” IEEE Trans. Geo. Rem. Sens., **55**, 6883–6892. doi:10.1109/TGRS.2017.2735862

Lin, Y.-C., Sarabandi, K., and Member, S. (**1999**). “A Monte Carlo Coherent Scattering Model For Forest Canopies Using Fractal-Generated Trees,” IEEE Trans. Geo. Rem. Sens., **37**, 440–451.

Lipa, J. E., Worthmann, B. M., and Dowling, D. R. (**2018**). “Measurement of autoproduct fields in a Lloyd’s mirror environment,” J. Acoust. Soc. Amer., **143**, 2419–2427. doi:10.1121/1.5032200

Lohmann, A. W., and Wirnitzer, B. (**1984**). "Triple Correlations," Proc. IEEE, **72**, 889–901.

Lunkov, A. A., and Petnikov, V. G. (**2014**). "The coherence of low-frequency sound in shallow water in the presence of internal waves," Acoust. Phys., **60**, 61–71. doi:10.1134/S1063771014010096

Lynch, P. J. (**1970**). "Curvature Corrections to Rough-Surface Scattering at High Frequencies," J. Acoust. Soc. Am., **47**, 804–815. doi:10.1121/1.1911963

Lynch, P. J., and Wagner, R. J. (**1970**). "Rough-surface scattering: Shadowing, multiple scatter, and energy conservation," J. Math. Phys., **11**, 3032–3042. doi:10.1063/1.1665090

McDaniel, S. T. (**1992**). "High-Frequency Forward Scatter from Arctic Ice: Temporal Response," IEEE J. Ocean. Eng., **17**, 216–221.

McDaniel, S. T. (**2004**). "Geometrical Optics Prediction of Surface Scattering Statistics," IEEE Trans. Geo. Rem. Sens., **42**, 361–366. doi:10.1109/TGRS.2003.817687

McDonald, J. F. (**1974**). "Fresnel-Corrected Second-Order Interfrequency Correlations for a Surface-Scatter Channel," IEEE Trans. Comm., **22**, 138–145.

Medwin, H., and Clay, C. S. (**1998**). *Fundamentals of Acoustical Oceanography*, Academic Press, New York.

Meecham, W. C. (**1956**). "On the use of the Kirchhoff approximation for the solution of reflection problems," J. Rat. Mech. Anal., **5**, 323–334.

Meng, Y. S., and Lee, Y. H. (**2010**). "Investigations of Foliage Effect on Modern Wireless Communication Systems: A Review," Prog. Electromag. Res., **105**, 313–332.

Meng, Y. S., Lee, Y. H., and Ng, B. C. (**2009**). "Study of propagation loss prediction in forest environment," Prog. In Electromagnetics Research B, **17**, 117-133. doi: 10.2528/PIERB09071901. doi:10.2528/PIERB09071901

Morelia, G. L. (**1994**). "A Review of Signal Detection Using the Bispectrum with Applications in Underwater Acoustics," Tech. Rep. ARL–Penn. State.

Morgan, D. R., and Smith, T. M. (**1990**). "Coherence effects on the detection performance of quadratic array processors, with applications to large-array matched-field beamforming," J. Acoust. Soc. Amer., **87**, 737–747. doi:10.1121/1.398888

Mu, T., and Song, Y. (**2019**). "Time reversal imaging based on joint space-frequency and frequency-frequency data," Int. J. Microw. Wireless Tech., **11**, 207–214. doi:10.1017/S1759078718001691

Neo, J. C., Fan, W., Huang, Y., and Dowling, D. (**2022**). "Frequency-difference backprojection of earthquakes," Geophys. J. Int., **231**, 2173–2185. doi:10.1093/gji/ggac323

O'Brien, M. J., Burkhart, B., and Shelley, M. J. (**2022**). "Studying Interstellar Turbulence Driving Scales Using the Bispectrum," Astrophys. J., **930**, 149. doi:10.3847/1538-4357/ac6502

Oglivy, J. A. (**1991**). *Theory of Wave Scattering from Random Rough Surfaces*, IOP Publishing Ltd., Bristol.

Olson, D. R. (**2021**). "A series approximation to the Kirchhoff integral for Gaussian and exponential roughness covariance functions," J. Acoust. Soc. Am., **149**, 4239–4247. doi:10.1121/10.0005282

Olson, D. R. (**2023**). "The effect of seafloor roughness on passive estimates of the seabed reflection coefficient," J. Acoust. Soc. Am., **153**, 586–601. doi:10.1121/10.0016846

Olson, D. R., and Jackson, D. (**2020**). "Scattering from layered seafloors: Comparisons between theory and integral equations," J. Acoust. Soc. Am., **148**, 2086–2095. doi:10.1121/10.0002164

Papoulis, A. (**1984**). *Probability, Random Variables, and Stochastic Processes*, McGraw-Hill, New York, 2nd ed.

Park, Y., Gerstoft, P., and Lee, J. H. (**2022**). "Difference-Frequency MUSIC for DOAs," IEEE Sig. Proc. Lett., **29**, 2612–2616. doi:10.1109/LSP.2022.3230365

Petroff, A. (**2012**). "A Practical, High Performance Ultra-Wideband Radar Platform," IEEE Radar Conf.

Petroff, A. (**2014**). "Ultra-Wideband: A Tool for Teaching Undergraduates," IEEE Int. Conf. on Ultra-WideBand.

Phillips, O. M. (**1977**). *The Dynamics of the Upper Ocean*, Cambridge U.P., New York, 2nd ed.

Plant, W. J. (**2002**). "A stochastic, multiscale model of microwave backscatter from the ocean," J Geophys Res Oceans, **107**, 3120. doi:10.1029/2001jc000909

Popstefanija, I., Mcqueen, D. S., and Mcintosh, R. E. (**1993**). "A Stepped-Frequency Delta-K Microwave Radar for Oceanographic Studies," IEEE Trans. Geo. Rem. Sens., **31**, 681-691.

Porter, M. B., and Bucker, H. P. (**1987**). "Gaussian beam tracing for computing ocean acoustic fields," J. Acoust. Soc. Am., **82**, 1349–1359. doi:10.1121/1.395269

Rawat, M., Lall, B., and Srirangarajan, S. (**2020**). "Angle of Arrival Distribution in an Underwater Acoustic Communication Channel with Incoherent Scattering," IEEE Access, **8**, 133204–133211. doi:10.1109/ACCESS.2020.3008602

Richards, E. L., Song, H. C., and Hodgkiss, W. S. (**2018**). "Acoustic scattering comparison of Kirchhoff approximation to Rayleigh-Fourier method for sinusoidal surface waves at low grazing angles," J. Acoust. Soc. Am., **144**, 1269–1278. doi:10.1121/1.5052256

Richardson, A. M., and Hodgkiss, W. S. (**1994**). "Bispectral analysis of underwater acoustic data," J. Acoust. Soc. Am., **96**, 828–837. doi:10.1121/1.410321

Rohatgi, A. (**2022**). *WebPlotDigitizer*, Available: https://automeris.io/WebPlotDigitizer,.

Rolt, K. D., and Abbot, P. A. (**1997**). "Littoral coherence limitations on acoustic arrays," In S. Lees and L. A. Ferrari (Eds.), Acoust. Imag., Springer, Boston, 537–542.

Sarabandi, K., and Lin, Y.-C. (**2000**). "Simulation of Interferometric SAR Response for Characterizing the Scattering Phase Center Statistics of Forest Canopies," IEEE Trans. Geo. Rem. Sens., **38**, 115–125.

Sarabandi, K., and Member, S. (**1997**). "Radar Equivalent of Interferometric SAR's: A Theoretical Study for Determination of Vegetation Height," IEEE Trans. Geo. Rem. Sens., **35**, 1267-1276.

Sarabandi, K., Member, S., and Nashashibi, A. (**1999**). "Analysis and Applications of Backscattered Frequency Correlation Function," IEEE Trans. Geo. Rem. Sens., **37**, 1895–1906.

Singh, G., Malik, R., Mohanty, S., Rathore, V. S., Yamada, K., Umemura, M., and Yamaguchi, Y. (**2019**). "Seven-Component Scattering Power Decomposition of POLSAR Coherency Matrix," IEEE Trans. Geo. Rem. Sens., **57**, 8371–8382. doi:10.1109/TGRS.2019.2920762

Tang, D., Moum, J. N., Lynch, J. F., Abbot, P., Chapman, R., Dahl, P. H., Duda, T. F., et al. (**2007**). "Shallow Water '06: A Joint Acoustic Propagation/Nonlinear Internal Wave Physics Experiment," Oceanography, **20**, 156–167. doi:10.2307/24860163

Taylor, J. R. (**1997**). *An Introduction to Error Analysis*, University Science Books, Sausalito, 2nd ed.

Thorsos, E. (**1984**). "Surface Forward Scattering and Reflection," Tech. Rep. APL-UW 7-83.

Thorsos, E. I. (**1988**). "The validity of the Kirchhoff approximation for rough surface scattering using a Gaussian roughness spectrum," J. Acoust. Soc. Am., **83**, 78–92. doi:10.1121/1.396188

Thorsos, E. I. (**1990**). "Acoustic scattering from a 'Pierson-Moskowitz' sea surface," J. Acoust. Soc. Am., **88**, 335–349. doi:10.1121/1.399909

Thorsos, E. I., and Broschat, S. L. (**1995**). "An investigation of the small slope approximation for scattering from rough surfaces. Part I. Theory," J. Acoust. Soc. Am., **97**, 2082–2093. doi:10.1121/1.412001

Thorsos, E., and Jackson, D. (**1989**). "The validity of the perturbation approximation for rough surface scattering using a Gaussian roughness spectrum," J. Acoust. Soc. Am., **86**, 261–277. doi:10.1121/1.398342

Tolstoy, M., Diebold, J., Doermann, L., Nooner, S., Webb, S. C., Bohnenstiehl, D. R., Crone, T. J., et al. (**2009**). "Broadband calibration of the R/V Marcus G. Langseth four-string seismic sources," Geochem., Geophys., Geosys. doi: 10.1029/2009GC002451. doi:10.1029/2009GC002451

Urick, R. J. (**1983**). *Principles of Underwater Sound*, McGraw-Hill, New York, 3rd ed.

Van Veen, B. D., and Buckley, K. M. (**1988**). "Beamforming: A Versatile Approach to Spatial Filtering," IEEE ASSP Mag., **5**, 4–24.

Wan, L., Zhou, J. X., Rogers, P. H., and Knobles, D. P. (**2009**). "Spatial coherence measurements from two L-shape arrays in Shallow Water," Acoust. Phys., **55**, 383–392. doi:10.1134/S1063771009030142

Wang, F., and Sarabandi, K. (**2007**). "A physics-based statistical model for wave propagation through foliage," IEEE Trans. Antennas Propag., **55**, 958–968. doi:10.1109/TAP.2007.891841

Wang, S. Y., and Tang, M. X. (**2004**). "Exact Confidence Interval for Magnitude-Squared Coherence Estimates," IEEE Sig. Process. Lett., **11**, 326–329. doi:10.1109/LSP.2003.822897

Wang, X., Sun, H., Zhang, L., Dong, C., and Guo, L. (**2022**). "Unambiguous broadband direction of arrival estimation based on improved extended frequency-difference method," J. Acoust. Soc. Am., **152**, 3281–3293. doi:10.1121/10.0016364

Weissman, D. E. (**1973**). "Two Frequency Radar Interferometry Applied to the Measurement of Ocean Wave Height," IEEE Trans. Antennas Prop., **21**, 649–656.

Welton, P. J. (**2015**). "Cross Correlation of Omnidirectional, Broadband Signals Scattered by a Random Pressure-Release Surface," IEEE J. Ocean Eng., **40**, 485–494. doi:10.1109/JOE.2014.2321511

Westervelt, P. J. (**1963**). "Parametric Acoustic Array," J. Acoust. Soc. Am., **35**, 535–537. doi:10.1121/1.1918525

Williams, K. L., Thorsos, E. I., and Elam, W. T. (**2004**). "Examination of coherent surface reflection coefficient (CSRC) approximations in shallow water propagation," J. Acoust. Soc. Am., **116**, 1975–1984. doi:10.1121/1.1785617

Wolfram Research, Inc. (**2022**). "Mathematica."

Worthmann, B. M., and Dowling, D. R. (**2017**). "The frequency-difference and frequency-sum acoustic-field autoproducts," J. Acoust. Soc. Amer., **141**, 4579–4590. doi:10.1121/1.4985440

Worthmann, B. M., and Dowling, D. R. (**2020a**). "Autoproducts in and near acoustic shadow zones created by barriers," J. Acoust. Soc. Am., **147**, 1863–1873. doi:10.1121/10.0000953

Worthmann, B. M., and Dowling, D. R. (**2020b**). “The effects of refraction and caustics on autoproducts,” J. Acoust. Soc. Am., **147**, 3959–3968. doi:10.1121/10.0001399

Worthmann, B. M., Song, H. C., and Dowling, D. R. (**2015**). “High frequency source localization in a shallow ocean sound channel using frequency difference matched field processing,” J. Acoust. Soc. Amer., **138**, 3549–3562. doi:10.1121/1.4936856

Worthmann, B. M., Song, H. C., and Dowling, D. R. (**2017**). “Adaptive frequency-difference matched field processing for high frequency source localization in a noisy shallow ocean,” J. Acoust. Soc. Amer., **141**, 543–556. doi:10.1121/1.4973955

Xie, L., Sun, C., and Tian, J. (**2020**). “Deconvolved frequency-difference beamforming for a linear array,” J. Acoust. Soc. Am., **148**, EL440–EL446. doi:10.1121/10.0002927

Yang, L., Wang, Y., and Yang, Y. (**2021**). “Aliasing-free broadband direction of arrival estimation using a frequency-difference technique,” J. Acoust. Soc. Am., **150**, 4256–4267. doi:10.1121/10.0008900

Yang, W., Liang, Y., Leng, J., and Li, M. (**2020**). “The Autocorrelation Function Obtained from the Pierson-Moskowitz Spectrum,” Global Oceans 2020: Singapore - U.S. Gulf Coast, 1–4. doi:10.1109/IEEECONF38699.2020.9389043

Yuan, Z., Niu, H., Li, Z., and Luo, W. (**2023**). “Difference frequency coherent matched autoproduct processing for source localization in deep ocean,” J. Acoust. Soc. Am., **153**, 2131–2147. doi:10.1121/10.0017788

Zhai, S., and Jiang, T. (**2013**). “A novel sense-through-foliage target recognition system based on sparse representation and improved particle swarm optimization-based support vector machine,” Measurement, **46**, 3994–4004. doi:10.1016/j.measurement.2013.08.018

Zhai, S., and Jiang, T. (**2014**). “Target detection and classification by measuring and processing bistatic UWB radar signal,” Measurement, **47**, 547–557. doi:10.1016/j.measurement.2013.08.031

Zhang, Y., Anderson, C. R., Michelusi, N., Love, D. J., Baker, K. R., and Krogmeier, J. V. (**2019**). “Propagation Modeling Through Foliage in a Coniferous Forest at 28 GHz,” IEEE Wireless Comm. Lett., **8**, 901–904. doi:10.1109/LWC.2019.2899299

Zhao, G., Liang, Q., and Durrani, T. S. (**2018**). “An EMD Based Sense-Through-Foliage Target Detection UWB Radar Sensor Networks,” IEEE Access, **6**, 29254–29261. doi:10.1109/ACCESS.2018.2841900

Ziadé, Y., Roussel, H., Lesturgie, M., and Tabbara, W. (**2008**). “A coherent model of forest propagation - Application to detection and localization of targets using the DORT method,” IEEE Trans. Antennas Prop., **56**, 1048–1057. doi:10.1109/TAP.2008.919150

Zoubir, A. M. (**2005**). “On confidence intervals for the coherence function,” In Proc. of ICASSP, IEEE Int. Conf. Acoust., Speech, and Sig. Proc., iv/413-iv/416. doi:10.1109/ICASSP.2005.1416033